Curso 2009/10
CIENCIAS Y TECNOLOGÍAS/18
I.S.B.N.: 978-84-7756-959-6

MARKUS RABUS

Estudio de planetas extrasolares por el método de tránsitos

Directores
JUAN ANTONIO BELMONTE
HANS J. DEEG

SERVICIO DE PUBLICACIONES
UNIVERSIDAD DE LA LAGUNA

SOPORTES AUDIOVISUALES E INFORMÁTICOS
Serie Tesis Doctorales

Für meinen Vater

Acknowledgments

En primer lugar quiero agradecer a Juan y a Hans por su esfuerzo, por su ayuda y por aceptarme como su estudiante. Gracias, Juan, por todas las correciones, y gracias a los dos por tener siempre la puerta de sus despachos abierta cuando les necesitaba. *"Danke Hans für die vielen hilfreichen Erklärungen."* Gracias a Roi y Jose por ayudarme con mis primeros pasos en astronomía. Roi tenía siempre buenas ideas para resolver problemas y Jose me enseñó como hacer buena fotometría, especialmente con STARE. Agradezco los consejos de los otros miembros del grupo SSEBE (Pere, Teo, Clara, Chano, Antonio –Eff-Darwich y Jiménez–, Fernando, Héctor, Rosa y David). Agradezco a Adriana sus correcciones de mi español para la memoria del DEA. El tiempo pasado junto a Maria Rosa y Nacho organizando los seminarios ha sido muy agradable. Estoy muy agradecido a Alex no solo por su continuo apoyo con STARE y sus problemas sino también por proporcionarme un acceso fácil a los telescopios del OT cuando me eran necesarios. Este hecho me ha permitido acabar mi tesis en un tiempo adecuado y con buenos datos. En este sentido, también quiero agradezer el buen trabajo que han hecho los astrónomos de soporte, los operadores y el personal de mantenimiento. Gracias al resto del personal del OT por proporcionarme un coche, una cama y un techo siempre que me hacían falta. La gestora del área de investigación (Irene), y su secretariado (Tanja, Eva y Judith) siempre fueron muy amables conmigo. Finalmente, gracias al evaluador interno del departamento, Enric, por sus interesantes sugerencias que han mejorado este trabajo.

Je tiens à remercier le groupe français à l'IAP pour l'accueil chaleureux. François particulièrement pour l'enseignement des observations spectroscopiques. Ainsi que le reste du groupe Guillaume, Alfred, Roger, Alain, Isabelle, David (Sing et Ehrenreich) et Jean-Michel. Je tiens également à remercier les personnes de l'OHP. J'ai eu un très agréable séjour. Je remercie Chantal pour son aide lors de mon séjour à Paris, en particulier pour la trés belle chambre à la cité uni-

versitaire. Enfin, je tiens à remercier Dr. Robert Mochkovitch pour m'accepter comme boursier Marie Curie.
I would like to thank Orlagh and Brandon for their English corrections and their support along these years, as well as a number of American colleagues. First and foremost, Tim, for letting me use the STARE telescope. Additional thanks go to: Ron (for the HST light curve of TrES-1, I could not have done the paper on this topic without you), Dave Latham (for doing most of the low resolution spectroscopic follow-up work), Georgi (for helping me improving my STARE pipeline), Dave Charbonneau (for organizing the yearly TrES-meetings), Francis and Ted (for all the helpful explanations).
Ein Dankeschön auch an meine Familie!

Markus

Resumen

1. Introdución

El primer planeta extrasolar fue descubierto en 1992 por Aleksander Wolszczan y Dale Frail (Wolszczan & Frail, 1992). Este exoplaneta órbita el pulsar PSR B1257+12 y fue detectado usando el método de "pulsar timing". Tres años después, en 1995, Michel Mayor y Didier Queloz anunciaron el descubrimiento del primer exoplaneta alrededor de una estrella de tipo solar, 51 Pegasi (Mayor & Queloz, 1995). El primer planeta con tránsitos se detectó en 2000 (Charbonneau et al., 2000; Henry et al., 2000) y recibe el nombre de HD 209458b. Desde la detección del tránsito del exoplaneta HD 209458b sabemos que somos capaces de detectar planetas con el método de tránsitos y desde entonces muchos proyectos han empezado la búsqueda de planetas extrasolares en que se dé esta fenomenología. El primer grupo en tener éxito ha sido el experimento OGLE con el planeta OGLE-TR-56b (Udalski et al., 2002; Konacki et al., 2003).
Hasta ahora el numero de exoplanetas con tránsitos sigue aumentando. La mayoría de los planetas extrasolares se han encontrado utilizando el método de velocidades radiales que nos da la masa $M_P \sin i$, pero en los cuales la inclinación i es desconocida. Sin embargo, gracias a una curva de luz de un tránsito, se puede romper la degeneración de $M_P \sin i$ y, por ejemplo, determinar los radios. Los planetas encontrados con el método de tránsitos son en la actualidad los exoplanetas más estudiados y mejor conocidos. Los estudios realizados por diversos equipos de investigación han permitido conocer los parámetros de los planetas en tránsito y de sus estrellas centrales con una precisión exquisita para realizar búsquedas de hipotéticos satélites orbitando en torno a sus planetas e incluso detectar componentes de la atmósfera.
En el presente, solo el método de tránsitos permite investigar la atmósfera planetaria y por eso es muy útil para comprobar modelos de gigantes gaseosos, como por ejemplo HD 209458b. Los últimos estudios parecen probar que la alta atmósfera de HD 209458b se halla en proceso de evaporación debido a su cer-

canía a la estrella. Sin embargo, parece que hay una cierta discrepancia entre el tamaño medido del exoplaneta y el que debería tener de acuerdo con los modelos de formación y evolución de los mismos. El radio medido para HD 209458b es entre un 20 % y un 30 % mayor que el predicho por estos modelos. Por lo tanto, las investigaciones comenzaron estudiar la atmósfera des estos Jupiteres calientes inflados. Varias teorías para explicar estos Jupiteres calientes inflados han sido presentadas. La mayoría de las teorías se concentran en la búsqueda de una nueva fuente de energía en el planeta que pueda aumenta el radio.
Además, no se esperaba la cercanía de estos planetas a su estrella matriz y por ello se ha de admitir que no se comprende bien su proceso de formación. Por tanto, las observaciones de tránsitos pueden ayudar a delimitar los parámetros de los modelos de formación de exoplanetas en órbitas muy cercanas a la estrella central. Hasta ahora hay dos escenarios diferentes de formación. Uno es el de acreción de núcleos rocosos y el otro el de inestabilidad de discos protoplanetarios. Además se ha desarrollado la teoría de migración planetaria, ya que las teorías estándares no permiten la formación de planetas en órbitas intramercurianas. Sin embargo, esta teoría aún tiene muchos problemas como, por ejemplo, cuál sería el mecanismo que detiene la migración. Descubrimientos y caracterizaciones detalladas de planetas gigantes calientes adicionales pueden ayudar a resolver estos problemas, por ejemplo, mejorando nuestros conocimientos sobre su ecuación de estado, y permitiendo imponer límites a la validez de algunos de estos modelos. El descubrimiento de nuevos exoplanetas podría demostrar que en promedio los planetas con un periodo más corto son más masivos y de esta forma se podría sugerir una evolución diferente a la de la migración canónica para estos sistemas planetarios (Wuchterl, 2007).
El límite superior de masa distingue a los planetas de las enanas marrones y otras estrellas enanas. Recientemente el Grupo de Trabajo de Planetas Extrasolares (WGESP) de la Unión Astronómica Internacional ha definido un planeta como un objeto con una masa por debajo del límite de la fusión del deuterio y el hidrógeno (generalmente se acepta que es de 13 M_J para objetos con metalicidad solar) que está orbitando una estrella o remanente estelar, independientemente de cómo se haya formado. Sin embargo, los "Free-floating objects" ("objeto en flotación libre") que se encuentran en cúmulos estelares jóvenes aun con masas por debajo del límite para fusionar deuterio e hidrógeno no son calificados como planetas sino como subenanas marrones. Los planetas extrasolares son por tanto y de forma obvia planetas orbitando alrededor de estrellas diferentes al Sol.
Los planetas extrasolares brillan solamente gracias a la luz reflejada y absorbida de la estrella matriz y por lo tanto su luminosidad es del orden de mil millones de veces más débil en el oṕtico que el de su estrella. Su falta de brillo y su

distancia provocan que su detección por imagen directa sea difícil. Por eso se tiene que pensar en otros métodos para su detección. De todos los métodos de detección, los más importantes son el método de tránsitos y el de velocidades radiales.

El método de velocidades radiales consiste en detectar planetas extrasolares de manera indirecta en la medida de la perturbación gravitatoria de la estrella matriz causada por el exoplaneta. Por ejemplo, Júpiter da una vuelta al Sol en 11.9 años en una órbita de 5.2 UA y con una velocidad de 13 km s^{-1} respecto al centro de gravedad del sistema. Ese movimiento hace que el Sol gire alrededor del centro de gravedad del sistema con el mismo periodo pero a una distancia de solo 0.005 UA (aproximadamente 1 $R_\odot$) y con una velocidad de 12 m s^{-1}. La velocidad radial se obtiene gracias al efecto Doppler por el que una onda electromagnética emitida por un objeto en movimiento con velocidad v cambia su longitud correspondiente a $\frac{v}{c} = \frac{\lambda - \lambda_0}{\lambda_0}$. Si medimos la velocidad radial en puntos de fase distintos, se puede hacer un ajuste suponiendo órbitas keplerianas. El ajuste y las efemérides resultantes se pueden comparar con los de la curva de luz (en caso que existe un tránsito) y confirmar de esta forma el carácter planetario.

En el método de tránsitos el planeta atraviesa entre el observador y la estrella y causa una disminución de la luminosidad estellar del orden de un 1%, que se refleja en la curva del luz. Ésta se puede describir con tres parámetros: la profundidad del tránsito ΔF, su duración t_T y su forma. La forma de la curva de luz depende de la latitud del tránsito en el disco de la estrella, es decir que depende de la inclinación i de la órbita del planeta. También se puede determinar de la curva de luz un término $\frac{a}{R_*}\cos i$, al que se suele denominar b, el parámetro de impacto, y que es la distancia proyectada del centro del planeta al centro de la estrella en el momento del acercamiento máximo, en unidades del radio de la estrella. El ingreso se define como la fase entre el primer contacto hasta que el planeta se encuentra por completo sobre el disco estelar (segundo contacto) y el egreso como su opuesto. El parámetro de duración del ingreso t_i viene determinado por la duración del tránsito t_T, la relación de los radios y el parámetro de impacto b. La curva de luz tiene una forma similar a una "U" si el planeta pasa por el centro de la estrella, es decir, para $i \approx 90°$, y una forma como una "V" si el ecplise es rasante. Gracias a la curva de luz se puede deducir el cociente entre el radio del planeta R_p y el de la estrella R_*, la inclinación i (o bien el parámetro de impacto b), y con conocimiento de la masa de la estrella, el radio de la órbita a.

Por un lado, un tránsito es un evento raro y por otro lado, las mediciones de velocidad radial tienen la ventaja de ser capaz de detectar exoplanetas, independientemente de su inclinación, pero uno tiene que observar las estrellas, una por

una. Mientras que en las busquedades por tránsitos se puede observar miles de estrellas simultáneamente, aumentando las probabilidades de detectar un tránsito en las observaciones. Generalmente, en las busquedades fotométricas se observa el mayor número posible de estrellas durante un largo período de tiempo y se generan series de tiempos de flujos en los cuales se buscan posibles disminuciones de flujo, es decir, eventos de tránsito.
Con el fin de observar el mayor número posible de estrellas, hay dos opciones extremos: por uno lado, se observan estrellas brillantes con telescopios de pequeña apertura, pero con un amplio campo de visión, y por otro lado, se observan estrellas débiles con telescopio de gran tamaño, en busquedades de campos profundos, teniendo en cuenta el efecto de volumen, es decir, el número de estrellas que aumenta con la disminución de flujo. Busquedas fotométricas detectan preferentemente exoplanetas en órbitas más pequeñas, debido a las órbitas pequeñas teniendo más probabilidades de tener una configuración eclipsante y además las posibilidades de observar más tránsitos aumentan, lo cual contribuye a mejorar la detección. Sin embargo, el inconveniente de las busquedades fotométricas es la alta tasa de detección de falsas alarmas de origen astrofísico. Podemos distinguir varios de los casos principales de falsas alarmas:

- Binaria eclipsante rasante compuesta de dos estrellas de la secuencia principal;
- Estrella de baja masa transitando una estrella mayor;
- Sistema binario eclipsante diluido por la luz de una estrella más brillante;

Brown (2003) estimó las frecuencias esperadas de detección, tanto de exoplanetas como de falsas alarmas en búsquedas fotométricas. Para un proyecto como STARE (ver capítulo 2) en un campo del plano galáctico, se estima que debería haber 1.4 exoplanetas en tránsito y 7.2 alarmas falsas por cada 10000 estrellas observadas con una precisión mejor que 0.01 magnitudes. Para investigar la verdadera naturaleza de los candidatos se emplea diferentes herramientos y observaciones de seguimiento.
Las binarias eclipsantes rasantes consisten en dos estrellas con una órbita en un ángulo muy inclinado que puede producir un eclipse de baja amplitud en la curva de luz. Esos casos son en su mayoría más profundos como tránsitos de planetas y, por tanto, más fáciles de distinguir. Típicamente exhiben también eclipses primarios y secundarios de profundidad diferente. Además, la forma de la curva de luz (como una "V") o ciertas modulaciones elípticas a causa de los efectos gravitatorios sobre la superficie de la binaria pueden distingir también este tipo de alarmas falsas. Otra forma de detectarlas es mediante el propio

ajuste de la curva de luz al determinar los parámetros "duración" y "profundidad" del tránsito planetario, pues ambos deben coincidir en un mismo valor del radio para el exoplaneta. Finalmente, las observaciones espectroscópicas normalmente nos ofrecen dos conjuntos de líneas espectrales diferentes en las binarias.
Un acompañante de baja masa, por ejemplo una enana M, transitando una estrella más grande, por ejemplo de la secuencia principal, puede producir una señal fotométrica similar a la de un planeta, porque la relación R_{*2}/R_{*1} es similar a R_P/R_*. Sin embargo, se resuelve este caso fácilmente velocidades radiales de baja precisión del orden de km s^{-1}.
Una binaria diluida consiste en un sistema doble y una tercera estrella en la misma línea visual de forma que todo el conjunto aparece como una única estrella que no se puede resolver con fotometría. Sin embargo, un sistema diluido se puede discriminar con espectroscopia de alta resolución debido a la casi segura presencia de diferentes líneas espectrales. Sin embargo, aun es posible que las líneas espectrales de la binaria sean mucho más débiles en comparación con las de la tercera estrella y que no se puedan detectar las variaciones de velocidad radial de la binaria. Estas variaciones también se pueden disimular por el ensanchamiento de las líneas espectrales. Para evitar estos problemas, Torres et al. (2004) han propuesto hacer un espectro detallado y analizar la asimetría de los bisectores de las líneas como indicación de la existencia de la binaria. Finalmente, también es posible eliminar estas alarmas falsas si el sistema binario tiene una diferencia significativa de temperatura con la tercera estrella pues, en este caso, el eclipse debe mostrar una dependencia de la profundidad con el color, o en muchos casos, se pueden detectar eclipses primarios y secundarios de profundidad diferente.

2. La red TrES

El capítulo 2 de la tesis está dedicado a la red TrES. La red TrES consiste en tres telescopios de gran campo. El objetivo de la red es encontrar tránsitos de planetas extrasolares alrededor de estrellas brillantes. Dos telescopios están situados en EE.UU. Uno de ellos es la cámara PSST (Planet Search Survey Telescope) situada en el Observatorio de Lowell en Arizona operada por G. Mandushev. El instrumento usa una lente de f/2.8 con una apertura de 10 cm; el campo de visión es de $6° \times 6°$ y la CCD tiene 2k $\times$ 2k píxeles. El telescopio 'Sleuth', situado en el observatorio de Mt. Palomar tenía una óptica similar al PSST, pero se ha sustituido en 2007 por el 'WATTS', situado en Texas. El tercer instrumento es el STARE, un telescopio situado en el Observatorio del Teide desde 2001, el más antiguo de la red, con lo cual se realizarón nues-

tras observaciones regularmente. Generalmente, STARE observa junto con sus homólogos el mismo campo durante meses para obtener una buena cobertura, con el fin de obtener una probabilidad alta de observar una cierta cantidad de tránsitos planetarios con un periodo de menos de ~ 5 días.
En las observaciones se supone que los "flats" y "darks" son estables durante meses y por eso se los toman solo al principio de cada campaña con un campo nuevo. Los flats tienen dos funciones: por un lado, corrigen por el tiempo de apertura del obturador, y por otro lado, aplanan el campo. Por lo tanto, se toman dos flats diferentes, un flat con tiempo de exposición corto y otro con tiempo de exposición largo. Adicionalmente, al principio de cada noche se toma imágenes de bias que proporcionan el mapeado del nivel cero mientras que la región de "overscan" proporciona el nivel cero instantáneo de cada imagen. Los primeros pasos en la calibración de las imágenes se obtienen mediante la sustracción del bias y del "overscan", seguido de la corrección de los "darks" y del proceso de "flat-fielding".
Un proceso importante es la construcción para cada campo de una "master star list" (lista maestra de estrellas) mediante una imagen de referencia obtenida en una noche fotométrica y sin luna. A esta imagen se le aplica fotometría ajustando una PSF usando DAOPHOT/ALLSTAR (Stetson, 1987, 1992). Esta fotometría tiene la ventaja de que produce un centroide y magnitudes de referencia con alta precisión, que necesitaremos luego para la substracción de las imágenes. La lista así obtenida es nuestra "master star list" y estos datos se usan como referencia para la posición y la fotometría para los siguientes pasos del proceso.
Actualmente, el análisis de los datos se basa en el método de Alard de substracción óptima de imágenes, "optimal image substraction" (Alard & Lupton, 1998; Alard, 2000). El resultado de la substracción son imágenes que contienen solo la diferencia respecto a la imagen de referencia. Entonces aplicamos fotometría de apertura a cada imagen de diferencia y obtenemos para cada estrella de la imagen una diferencia en flujo $\Delta F_{s,i}$ y un error estándar $\sigma_{\Delta F_{s,i}}$. Con este procedimiento obtenemos las curvas de luz.
Las curvas de luz muestran errores sistemáticos (Pont, 2006; Pont et al., 2006). Hay diferentes algoritmos para intentar subsanarlos. Los algoritmos más frecuentes son el "Trend-Filtering Algorithm" (TFA; Kovács et al. 2005, Kovacs & Bakos 2006) y el algoritmo "SysRem" (Tamuz et al., 2005; Mazeh et al., 2006b,a). Para STARE usamos un algoritmo propio de decorrelación, desarrollado por G. Mandushev. Para STARE los errores sistemáticos aumentan el nivel de ruido en un orden de 2.5, siendo poco dependientes del brillo de las estrellas.
Después de la decorrelación se promedian las curvas de luz en 0.0062 d ($\sim$ 9

min.) y se buscan tránsitos en las curvas de luz. Para la búsqueda se usa el algoritmo "Box-fitting Least Squares" (BLS) (Kovács et al., 2002). Este algoritmo busca señales que alternen entre dos niveles diferentes, normalmente un nivel alto (H) y uno bajo (L), es decir, por ejemplo la parte fuera y dentro de un tránsito planetario. Se ajusta una función de caja a la curva de luz doblada en fase y se calcula un índice para la presencia de una señal SR para cada periodo de prueba. Para evaluar las detecciones se define la eficiencia de detección de señal (SDE) que se puede considerar como un valor umbral. Al final se lleva a cabo una inspección visual de las curvas de luz con los SDE más altos que proporciona el algoritmo.
Sin embargo en la lista de los candidatos hay muchas falsas alarmas como hemos descrito en capítulo 1. Para eliminar las falsas alarmas se investigan las curvas de luz en más detalle. Primero se estiman las densidades de las estrellas a partir de un ajuste de la curva de luz de forma de trapezoide que simula el tránsito. Esta densidad se compara con la estimada a partir de tipos espectrales basado en los colores J-K del catálogo 2MASS. Otra de las formas de eliminar falsas alarmas es detectar una modulación fuera del eclipse debido a la variabilidad provocada por la forma elíptica de la estrella (Sirko & Paczyński, 2003) o debido a luz reflejada. Para esto se ajusta una ecuación con diferentes senos y cosenos a la parte fuera del tránsito.
Después de la inspección de las curvas de luz se empiezan las observaciones de seguimiento. Para la fotometría de alta precisión usamos el telescopio IAC80. Estas observaciones sirven para resolver una posible sobreposición de las estrellas en las cámaras con pequeñas aperturas. STARE, por ejemplo, cuenta con una PSF en las imágenes de ≈ 9 segundos de arco y cada estrella dentro de esta PSF aparecerá en las imágenes como una única estrella. Considerando que el IAC80 tiene una escala de píxeles de 0.3 segundos de arco/pixel y normalmente observamos sólo ligeramente fuera de foco con una anchura a mitad de altura entre 4 y 6 píxeles, por lo tanto podemos resolver con el IAC80 entre 1.2 y 1.8 segundos de arco y en el caso de que más de una estrella caiga en la apertura de la fotometría del STARE, podemos determinar cual estrella muestra el eclipse. Otra aplicación es observar el tránsito en más de un filtro. Esto ayuda a descartar posibles binarias eclipsantes. En el caso de las binarias eclipsantes y si las estrellas tienen diferentes temperaturas, la profundidad del tránsito dependerá del color y si se trata de un planeta la profundidad debería ser la misma. Finalmente, en el caso de un planeta en tránsito, esta curva de luz de alta precisión nos ayuda a obtener estimaciones precisas de los parámetros. Por lo tanto, a las curvas de luz se está aplicando un modelo de tránsito.
Finalmente se observa el candidato con espectroscopía de resolución intermedia y después con alta resolución para obtener las velocidades radiales y

demás parámetros de la estrella como su temperatura efectiva, su velocidad de rotación, su gravedad superficiál y su tipo espectral. A las velocidades radiales se ajusta una orbita kepleriana para obtener la masa en función de la inclinación de la orbita y así se puede finalmente confirmar o rechazar el carácter planetario.

3. Fotometría de alta precisión en el infrarojo

El rango de la longitud de onda infrarroja (IR) se encuentra entre 0.78 y 1 000 μm. La astronomía divide la región espectral de infrarrojo en tres sectores: el infrarrojo cercano (0.9 a 5 μm), el infrarrojo medio (5 a 40 μm) y el infrarojo lejano (40 a 350 μm). La atmósfera es en general opaca en el infrarrojo, aunque hay algunos secciones de IR, llamadas ventanas, donde la transmisión se incrementa. Por lo tanto, las observaciones en el IR desde tierra se centran en estas ventanas. Hay que tener en cuenta que las observaciones terrestres en el IR cercano son bastante estándar, pero las observaciones en el IR medio, con las ventanas entre 8-13 μm y 16-25 μm, siguen siendo difíciles.
Los Júpiteres calientes son objetos que orbitan alrededor de sus estrellas en órbitas de $\leq$ 0.05 UA. Esta proximidad a la estrella es la causa de que estos objetos tengan temperaturas alrededor de 1 000 K y, por tanto, su observación en el rango de longitud de onda infrarroja es más favorable que en la longitud de onda visible. Recientemente, la utilidad de la aplicación de esta técnica se ha demostrado con la detección de un eclipse secundario (de Mooij & Snellen, 2009) en el infrarrojo mediante telescopios terrestres. En lo que sigue, vamos a usar el término tránsito primario, o simplemente 'tránsito', para el paso de un planeta por delante de su estrella central y el término 'eclipse' secundario, o simplemente eclipse, para la ocultación completa de un planeta por parte de su estrella cuando éste transita por detrás de ella.
Las medidas de eclipses secundarios implican la detección de la luz emitida y reflejado por los propios exoplanetas, proporcionando información sobre su temperatura y su albedo. Se distinge una temperatura de equilibria (téoretica) y una temperatura de brillo (observada), que esta relacionada con la profundidad del eclipse secundario, con el fin de comparar ambas. Además, la estimación precisa del tiempo medio o central del eclipse secundario restringe la excentricidad de la órbita del planeta con mejor precisión que basado sólamente en medidas de la velocidad radial.
Para nuestro trabajo hemos utilizado principialmente dos telescopios, el Carlos Sánchez de 1.5m del Observatorio de El Teide (TCS), en la isla de Tenerife, y el William Herschel de 4.2m del Observatorio de El Roque de los Muchachos (WHT), en la isla de La Palma. En el TCS hemos usado el detector CAIN, un instrumento poderoso y versátil diseñado y construido en el IAC. Por otro

lado, en el WHT utilizamos el espectrógrafo infrarrojo de resolución intermedia de rendija larga (LIRIS - Long-slit Intermediate Resolution Infrared Spectrograph). Se trata de una cámara CCD y de un espectrógrafo en el infrarojo cercano, construido y desarrollado también en el IAC.
Por lo general, aplicamos la misma técnica de observación y análisis de datos en ambos telescopios a fin de evitar la saturación del detector por estrellas brillantes y reducir al mínimo el efecto instrumental del detector, empleando un desenfoque del PSF a la forma de un anillo.
Las observaciones de tránsitos primarios en el IR son una herramienta poderosa puesto que se ven menos afectadas por los errores en el efecto de oscurecimiento hacia el borde. El fondo de los tránsitos, observados en el IR, es más plano y los ingresos y egresos de éstos son más angulosos que en el visible. Este hecho permite medir los parámetros de un tránsito, como su tiempo central o su duración, con mucha más precisión ya que normalmente los errores en los parámetros para fotometría de alta precisión estan limitados por el efecto de oscurecimiento hacia el borde.
Por otra parte, la poca profundidad de los eclipses secundarios (por debajo del 1 %) requiere una alta precisión en las observaciones con el fin de detectarlos y así poder estimar sus parámetros, tales como su profundidad, su duración o su tiempo central. A partir de estos parámetros se pueden estimar las propiedades físicas del sistema. Por ejemplo, la profundidad del eclipse es una medida directa de la emision del planeta y por tanto se puede comparar dicha profundidad con la esperada en base a modelos teóricos de la atmósfera, confirmando o señalando los problemas de la modelización.
En el caso de las observaciones de HD 189 733b con el TCS detectados tanto en tránsitos primarios, como eclipses secundarios, hemos demostrado que nuestros datos son consistentes con los de la literatura, es decir, nuestra profundidad del tránsito es de 2.39 %, y podemos descartar la detección de un eclipse secundario significativo por encima de 0.05 %, dentro de un límite de confianza de 2-σ. Se estima una temperatura de equilibrio para un albedo de cero de T_{eq}=1 534 K, indicando una profundidad esperado de 0.03 %, lo cual es consistente con las observaciones para este exoplaneta.
Las observaciones de Corot-2b en el WHT también han dado resultados muy interesantes. De este exoplaneta se ha obtenido un eclipse secundario tentativo en el filtro K_s de 0.16 $\pm$ 0.09 % y un límite superior de un eclipse secundario en el filtro H de 0.17 %. También se estima una tempertura de equilibrio de $T_{eq} = 1964 \pm 35$ K, implicando una profundiad esperada del eclipse secundario en el filtro H de 0.11 % y en el filtro Ks de 0.23 %. Ambas estimaciones son consistentes con las observaciones.
Pasamos a discutir la posibilidad de un segundo planeta en el sistema GJ 436.

Uno de los efectos previstos de un planeta adicional con 4.8 $M_\oplus$ como fue propuesta por Ribas et al. (2008) sería la variación de la inclinación de la órbita (y por lo tanto, la duración total del tránsito) del primer planeta GJ 436b. Para probar este hecho, hemos comparado nuestras observaciones de este exoplaneta con el TCS con un tránsito obtenido con Spitzer, encontrándose una diferencia despreciable de $\Delta i_{obs} = 0.02 \pm 0.04°$ entre ambas. Tampoco encontramos ninguna variación significativa en el tiempo central de tránsito (TTV). Tanto, la baja Δi_{obs} como la ausencia de cambios importantes en el TTV hablan en contra del supuesto planeta de baja masa. Así pues, hemos demostrado para el caso de GJ436c que la precisión de la observación del tránsito en el IR ha sido suficiente para establecer limitaciones a previsiones para otros planetas. Estas observaciones nuestras fueron publicadas por Alonso et al. (2008a).
En resumen, hemos demostrado que las observaciones de tránsitos primarios y de eclipses secundarios en el IR son especialmente útiles para el estudio de los exoplanetas. Las ventajas de observar tránsitos en el infrarrojo, como en los casos de HD 189 733b y GJ 436b, han sido de gran utilidad para el estudio del sistema planetario. Por otra parte, los intentos de observación de los eclipses secundarios de COROT-2b y HD 189 733b, confirmados en algunos casos, nos han permitido especular sobre ciertas propiedades de sus atmósferas.

4. ¿Una mancha o un segundo planeta en el sistema exoplanetario TrES-1?

En el capítulo 4 se investigará el origen de un aumento de flujo durante un tránsito de TrES-1, lo cual fue observado con el HST (Telescopio Espacial de Hubble). Esta característica en la curva de luz de HST no se puede atribuir al ruido y es supuestamente una zona oscura en la superficie de la estrella matriz eclipsada por TrES-1 durante su tránsito. Estamos investigando la posibilidad de dos hipótesis distintas para su origen: una mancha estelar o un segundo planeta en tránsito.
En manchas estelares, campos magnéticos intensos pueden suprimir el flujo convectivo a la superficie, y por lo tanto, en esa zona se irradia menos luz, provocando una región oscura en la superficie estelar. Las manchas pueden cubrir hasta el 55 % de la superficie de una estrella (O'Neal et al., 1998) y en general son entre 500 y 2 000 K más frías que el área circundante. La posibilidad de detectar manchas durante los tránsitos se mencionó por primera vez en Silva (2003). Sus simulaciones mostraron que una mancha total o parcialmente oculta por el planeta en tránsito deja un breve aumento de brillo en la curva de luz del tránsito. El aumento del flujo de la mancha depende de dos parámetros. Por un lado, su duración depende de la evolución de la mancha sobre la su-

perficie estelar, de la velocidad de rotación de la estrella, y de la proyección de la velocidad orbital del planeta. La amplitud del aumento, por otra parte, depende de la diferencia de temperatura entre la superficie de la estrella y de la mancha, así como de la fracción de la sombra del planeta sobre la mancha, a menos que el planeta proyectado se encuentre plenamente dentro de la mancha, en cuyo caso sólo las temperaturas son pertinentes.
En esta tesis también hemos presentado una segunda hipótesis para el origen del breve aumento de flujo observado con HST, lo cual se podriá producir cuando dos planetas transitan la estrella simultáneamente y uno de los planetas está ocultando al otro. Para una curva de luz de dos planetas en tránsito, la cuantidad del aumento depende de la proporción de las áreas y del parámetro de impacto entre ambos planetas, mientras que la duración depende de la proporción de los áreas y de las respectivas velocidades orbitales de ambos planetas.
Hemos hecho uso de varias observaciones de tránsitos de TrES-1 desde el espacio con el HST-ACS/HRC y desde tierra con el IAC80. Sobre la base de estas observaciones hemos hecho un estudio estadístico de las variaciones de flujo en cada una de las curvas de luz observadas, para investigar si aumentos de flujo similares al detectado en los datos del HST están presentes en otras series del conjunto de datos.
Las dos hipótesis presentadas anteriormente, es decir, el área oscura esta causada por a) una mancha fría o b) un segundo planeta que transita, se pueden distinguir por las siguientes propiedades que las diferencian. Por un lado, una mancha debe mostrar un aumento en flujo que depende de la longitud de onda, con un mayor aumento en flujo en el azul que en el rojo. Por el contrario, un aumento de flujo por ocultación de un planeta por otro no debe tener una dependencia en longitud de onda. Igualmente, una mancha es un fenómeno temporal en escalas de tiempo de semanas a meses; las manchas aparecen y desaparecen con diferentes tamaños en diferentes posiciones, mientras que la ocultación de dos planetas sería un caso singular, salvo si los dos planetas se encuentran en una órbita resonante.
Primero verificamos si existe alguna dependencia de flujo con la longitud de onda durante su aumento en el tránsito de TrES-1. Con este fin, hemos creado modelos de las curvas de luz de HST en colores diferentes y hemos sustraído los modelos de las observaciones. Se estimó en las curvas de luz la pendiente del aumento de flujo en cada longitud de onda. Las estimaciones de las pendientes se normalizaron con la de la pendiente de la curva de luz blanca.
Después de aplicar un test estadístico, encontramos que no existe ninguna diferencia significativa entre ambas hipótesis y por tanto, en principio, no podemos discernir si el evento se debe a una mancha o a un segundo planeta transitante. Además, hemos utilizado los datos del IAC80 para comprobar si estas observa-

ciones contienen variaciones de flujo idénticas o similares a las detectadas en la curva de HST. No obstante, las observaciones con el IAC80 son más ruidosas y, por tanto, eventos similares al encontrado con el HST no se pueden ver tan fácilmente. Por lo tanto, hemos creado un modelo para los tránsitos del IAC80 que se restarán a los datos respectivos. Luego se va a utilizar el aumento de flujo de la curva de luz de HST como plantilla y se va a aplicar un algoritmo de "Matched Filter detection" para los observaciones del IAC80. Basado en este algoritmo pudimos identificar dos casos de eventos en las curvas de luz del IAC80 similares al del aumento del flujo en las observaciones de HST.
Un buen modelo de ajuste para el aumento del flujo se puede obtener mediante el uso de un área circular oscura en la superficie de la estrella. Suponiendo además que el área oscura y TrES-1 tienen el mismo parámetro de impacto entre ambos y usando la velocidad orbital de TrES-1 de $v_{rot} = 140$ km/s, entonces podemos estimar que en un intervalo de 10 min, TrES-1 cruza 84 000 km de la superficie de la estrella, lo que nos da un límite inferior para el diámetro del área ocultada resultante. El verdadero diámetro depende de la rotación estelar (para la hipótesis de una mancha) o de la velocidad orbital de los planetas (para la hipótesis planeta-planeta).
En las observaciones de HST se presenta un aumento de flujo único y evidente durante un tránsito, mientras que las observaciones del IAC80 conducen a la detección de dos de estos eventos, pero con poca significancia. En el caso de haber observado una mancha estelar en los datos de HST, suponiendo un impacto central entre la mancha y TrES-1, se obtendría un límite inferior para el radio de la mancha de 42 000 km. Para este radio la temperatura de la mancha sería de 4 690 K, es decir, 560 K inferior a la temperatura de la superficie estelar de unos 5 250 K. Para un supuesto segundo planeta en tránsito, se puede fijar un límite inferior de su radio en 0.37 R_J, aunque para períodos de menos de 10.5 días, podemos establecer adicionalmente un límite superior a 0.72 R_J.
Partiendo de una interpretación convencional, esta observación de HST podría ser la manifestación de una mancha; si bien, alternativamente, este aumento de flujo también podría ser causado por un planeta en tránsito. La verdadera naturaleza del origen podría revelarse o descartarse con mayor certeza si se pudiera demostrar una dependencia con la longitud de onda en el aumento del flujo correspondiente. Además, la presencia de un segundo planeta pudiera ser confirmada por medidas de velocidad radial de alta precisión. Por ahora, como hemos mencionado, no tenemos la solución definitiva a este dilema. El trabajo descrito en este capítulo fue publicado por Rabus et al. (2009) en 'Astronomy and Astrophysics'.

5. Un análisis de tiempo de los tránsitos de TrES-1 y TrES-2

El objetivo del capítulo 5 es llevar a cabo un análisis detallado de las curvas de luz de los tránsitos de TrES-1 y TrES-2 a través de un período de tres a cuatro años, con el fin de buscar una alteración del tiempo de los tránsitos y de establecer límites para la presencia de terceros cuerpos.
Mediante el estudio de las variaciones del momento de la aparición de los tránsitos de exoplanetas se obtiene una posibilidad de encontrar otros planetas o lunas que acompañan al estudiado, incluso hasta límites de masa similares a la de la Tierra. Existen diferentes mecanismos que causan estas variaciones. Por un lado, la influencia gravitacional de un cuerpo perturbador puede alterar el periodo orbital del planeta en tránsito (Holman & Murray, 2005; Agol et al., 2005). Este efecto es particularmente sensible para la detección de cuerpos adicionales en las resonancias orbitales que se puedan dar con el planeta en tránsito o para detectar lunas alrededor de ese planeta. Por el otro lado, un perturbador con masas de estrellas enanas en una órbita más grande que el planeta en tránsito puede causar que el sistema "estrella-planeta" se desplaza alrededor de su baricentro y de esta forma puede modificarse la periodicidad observada, algo que se conoce como "Light time effect" (Irwin, 1959; Schneider & Doyle, 1995; Doyle & Deeg, 2004; Schneider, 2005). Estas anomalías se reflejan en los tiempos centrales del tránsito. Por lo tanto, utilizando una efeméride fija y varias observaciones de los tránsitos es posible obtener la diferencia "O-C" entre el tiempo de tránsito que se observó (O) y lo que se calculó (C) a partir de las efemérides correspondientes. De esta diferencia podemos averiguar las perturbaciones que afectan a la periodicidad orbital, causadas por un posible compañero que no haya sido detectado todavía.
Para TrES-1 se obtuvieron ocho observaciones útiles y para TrES-2 cinco. Con el fin de medir los tiempos de tránsito observado, hemos creado un modelo de tránsito que desplazamos en el tiempo sobre las curvas de luz observadas, calculando el χ^2. Por último, restamos el tiempo observado a los tiempos de tránsito calculados con el fin de obtener los valores de O-C. Se obtuvo el cálculo de los tiempos de tránsito de TrES-1 a partir de la efeméride $\mathrm{T}_c = 2\,453\,186.8060 + 3.0300737 \times \mathrm{Epoca}$ (Winn et al., 2007) y para TrES-2 se utilizó $\mathrm{T}_c = 2\,453\,957.6348 + 2.470621 \times \mathrm{Epoca}$ (Holman et al., 2007).
Para análizar el "Light time effect" hemos ajustado tres polinomios de diferentes órdenes a los valores encontrados de O-C, o lo que es lo mísmo, una recta, $OC_{fit} = \kappa_0 + E\kappa_1$, una parábola, $OC_{fit} = \kappa_0 + E\kappa_1 + E^2\kappa_2$, y un polinomio de tercer grado, $OC_{fit} = \kappa_0 + E\kappa_1 + E^2\kappa_2 + E^3\kappa_3$, donde E es la epoca y κ son los coeficientes del polinomio respectivo. También se analizó el caso de las efemérides originales ($OC_{fit} = 0$), asumiendo que no hay cambios en el tiempo,

y finalmente el caso en que se mantiene el periodo original y se ajusta sola una constante ($OC_{fit} = \kappa_0$).
En referencia a los coeficientes lineales κ_0 y κ_1, aunque éstos no tienen significado físico, pueden indicar una efeméride ligeramente diferente, donde κ_0 es una variaciíon del tiempo central del tránsito en época 0 y κ_1 una corrección al periodo de la efeméride correspondiente. Sin embargo, sí podemos dar un significado físico al coeficiente cuadrático (κ_2) lo cual nos informa sobre la aceleración del sistema a lo largo de la línea de visión.
La otra causa de variaciones de los tiempos medios de tránsito podría ser una perturbación del periodo intrínseco del planeta P, debido a la influencia gravitatoria de un tercer cuerpo. En cuanto a tales perturbaciones, no existen ecuaciones analíticas que describan adecuadamente el fenómeno. En general, se utilizan simulaciones de N-cuerpos, iterando sobre muchos parámetros orbitales para un rango máximo de posibles masas.
Con el fin de encontrar un tercer cuerpo compatible con el tiempo de tránsito observado hemos creado una simulación numérica en dos dimensiones mediante la integración de las ecuaciones de movimiento del sistema. Al considerar el problema en dos dimensiones, asumimos que las órbitas del exoplaneta del perturbador están coalineados. Además, consideramos el problema en un marco heliocéntrico, con la estrella en el centro del sistema de coordenadas, lo que significa que despreciamos el "Light Time effect" en este contexto. Para integrar las ecuaciones de movimiento utilizamos el algoritmo "Burlisch-Stoer" (Press et al., 1992) con 1 segundo de tiempo de intervalo de paso.
Una vez hechos las simulaciones, para establecer posibles parámetros orbitales del tercer cuerpo, ajustamos, para cada distancia de éste último, el O-C simulado, que se había generado para masas de 1 - 100 M $_{\oplus}$, al O-C observado. En todo el proceso, hemos dejado un total de tres parámetros libres.
Con el fin de buscar periodicidades sinuosidales en los datos con períodos del orden de la campaña observacional o bien de una duración menor, ajustamos una función sinuosidal con una cierta amplitud y fase a los O-C observados después de restar un ajuste lineal.
Encontramos que para TrES-1 que los polinomios lineales y cuadráticos son los que describen mejor los datos. Un ajuste de las residuos O-C del TrES-1 a la simulación de los diagramas O-C muestran un alto χ^2 para objetos en los resonancias orbitales de baja orden, sin encontrar picos significativos de bajos de valores de χ^2. Asimismo, no se encontraron ajustes especialmente buenos de los sinusoides a los residuos O-C. En cuanto a TrES-2, el ajuste lineal indica una efeméride diferente. Se obtuvieron bajos valores de χ^2 para algunos tipos de simulaciones y altos valores de χ^2 para el resto. Adicionalmente, encontramos un valor bajo de χ^2 en un ajuste sinusoidal con una frecuencia de 4.8 ciclos/día

y una amplitud de 57 s, compatible con una luna alrededor del TrES-2.
En resumen, mostramos que es posible poner límites a posibles terceros cuerpos con las observaciones desde tierra. Sin embargo, la presencia del "light time effect" causado por una tercera masa que cumple $\frac{m_3}{M_\odot} \geq 34 \left(\frac{\theta}{\mathrm{arcsec}}\right)^2$ es aún posible. Esta ecuación ayudará a limitar la masa de las estrellas que aparezcan en imágenes de alta resolución espacial. En cuanto a TrES-2, encontramos una mejor efeméride de $\mathrm{T}_c = 2\,453\,957.63512(28) + 2.4706101(18) \times \mathrm{Epoca}$.

6.1 Conclusiones

Con el trabajo desarrollado para esta tesis hemos contribuido a un avance en la investigación de exoplanetas, obteniendo resultados muy interesantes e innovadores que nos han permitido llegar a las siguientes conclusiones:

- Mediante las observaciones llevadas a cabo con la red TrES, y el nodo canario STARE, y su seguimiento posterior, hemos desarrollado un procedimiento para la detección de planetas transitantes en búsqueda fotométricas. Empezamos por el análisis, que va desde las imágenes originales del telescopio a las curvas de luz que se han de decorrelar debido al ruido sistemático. Como resultado final de este proceso se han obtenido varios candidatos. Para estos candidatos, mostramos que es posible descartar algunos de ellos mediante un análisis detallado de sus curvas de luz. Se aplican observaciones de seguimiento espectroscópicas y fotométricas detalladas al resto de los candidatos posibles. Por medio de estas observaciones se puede reducir aún más el número de posibles falsas alarmas. Finalmente, el proceso se reduce a tres candidatos que todavia estan pendientes de confirmar con medidas de velocidades radiales de alta precisión que no han ofrecido aún resultados concluyentes. Sin embargo, la confirmación de otros candidatos como TrES-2 en la que hemos participado muestran las bondades del método.

  Hemos mostrado las aplicaciones y demostrado las ventajas de observaciones de tránsitos primarios y eclipses secundarios en el infrarrojo, con ejemplos en los exoplanetas HD 189 733b, GJ 436b y COROT-2b:

  - Para HD 189 733b, observado en reiteradas ocasiones, hemos encontrado que nuestro límite de 2-σ en la profundidad del eclipse secundario (< 0.05 % en el filtro K_s) es coherente con observaciones publicadas en la literatura. Además, nuestras observaciones de los

tránsitos primarios de HD 189 733b son también coherentes. Se estima una temperatura de equilibrio con albedo nulo de $T_{eq} = 1\,534$ K y, adicionalmente, utilizando esta temperatura se estima una profundidad esperada en el filtro Ks de 0.03 %, consistente con las observaciones y la literatura.

- Continuando, también se ha realizado fotometría infrarroja utilizando LIRIS en el WHT, con los filtros H y K_s. Se ha observado la estrella matriz de CoRoT-2b en torno a dos eclipses secundarios en dos noches con buenas condiciones fotométricas. Para la profundidad del eclipse secundario en la banda de H se ha obtenido un límite superior de 3-σ del 0.17 %, mientras que se ha confirmado una detección tentativa de un eclipse con una profundidad de 0.16 $\pm$ 0.09 % en la banda K_s. Se ha estimado una temperatura de equilibrio de 1964 $\pm$ 35 K y una profundiad de 0.11 % en el filtro H y 0.23 % en el filtro Ks. Ambas profundidades son consistente con las observaciones.

- Finalmente, con observaciones infrarrojas, hemos obtenido un tránsito del Neptuno caliente GJ 436b en la banda H. Una vez que se combinaron los observaciones del TCS con unas observaciones de Spitzer ya publicadas, nuestros datos han resultado ser de calidad comparable a éstos últimos, alcanzando el mismo nivel de precisión. Se han analizado las dos series de observaciones de una manera coherente y se ha encontrado que el cambio de la inclinación orbital es de 0.02 $\pm$ 0.04° en el lapso de tiempo entre las dos observaciones. Como consecuencia, un candidato a un exoplaneta adicional, GJ 436c, propuesto para este sistema en la literatura debe ser rechazado.

- Se han obtenido varias observaciones de tránsitos de TrES-1 con el Hubble Space Telescope (HST) y desde tierra con el telescopio IAC80. Sobre la base de estas observaciones hemos hecho un estudio estadístico de las variaciones del flujo en cada una de las observaciones, para investigar si aparecen aumentos de flujo en el conjunto de datos. Curiosamente, las observaciones con el HST han presentado un aumento de flujo único y claro durante un tránsito, mientras que las observaciones terrestres conducen a la detección de dos de estos eventos, pero con baja significancia. Se han planteado dos posibilidades: asumiendo una interpretación convencional,

esta observación pudiera corresponder a la detección de una mancha; alternativamente, este aumento de flujo también pudiera ser causado por un planeta transitante adicional en el sistema. En el caso de haber observado una mancha en los datos del HST, y suponiendo un impacto central entre la mancha y TrES-1, se obtendría un límite inferior para el radio de la mancha de 42 000 km. Para este radio, la temperatura de la mancha sería de 4 690 K, es decir, 560 K inferior a la superficie estelar de 5 250 K. Para un supuesto segundo planeta transitante, se puede fijar un límite inferior de su radio de 0.37 R_J y, para períodos de menos de 10.5 días, podemos establecer un límite superior de 0.72 R_J. La verdadera naturaleza de este fenómeno esta por ahora pendiente de futuros datos.

- Usando el telescopio IAC80, hemos llevado a cabo observaciones sistemáticas de tránsitos de TrES-1 y TrES-2 durante varios años consecutivos. Se han estudiado las curvas de luz observadas y se ha realizado un análisis de las diferencias entre el tiempo central del tránsito observado y calculado (basado en efemérides fijas). Para modelar posible variaciones en los tiempos centrales de tránsito hemos utilizado polinomios de diferentes órdenes, hemos simulado diagramas O-C correspondientes a terceros cuerpos en el sistema, y, finalmente, hemos procedido a llevar a cabo ajustes sinusoidales. Esto nos permite poner límites a posibles terceras masas mediante observaciones terrestres. Finalmente, para el caso de TrES-1, es posible detectar la presencia del efecto "light time" causado por un potencial cuerpo que cumpla la norma siguiente: $\frac{m_3}{M_\odot} \geq 34 \left(\frac{\theta}{\mathrm{arcsec}}\right)^2$. Esta ecuación pudiera ayudar a limitar la masa de las estrellas que puedan aparecer en imágenes de alta resolución espacial. Para TrES-2 hemos mejorado el efeméride: $T_c = 2\,453\,957.63512(28) + 2.4706101(18) \times \mathrm{Epoca}$. Tanto para TrES-1 como para TrES-2, cualquier variación sinuosidal debiera ser confirmada con mayor significación estadística para lo que sería necesario llevar a cabo más observaciones con una mejor precisión en el futuro.

6.2 Desarollo futuro

El trabajo futuro podrá centrarse de manera adicional en la detección de planetas más pequeños, es decir, con una masa menor que la de Neptuno. En particular, una investigación sobre las propiedades de esta clase de planetas -como, por ejemplo, su número alrededor de estrellas de la vecindad solar, su

excentricidad, su función de masas y la metalicidad de sus estrellas matrices- y su comparación con los gigantes gaseaosos conocidos pudiera ser una tarea muy interesante y provechosa. Puede que se logren estos objetivos a través de misiones espaciales ya operativas como Kepler o CoRoT. De hecho, las missiones espaciales como Kepler, SIM, JWST y TESS de la NASA o PLATO de la ESA en las que espero involucrarme en algunas de ellos pueden ser determinantes en el estudio científico futuro de los exoplanetas.

Sin embargo, las búsquedas terrestres también han mejorado singularmente sus capacidades, bajando su nivel de detección de exoplanetas a la masa de Neptuno, como ha demostrado recientemente la red HAT con el descubrimiento de HAT-P-11b. Este es el único exoplaneta con una masa cerca a la de Neptuno descubierto por búsqedas fotométricas de exoplanetas transitantes. Hasta la fecha, la red HAT ha observado sólo en el hemisferio norte, pero se llevará a cabo una ampliación hacia el hemisferio sur a lo largo de 2009 en que espero estar involucrado. La observación desde tres localizaciones en Chile, Australia y Namibia permitirá la toma de datos ininterrumpidos. Para HAT-Sur se estima una eficiencia de detección de 25 planetas transitantes cada año alrededor de estrellas brillantes.

La red TRES pionero en el campo de las busquedades fotométricas de exoplanetas transitantes alrededor de estrellas brillantes ha encontrado 4 planetas en tránsito. Sin embargo, TRES es obsoleta, y su pequeña cobertura del cielo, en comparación con WASP y HAT, no es más competitivo y será desmantelada en breve. WASP, que ha estado operando por varios años en La Palma, ha generado el mayor número de detecciones de planetas transitantes, conduciendo al descubrimiento de 10 planetas solo en 2008.

Hasta ahora, el espectrógrafo de alta precisión HARPS ha sido el único instrumento en el mundo con capacidad de alcanzar una precisión en las medidas de velocidad radial por debajo de 1 m/s. Sin embargo, nuevos instrumentos terrestres se están desarollando capaces de confirmar exoplanetas de masa más pequeña como, por ejmplo, HARPS Norte para el WHT, ESPRESSO, que se propone como un instrumento de segunda generación para VLT, o el espectrógrafo CODEX para el eventual EELT.

Además, se espera comenzar a explorar las atmósferas de los jupiteres calientes, determinando su composición, incluso desde tierra, ya que antes sólo era posible examinarlas con telescopios espaciales como Spitzer y Hubble. La posibilidad de observaciones terrestres permitirá estudiar más sistemas en un tiempo menor y, por tanto, puede permitir llevar a cabo un estudio estadístico.

La búsqueda con el fin de descubrir otros sistemas multiplanetarios debe seguir, en particular aquellos que presenten tránsitos. Hasta ahora no se ha detectado ningún sistema planetario extrasolar en que se produzcan tránsitos con varios

planetas. Establecer la coplanaridad de estos sistemas multiplanetarios es una investigación muy importante y sugerente.
Singularmente, el inicio de las observaciones con el Gran Telescopio Canarias (GTC) en 2009 nos ofrece excelentes oportunidades para caracterizar los exoplanetas descubiertos.
GTC es un instrumento con un espejo primario de 10.4 metros compuesto por 36 segmentos. Por un lado, una idea sería observar tránsitos en diferentes filtros con OSIRIS. Es de esperar que se produzcan pequeñas diferencias en las profundidades de los tránsitos para varias longitudes de onda, pues elementos más ligeros se extienden más allá en el espacio que otros más pesados. Las observaciones espectroscópicas con OSIRIS, gracias a sus filtros sintonizables, pueden de hecho escanear diferentes capas de la atmósfera al llevar a cabo medidas en líneas de absorción durante el tránsito. Esto nos puede ayudar a entender los modelos de atmósfera de planetas extrasolares. En los observaciones queremos selecionar el paso de banda más estrecho posible y simultáneamente mantener una precisión fotométrica y una cadencia elevada, sin aumentar innecesariamente el tiempo de exposición.
GTC/OSIRIS también nos puede permitir un siguimiento de aquellos exoplanetas con un tránsito poco profundo, como por ejemplo COROT-7b, con fotometría de alta precisión. Una forma de conseguir este objetivo sería observar CoRoT-7b con el modo de fotometría rápida de OSIRIS aunque otra posibilidad muy sugerente es la de utilizar los 36 segmentos del espejo como si fuesen telescopios independientes y obtener de esta forma 36 imágenes siguiendo un patrón regular, con lo que esperamos que nos permita alcanzar una precisión fotométrica exceptional.
Esta potencial riqueza de las observaciones es indicativo que el tema de la investigación de los exoplanetas ha pasado de una fase de descubrimiento en una con el objetivo de una mejor caracterización de los sistemas encontrados.

Glossary and Acronyms

2MASS	The Two Micron All Sky Survey at IPAC
ACS	Advanced Camera for Surveys (HST instrument)
ADU	Analog-Digital Unit
AMOEBA	Simplex-Downhill Fitting algorithm
AU	Astronomical Unit
BLS	Box-fitting Least Squares
CAIN	CÁmara INfrarroja
CCD	Charge Couple Device
CCF	Cross-Correlation Function
CfA	Centre for Astrophysics
CGEP	Close-in Giant Extrasolar Planet or Hot Jupiter
CNES	Centre National d'Etudes Spatiales
CO	Carbon Monoxide
CODEX	High stability high resolution optical spectrograph (E-ELT)
CORALIE	Spectrograph on the 1.2m Swiss telescope at ESO, La Silla
CoRoT	COnvection, ROtation & planetary Transits
CST	Carlos Sánches Telescope
DAOPHOT	community-standard software suite for multiple, simultaneous profile fitting photometry and astrometry for point sources in crowded fields
E-ELT	European Extremely Large Telescope
ELODIE	cross-dispersed echelle spectrograph
ESA	European Space Agency
ESO	European Southern Observatory
ESPRESSO	Echelle SPectrograph for Radial vElocity Super Stable Observations
FAP	False Alarm Probability
FLAMES	Fibre Large Array Multi Element Spectrograph

FWHM	Full Width Half Maximum
GEP	Giant Extrasolar Planet
GTC	Gran Telescopio Canarias
H_2O	Water
HAO	High Altitude Observatory
HARPS	High Accuracy Radial velocity Planet Searcher
HAT network	Hungarian-made Automated Telescope
HE	High Efficiency
HgCdTe	Mercury Cadmium Telluride
HiRES	High Resolution Echelle Spectrometer
HJD	Heliocentric Julian Day
HR	High Resolution
HRC	High Resolution Channel
HST	Hubble Space Telescope
IAC	Instituto de Astrofísica de Canarias
IAC80	IAC 80cm telescope
IAU	International Astronomical Union
IDL	Interface Description (Definition) Language
IPAC	Infrared Processing and Analysis Center
IR	Infrared
IRAF	Image Reduction and Analysis Facility
IRS	Infrared Spectrograph
JWST	James Webb Space Telescope
Kepler	Space mission dedicated to search for transiting exoplanets
LIRIS	Long-slit Intermediate Resolution Infrared Spectrograph
MMR	Mean-motion resonance
NASA	National Aeronautics and Space Administration
NICMOS	Near Infrared Camera and Multi-Object Spectrometer
O-C (OC)	Observed minus Calculated
OHP	Observatoire de Haute Provence
OSIRIS	Optical System for Imaging and low Resolution Integrated Spectroscopy
pc (parsec)	parallax of one arcsecond
PLATO	Planetary Transit And Oscillations of Stars
PSF	Point Spread Function
PSST	Planet Search Survey Telescope
RM	Rossiter-McLaughlin effect
RV	Radial velocity
SDE	Signal Detection Efficiency
Sleuth	10cm wide-field camera at Mt. Palomar observatory

SIM	Space Interferometry Mission
SOPHIE	Spectrograph for Observation of Astroseismologic Phenomenon and Extrasolar Planets
STARE	STellar Astrophysics and Research on Exoplanets
SVD	Singular Value Decomposition
TELAST	30 cm telescope at the Teide Observatory
TEP	Transiting ExoPlanet
TESS	Transiting Exoplanet Survey Satellite
TFA	Trend-Filtering Algorithm
Ti	Titanium
TrES	Transit-Atlantic exoplanet Search
TRES	Tillinghast Reflector Echelle Spectrograph
TTV	Transit-timing Variation
UTM	Universal Transit Modeler
UVES	Ultraviolet and Visual Echelle Spectrograph
V	Vanadium
VLT	Very Large Telescope
WASP	Wide Area Search for Planets
WATTS	10cm wide-field camera at Sam Houston State University
WGESP	The Working Group of Extrasolar Planets of the IAU
WHT	William Herschel Telescope at the Roque de los Muchachos observatory

Contributions to publications

During the work of my thesis, I contributed to the following publications:

Publication	Contribution
Rabus et al. (2009) A&A 494, 391	Photometric transit observations, image reduction and data analysis
Rabus et al. (2009) submitted to A&A	Photometric transit observations, image reduction and data analysis
Deeg et al. (2009), accepted by A&A	Photometric follow-up observations
Cabrera et al. (2009), submitted to A&A	Photometric follow-up observations
Moutou et al. (2009), submitted to A&A	Photometric and spectroscopic follow-up observations
Sozzetti et al. (2009), ApJ, 691, 1145	Photometric transit observation
Fox et al. (2008), CoAst., 157, 307	Photometric observations
Devor et al. (2008), ApJ, 687, 1253	Photometric eclipse observation, image reduction
Hébrard et al. (2008) A&A, 488, 763	Photometric and spectroscopic transit observation and image reduction
Moutou et al. (2008) A&A Letter, 488, 47	Photometric and spectroscopic follow-up observations
Alonso et al. (2008), A&A Letter, 487, 5	Photometric transit observations
Mandushev et al. (2007) ApJ Letter, 667, 195	Discovery observations
O'Donovan et al. (2007) ApJ Letter, 663, 37	Discovery observations
O'Donovan et al. (2006) ApJ Letter, 651, 610	Photometric transit observations and image reduction

Observations from ground-based telescopes

In the course of my thesis, I performed the following observations:

Exoplanet	Telescope/Instrument	Remarks
TrES-1 (V=11.8, K0V)	IAC80/CCD	$\sim$ 11 primary transits
TrES-2 (V= 11.4, G0V)	IAC80/CCD, TELAST/CCD	$\sim$ 9 primary transits
TrES-3 (V=12.4, G)	IAC80/CCD	1 primary transit
HD 189 733b (V=7.7, K1-K2)	TCS/CAIN	$\sim$ 9 primary transits and 3 secondary eclipses (several attempts more with bad weather)
GJ436b (V=10.7, M2.5)	TCS/CAIN	1 primary transit (several attempts more with bad weather)
CoRoT-2 (V=12.6, K0V)	WHT/LIRIS	1 secondary eclipse
XO-3b (V=9.8, F5V)	1.93mOHP/SOPHIE, TELAST/CCD	2 primary transits (one spectroscopically and one photometrically)
CoRoT-7 (V=11.7, K0V)	IAC80/CCD	1 primary transit attempted
XO-5b (V=12.1, G8V)	IAC80/CCD	1 primary transit
HD17156b (V= 8.1, G0)	IAC80/CCD	1 primary transit attempted, but bad weather
HD 209 458b (V=7.7, G0V)	IAC80/CCD, TCS/CAIN	2 primary transits

Planet candidates	Telescope/Instrument	Remarks
TrES candidates	IAC80/CCD	∼30 nights
TrES candidates	1.93mOHP/SOPHIE	2 nights
TrES candidates	Keck/HiRES	1 night
CoRoT candidates	IAC80/CCD	10 nights
CoRoT candidates	SOPHIE	23 nights
Other objects	**Telescope/Instrument**	**Remarks**
CM-Dra	IAC80/CCD	two eclipses
White/Red dwarf eclipsing binary (V∼ 19)	TNG/DOLORES	1 night
Kepler field	INT/Wide-field camera	3 nights
CoRoT field	IAC80/CCD, INT/Wide-field camera	5 nights

Abstract

Planets showing transits during their orbit are so far the best studied exoplanets. A transit occurs when the orbit of an exoplanet is oriented in such a way that during an orbital phase (transit phase) the planets occults part of the stellar surface. This occultation, when photometrically observed, will cause a decrease in the observable flux during transit.
The first step to find more transiting exoplanetary systems is by surveying large areas of the sky. The most successful approach to date is by using a network of small wide-field cameras scanning the sky for transiting planets, as was pioneered by the TrES (Trans-Atlantic Exoplanet Search) network. After reducing the images, light curves are obtained and searched for transit-like events. However, transit surveys are plagued by a high rate of false positives, which are systems mimicking a transit of an exoplanet. There are three major types of false alarms, namely: grazing eclipsing binaries, dwarf stars eclipsing giant stars and diluted eclipsing binaries (binaries that are close to a bright star). Therefore, extensive light curve analysis and follow-up observations are necessary to discard as many false positives as possible. The final confirmation of a planet is done by measuring a star's radial velocity with a high precision to confirm the mass of the orbiting object.
After a transiting exoplanet around a star has been confirmed, one can start to further characterize the system. One way is by observing the system in the infrared (IR) wavelength range, another way is to search for star spots, to search for additional transiting planets or to search for unseen objects, influencing the system gravitationally.
Infrared photometric observations can be done for primary transit or secondary eclipse phases. Photometric infrared observations of the primary transit are less affected by errors in the limb darkening coefficients than in the optical and, hence, allow a more precise parameter estimate, like the transit duration and the transit depth. This more precise parameter estimation could help to

constrain the presence of possible additional bodies in the system. Secondary eclipse observations indicate the light from the planet, composed of emitted and reflected light. In the IR wavelengths, the emission component is stronger than the reflected component. The secondary eclipse depth can be converted into brightness temperature, which can be compared to the theoretical planet's equilibrium temperature. Also, the timing of the secondary eclipse can put constraints on the eccentricity.
For the detection of star spots or additional transiting planets, usually high precision photometric transit observations are used. Star spots and additional transiting planets, when aligned favorably, will leave in the light curve a flux increase during transit. Based on multi-color photometry, one may be able to distinguish the nature of this flux increase, i. e. if it is caused by a star spot or another transiting planet. Additionally using the height and duration of the flux rise one can estimate a limit for the radius of the planet respective to the star spot and with the additional information of multi-color photometry one may be able to infer the temperature of the star spot.
Not only objects seen in the light curves, i. e. additionally transiting objects, can be detected, but also the gravitational influence of additional non-transiting masses can be observed. If there is no third body present in a transiting exoplanetary system, then the transits of the exoplanet will occur with strict periodicity. By measuring a deviation from this periodicity it is possible to detect or at least to put upper limits on the presence of additional objects. These objects can be dwarf stars, additional exoplanets or moons. Dwarf stars, at distances of some arc-seconds in an orbit of several AUs around the transiting exoplanetary system, will show themselves by means of the light time effect. Objects like additional exoplanets or moons can be detected by comparing the observed deviation in mid-transit times with N-body simulations or by detecting a sinusoidal variation within a certain range of frequencies.
This thesis presents the process of detecting transiting exoplanets by means of a multi-site photometric wide-field survey (TrES-network) and shows the exemplary follow-up characterization of some known transiting systems. In particular, IR observations of HD 189 733, CoRoT-2b and GJ 436b are presented. The primary transit and secondary eclipse depth are estimated and compared with the literature. The secondary eclipse depths were also compared to the expected ones, based on the planet's equilibrium temperature. All depths were in agreement. Notably, a ground-based IR primary transit observation of GJ 436b showed comparable quality to one obtain by the Spitzer Space Telescope, and both were used to constrain the presence of an additional planet, claimed in the literature, in the system GJ 436. TrES-1 was searched for asymmetries in its light curve. One was found in observations of its transits with the HST and two

additional ones in ground-based observations with the IAC80, but with lower significance. For these asymmetries in the transit light curve, two explanations were given: a) the transiting planet crosses a star spot; b) an additional transiting planet. Additional observations are necessary to differentiate between both hypotheses. Finally, transit timing observations of TrES-1 and TrES-2 are presented, which allowed us to put constraints on additional planets. TrES-1 might have an additional companion at a large distance, showing itself as light time effect, and TrES-2 showed indications of a sinusoidal transit timing variation, indicating a possible moon, but pending on further observations. The above investigations showed the rich information obtained from characterizing observation of transiting exoplanets.

Organization

This thesis treats the detection and characterization of transiting exoplanets, and it is divided in six chapters. The first chapter will give an introduction into the subject of exoplanets. The methods used to detect transiting exoplanets are further explained and finally an overview of follow-up observations used to characterize known exoplanets and especially transiting ones is given. Chapter 2 goes into the details of detecting transiting exoplanets by means of a multi-site photometric wide-field surveys, namely the TrES-network. The instruments and data analysis procedure will be explained. After the light curve is obtained it will be shown how false positives can be discarded by a detailed light curve analysis and by photometric and spectroscopic follow-up observations. Finally, some real candidates and planets will be discussed and it will be shown how the procedure to reject false positives was applied to them. Chapter 3 deals with high precision infrared (IR) photometry. Primary transit and secondary eclipse observations of HD 189 733b, CoRoT-2b and GJ 436b will be presented. For HD 189 733b IR observations of primary transits and secondary eclipses will be shown and compared to the literature and theoretical values. Similarly, the observed secondary eclipse in two distinct filters for CoRoT-2b will be compared with theoretical values. Finally in this chapter, the primary transit observation of GJ 436b, and an additional observation published in the literature, will be used to constrain the parameters of possible additional planets in the system. In Chapter 4, a detailed light curve analysis of TrES-1 will be discussed. Space- and ground-based observations are used to search for star spots or additional transiting planets. It will be shown that both hypothesis (a star spot/ an additional transiting planet) are possible and how in the future these two can be distinguished. The next chapter, Chapter 5, treats the search for additional photometrically unseen companions. Ground-based transit observations over several years of TrES-1 and TrES-2 are used with the aim to search for an alteration in the mid-transit times from strict periodicity. These alteration

might have been caused by a gravitationally influencing body in the transiting exoplanetary system. Several models will be fitted to the difference between observed and expected transit times. The last chapter gives an overview and discussion of the chapters before and future work will be shown.

Contents

1

Introduction

In this thesis a search for transiting planets by means of a multi-site photometric wide-field survey and in-depth studies of some known transiting planetary systems will be presented.
I will introduce exoplanets by starting with their history, then I will explain some definition and abbreviations. Afterwards, the detection methods are briefly described with an emphasis on the transit and radial velocity method, both of which play an important role in this thesis. At the end of this chapter I will briefly introduce follow-up techniques of confirmed exoplanets for characterization.

1.1 The history of exoplanets

The first exoplanets were discovered in 1992 by Aleksander Wolszczan and Dale Frail (Wolszczan & Frail, 1992), forming a planetary system. These exoplanets orbit the pulsar PSR B1257+12 and they were detected using the pulsar timing method. Three years later, in 1995, Michel Mayor and Didier Queloz announced the discovery of the first exoplanet around a solar type star, 51 Pegasi (Mayor & Queloz, 1995). This planet was discovered by measuring the host star's radial velocities; it has a mass of 0.5 M_J and a period of 4.2 days. This discovery inspired many astronomers and the search for more planets begun.
Until the year 2000, only exoplanets by means of radial velocity measurements had been detected, but that year, the first exoplanetary transit was found. This transit was detected for the exoplanet HD 209 458b (Charbonneau et al., 2000; Henry et al., 2000), an already known planet by measurements of the star's radial velocities. Its transit detection also permitted for the first time an es-

timate of the size of the planet and a determination of the orbital inclination. Since the transit detection of the exoplanet HD 209 458b, we know that searches for transiting exoplanets are viable and are able to greatly expand our knowledge on the planets under investigation. Since then, many projects have begun to search for them. The first systematic survey for transiting planets which had success in finding one was the Optical Gravitational Lensing Experiment (OGLE) with the discovery of OGLE-TR-56b (Udalski et al., 2002; Konacki et al., 2003). However, this exoplanet transits around a faint (17 mag) star and is not an ideal target for detailed follow-up characterizations.

In 2005, Alonso et al. (2004b) detected the transiting planet TrES-1 based on observations with the STARE telescope at the Teide Observatory. TrES-1 was the first planet discovered by a systematic ground-based transit survey (TrES-network) concentrating on bright stars. Until 2004 all detected planets had a mass similar to Jupiter, but that changed with the discovery of GJ 436b (Butler et al., 2004), the first Neptune mass exoplanet, whose transits were detected three years later (Gillon et al., 2007b). The HAT network was the first systematic transit survey detecting a transiting hot Neptune, HAT-P-11b (Bakos et al., 2009). In Dec. 2006, CoRoT was launched, the first space-based survey for transiting exoplanets. CoRoT discovered the first transiting object on the planet/brown-dwarf boundary with 22 M_J, CoRoT-3b (Deleuil et al., 2008), and it also discovered the first transiting super-Earth, CoRoT-7b. The first direct images of exoplanets have been made very recently by Kalas et al. (2008) and Marois et al. (2008). Figure 1.1 shows a histogram of the exoplanets discovered so far, and of those with transits. One notes the increasing importance of transit detections, which currently provide about half of the planets found.

In the history of exoplanets, with each new discovery new problems arise and theoretical models were not able to explain certain parameters of many newly discovered exoplanets. Hence, besides detecting exoplanets, investigations on known exoplanets started, especially around transiting ones. Transiting exoplanets have the advantage that for one it is possible to break the $M_P \sin i$ degeneracy of radial velocity data, by obtaining the orbital inclination i. For another one can estimate the radius of the planet and combined with its mass – obtained by the radial velocity measurements – one can derive the planetary density. Figure 1.2 shows a mass-radius (M-R) diagram of the known transiting planets as of March 2009. So far no theory can explain the observed mass-radius relation of all these planets.

The first such problem already arose with the discovery of the first transiting exoplanet HD 209 458b, which appeared to have a radius about 20% to 30% larger than predicted by atmosphere models; later on many more bloated hot Jupiter exoplanets were detected. Therefore investigations started to probe

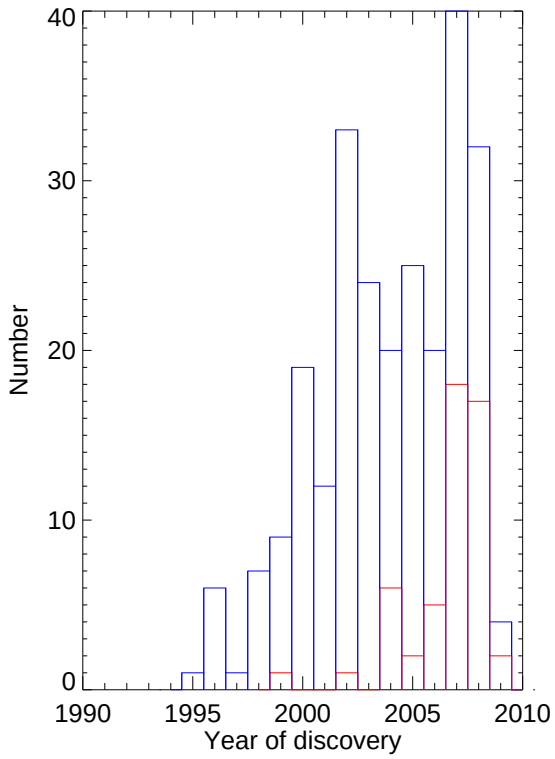

FIGURE 1.1— Total number of detected planets versus year of discovery (blue line) and exoplanets showing a transit (red line) as of March 2009.

the atmosphere of these bloated hot Jupiters. Several theories to explain these inflated hot Jupiters have been brought forward. Most theories concentrate on finding an additional energy source in the planet which might increase the radius. A study by Vidal-Madjar et al. (2004) also seems to prove that the upper layers of the atmosphere of HD 209 458b are in the process of evaporation because of its proximity to the star, forming a large 'exosphere' around the planet.

Another problem was the unexpected proximity of many exoplanets to their host stars, whose formation is not well understood yet. Thus, observations of transits can help to estimate important parameters and, hence, constrain the models of planetary formation. Fig. 1.3 shows the orbital semi-major axis against the mass for detected exoplanets. From Fig. 1.3 we see that transiting planets are biased towards shorter orbits and higher masses (red dots), whereas

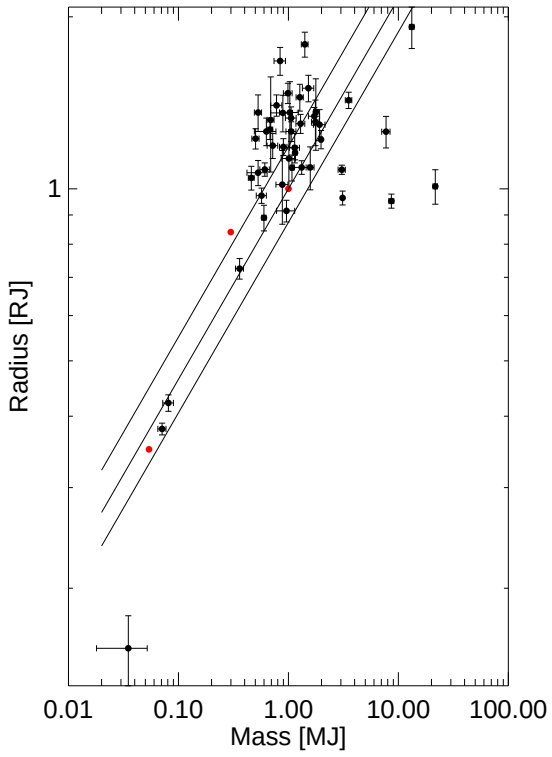

FIGURE 1.2— Mass-Radius diagram for transiting planets. Lines of equal density are also shown. Upper line: 0.75 g/cm^3, middle line: 1.25 g/cm^3 and lower line: 1.87 g/cm^3. Red dots correspond to Jupiter, Saturn and Neptune.

planets detected by radial velocity surveys clump between 1 - 5 AU. So far, two different scenarios for exoplanetary formation have obtained the most important attention. One is the gravitational protoplanetary disk instability scenario and the other the core accretion scenario. For a detailed review of both scenarios see e. g. Papaloizou & Terquem (2006) or Terquem & Halbwachs (2006a).

According to the gravitational disk instability scenario, giant planets are formed through a collapse and fragmentation of the protostellar disk. This allows to grow giant planets on a very short timescale. Therefore, the gaseous disk has to cool down and has to have sufficient mass in order to allow for its instability. When the disk reaches sufficient instability for the gas and dust to clump, then the dust grains coagulate and sediment to form a central protoplanetary core. The problem with this theory is the need of a very massive

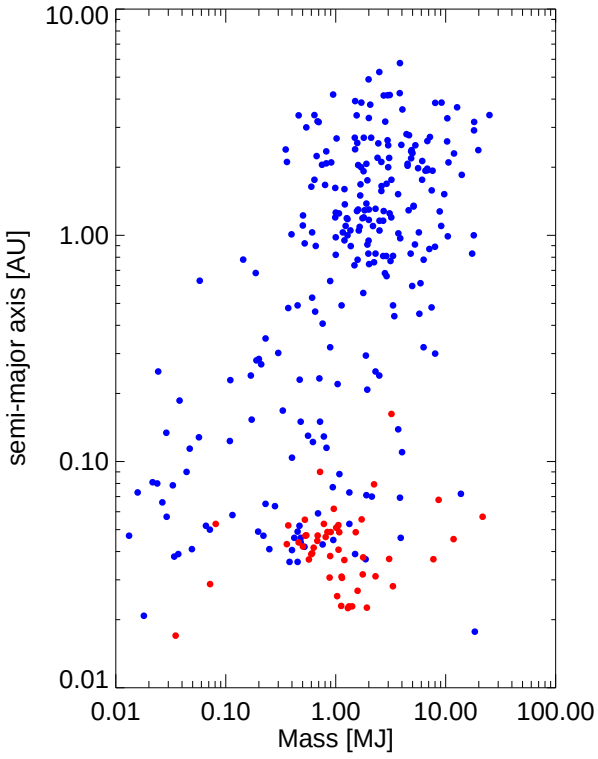

FIGURE 1.3— Orbital semi-major axis in function of mass for exoplanets (blue dots) and exoplanets showing a transit (red dots) as of March 2009.

disk, but above a certain disk mass the star starts to accumulate mass again, lowering the disk mass.

In the core accretion scenario, a solid core grows in mass along with the atmosphere in a quasi-static thermal equilibrium until it reaches a critical mass M_{crit}. The widely accepted critical mass is around 10 $M_{\oplus}$ and depends on the physical conditions and assumptions like e. g. grain opacity. Below the critical mass, both core and atmosphere grow very slowly in equilibrium between the energy radiated from the envelope into the surrounding disk and the gravitational energy by collision between the planetesimals and the surface of the core (coagulation of planetesimals). Above the critical mass, no equilibrium solution can be found and the atmosphere has to contract gravitationally to supply more energy at which point a runaway gas accretion occurs. However, the problem of this theory is the slow core accretion phase that may easily exceed the lifetime

of the protoplanetary disk. Furthermore, planetesimals and cores may undergo a phase of rapid inward migration when they reach a certain size.
In addition, as the standard theories do not allow for the formation of planets in orbits smaller than the one of Mercury, scientist have developed the theory of planetary migration, see e. g. Papaloizou & Terquem (2006) and Terquem & Halbwachs (2006b). Basically, in the migration theory the planet forms in the outer region of the protoplanetary disk and then moves inward by a) gravitational interaction between two or more Jupiter mass planets, b) resonant interactions between other planets and planetesimal and c) tidal interaction between the protoplanet and the gas. Alternatively, the discovery of new exoplanets shows that on average the planets with a shorter period are more massive which could suggest an evolution different from the migration of these planetary systems (Wuchterl, 2007), having formed 'in-situ' similar to a stellar binary system.
Other investigations concentrate on the detection of additional companions. In the case of exoplanets which do not show transits, continuous radial velocity measurements help to disentangle the different Keplerian orbits introduced by the planets and describe the planetary system. For transiting planets it is possible to detect additional planets by measuring the mid-transit time or transit duration and compare these to the expected values, i. e. times which would have been observed without an additional planet. In very rare cases it might be possible to observe the transit of an additional companion.
More discoveries and detailed characterizations of additional exoplanets can help to solve the previously mentioned problems, and improve our knowledge of the planetary equation of state, and allow to impose limits on the validity of some of these models.

1.2 Definition of a planet and exoplanet

An upper mass limit distinguishes between planets, brown dwarfs and stars. The Working Group of Extrasolar Planets (WGESP) of the International Astronomical Union has defined a planet as an object with a mass below the limit of the fusion of deuterium and hydrogen and that it is orbiting a star or stellar remnant, regardless of how it has been formed. It is generally accepted that the fusion limit is at 13 M_J for objects with solar metallicity. However, free-floating objects, found in young star clusters even with masses below the limit to fuse hydrogen and deuterium are not classified as planets but as sub-brown dwarfs. Exoplanets are planets orbiting around stars other than the Sun. Until now 347 exoplanets are known (Extrasolar Planets Encyclopedia, as of April 30, 2009).

Terms referring to Jupiter-sized exoplanets are also Giant Extrasolar Planet (GEP) and if they orbit their host stars at ≤ 0.05 AU or P ≤ 5 d, then they are referred to as Close-in Giant Extrasolar Planet (CGEP) or Hot Jupiter. If a system shows a transit it may be referred as a Transiting Exoplanet (TEP). Similarly to the classification of the dwarf M- and L-stars, recently, exoplanets have been grouped into two groups, namely cool pL-class and hot pM-class exoplanets (Fortney et al., 2008), mainly depending on the insulation they receive, with a break around a flux of 10^9 erg s^{-1} cm^{-1} (see Fig. 1.4). The difference between them is the existence of an inversion layer, where the temperature increases with height (hot stratosphere), due to absorption of incident flux at low pressure. In the atmosphere of hot pM-class planets, high levels of irradiation prevent condensation of titanium (Ti) and vanadium (V) bearing compounds and therefore no appreciable opacity due to TiO and VO gases appears. These planets exhibit molecular bands in emission rather than absorption; appear anomalously bright in the IR wavelength range and have a large day/night side temperature contrast, because the absorbed energy is re-radiated before it could be transported to the night side. On the other hand, pL-class planets do not show inversion layers since Ti and V compounds are condensed. They absorb the incident flux deep in the atmosphere and are more likely to redistribute absorbed energy; have a cooler day side and a warmer night side, and strong jet-flows cause significant phase-shifts in the thermal emission light curves.

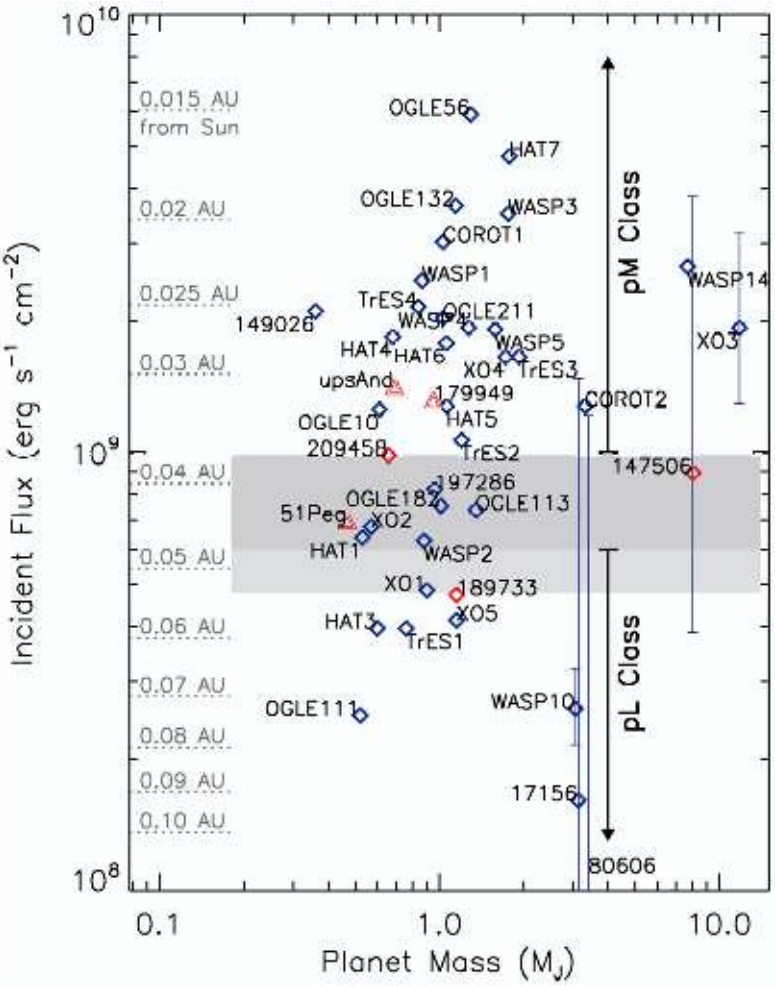

FIGURE 1.4— Flux incident upon a collection of hot Jupiter planets, as of 30 June 2008. The labeled dotted lines indicate the distance from the Sun that a planet would have to be to intercept this same flux. Diamonds indicate the transiting planets while triangles indicate non-transiting systems (with a minimum masses plotted). The error bars for some planets indicate the variation in flux that each receive over their eccentric orbits. Flux levels for pM Class and pL Class planets are shown, with the dark shaded region around ∼0.04-0.05 AU indicate a possible transition region (based more on data available in Fall 2007, than on theory). The lighter shaded region reaches down to XO-1b. Taken from Fortney (2009).

1.3 A brief overview of the detection methods

Mature extrasolar planets shine only through the reflected or re-radiated light from the parent star and thus their optical luminosity is about a billion times weaker than that of their host stars. This lack of brightness and the short distance to their host stars, causes that their direct imaging is difficult and has only been achieved very recently by Kalas et al. (2008) and Marois et al. (2008). Figs. 1.5 and 1.6 shows a direct image of an exoplanetary system obtained by these authors. That's why other methods for detection have to be employed. Fig. 1.7 shows a summary of detections methods for exoplanets. For this thesis the most important methods are detecting transiting exoplanets by photometric observations and confirming exoplanets by measuring the star's radial velocities; both will be described briefly in the next sections.

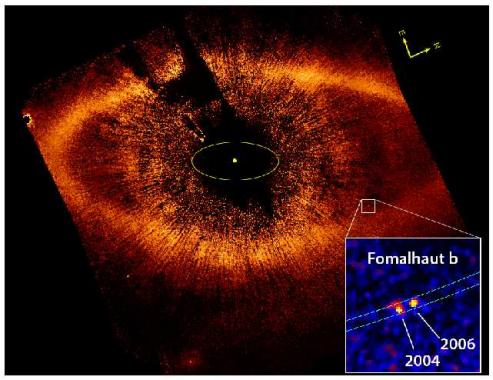

FIGURE 1.5— HST corongraphic image of Formalhaut at 0.6 μm showing the location of Formalhaut b (white square) 12.7″ radius from the star and just within the inner boundary of the dust belt. The yellow circle marks the location of the star behind the occulting spot. The yellow ellipse has a semi-major axis of 30 AU at Formalhaut (3.9″) that corresponds to the orbit of Neptune in our solar system. The inset is a composite image showing the location of Formalhaut b in 2004 and 2006 relative to Formalhaut. Taken from Kalas et al. (2008).

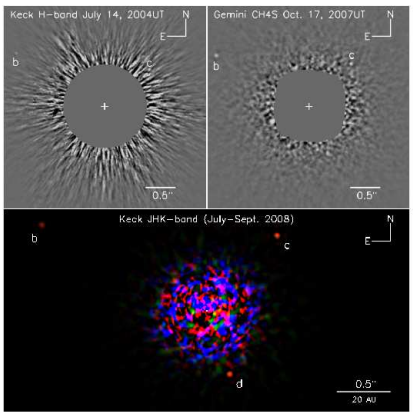

FIGURE 1.6— HR 8733bcd discovery images after the light from the bright host star has been removed by ADI processing. (Upper left) A Keck image acquired in July 2004. (Upper right) Gemini discovery ADI image acquired in October 2007. Both b and c are detected at the 2 epochs. (Bottom) A color image of the planetary system produced by combining the J-, H-, and Ks-band images obtained at the Keck telescope in July (H) and September (J and Ks) 2008. Taken from Marois et al. (2008).

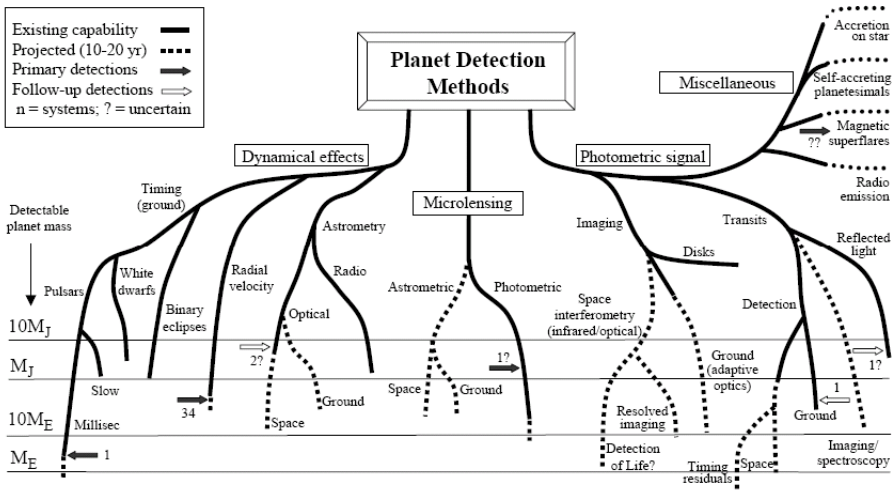

FIGURE 1.7— Summary of the detection methods (Perryman, 2000).

1.3.1 Radial velocity measurements

This method is detecting extrasolar planets by an indirect measurement of the gravitational disturbance of the parent star caused by the exoplanet. An excellent overview of the principle of the radial velocity (RV) measurements can be found in Bouchy & Halbwachs (2006). For example, our Jupiter orbits the Sun in 11.9 years, at a distance of 5.2 AU and with a speed of 13 km s^{-1} relative to the center of gravity of the system. That movement causes the Sun to wobble around the center of gravity of the system with the same period but at a distance of only 0.005 AU (about 1 $R_\odot$) and with a speed of 12 m s^{-1}. The radial velocities are measured through the Doppler effect by which an electromagnetic wave emitted by a moving object with speed v changes its length fulfilling $\frac{v}{c} = \frac{\lambda - \lambda_0}{\lambda_0}$. If we measure the radial velocities at different orbital phases and with an estimate of the stellar mass (from spectroscopic observations and stellar evolution models), one can fit for a Keplerian orbit and infer the orbital parameters (period P, eccentricity e, periastron ω), and the planet mass ($M_P \sin i$), which is ambiguous due to the generally unknown value of the orbital inclination i.
Figure 1.8 shows the parameters of the orbits of a planet and a star. In this Figure, the star has a mass M_s and orbits the center of mass (cm) at a distance of a_s, whereas the planet has a mass of M_P in an orbital distance of a_P. The speed that one would detect by RV measurements, is the component of the velocity V_s along the line of sight, which depends also on the inclination i. The radial velocity can be expressed as:

$$V_{rad} = V_0 + K\left[\cos\left(\nu(t) + \omega\right) + e\cos\omega\right], \tag{1.1}$$

where V_0 is an offset and specific to each spectrograph and observation site, ω is the periastron and ν the true anomaly. For the semi-amplitude K we get the following relation (Bouchy & Halbwachs, 2006):

$$K[m/s] = 28.45\frac{M_P[M_J]\sin i}{\sqrt{a_P[AU]M_S[M_\odot]}} = 203\frac{M_P[M_J]\sin i}{M_S^{2/3}[M_\odot]P^{1/3}[d]}, \tag{1.2}$$

As mentioned above, the radial velocities of a star are obtained through the displacement of spectral lines, usually for absorption. This effect is relatively small: a radial velocity variation of 12 ms^{-1}, as in the case of Jupiter, would shift a spectral line in visible by only 0.2 mÅ.

Generally, the displacement of a spectral line is estimated with the help of a (synthetic) reference spectrum, cross-correlating the science data with the reference spectrum. A reference spectrum can be a numerical mask or an observed

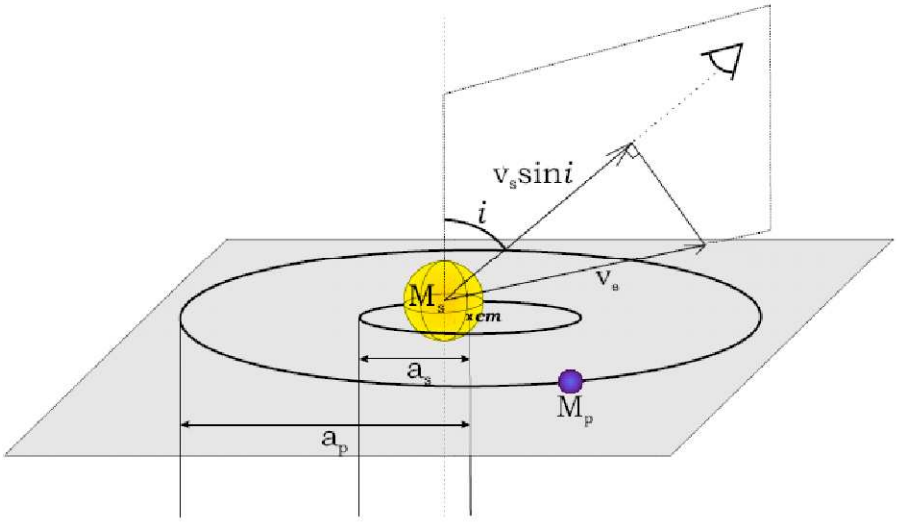

FIGURE 1.8— Schematic view of the main orbital definitions. The star s and the planet p orbit their center of mass cm, in circular orbits with a radius of a_s and a_p respectively. The orbital plane is plotted in gray, and the inclination i is defined as the angle between the normal to this plane and the observer's line of sight. The observer is marked by the eye-symbol. The reflex motion of the star V_s, when measured along the line of sight is affected by the sine of this angle (Taken from Alonso 2005).

spectrum. From the results obtained in this way we must subtract the components of the velocity due to the deviation of the instrumental components of the spectrograph and the movement of the Earth.

The deviations due to the instrument are mostly caused by the variation of the refractive index of the air which depends on temperature and atmospheric pressure. Its variation is temporary and random. Another cause of deviation of the instrument comes from the thermo-mechanical flexions of the instrument. That is why it is extremely important to stabilize the instrument and consequently it is necessary to measure its drifts with the help of a stable spectral source.

One of the Earth's RV components is around hundreds of ms^{-1} and is caused by the daily rotation of the Earth, whereas the other component is caused by the movement of the Earth around the Sun and is of the order of $\pm$ 30 km s^{-1}. The uncertainty of this calculation is estimated to be around 0.09 ms^{-1} (Bouchy & Halbwachs, 2006).

There are two main techniques for accurate measurements of the radial velocities, that is the iodine cell and the simultaneous thorium argon lamp technique. In the iodine cell technique, the light passes through a cell in which molecular

absorption occurs. This overlaps the absorption spectrum of the star and allows its calibration. In this case, the light from the star and the calibration follow the same path through the spectrograph. The Doppler shift is estimated by adjusting a global spectrum composed of light from the star and the iodine cell. This method requires a precise modeling of the response of the spectrograph (PSF) and then deconvolve the compound spectrum. This integrated system has the advantage that it is not so important to maintain a stable temperature and pressure of the spectrograph. On the other hand, its drawback is the high absorption between 500 and 630 nm, i. e. this method is only useful for bright stars or for telescopes with a large aperture. This method is used by the spectrographs UVES on the Very Large Telescope (VLT), HiRES on the Keck telescope and Hamilton on the Shane telescope.
In the simultaneous thorium-argon lamp technique, an optical fiber carries the light of the star toward the spectrograph while a second fiber sends the light from a calibration lamp, with a cathode of thorium-argon. The lamp offers many lines and is rich in contrast, which is very useful for measuring the derivation of the instrument during the night, with the condition that the instrument is relatively stable in temperature and pressure, so the relative drifts between the two fibers are negligible. This technique is not so limited in terms of spectral domain and covers the entire visible range of 380 to 680 nm, but it needs a good environmental stability to avoid a relative drift between the 2 fibers. The major spectrographs applying the simultaneous thorium-argon lamp technique are ELODIE and SOPHIE on the 1.2m OHP, CORALIE on the 1.2m Euler telescope, HARPS on the 3.6m ESO and FLAMES on the VLT.
Generally, methods to calculate the RV are based on a cross-correlation between the science spectrum and a (observed or synthetic) reference. The synthetic reference is normally based on a binary mask that contains areas with the values 0 and 1. Areas other than 0 correspond to the position of a spectral absorption line without a displacement due to the Doppler effect. These masks are constructed from synthetic spectral libraries or from a real spectra obtained with high resolution and high S/N. The cross-correlation is to shift the mask and the observed spectrum against each other and obtain the cross-correlation function (CCF). Fig. 1.9 shows how the principle of obtaining the RV measurements works by cross-correlating the stellar spectrum with a binary mask. The RV is given by the position of the minimum in cross-correlation function (marked as v_0 in Fig. 1.9), which is estimated in general by an adjustment of the CCF to a Gaussian function.

Generally, to confirm the planetary nature by means of RV measurements, one assumes first a circular Keplerian orbit of one object to obtain the mass. Large residuals from this Keplerian fit can be explained with two causes: an

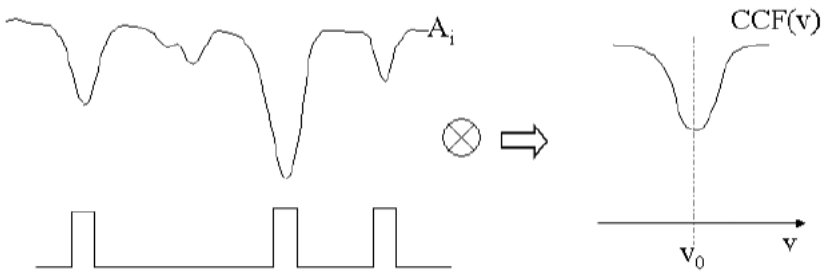

FIGURE 1.9— Principle to calculate the radial velocity by cross-correlation with a numerical mask. Left side: the upper observed spectrum is cross-correlated with the lower binary mask. Right side: resulting cross-correlation function (CCF). (Bouchy & Halbwachs, 2006).

eccentric orbit and/or another body in the system. An interesting discussion of large residuals has been done on GJ436b, indicating another planet of very low mass (Ribas et al., 2008), which will be outlined in Chapter 3. Long-term RV measurements might help to identify a linear trend in the RV curve, also indicating an additional body in the system. Many systems with multiple planets have been found with this method. Fig. 1.10 shows an example of radial velocities as observed by HARPS for HD 69 830 (Lovis et al., 2006), a system with three Neptune-mass planets.

The RV method has discovered most of the known extrasolar planets to date. The mass of the discovered bodies ranges from 0.006 to 25 M_J, with a period range between 1.3 and 5218 days. The spectroscopic observations are used to estimate the period and the eccentricity of the planetary orbit and provide a lower limit of the mass of the planet, provided the mass of the star can be determined; e. g. by comparing its spectrum with a spectrum from stellar atmosphere models. The diversity of objects found with this method permits us to extract a number of common characteristics among exoplanets, or their host stars, such as the fraction of those that have planets (up to a lower value of the planetary mass), the function of secondary mass of the object, the distribution of the eccentricities, dependence on the metallicity of stars with exoplanets, or the distribution of the period compared to the mass of these objects. By combining RV results with the measurements obtained by the transit method, one can also determine the exact mass of the planet M_P and its density ρ_P.

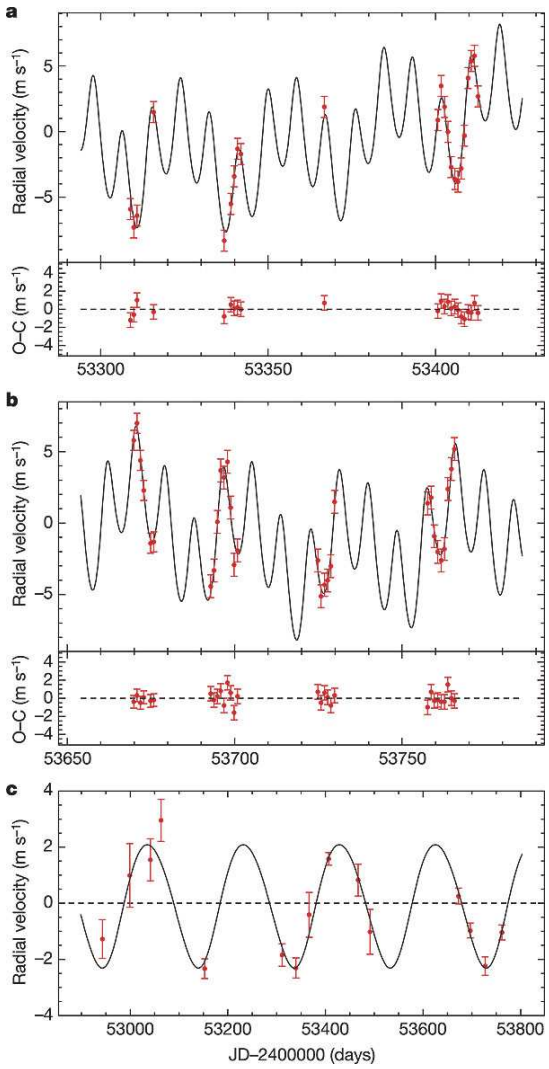

FIGURE 1.10— Example of close-up views of radial velocity measures of HD 69 830, showing the cumulative signal of three planets. The short-period planet (P = 8.67 days) shows up as a high-frequency modulation, whereas the intermediate planet (P = 31.6 days) is revealed through the varying values of successive minima and maxima. The outer planet (P = 197 days) is not easily seen on these magnified views, but its presence becomes clear when removing the signal of the inner planets and binning the data points (one per observing run), as shown in c. Note that only high-quality radial velocity measurements are able to resolve this system. Taken from Lovis et al. (2006).

1.3.2 Photometric detection of transiting extrasolar planets

Since the observation of a transit of HD 209 458b, the photometric detection of transiting exoplanets has had a great significance within the various techniques available for the discovery of exoplanets.
Among the various methods for the detection of exoplanets, the transit method has received great attention due to its simplicity and its future potential for detecting Earth-type planets. This method also offers the opportunity to study the existence of planetary satellites (Sartoretti & Schneider, 1999), additional planets (Holman & Murray, 2005; Agol et al., 2005), rings or even detect elements in the atmosphere as atomic hydrogen (Vidal-Madjar et al., 2003), sodium (Charbonneau et al., 2002), methane (Swain et al., 2008b), water (Tinetti et al., 2007; Beaulieu et al., 2008; Swain et al., 2008b; Grillmair et al., 2008), oxygen and carbon (Vidal-Madjar et al., 2004), or detect the existence of haze, such as detected in HD 189 733b with data from the Hubble Space Telescope (HST) (Pont et al., 2008). For a review of photometric transit observations see Charbonneau et al. (2007) and for spectroscopic observations see Tinetti & Beaulieu (2009).
During transit, the planet crosses between the observer and the star and causes a decrease in brightness, which is reflected in the light curve. This light curve can be described with three parameters: the relative depth of the transit ΔF, the total transit duration t_T and its shape. Comparing Figs. 1.11 and 1.12 we see that the shape of the light curve depends on the latitude of the transit on the stellar disk, i. e. it depends on the inclination i of the planetary orbit. From the transit light curve, we also can determine the impact parameter b, which is the projected distance from the center of the planet to the center of the star at the moment of maximum approach in units of the radius of the star. The impact parameter b can be described by $b = a_p/R_s \cos i$. The ingress is defined as the phase between the first contact until the planet lies entirely in the stellar disk (second contact) and the egress is the opposite. The light curve has a form similar to a "U" if the planet passes through the center of the star (Fig. 1.11), i. e. $i \approx 90°$, and a form of a "V" if the eclipse is grazing (Fig. 1.12).

Several formalism and light curve simulations have been brought forward in order to describe a light curve and to derive parameters like e. g. the ratio between the radii of the planet R_P and the star R_S, the inclination i (or impact parameter b) and by knowing the mass of the star the radius of the planetary orbit a. The most important formalisms are Seager & Mallén-Ornelas (2003), Mandel & Agol (2002) and Giménez (2006a), and an important transit light curve simulation tool is the "Universal Transit Modeler" (UTM, Deeg 2008).

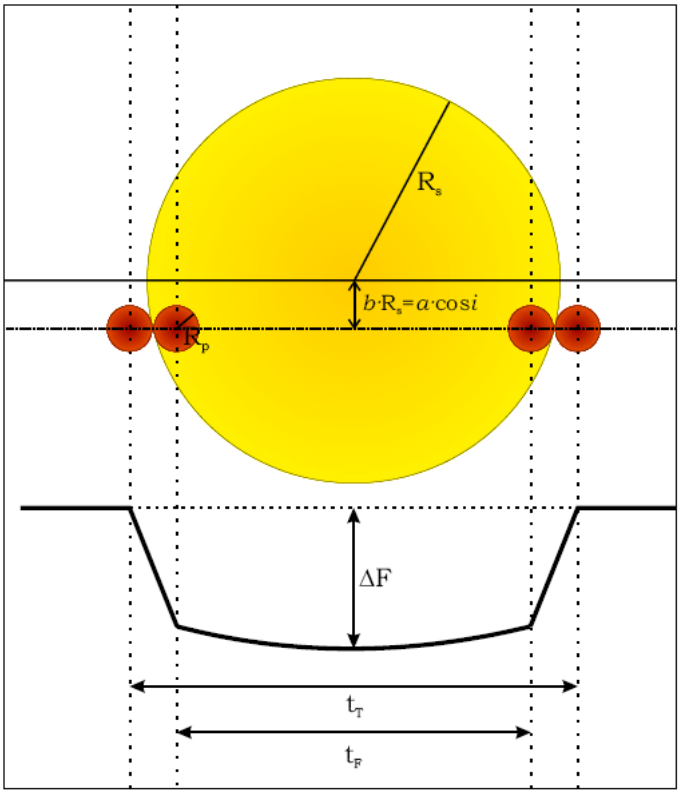

FIGURE 1.11— Schematic of a transit and transit light curve with central impact b close to zero.

Seager & Mallén-Ornelas (2003) assume that the planetary orbit is circular, the planet is dark compared to the central star and the stellar mass-radius relation is known. Based on these assumptions they derive three equations, describing the geometry of the transit light curve:

$$\Delta F = \frac{F_{off} - F_{on}}{F_{off}} \approx \frac{R_P^2}{R_S^2}; \tag{1.3}$$

$$t_T = \frac{P}{\pi} \arcsin\left(\frac{R_S}{a} \sqrt{\frac{\left[1 + \frac{R_P}{R_S}\right]^2 - b^2}{1 - \cos^2 i}} \right); \tag{1.4}$$

$$\frac{\sin(t_F \pi)/P}{\sin(t_T \pi/P)} = \frac{\sqrt{\left[1 - (R_P/R_S)\right]^2 - b^2}}{\sqrt{\left[1 + (R_P/R_S)\right]^2 - b^2}}. \tag{1.5}$$

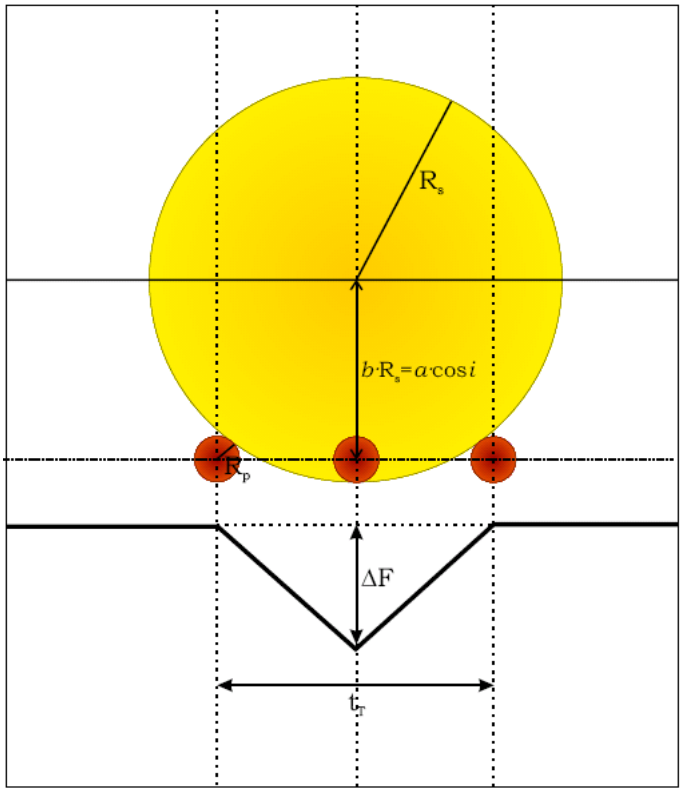

FIGURE 1.12— Schematic of a transit and transit light curve with higher impact parameter b.

The transit depth ΔF is just the square of the radii ratio of the planet and the star, which is obtained by observing the flux outside the transit part F_{off} and during transit F_{on}. Assuming a reasonable good estimate for the stellar radius one can obtain the planetary radius from this equation. The transit duration t_T depends on the period P or orbital distance a, the stellar radius R_S and the inclination i and the transit shape is described by the ratio between duration of the transit flat part, t_F, and total transit duration, t_T. Fitting a trapezoid to the observed light curve one can obtain the geometric parameters for Eqs. 1.3 to 1.5 and with additional knowledge of the period P and stellar radius R_S it is possible to estimate the unknown parameters R_P, i, a, R_S and M_S, which can be derived from the following equations (Seager & Mallén-Ornelas, 2003):

$$\frac{R_P}{R_S} = \sqrt{\Delta F}, \tag{1.6}$$

$$b = \frac{a}{R_S}\cos i = \sqrt{\frac{(1-\sqrt{\Delta F})^2 - \left[\sin^2(t_F\pi/P)/\sin^2(t_T\pi/P)\right](1+\sqrt{\Delta F})^2}{1-\left[\sin^2(t_F\pi/P)/\sin^2(t_T\pi/P)\right]}}, \tag{1.7}$$

$$\frac{a}{R_S} = \sqrt{\frac{(1+\sqrt{\Delta F})^2 - b^2\left[1-\sin^2(t_T\pi/P)\right]}{\sin^2(t_T\pi/P)}}, \tag{1.8}$$

$$\rho_S = \frac{M_S}{R_S^3} = \left(\frac{4\pi^2}{P^2G}\right)\left\{\frac{(1+\sqrt{\Delta F})^2 - b^2\left[1-\sin^2(t_T\pi/P)\right]}{\sin^2(t_T\pi/P)}\right\}^{3/2}. \tag{1.9}$$

However, the formalism of Seager & Mallén-Ornelas (2003) neglects the limb darkening effect, which causes a star to appear slightly brighter at the center of the stellar disk than on its border. The light curve with limb darkening will be slightly deeper and its shape rounder. An example of the effect of the limb darkening is shown in Figure 1.13, where the green line is without limb darkening, the red line by using a linear limb darkening relation:

$$I(\mu) = I(1)[1-u(1-\mu)] \tag{1.10}$$

and the blue line indicates a quadratic limb darkening relation:

$$I(\mu) = I(1)[1-u_a(1-\mu)-u_b(1-\mu)^2] \tag{1.11}$$

In the equations above, $I(1)$ is the luminosity at the center of the star, μ is the cosine of the angle between the normal of the stellar surface and the line of sight, and u, u_a and u_b are the limb darkening coefficients for the corresponding relations, which depend on the wavelength range of observation. For Fig. 1.13 I used the parameters of TrES-1 and the following limb darkening coefficients: $u = 0.29$, $u_a = 0.28$ and $u_b = 0.21$.

The further formalisms do not neglect the limb darkening relation and describe the light curves more accurate. Mandel & Agol (2002) presents analytic formulae to describe the transit as an eclipse of a spherical star by an opaque dark, sphere, including limb darkening. Mandel & Agol (2002) will not be further discussed, because it is not used in this thesis and a better formalism has been presented by Giménez (2006a). Giménez (2006a) starts by describing the total luminosity $l(t)$ at any given time t received by the observer as the sum of the stellar luminosity L_S and the planetary luminosity L_P (normally zero), and subtracting a term $\alpha(t)L_S(t)$ describing the relative loss of the light due to occultation of the star. He further defines the phase $\theta = \frac{2\pi}{P}(t-t_0)$, where t_0 is the central transit time and the transit phase of the ingress is denominated θ_l . Generally, light curve observation are normalized that the flux outside the

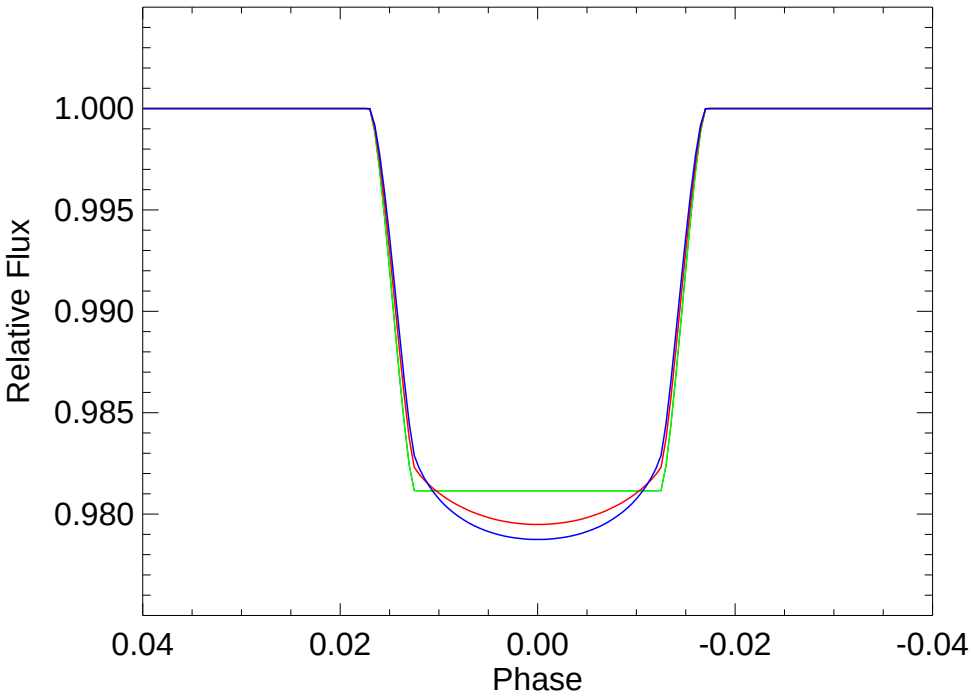

FIGURE 1.13— Model light curves for TrES-1 with different limb darkening relations using the formalism of Giménez (2006a), see text for details.

transit is 1, i. e. $L_S + L_P = 1$, with this Giménez (2006a) derives the light curve equation:

$$l(\theta) = 1 - \alpha(\theta) L_S. \tag{1.12}$$

In order to solve Eq. 1.12, one has to evaluate $\alpha = \int_S I \cos\gamma d\sigma$ at any given phase and over the entire stellar disk S, where I represents the brightness distribution of the stellar disk, $d\sigma$ is a surface element and γ is the angle between the surface normal and the line of sight. As we have seen before, the stellar disk is affected by the limb darkening effect, therefore, Giménez (2006a) uses a general limb darkening law, to describe the brightness distribution of the stellar disk, of the form $I(\mu) = I(l)\left[1 - \sum_{n=1}^{N} u_n \left(1 - \mu^n\right)\right]$. In the case of a quadratic limb darkening relation the coefficients u_a and u_b, used by Claret (2000), have to be converted into u_1 and u_2, used by Giménez (2006a), following: $u_1 = u_a + u_b$ and $u_2 = u_a - u_b$. Finally, Giménez (2006a) derives a general expression for the α_n functions in terms of Jacobi polynomials, where the precision of the light

curve depends on the number of terms used for the Jacobi polynomials and on the order of the limb darkening relation. The advantages of the formalism of Giménez (2006a) are that it is valid for any limb darkening relation and eccentricity. Furthermore the formalism of Giménez (2006a) has been expanded by Giménez (2006b) to model the Rossiter-McLaughlin effect.
Finally, UTM is an IDL-routine permitting simulations of transit light curves of multiple bodies, including rings and moons, and the fitting of observed light curves. A practical application of UTM will be seen in Chapter 4.
Even though the light curve models, mentioned above, describe a planetary transit very accurately, there is still a degeneracy between R_P, R_S and i. By reducing the radii of the planet and the star, one can increase the inclination i in order to preserve the transit depth and also the chord length across star. This degeneracy dominates the uncertainty for R_P, and it is typically solved by assuming a value for R_S based on stellar models, requiring precise knowledge of the spectral type and metallicity of the central star. Alternatively, it can be resolved by high signal-to-noise (S/N) light curve observations with for example the HST. For these high S/N light curves, we can estimate the exact ingress time and limb darkening (curvature in mid-transit) by only assuming one parameter, namely M_P. Simultaneously fitting of multi-color photometry, under assumed values for the stellar-limb darkening, which serves to isolate the impact parameter of the planet's path across the star, can also break the degeneracy amongst R_P, R_S and i (Jha et al., 2000; Deeg et al., 2001).
The probability that an exoplanetary system with unknown inclination shows a transit is given by (Charbonneau et al., 2007):

$$P_{tran} = 0.0045 \frac{1\mathrm{AU}}{a_P} \frac{R_S + R_P}{\mathrm{R}_\odot} \left[\frac{1 + e\cos(\frac{\pi}{2} - \varpi)}{1 - e^2} \right], \tag{1.13}$$

where e is the eccentricity and ϖ is the longitude of periastron. Since for FGK stars the planetary radius is much smaller than the stellar radius, $R_P << R_S$, and the stellar radius is smaller than the orbital distance, $R_S < a_P$ and assuming circular orbits, one can simplify the equation above to:

$$P_{tran} = \frac{R_S}{a_P}. \tag{1.14}$$

One can see from this equation that transit surveys are most effective for short period planets and around stars with a large radius. However, the latter case, a star with a large radius, is also a common source for false positives (see Subsect. 1.3.4), like e. g. a giant star eclipsed by a dwarf star.

1.3.3 Transiting planet detection approaches

There are mainly two approaches to detect transiting exoplanets. One approach is to conduct a photometric survey, searching for possible planetary transit and then confirm the planetary character by follow-up observations, especially radial velocity measurements. This approach is used for some work in this thesis and will be discussed in more detail in the following subsection. The other approach would be to photometrically follow-up known exoplanets, where transits have not been detected yet, e. g. detected by radial velocity surveys, and try to detect a transit in these systems. This way the first transits in an exoplanetary system, namely HD 209 458b (Charbonneau et al., 2000; Henry et al., 2000) and the first transit of a Neptune mass planet GJ 436b (Gillon et al., 2007b) have been detected.
Additionally, transits of long-period planets from the ground can only be detected with reasonable chances of success by following-up photometrically planets which have already been confirmed by the radial velocity method. Kane (2007) showed how the possible transit ephemeris can be estimated for exoplanets detected by the radial velocity method. However, these ephemeris have high uncertainties associated with the fitted orbital parameters and uncertainties depending on the time elapsed since the most recent radial velocity measurement. Both uncertainties make it very difficult to find a transit in known exoplanets. Long-term radial velocity observations combined with a prompt photometric observing strategy, after the orbital parameters have been revised, can help to narrow down the transit windows and to possibly detect the transit, especially for long-period exoplanets. Examples of transit observations of long-period exoplanets, detected first by radial velocity, are HD 17 156b with P $\sim$ 21 days (Barbieri et al., 2007) and HD 80 606b with P $\sim$ 111 days (Moutou et al., 2009; Fossey et al., 2009).

1.3.4 Introduction into photometric transit surveys

As previously have been shown, a transit is a rare event and even though radial velocity measurements have the advantage of being able to detect exoplanets independent of its inclination, one has to observe the stars one by one. Whereas in transit surveys one may probe thousands of stars simultaneously for transits, increasing the odds of observing one. Generally, in photometric transit surveys, one observes as many stars as possible over a long period of time and creates a flux time series which is then searched for possible flux decreases, i. e. transit events.
In order to observe as many stars as possible, there are two strategies one can follow: case one, where one observes bright stars with small aperture telescopes

but with a wide field-of-view, namely wide-field surveys and case two, where one observes also faint stars with large aperture telescope, so-called deep-field surveys, taking into account the volume effect, i. e. that the number of stars increases with decreasing flux. The advantages of wide-field surveys of bright stars are for one the easier follow-up, especially radial velocity follow-up observations and for another the possibility to create a cheap network of multi-site surveys, whereas for deep-field surveys the costs for a large aperture telescope network might be higher and the follow-up observations of the fainter objects might be more difficult. The advantage of multi-site surveys compared to single-site ones is, that they are less biased over a wider range of periods, e. g. single site survey are biased towards transiting planets with 2-3 days periods, whereas multi-site can recover transiting planets for periods up to 6 days.
Transit surveys detect preferably exoplanets in smaller orbits, because smaller orbits are more likely to have an eclipsing configuration, as can be seen from Eq. 1.14, and with shorter periods the chances of observing more transits increases, which helps to improve the detection statistics. However, the drawback of transit surveys are the high rate of astrophysical false positives and some instrumental false positives. We can distinguish several major cases of astrophysical false positives:

- A grazing eclipsing binary;
- A dwarf low-mass star/brown dwarf eclipsing a giant star/main sequence star;
- An eclipsing binary system diluted by another star (triple system).

Brown (2003) estimated the expected frequencies of occurrence of both transiting exoplanets and false alarms in photometric wide-field surveys. For a project like STARE and in a field of the Galactic plane, it is estimated that for every 10 000 stars observed with an accuracy better than 0.01 magnitudes, there should be 1.4 transiting exoplanets and 7.2 false alarms.
A grazing eclipsing binary consists of two stars with an orbit inclined at an angle which can produce a shallow transit in the light curve. These eclipses are mostly deeper, and therefore in most cases easy to distinguish. Also, typically they exhibit primary and secondary eclipses of different depth. Furthermore, the light curve is more "V"-shaped or certain sinusoidal modulations of the light curve part outside the transit, due to gravitational effects on the surface of the binary, can be found for this type of false alarms. These sinusoidal modulations can be detected by fitting a sine function to the light curve part outside the transit. Another way to detect them is through fitting the light curve and to

determine the transit length and transit depth, both must agree on a value for the radius compatible with an exoplanet and stellar density compatible with the host star (Seager & Mallén-Ornelas, 2003). Both, the sinusoidal variation and the light curve parameter consistency check, will be discussed in more detail in Chapter 2. Finally, spectroscopic observations usually offer two different sets of spectral lines in this case, from each of the binary components.
A low-mass companion, i.e. a M dwarf or brown dwarf, crossing a larger giant star or main sequence star can produce a photometric signal similar to that of a planet, because the ratio R_{S2}/R_{S1} might be similar to R_P/R_S. However, this case shows also sinusoidal modulations of the off-transit part and a too short transit event and can typically be resolved by calculating the stellar density from the light curve. They can also be resolved easily with low-precision radial velocities of the order of km s^{-1}.
A diluted binary system consists of a binary and a third star in the same line of sight so that the observed configuration appears as a single star that cannot be resolved photometrically. Such a system may be discriminated with high-resolution spectroscopy because of the presence of different spectral lines. However, it is possible that the spectral lines of the binary are much weaker compared to the third star and one will not be able to detect the radial velocity variations of the binary. The variations of the binary's spectral lines can be masked by the broadening of spectral lines through the third star's rotation. To avoid these problems, Torres et al. (2004) proposed to take a detailed spectrum for an analysis of the bisector asymmetries of the lines in this spectrum, indicating the existence of a diluted triple system. Finally, it is also possible to eliminate this false alarm if the binary system has a significant difference in temperature to the third star because in this case, the eclipse should show a dependence of the depth with color, i. e. multi-color photometry, may detect that eclipses with different depths at different wavelength.

1.4 Follow-up observations to characterize transiting exoplanets

After detecting transiting exoplanets, many investigations continue with more detailed observations from ground or space. Generally, follow-up observations to characterize transiting exoplanets can be done spectroscopically or photometrically for the whole planetary orbit or at certain times, like e. g. at the primary transit phase or secondary transit phase. Fig. 1.14 shows a schematic of a light curve over the whole orbit of an exoplanet in transiting configuration. The primary transits and secondary eclipse can be seen at phases 0, $\pi/2$ and

π and the sinusoidal modulation represents star light reflected by the planet. Recently, Snellen et al. (2009a) claimed the first photometric observation of the reflected star light over a whole orbit and gave an upper limit of the geometric albedo of < 0.2 based on CoRoT observations of CoRoT-1b. Alternatively, reflected star light can be observed spectroscopically. The observed spectra of a system star-planet will contain reflected components of the stellar light, which vary in amplitude and Doppler shift as the planet rotates around its axis and orbits the star. Both, photometric and spectroscopic observations over the whole orbit will not further be considered because it is not part of this thesis. However, photometric follow-up observations at special times like the primary transit phases or secondary eclipse phases will be further discussed, because they are part of this thesis. These primary transit and secondary eclipse observations can be used in order to

- search for star spots or additional transiting bodies;
- find variations in the timing of the transits that indicate deviation from strict periodicity that might have been caused by additional bodies in the system;
- observe transits with higher precision to get a more precise estimate of the parameters;
- measure the stellar spin and planetary orbit alignment (spin-orbit angle) by measuring the radial velocities during transit (RM-effect);
- probe the atmosphere by transmission spectroscopy or observations of the secondary eclipse.

1.4.1 Primary transit observations

Photometric primary transits of confirmed planets form a major part of this thesis and I am using them to measure the time of the transit occurrence or to search for intriguing asymmetric features in the transit light curve. Additionally, high-precision photometric light curves also could help to resolve the R_P, R_S and i degeneracy; and provide more reliable values of the basic planetary parameters.
Ideally and neglecting high eccentricities, the shape of a transit light curve should be symmetric. However, on several systems (TrES-1 by Charbonneau et al. 2007 and Rabus et al. 2009; HD 209 458 by Silva 2003 based on data from Deeg et al. 2001; HD 189 733 by Pont et al. 2007), there have been reports of asymmetric features in the transit light curve. Generally, the asymmetric

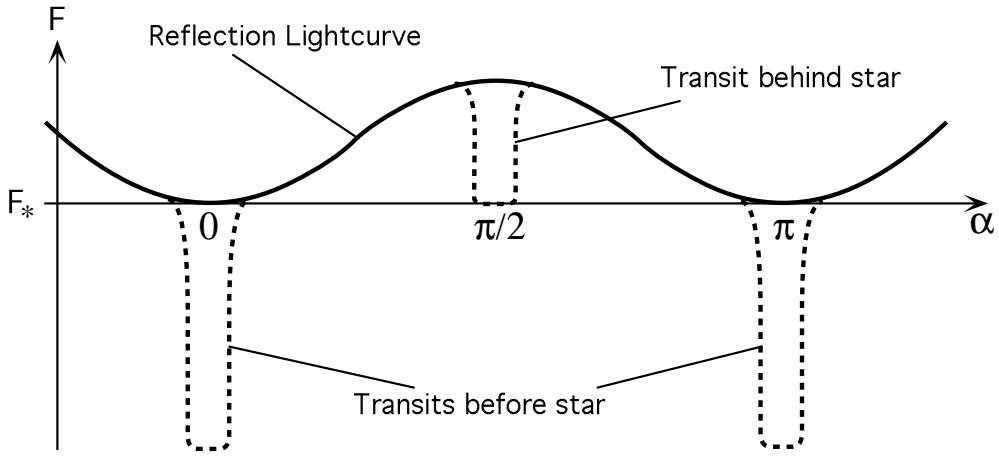

FIGURE 1.14— Taken from Deeg (1998): Light curve of a star with a reflecting planet (solid line). F_S is the flux from the star without planet. The horizontal axis (α) is the phase of the planet, given by the angle between planet, star and observer. Dashed lines indicate front (primary) and back (secondary) transits. Note that the depth of the front transits is orders of magnitudes larger than that of the back transits. This curve assumes no relevant emission arising from the planet itself.

features are explained by the transiting planet occulting a star spot. For the case of TrES-1, which will be treated in Chapter 4, I also present an alternative hypothesis, indicating that these features may have been caused by an additional transiting body.

By studying variations in the time of the mid-transit occurrence, transiting exoplanets give a possibility to find additional companions, even down to Earth masses. These variations will be the subject of Chapter 5 of this thesis. There are different mechanisms causing these variations. For one the gravitational influence of a perturbing body can alter the orbital period of the transiting planet (Holman & Murray, 2005; Agol et al., 2005). For another, a perturbing mass in an orbit larger than the transiting planet can cause the "star - transiting planet" system to wobble around the barycenter and alter the observed periodicity, something that is known as the light-time effect (Irwin, 1959; Schneider & Doyle, 1995; Doyle & Deeg, 2004; Schneider, 2005). These anomalies are reflected in the times of the transit occurrence. Hence, using a linear ephemeris and several observations of transits, it is possible to get the difference 'O-C' between the observed transit times and the calculated ones from the ephemeris. From this difference one can learn about perturbations on strict orbital periodicity from a possible companion object which has not been detected yet.

Not treated in this thesis are spectroscopic primary transits observations in order the measure the stellar spin - planetary orbit alignment or to probe the planetary atmosphere by transmission spectroscopy. Continuous measurements of the star's radial velocity, when done during a transit, permit to estimate the stellar spin - planetary orbit alignment (spin-orbit alignment) by observing the so-called Rossiter-McLaughlin (RM) effect (Rossiter, 1924; McLaughlin, 1924). The observation of the RM-effect can help to constrain the stellar obliquity. As the star rotates one half of the stellar spectrum will be red shifted, while the other side will be blue shifted. Depending on the orientation between the stellar spin and the planetary orbit, during transit the planet occults the respective halves, hiding some of the velocity components. When the planet is in front of the approaching (blue-shifted) half of the star, the net starlight appears slightly red-shifted. Measuring the spin-orbit alignment can help to place constraints on how the planet have migrated. Fig. 1.15 shows a schematic of different orbital configuration with respect to the stellar spin axis and the resulting observed RM-effect. An interesting discovery was made by Hébrard et al. (2008) with the discovery of a misaligned spin-orbit in the XO-3 planetary system (Fig. 1.16). An up-to-date overview of all published RM-effects, observed during planetary transits, can be found in Fabrycky & Winn (2009).

For transmission spectroscopy, the star is observed outside and inside the

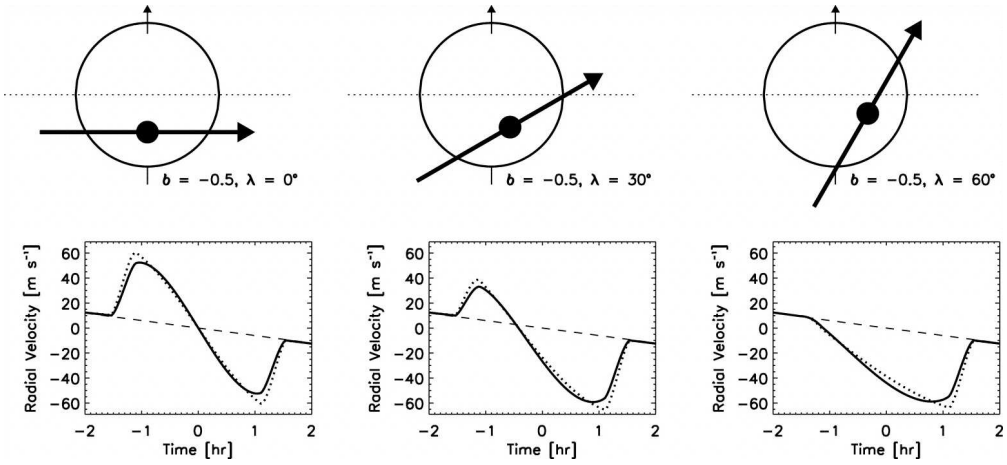

FIGURE 1.15— Schematic of the Rossiter-McLaughlin effect for different orbital inclinations with respect to the stellar spin axis (upper graphs) and resulting radial velocity measurements during transit (lower graphs). The dotted lines are for the case of no limb darkening ($\epsilon = 0$), and the solid lines are for $\epsilon = 0.6$. Left: perfect alignment between stellar spin and orbit. Middle: well-aligned system. Right: miss-aligned system. (Gaudi & Winn, 2007)

primary transit phases and the difference between both spectra will give the

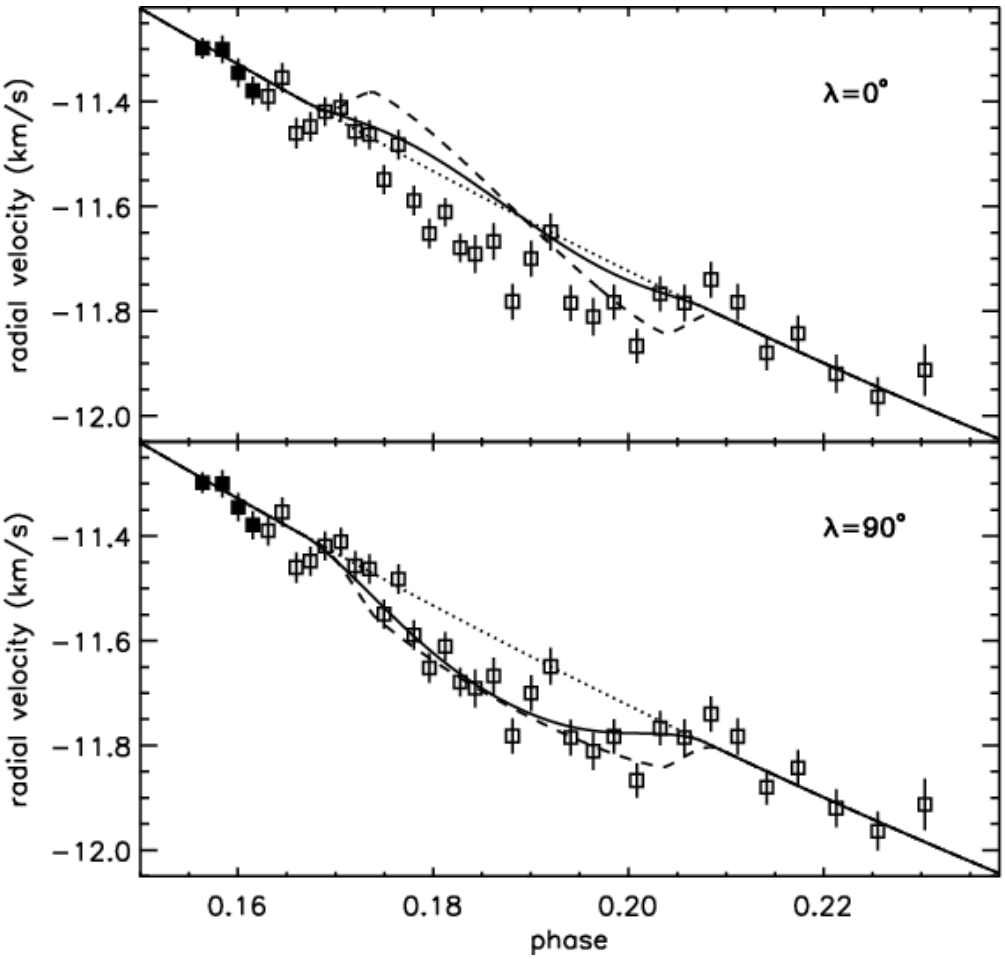

FIGURE 1.16— Rossiter-McLaughlin effect observations and models. Top: $\lambda = 0^\circ$ (spin-orbit alignment). Bottom: $\lambda = 90^\circ$ (transverse transit). On both panels, the squares (open and filled) are the SOPHIE radial-velocity measurements of XO-3 with 1σ error bars as a function of the orbital phase. Only the first four measurements (filled squares) are used for the Keplerian fit (together with 19 measurements at other orbital phases; see Sect. 4.1). The dotted line is the Keplerian fit without Rossiter-McLaughlin effect. The two other lines show Rossiter-McLaughlin models with $i = 78\overset{\circ}{.}6$ and $a/R_\star = 4.8$ (solid line) and $i = 84\overset{\circ}{.}9$, and $a/R_\star = 7.2$ (dashed line). Taken from Hébrard et al. (2008).

light absorbed by the planet's atmosphere. Transmission spectroscopy was first theoretically proposed by Seager & Sasselov (2000). During transit, the atmosphere of a transiting planet leaves an absorption signature on the observed stellar spectra. However, the imposed signal is small; for a hot giant planet

only roughly about 10 % of the total planetary radius is varying in opacity depending on the wavelength. When superposed on the star's disk, the total area that can act as probe for the atmosphere is on the order of 10^{-3} to 10^{-4} of the star's area. The difference in star light blocked by the planet at different wavelengths is the best diagnostic for the planet's atmosphere.
Based on transmission spectroscopy of HD 209 458b, Charbonneau et al. (2002) gave an estimate of the sodium abundance from HST high precision spectrophotometric observations. Ground-based observations by Deming et al. (2005a) allowed to put an upper limit for the presence of various other chemical species and Redfield et al. (2008) were able to detect sodium in the transmission spectra of HD 189 733b. Tinetti et al. (2007) claimed also the detection of H_2O in the same planet. Fig. 1.17 shows three models of a transmission spectra for HD 209 458 from Charbonneau et al. (2002).

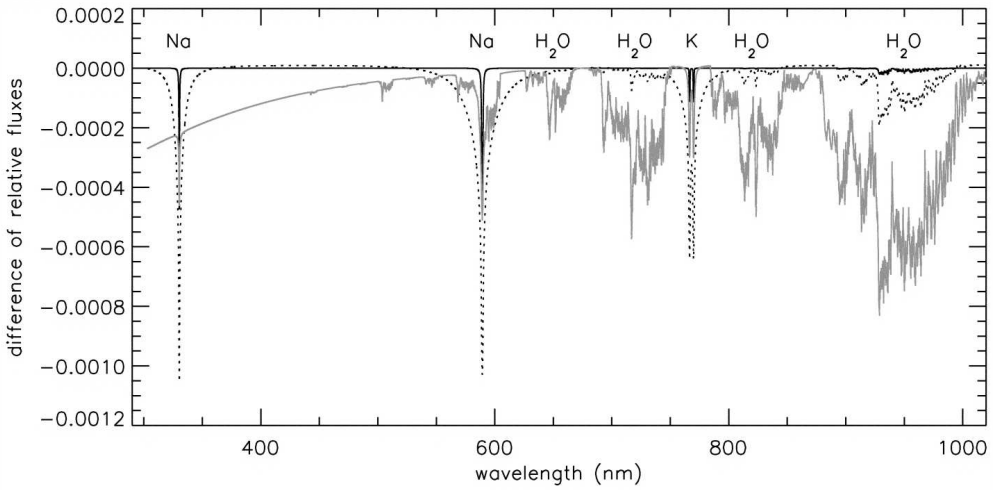

FIGURE 1.17— Three model transmission spectra for HD 209458. The fiducial model with a solar abundance of sodium and cloud tops at 0.0368 bar (3680 Pa or 0.0363 atm) is shown as a dotted line. A model with very high clouds reduces the depth of the sodium absorption feature is shown as the black solid line. Another model were the abundance of atomic sodium in the planetary atmosphere is reduced greatly from the solar value is shown by the gray solid line. Taken from Charbonneau et al. (2002).

1.4.2 Secondary eclipse observations

In a secondary eclipse or back transit, the planet disappears behind the star causing also a dip in the light curve. The secondary eclipse depth is a direct

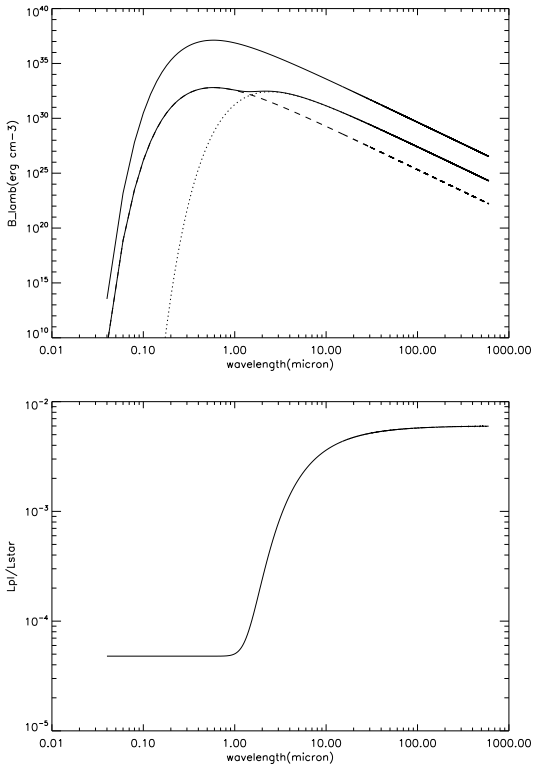

FIGURE 1.18— Upper plot: Stellar radiation in black body approximation (upper solid line) and planet radiation (lower solid line) of a typical hot giant, which is the sum of reflected light (dotted line) and thermal black body radiation (dashed line). For the stellar radiation, a T_{eff} of 4 980 K was used. The assumed bond albedo for planetary reflected light is 0.05 and for planetary thermal emission, a redistribution factor f of 0.25 and T_{eff} of 1 190 K was used. Lower plot: The planet-star flux ratio as a function of wavelength.

measurement of the planets light, which is composed of reflected stellar light (dominant in the visible wavelength range) and the thermal emission from the planet (dominant in the infrared wavelength range) and reaches up to a few milli-magnitudes in the near infrared wavelengths (Fig.1.18). Photometric observations around secondary eclipse phases in the infrared will be discussed in Chapter 3.

An overview of recent secondary eclipse detections is given by Deming (2009). Simultaneously, secondary eclipse observations give us the wavelength dependent brightness and the equilibrium temperature. From the equilibrium temperature the bond albedo as a function of wavelength of the planet can be derived, see e. g. Charbonneau et al. (2005). Since the planet/star brightness

ratio is more favorable in the IR (see Fig. 1.18 lower panel), most observations are done at these wavelengths. The amount of thermal light emitted by the planet has been measured from such observations, and molecular features in the infrared planetary spectra have been identified. Fig. 1.19 shows how secondary eclipse IR observations mostly done with the Spitzer space telescope, can provide constrains for atmospheric models.
Additionally, the time of the secondary eclipse is very sensitive to the eccentricity of the planetary orbit (Charbonneau et al., 2005) by measurement of the difference in orbital phase between primary transit and secondary eclipse:

$$n(t_2 - t_1) = \psi - \sin\psi, \tag{1.15}$$

where $n = 2\pi/P$, with P being the period of the planet, t_1 and t_2 are the times of transit and secondary eclipse respectively, and

$$\psi = \pi + 2\tan^{-1}\left(\frac{e\cos\omega}{\sqrt{1-e^2}}\right), \tag{1.16}$$

where e is the eccentricity and ω is the argument of the periastron. Fig. 1.20 shows an example of confidence limits for the eccentricity based on secondary eclipse observations for TrES-1.
Sing & López-Morales (2009) and de Mooij & Snellen (2009) were the first in detecting the secondary eclipse of a transiting exoplanet from ground, thus extending the studies of exoplanet's atmosphere to ground-based facilities. A further tentative ground-based detection of a secondary eclipse is shown in Chapter 3 for CoRoT-2b.
The first emission spectra of two exoplanets, for HD 209 458b and HD 189 733b by means of the Spitzer's IRS instrument using observations centered at the secondary eclipse were obtained by Richardson et al. (2007); Grillmair et al. (2007); Swain et al. (2008a). Their results coincide in the non-detection of a flux-absorption due to H_2O at wavelength shorter than 10 microns, whereas Grillmair et al. (2008) detected a strong water absorption by spectroscopic observations during the secondary eclipse. This absorption was predicted by all atmosphere models for these objects.

1.5 Motivation for the following study

Transiting exoplanets provide us with valuable physical information, like a radius and density estimation, information about the atmosphere composition or presence of additional planets. This information can help us to provide constraints on atmosphere models, and planetary formation and evolution theories.

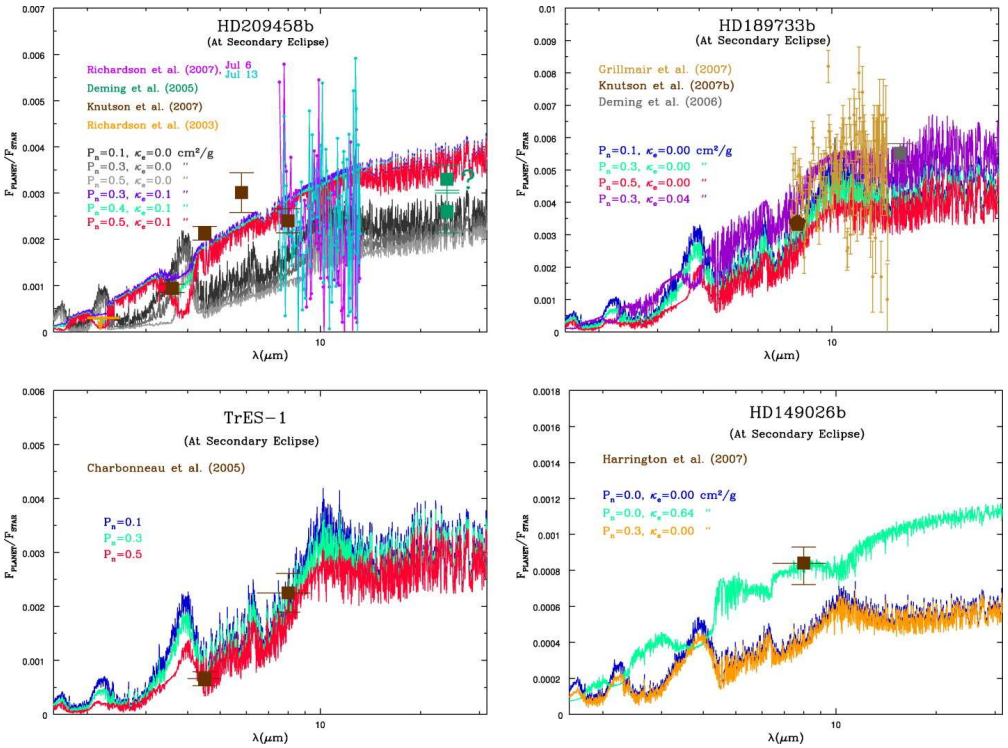

FIGURE 1.19— Planet/star flux ratios versus wavelength from ∼1.5 to 30 μm for various models of four transiting EGPs measured by Spitzer at secondary eclipse (Top right: HD 209 458b, top left: HD 189 733b, bottom right: TrES-1 and bottom left: HD 149 026b). Notice the different scales employed in each panel. Models for different values of P_n and κ_e are provided where appropriate. On the top left panel (HD 209458b), models with the lighter gray shade(s) are for the higher value(s) of P_n. Notice also that two different values for the flux at 24 μm (green) are shown on this same panel. The one with the question mark is a tentative update to the (Deming et al., 2005b) 24 μm measurement. If the flux at 24 μm is indeed ∼0.0033±0.0003, then our model(s) with inversions provide the best fit at that wavelength as well. Taken from Burrows et al. (2008).

Motivated by these possibilities I first show in Chapter 2 the detection procedure for transiting exoplanets of the Trans-Atlantic Exoplanetary Search (TrES) experiment, which was among the first successful survey for transiting planets undertaken. Nightly observations of three small wide-field telescopes are analysed and after obtaining the light curves of the observed stars, they are searched for transits. After the transit-like signal has been detected, a detailed analysis of the light curves and different follow-up techniques are applied, using photometric or spectroscopic observations, and I show how these help to confirm transiting exoplanets. Finding more transiting planets will help to im-

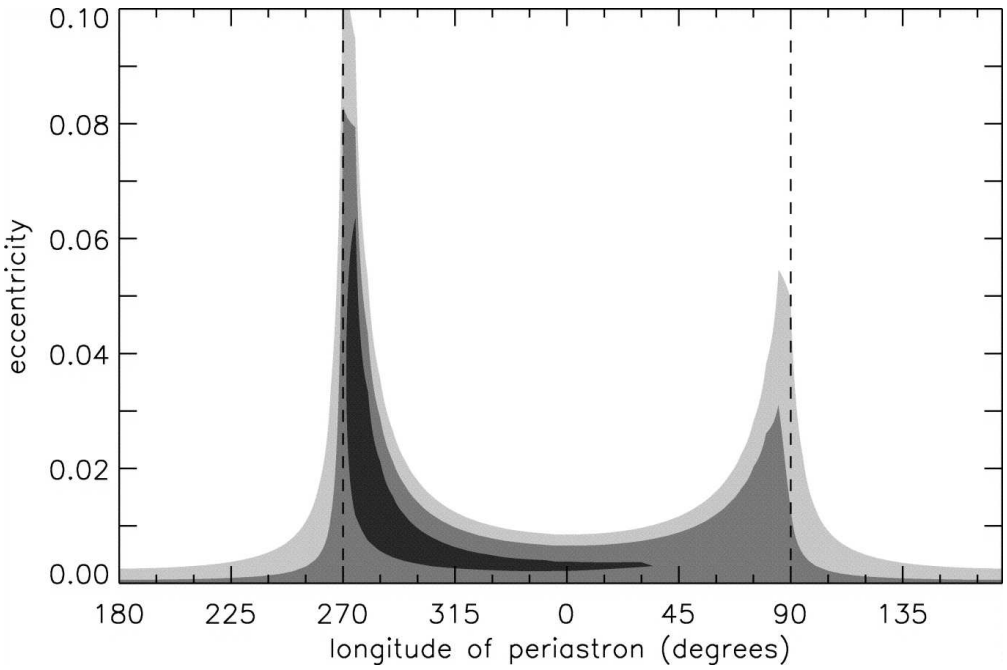

FIGURE 1.20— The 1 σ, 2 σ, and 3 σ confidence spaces of the orbital eccentricity e and the longitude of periastron ω. Since it is the combined expression $e\cos\omega$ that is constrained by the time of secondary eclipse, there exists a small range of ω (near $\cos\omega = 0$) for which a significant eccentricity is permitted. For this situation to occur, however, the orbital ellipse would need to be very nearly aligned with our line of sight. Additional radial velocity observations will further restrict the allowed parameter space. Taken from Charbonneau et al. (2005).

prove the statistics of transiting hot Jupiters that allow investigations of their global properties, e. g. the fractions of stars and their properties (spectral class, metallicity, age) that have planets, the planet eccentricity distribution, the planet mass function, planet illumination, temperature, sizes etc.
Next, in Chapter 3 I show the detailed characterization of several exoplanetary systems. First, observations in the infrared wavelength range of HD 189 733b, GJ 436b and CoRoT-2b are shown that can provide high precision primary transit light curves and light curves of the secondary eclipse. High precision primary transit light curves can help to put limits on the presence of an additional body in the system and the secondary eclipse light curves are used to estimate the brightness temperature of the planets and/or constrain their eccentricity. These parameters can be compared with atmosphere models, i. e. does the brightness temperature corresponds to the equilibrium temperature, whereas the eccentricity may be indicative of the age of the currently observed

planetary orbit as well as of the existence of further planets in the system.
In a further chapter (4), TrES-1 is searched for asymmetric features in its light curves, which may have been caused by a star spot or an additional transiting planet. Therefore, I first search in high-precision primary transit light curves of TrES-1, obtained with the Hubble Space Telescope (HST), for any asymmetric feature. Such features are then used as a template to search for a similar features in ground-based primary transit observations, which I obtained with the IAC80. I interpret the result physically and provide two hypotheses: the feature may be caused by a star spot or by an additional transiting planet. If the system contains an additional transiting planet, this would allow to establish the co-planarity of the multi-planet system, similar to the Solar system.
Finally, in Chapter 5 I search the primary transit mid-times of TrES-1 and TrES-2 for deviation from strict periodicity, indicating the presence of an additional body. The presence or absence of small planets in low-order mean-motion resonances has implications for theories of the formation and evolution of planetary systems and helps to determine the dominant mechanism of planet formation and evolution, e. g. a small mass planet might have been trapped while the giant planet migrates inward.

2

The TrES network

In this chapter I treat the detection and confirmation of transiting extrasolar planets. I start by describing the instruments of the TrES network, used for the first detections of planetary transit events. Then I describe the different procedures to discard possible false positives by a) inspecting the light curve very carefully, b) doing photometric multicolor follow-up observations and by observing the candidates with intermediate and high-resolution spectrographs to obtain the radial velocities, where the high-resolution spectrography may lead to the final confirmation of the planet.

The observations and analyses shown in this chapter are part of the work of the TrES (Trans-Atlantic Exoplanetary Search) project. The objective of the network is to find transits of extrasolar planets around stars with magnitudes between 8 and 14. It consists of three wide-field cameras at different sites. Two telescopes are located in the U.S: One of them is the Planet Search Survey Telescope (PSST) (Dunham et al., 2004), located at the Lowell Observatory in Arizona and operated by G. Mandushev. The instrument uses a lens with f/2.8 and an aperture of 10 cm, the field-of-view is $6^\circ \times 6^\circ$ and the CCD has 2k $\times$ 2k pixels. The Sleuth system (O'Donovan et al., 2003) is located at the Mt. Palomar Observatory and it is operated by Francis O'Donovan at the California Institute of Technology; it was replaced in summer 2008 by the WATTS system in operation at the Sam Houston State University in Texas by B. Oetiker. Sleuth and WATTS have similar optics to PSST. The third instrument is STARE (STellar Astrophysics & Research on Exoplanets), the oldest telescope in the network, with which my observations at Teide Observatory were made regularly.

STARE is an instrument belonging to HAO (High Altitude Observatory, Boul-

der, Colorado) and has been installed at Teide Observatory since July 2001. The optical design is a "flat-fielded" Schmidt-Newton telescope with f/2.8 and a field-of-view of $6^\circ \times 6^\circ$. In the summer of 2006, STARE went through a process of renewal and modernization of its components. The most significant changes has been a new mount and a new backside illuminated CCD from Princeton Instruments with a 2k $\times$ 2k chip and a pixel size of 13.5 μm. The mount is much more stable than the previous one (Alonso et al., 2004a), reducing systematic errors.

2.1 The TrES network observations

Generally, STARE observes with its TrES-counterparts the same stellar field for months as long as it is visible, between six and eight hours each night. This is done in order to get a good coverage, i. e. to get a high probability to observe a certain number of planetary transits with a particular period. All STARE observations are done in R-filter with an exposure time of 80 s. Figure 2.1 shows an example of the coverage of one field, namely Lac0 which also was the first field observed with the updated STARE instrument. The upper graph in Fig. 2.1 shows the recovery rate. This recovery rate is based on a simulation of different transiting planets. The transits of these planets are arranged in time randomly, then the actual observational coverage is used to indicate the fraction of planetary transits one could recover with the observations. One can see that for transiting planets with a period of up to 4 days and a minimum of 4 transits to be recovered, one will be able to recover nearly all planets. The peaks in this graph are at integer orbital periods, indicating aliasing effects; e. g. if we did not observe the first transit and the transiting planet has an integer period, we will never be able to recover a transit. The lower graph in Fig. 2.1 shows the hours of observation for each telescope and for the whole network. We can see that STARE observed the field Lac0 for 183 hours and the whole network was able to obtain 686 hours of observations.
At the end of a campaign, on a given field, I reduce the images obtained with the STARE telescope and create the light curves for each star. The light curves of each telescope are then combined together and searched for transiting planet candidates. Table 2.1 gives an overview of all fields observed with the STARE telescope since its renewal in 2006. The field Per2 and Aur1 were not reduced, the first because of problems with the CCD and the latter is the most recently observed field. In total, STARE obtained 204 000 light curves of stars with magnitudes between V=8-14 from 2006 to 2009.

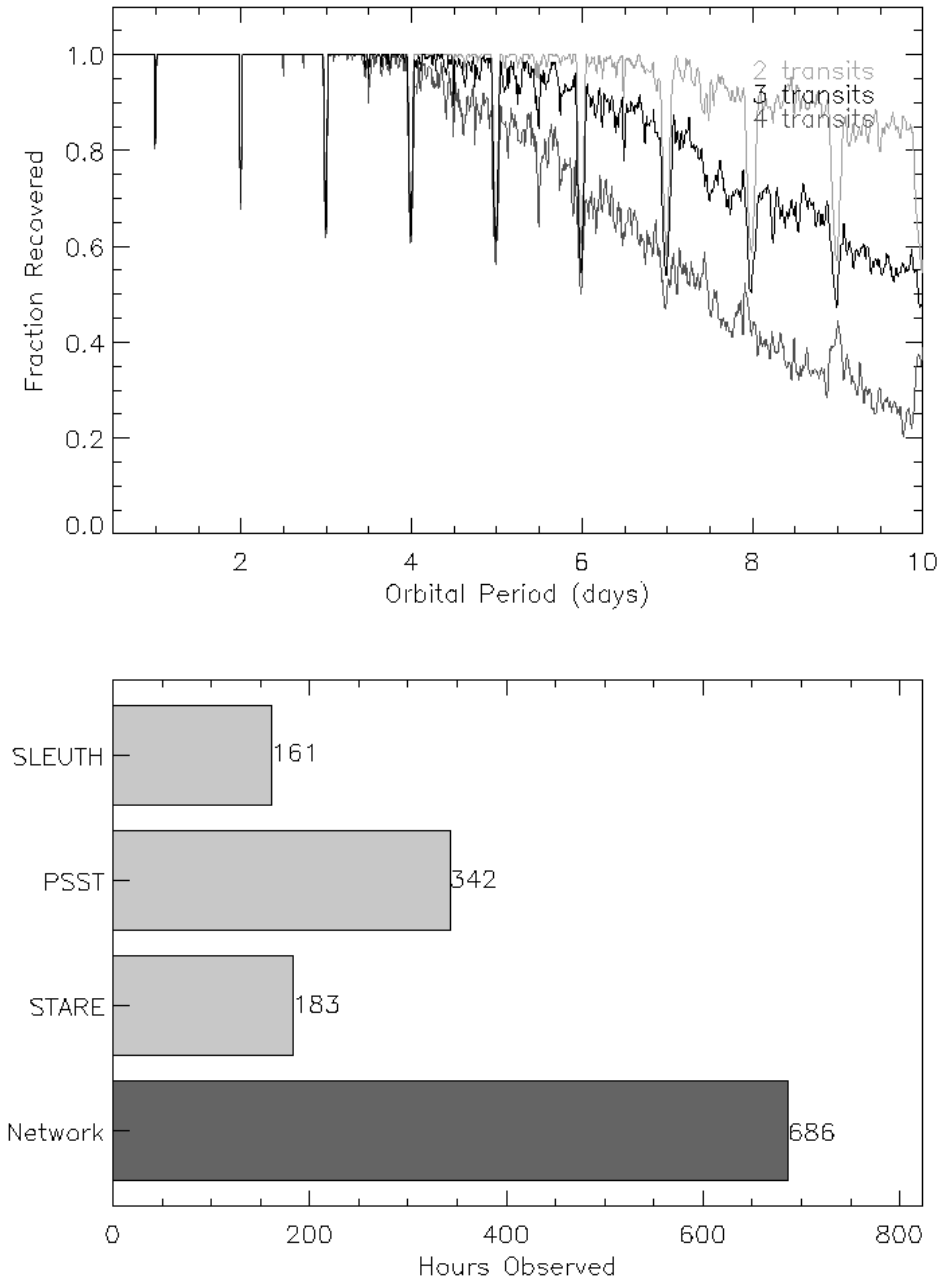

FIGURE 2.1— Upper graph: Network transit recovery of the Lac0-field as of Oct. 20, 2006. Lower graph: Hours of observations per telescope and for the whole network of the Lac0-field.

TABLE 2.1— Observed fields with STARE since summer 2006.

Field	RA	DEC	number of light curves	time span of light curves [HJD-2 400 000]
Lac0	22:21:01	+46:32:11	30 000	53978.409 - 54030.579
Per2	04:14:53	+40:29:01	-	-
LMi0	09:57:41	+41:03:20	22 000	54141.500 - 54219.482
Her2	16:42:53	+38:55:20	24 000	54220.564 - 54288.631
Cyg2	20:13:23	+56:34:06	28 000	54301.426 - 54380.520
Per3	03:32:26	+46:03:24	34 000	54406.603 - 54481.579
Gem0	08:03:31	+27:47:40	24 000	54501.335 - 54575.485
Dra1	15:57:47	+54:44:59	10 000	54579.453 - 54667.458
And3	23:12:33	+49:24:22	32 000	54669.593 - 54709.716
Aur1	06:00:58	+47:54:07	-	-

2.2 Data analysis

During the observation of one field, i. e. a campaign, I suppose that calibration images, like flat-fields and dark currents, are stable for months and therefore I take calibration images only at the beginning of each campaign with a new field. The flats have two functions: one is to correct for the finite opening time of the shutter, and the other one is to correct for non-uniform illumination of the detector and for variations in sensitivity among detector pixels. Therefore, I take two different flats, one flat with a short exposure time and another one with long exposure time. Additionally, at the beginning of each night bias images are taken; by averaging them they give the mapping of the zero level, while the over-scan region gives the level of bias for each image. In calibrating the frames, first I subtract the zero level based on the over-scan region and the the bias image from all others. In the next step, I subtract an averaged dark image from the science and flat frames. In order to correct for the finite opening time of the shutter, and to flat-field the images, I construct two calibration images. The first one is an average normalized flat-field and the second one is a shutter correction image, which is an estimate of the difference between the effective shutter close and open times for each position on the CCD image. The final calibrated science image is obtained by:

$$\text{science image}_{\text{calibrated}} = \frac{\text{science image}_{\text{raw}} \times (\text{exp. time} + \text{shutter correction})}{\text{normalized flat-field} \times \text{exp. time}}, \tag{2.1}$$

where the 'raw' images have already been corrected for bias and dark current. In the next step I reject images with low quality and mask the saturated pixels

following Alonso et al. (2004a). To this end, I choose a reference image by visual inspection of a good night's data and divide this image into nine 128 × 128 sub-images in order to estimate the translation, rotation and scale changes on a nightly basis. The position of one reasonably isolated star in the field is used to get a first rough measurement of the sky background level and of the atmospheric transmission. Quality-control plots are computed and stored for each observing night; an example of these plots for one typical night is presented in Fig. 2.2 and I use these plots to better filter the data, eliminating from the further analysis the images with doubtful quality due to weather or technical problems.

In the images appears a strong vignetting, which causes many bright stars

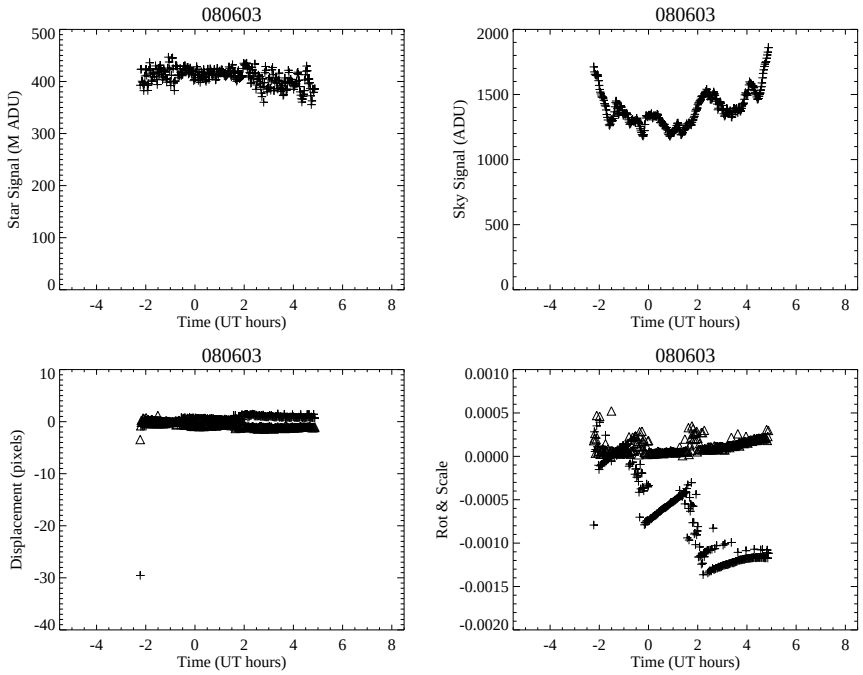

FIGURE 2.2— Example of a plot for quality evaluation in a good night of observation on Jun. 3, 2008. The observed field was Dra1. Top left: Signal of a bright unsaturated star. Top right: Estimated sky signal. Bottom left: Displacement of the images on this night from the reference image. Bottom right: Field rotation and scaling trends during the night.

near the corners to appear weaker. That is why I do not use a constant saturation level over the entire image. Rather, I make an image that represents the saturation cutoff I_c, in order to get the saturated pixels as follows: A quadratic surface is fitted to the flat and every pixel threshold I_c is set to the obtained

fit values. The inverse of I_c will be normalized, where the value in the middle of I_c corresponds to the saturation level at the center of the image. An image in which each pixel has a value close to the saturation level is then obtained. Now I only need to mask those pixels in the images that exceed the value I_c of the pixel in the same position of the image for the reference. Alternatively, it is possible to mask saturated pixels, using the raw image, i. e. before the image calibration and check where the count is $> I_c$.

An important task for each field is the construction of a master star list, by using a reference image obtained in a photometric and moonless night. On this image I apply DAOPHOT/ALLSTAR (Stetson, 1987, 1992) to obtain the master star list. This procedure has the advantage of producing centroids and magnitudes of the reference stars with high precision. The coordinates of this list are calculated through a transformation of the coordinates with the Tycho-2 catalogue (Hog & et al., 2000), which also supplies the magnitudes of many stars. These data are used as a reference for the position and photometry of the following steps. Then, the stars in the rest of the images are located.

The data analysis is based on the method of optimal image subtraction (Alard & Lupton, 1998; Alard, 2000). The results of this image subtraction are residual images that contain only the difference to the reference image. The steps of the image subtraction are: first, I must align the images. For this reason I use a program with an iterative algorithm, fitting a linear polynomial and then a quadratic polynomial to x and y. This process is simple because there is not a lot of rotation nor scaling in the images. The new coordinates are calculated finding the least-square of the following equations:

$$x = a_0 + a_1 y_{ref} + a_2 x_{ref} + a_3 y_{ref}^2 + a_4 x_{ref}^2 + a_5 x_{ref2} y_{ref} \tag{2.2}$$

$$y = b_0 + b_1 y_{ref} + b_2 x_{ref} + b_3 y_{ref}^2 + b_4 x_{ref}^2 + b_5 x_{ref2} y_{ref} \tag{2.3}$$

In these equations x_{ref} and y_{ref} are the coordinates of the star in the reference image. The x and y coordinates for each star in the star list and in each image are calculated based on aperture photometry, using APHOT, and then are matched to the same stars in the reference image (x_{ref} and y_{ref}).

Once all images have been aligned, I built a reference image by adding between 10 and 20 of the best images from the same night in order to increase the signal to noise ratio. The reference image R supposedly has the best seeing and the images I, which I am going to subtract, usually have a worse seeing. If one would subtract the two images one would obtain an image that contains the difference dominated by the seeing. Therefore, I need to find an optimal kernel K which converts the reference image R to an image I, so that both have similar seeing. The kernel K depends on the position in the image and is calculated by

finding the minimum of the following equation (Alard & Lupton, 1998; Alard, 2000):

$$\sum_i ([R \otimes K](x_i, y_i) - I(x_i, y_i))^2. \tag{2.4}$$

Following Alard & Lupton (1998); Alard (2000), I generate a difference image of $R \otimes K - I$, in which only the variables and moving objects will have a signal. Then I apply aperture photometry to each difference image and I obtain for each star, s, of the image, i, a flux difference $\Delta F_{s,i}$ and a standard error $\sigma_{\Delta F_{s,i}}$. As a result of this process, I can calculate the differential magnitude:

$$\Delta m_{s,i} = -2.5 \log \frac{F_{s,0} - \Delta F_{s,i}}{F_{s,0}}, \tag{2.5}$$

where $F_{s,0}$ is the flux of the star s in the reference image and the error is estimated as $\sigma_{\Delta m_{x,i}} = 1.0857 \frac{\sigma_{F_{s,i}}}{F_{s,0}}$, where $\sigma^2_{F_{s,i}} = \sigma^2_{F_{s,0}} + \sigma^2_{\Delta F_{s,i}}$. At the end of this procedure, I get the light curves from the STARE observations.

These light curves show systematic errors, see Section 2.3 and Pont et al. (2006). There are different algorithms to address them. The algorithms "Trend-Filtering Algorithm"(TFA) (Kovács et al., 2005; Kovacs & Bakos, 2006) and SysRem (Tamuz et al., 2005; Mazeh et al., 2006b,a) are the most frequent ones. For the TrES telescopes we use our own decorrelation algorithm, developed by G. Mandushev at the Lowell Observatory. The algorithm uses between 100 and 500 template stars below a given root-mean-square (r.m.s.) to do a Singular Value Decomposition (SVD) to identify a set of orthogonal modes that capture the greatest amount of variance and the resulting principal components of the covariance matrix are then applied to the rest of the stars without doing the SVD again.

After the decorrelation, I bin the light curves in bins of 0.0062 d ($\sim$ 9 min.). The light curves of all telescopes are then combined and searched for transits. To those ends, the transit search algorithm "Box-fitting Least Squares" (BLS) by Kovács et al. (2002) is used. This algorithm seeks signals that alternate between two different levels, usually a high (H) and a low level (L), corresponding to the outside and inside of a planetary transit. The duration of an event is qP_0, where q is the duration of the event in fractions of P_0, and P_0 is the period between consecutive events. The program runs over test periods from a minimum to a maximum period, and seeks the best solution for the 4 parameters: L, H, q and t_0. The last parameter t_0 is the central time of the event. An index for the presence of a signal SR for each test period is then estimated and in order to assess the detections, the Signal Detection Efficiency (SDE) which

can be regarded as a threshold value is defined as:

$$SDE = \frac{SR_{peak} - < SR >}{\sigma_{SR}}, \tag{2.6}$$

where σ_{SR} is the standard deviation of SR of all test periods, SR_{peak} is the highest value of SR and $< SR >$ is the average among all test periods. In the end, the light curves with the highest SDE provided by the algorithm are inspected. Running the BLS algorithm and defining candidates were mostly performed by other members of the TrES-team and is therefore not described in detail in this thesis. An example of the field Lac0 can be seen in my Master's thesis (Rabus, 2007), where I applied the BLS algorithm to the brightest 10 000 stars of this field and 94 candidates were obtained. From this ∼1 % of candidates, the parameters of the BLS algorithm and a visual inspection are being used to select the candidates that go into further follow-up.

2.3 STARE's red noise characteristics

Pont et al. (2006) analyzed the influence of correlated noise with a lower frequency component ("red noise") on photometric observations, increasing the noise level of the observation, i. e. the noise is the sum of white and red noise. Red noise emanates from systematic effects like for example, changing airmass, atmospheric condition, telescope tracking and flat-field errors. Fig. 2.3 shows examples of white and red noise and their sum. In fact, assuming white noise only, the transit signal-to-noise is given as $S_d \equiv d/\sigma_d$, where d is the difference between the mean of the data points in the transit and the flux level outside and σ_d is the uncertainty of that difference. Assuming an equal photometric uncertainty σ_0 for all points, and furthermore, assuming that the uncertainty of the off-transit flux level is negligible, then $\sigma_d = \sigma_0/\sqrt{n}$, where n is the number of data points in the transit. However, in the presence of red noise, σ_d consists of the white noise component σ_w plus the red noise component σ_r, e. g. $\sigma_d = \sqrt{\sigma_w^2 + \sigma_r^2}$. Red noise introduces covariances between light curve data points on time scale similar to the duration of the planetary transit and can be expressed as $\sigma_r = \sqrt{\frac{1}{n^2}\sum_{i \neq j} C_{ij}}$, where C_{ij} are the covariance coefficients between the i^{th} and j^{th} measurements and the indexes run over the measurements taken during the transit. The transit signal-to-noise under the influence of red noise can then be expressed as:

$$S_r = \frac{d}{\sqrt{\frac{\sigma_0^2}{n} + \frac{1}{n^2}\sum_{i \neq j} C_{ij}}}. \tag{2.7}$$

From Eq. 2.7 one can see that the additional term in the denominator will lower the signal-to-noise. A lower signal-to-noise will affect the transit detection threshold, the significance levels of the transit signals and the estimates for uncertainty on planetary parameters.

For STARE's red noise characterization, I used the approach of Pont et al.

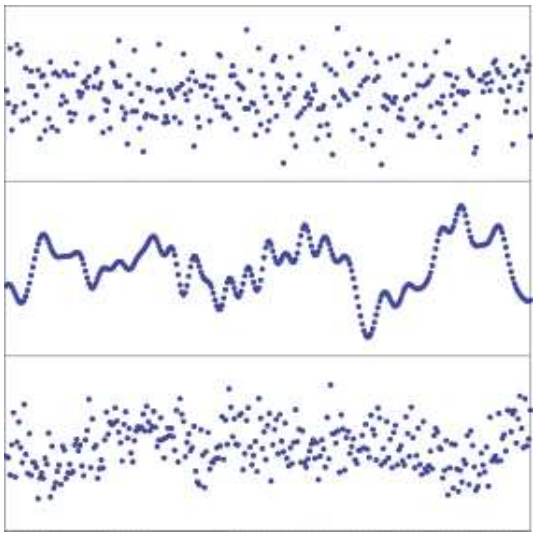

FIGURE 2.3— Light curves with white noise only (top panel), red noise only (middle panel) and white and red noise (bottom panel). Typical light curves from a high-precision rapid time-series photometry for bright targets in transit surveys resemble portions of the bottom-panel curve. Taken from Pont et al. (2006).

(2006). Following this approach, I first eliminated any known systematics from the light curve. Therefore, for calculating the noise, I choose non-variable stars by inspecting the light curves of stars which I obtained as described previously. In Figure 2.4 I show for a sample of non-variable stars the r.m.s. over magnitude for individual points, σ_i (blue circles). The red triangles are the r.m.s. of a sliding average over a transit duration of 3 hours, which expresses the amplitude of systematics in a 3 hour interval (Pont et al., 2006). The green crosses are calculated assuming that the individual measurements contain only white noise, and is given according to $\frac{\sigma_i}{\sqrt{N}}$, where N is the number of points in a 3 hours interval. The difference between the red and the green points indicates then the amount of red noise on a 3 hours timescale.

Comparing the different r.m.s. values in Figure 2.4, one can see that in the STARE data a correlated red noise component is present, which increases the noise on a 3 hours timescale by a factor of about 2.5 over data that would

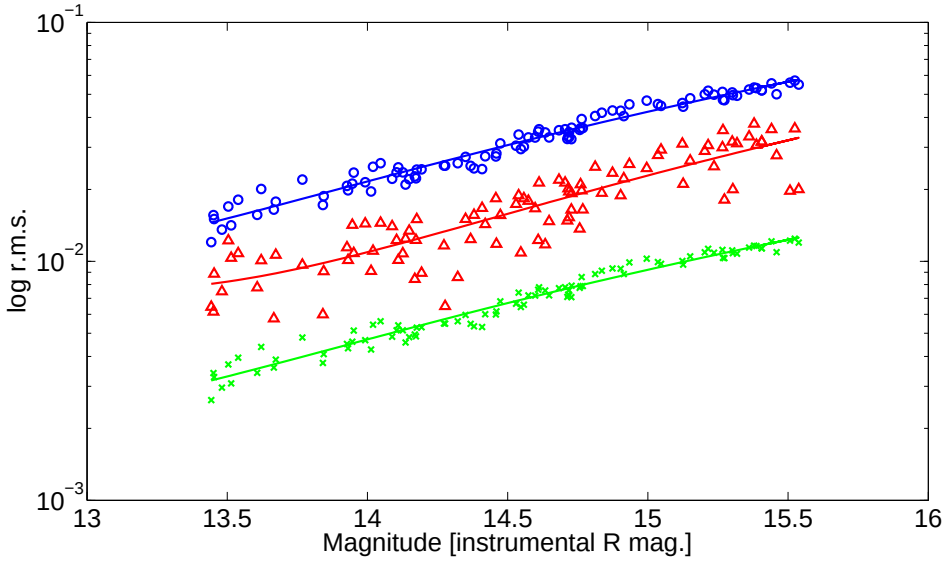

FIGURE 2.4— Different types of noises in light curves of 100 non-variable stars, spanning an observation of several days with STARE. The symbols are explained in the text. The lines are 2nd order polynomial fits to the points. The distance between the red and the green line corresponds to a factor of ∼2.5.

contain only white noise. The additional red noise component has little dependence on the stellar brightness. This component increases the noise in the data and makes it harder to achieve the milli-magnitude precision necessary to observe planetary transits.

2.4 Detailed light curve analysis and photometric multicolor follow-up observations

As mentioned earlier, there are different cases that mimic planetary transits. Therefore, after processing the images, we will have to study in detail the light curves of possible candidates in order to reject as many false positives as possible. The BLS-algorithm returns any stars that show in their light curve a high and a low level. This includes also variable stars and eclipsing binaries. Therefore, most of the detections are excluded, using a visual inspection of the light curves and clearly identifying the high and low levels in the light curves are due to a variable star or eclipsing binary. The depth of the transit signal is also checked – depths deeper than 10 % can be easily rejected – and

the period was doubled to search for secondary eclipses of different depths indicative of eclipsing binaries. In order to obtain reliable candidates for follow-up observations, I apply two further tests to the candidates obtained by the TrES-team, the density test and the test for out-of-ellipse modulation.
To describe a planetary transit, Seager & Mallén-Ornelas (2003) proposed a system of five equations. These describe the depth ΔF, its duration t_T and the relation between the duration of the flat part of the transit t_F and the complete transit duration t_T (see in Chapter 1 the Eqs. 1.3-1.5). The other two equations introduce the physics, i.e. Kepler's third Law:

$$P^2 = \frac{4\pi^2 a_P^3}{G(M_S + M_P)}, \tag{2.8}$$

and the stellar mass-radius relation:

$$R_* = kM_S^x, \tag{2.9}$$

where k is a constant and x provides us with a power law (e. g. k $\simeq$ 1.0 and x $\simeq$ 0.8 for main sequence stars).
Using these equations, one can estimate the density of the star from an adjustment of the light curve to a trapezoid, where the trapezoid simulates the transit. One can compare this stellar density with the estimated ones from the spectral type of the star based on the J-K colors of the 2MASS catalogue. The estimated densities are obtained from a table in Allen (1976) with the intermediate values being adjusted by a polynomial.
Another way to eliminate false positives is from the detection of a modulation of the part outside the eclipse, which might be due to a variability caused by the elliptical shape of stars in a binary system; by star spots on stars in a binary system (Sirko & Paczyński, 2003); or by reflected light among binary components. Therefore, based on the previous light curve fit, from the light curve the transit part is removed and then the following equation is fitted to the residuals:

$$I_k = a_0 + a_{c1}\cos p_k + a_{s1}\sin p_k + a_{c2}\cos(2p_k) + a_{s2}\sin(2p_k). \tag{2.10}$$

In this equation, I_k is the kth point of light curve and p_k its phase, based on the period of the transit-event. A least square fit is used to estimate the five parameters, a_0, a_{c1}, a_{s1}, a_{c2} and a_{s2}. As one can see, the term $a_{c2}\cos 2p_k$ describes a variation with half the period, such as ellipsoidal variability, and $a_{c1}\cos p_k$ describes a variability in phase with the orbital period, as may arise from heating the companion and/or the reflected light. One can define the

significance D_i of the fitted parameters as $D_{c1} = \frac{a_{c1}}{\sigma_{c1}}$, $D_{s1} = \frac{a_{s1}}{\sigma_{s1}}$, $D_{c2} = \frac{a_{c2}}{\sigma_{c2}}$ and $D_{s2} = \frac{a_{s2}}{\sigma_{s2}}$, where σ is the standard deviation between the fit and the data points. Based on significance values of $D_i \geq 3$ one can reject possible binary systems.

2.5 High precision follow-up photometry

My workhorse for high precision follow-up photometry of promising candidates is the 80cm IAC telescope (IAC80). The IAC80's CCD camera has a E2V chip of 2048 × 2048 pixels, equivalent to a size of 13.5 × 13.5 micron/pixel, a closed-cycle cooling system (Cryotiger series 600), while the user interface is designed by the IAC. The CCD has a 50 pixel over-scan region on both sides. The pixel size is $0''.304$ resulting in a field of view of $10'.25 \times 10'.25$.
IAC80 observations serve to resolve candidates that appear as unresolved blends in the small aperture cameras of TrES: STARE for example has a point spread function (PSF) in the images of $\sim 9''$; stars separated by less than this may appear as one star. Whereas the IAC80 has a pixel scale of $0''.3$/pixel and we usually observed only slightly out of focus with a FWHM in pixel between 4 and 6 pixels. Therefore I can resolve with the IAC80 separations between $1''.2$ and $1''.8$. In the case that more than one star falls into the STARE PSF aperture, I can also determine which star shows the eclipse.
Another application is to observe the transit in more than one filter. This helps to discard possible eclipsing binaries. In the case of eclipsing binaries and if the stars have different temperatures, the transit depth will depend on the filter of observation. The higher precision of IAC80 will also allow more reliable candidate rejections from the light curve analysis described in Sect. 2.4. Finally in the case of a transiting planet, a high precision light curve helps us to obtain precise parameter estimates. Therefore, the observed light curves are fitted using model transits.

2.6 Intermediate and high-precision radial velocity follow-up observations

Simultaneously to photometric follow-up observations, intermediate radial velocity follow-up observations are performed to further reject false positives. The candidates surviving the photometric and intermediate radial velocity follow-up observations are then observed with high-precision radial velocity instruments, like SOPHIE or HiRES, to finally confirm the planetary character.
The intermediate spectrograph used by TrES until 2007 was the CfA Digi-

tal Speedometer. This instrument records a spectral section of 4.5 nm near 518.7 nm, which samples the Mg b lines, with a spectral resolution of about 8.5 km/s. For the typical magnitudes of the TrES candidates, and if the star is not rapidly rotating, a precision of better than 0.5 km/s can be achieved, allowing the detection of objects with masses above 5-10 M_J. Additionally, with the information on the surface gravity and the effective temperature of the primary star, recorded in the spectra, it is possible to estimate the radius for the primary star.
However, the CfA Digital Speedometer was substituted in Sept. 2007 by TRES (Tillinghast Reflector Echelle Spectrograph), which is a fiber-fed (sky + object + calibration spectrum) optical Echelle spectrograph on the 1.5-meter Tillinghast telescope at the Smithsonian Astrophysical Observatory's Fred L. Whipple Observatory on Mt. Hopkins in Arizona. Its usable spectral range is between 370 and 900 nm with a resolution of 5 km/s.
For high precision radial velocity we use for one the SOPHIE spectrograph on the 1.2m OHP telescope at the Haute-Provence Observatory, France, and for another the HiRES spectrograph on the 10m Keck telescope. Both instruments are Echelle spectrographs; however, the calibration is different. The SOPHIE spectrograph is a fibre fed Echelle spectrograph with two fibers; one fibre is centered at the object, the other one can be centered on the sky or can be fed by a Thorium-Argon lamp. The CCD detector is an EEV 44-82 with 4102 $\times$ 2048 pixels of 15 microns. The CCD is thinned, backside-illuminated and has an anti-reflection coating. The whole spectrograph is kept at a constant temperature of -100° C in a dewar with an autonomy of 48 hours. The SOPHIE spectrograph can be run in two modes, namely the high resolution (HR) mode with R=75 000 and the high efficiency mode (HE) with R=39 000. SOPHIE observations were all performed by myself; whereas the other RV observations were done by collaborators of TrES.
Generally, all of our candidates are F, G, K and M-spectral type main-sequence stars. We assume to detect planets with masses in the range from 0.8 to 1.9 M_J, inducing a radial velocity variation on their parent star on the order of 100 to 300 m/s. The magnitude range of our candidates is between 8 and 14 mag. Therefore I observed candidates in HE mode and with slow read-out. At the beginning of the nights I took bias, tungsten and thorium calibration images. For the expected velocities of hundreds of m/s it was not necessary to use the simultaneous thorium mode. However, I took every two to three hours a Th/Ar lamp calibration spectra to measure the wavelength drift. Different S/N ratio might introduce systematic effects. Therefore, all candidates were observed with the same S/N ratio of $\sim$25 and the exposure time was adjusted correspondingly.

In order to obtain radial velocities I used SOPHIE's automatic data reduction pipeline. The final radial velocity is obtained by cross-correlating the wavelength calibrated spectra with different masks; available masks are F0, G2, K0, K5 and M4. To observe as many candidates as possible and given that we know the period of the systems, I can efficiently derive a first estimation of the RV orbits with only 2 observations per candidate, obtained at the orbital phases of greatest radial velocity amplitude. The pipeline further returns the bisector velocity span. I checked the spectra with different masks; checked the bisector for possible asymmetries and checked for additional bumps in the CCF over a large velocity range, indicating a double lined binary. For the bisector analysis, the CCF is divided into 100 different levels and these 100 levels are divided into 2 parts, i. e. V_b bottom velocity (averaging 10 - 35% of the CCF depth) and V_t top velocity (averaging 70 - 95% of the CCF depth). The difference V_t - V_b is equivalent to the bisector velocity span, which is used to measure the variations of the line profile. Fainter unresolved eclipsing binaries will produce distortions on the top of the spectral lines, while the bottom will remain unaffected.
The HiRES spectrograph on the Keck telescope (Vogt et al., 1994) uses a different method for wavelength calibration. In the light path of this spectrograph is a iodine absorption cell so that the stellar light crosses this cell. This cell causes the final spectra to have defined absorption lines. As a mask for the cross-correlation we use a template spectra, taken at the first time when a candidate was observed. This template is cross-correlated with the other spectra, taken at a later time, and we obtain from this the radial velocities. However, since the light crosses an iodine absorption cell, the telescope has to be a large aperture telescope, in order to obtain as many photons as possible. Also, this method is limited to bright stars, but no temperature and pressure stabilization of the spectrograph is necessary.

2.7 Candidates in detail

In the following I describe a few candidates, which were amongst the most promising cases for further follow-up observations, after intermediate radial velocity observations had been done on them. These candidates were then followed-up with high precision photometric observations, in order to recover the transit and to get better parameter estimates, and with high precision radial velocity follow-up observations to discard or confirm the planetary character. Observations were done by collaborators and by myself.

2.7.1 And1-04334

The candidate And1-04334 shows an eclipse depth of 0.018 mag with a duration of 2.5 h and a period of 1.9 days. Figure 2.5 shows the light curve as obtained by the cameras of TrES, where the red line shows the fitted trapezoid, see Table 2.2 for fitted parameters. Table 2.3 shows parameters as inferred from the 2MASS J-K color. Comparing both $\log \frac{\rho}{\rho_\odot}$ values, I get a difference ($\Delta = \log(\frac{\rho}{\rho_\odot})_{J-K} - \log(\frac{\rho}{\rho_\odot})_{Fit}$) of -0.13 and a ratio among the stellar densities of 0.74, indicating that the densities differ less 60 % which makes it a good candidate. From Table 2.4, where the results of the search for modulations of the part outside the transit is shown, one can see that the term a_{c1} has the highest significance of $D_{c1} = 4.13$ sigmas. Considering a 3-sigma threshold one can conclude that we have significant reflected light in the light curve (Fig. 2.6).
We also obtained 4 intermediate resolution spectra from D. Latham, spanning 378 days. These spectra indicated a fairly rapid rotating host star ($v_{rot} = 22.2$ km/s), which causes the spectral line to broaden rotationally which makes very precise velocity estimations difficult. The intermediate resolution spectra showed a variation of 1.2 km/s (Fig. 2.7).
I then observed And1-04334 photometrically in order to observe the transit with the TELAST telescope at Teide Observatory on Nov. 09, 2006 and with the IAC80 telescope on Sept. 14, 2007 between 23:34 and 1:25 UT (15 min. after predicted mid transit until 1 hour after point of last contact). In both cases, no transit or egress, respectively, was found (see Figs. 2.8 and 2.9). This may be due to large errors in the ephemeris of 0.0001 days in the period. The first transit was observed in April 9, 2005 and I tried to re-observe the object one, respectively two years later. By propagating the error in the period to one and a half year later, I get an uncertainty of 1.3 hours and that uncertainty maybe the reason for not having observed the transit again, possibly the transit occurred significantly earlier were observation coverage was not given.
I also observed T-And1-04334 with high precision radial velocity measurement on Sept. 1 and 2, 2008, corresponding to the phases ∼0.4 and ∼0.9. From Fig. 2.10's upper graph, one can see a variation of ∼120 m/s, but in the second graph one also can identify some systematics of the radial velocity measurements depending on which mask I used for cross-correlation; especially the K5 mask is offset with respect to the rest. One also finds an anti-correlation of the bisector with phase and a correlation of the bisector with radial velocities (two lower graphs in Fig. 2.10). Therefore, one might explain the observed eclipse as being due to an eclipsing binary.

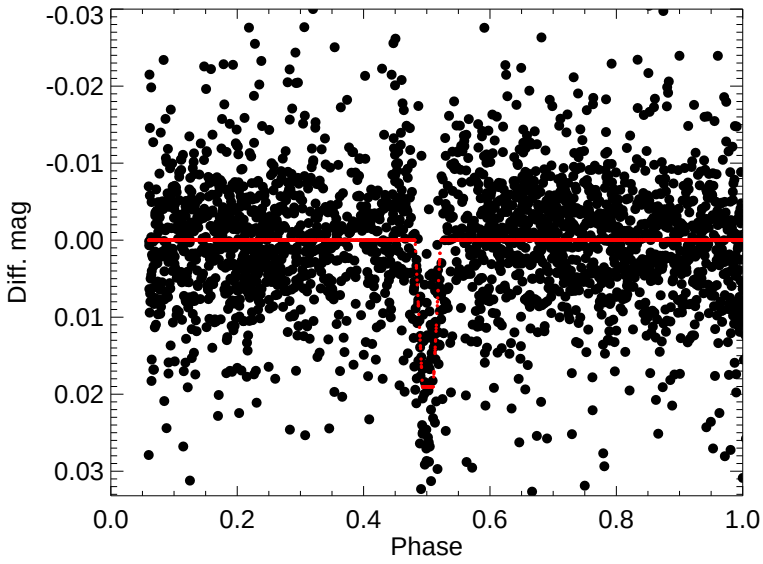

FIGURE 2.5— Phased light curve of And1-04334 transits observed with the TrES telescopes and with the best fit trapezoid over-plotted (red line).

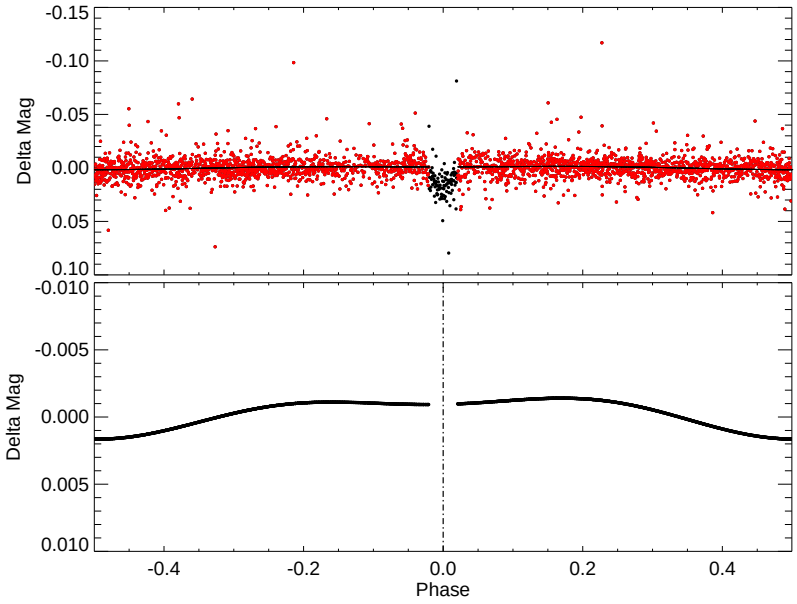

FIGURE 2.6— Upper plot: red dots for out-of-transit part and black dots for transit part of And1-04334. Lower plot: best fit I_k (Eq. 2.10).

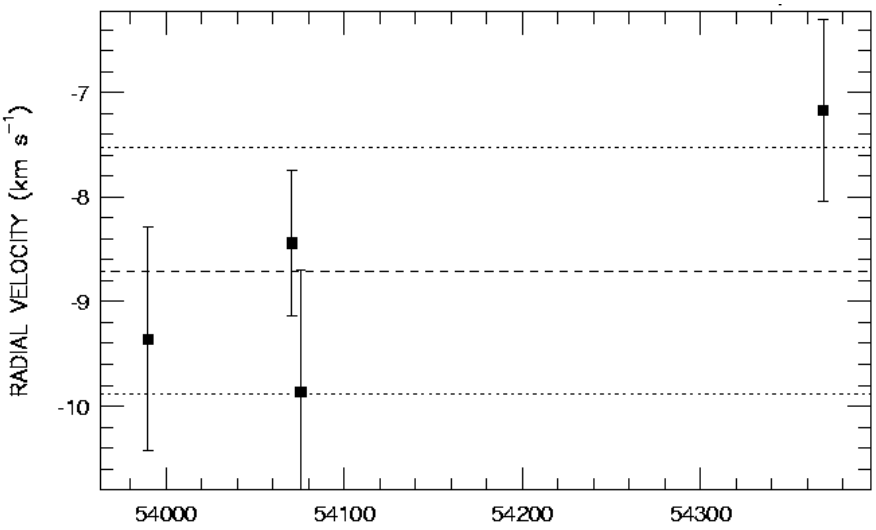

FIGURE 2.7— Intermediate radial velocity observation of And1-04334 from D. Latham. Dotted horizontal lines show RV variation of 1.2 km/s. Dashed line shows zero point.

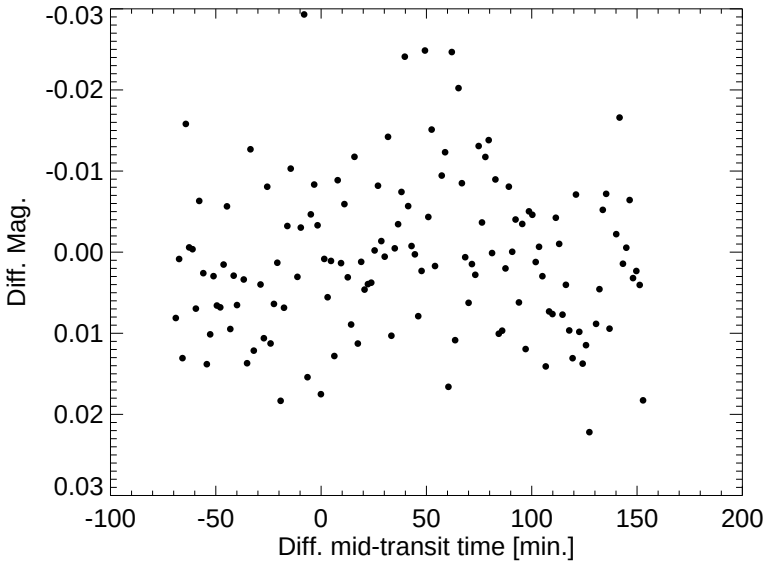

FIGURE 2.8— Photometric follow-up observations with TELAST of And1-04334 in R-filter on Nov. 9, 2006. Differential magnitude as function of difference to predicted mid-transit time based on ephemeris from network telescope observations. Expected 1st/4th and 2nd/3rd are at -/+55 min, -/+23 min,

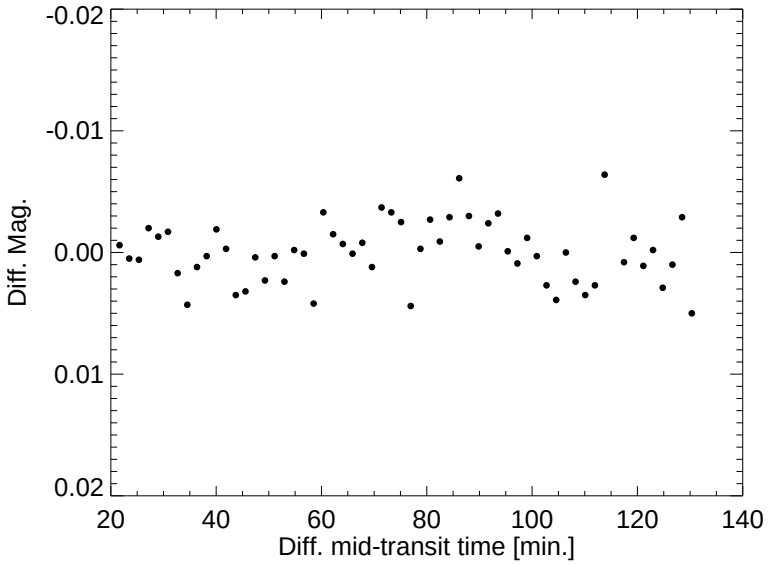

FIGURE 2.9— Photometric follow-up observations with IAC80 in R-filter of And1-04334 on Sept. 14, 2007. Differential magnitude as function of difference to predicted mid-transit time based on ephemeris from network telescope observations.

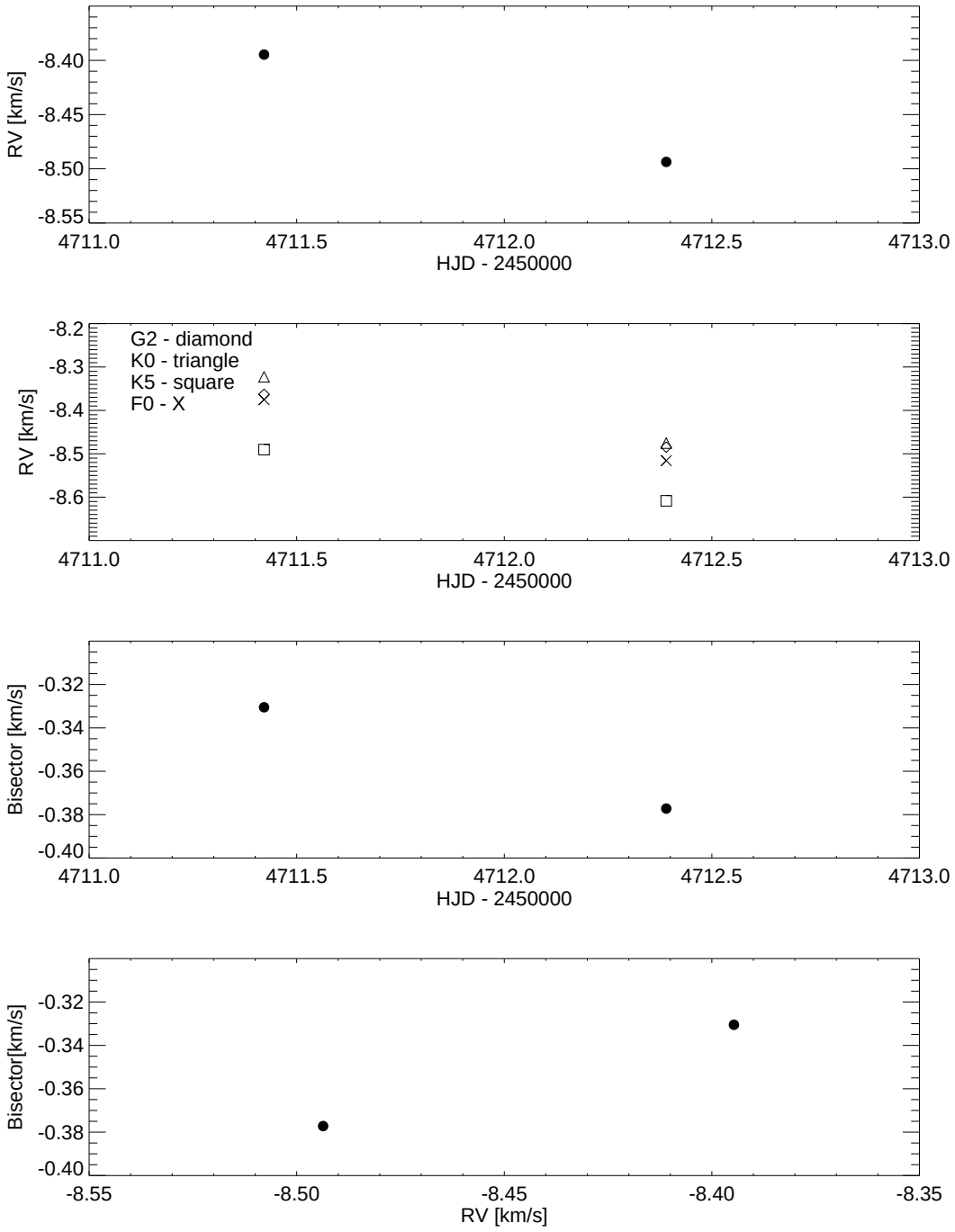

FIGURE 2.10— From top to bottom for And1-04334: Radial velocity observations (taken in Sept. 2008) of And1-04334 from the SOPHIE spectrograph 1.93m OHP cross-correlated with the mask of highest contrast, radial velocity measurements cross-correlated with different masks, bisector velocity span (V_t-V_b) in function of HJD and bisector velocity span vs. radial velocity, respectively.

TABLE 2.2— Results of the trapezoidal fit for And1-04334.

Parameter	Value
Final chisq	0.30
Total duration [hours]	1.82
Depth [mags]	0.019
Ingress time [hours]	0.53
Flat time [hours]	0.76
Central star density [Solar units]	0.987
$\log \frac{\rho}{\rho_\odot}$	-0.01
Impact parameter b	0.80

TABLE 2.3— Parameter estimates from the J-K color for And1-04334.

Parameter	Value
J-K	0.273
$\log \frac{\rho}{\rho_\odot}$	-0.12
Spectral type of the star	F5
Radius assuming main sequence star	1.18
Planetary radius	1.51

TABLE 2.4— Results of the fit of I_k to the phased light curve considering only the part outside the transit for And1-04334.

a_0	a_{c1}	a_{s1}	a_{c2}	a_{s2}
-2.89 $\times 10^{-5}$	-1.29 $\times 10^{-3}$	-1.48 $\times 10^{-4}$	6.38 $\times 10^{-4}$	-1.98 $\times 10^{-5}$
σ_0	σ_{c1}	σ_{s1}	σ_{c2}	σ_{s2}
2.12 $\times 10^{-4}$	3.13 $\times 10^{-4}$	2.84 $\times 10^{-4}$	2.98 $\times 10^{-4}$	2.96 $\times 10^{-5}$
D_0	D_{c1}	D_{s1}	D_{c2}	D_{s2}
-1.36	-4.13	-0.52	2.14	-0.07

2.7.2 Cyg1-03024

Another candidate is Cyg1-03024, showing an eclipse depth of 0.011 mag with a period of 2.07 days. See Fig. 2.11 and Table 2.5 for the obtained values of the trapezoidal fit parameters while Table 2.6 shows the parameters estimated from the J-K colors. For this candidate I get a difference $\Delta = -0.68$ between $\log(\frac{\rho}{\rho_\odot})_{J-K}$ and $\log(\frac{\rho}{\rho_\odot})_{Fit}$. Both stellar densities differ by more than 60 %, indicating a not ideal candidate. The dominant sinusoidal term for the part outside the eclipse is the term $a_{s2}\sin(2p_k)$ with a high significance of $D_{s2} = 3.33$. This candidate was also observed four times with intermediate spectroscopic observations, spanning 178 days. The result of these spectroscopic observations showed a rapidly rotating star ($v \sin i$ ∼40 km/s). Later, I observed Cyg1-03024 twice with the IAC80 telescope on Sept. 7, 2006 and Sept. 9, 2006 in the I-filter (Figs. 2.13 and 2.14). In both cases I could recover the transit with the same depth. Cyg1-3024 was also observed with other telescopes, like the Palomar Observatory's 60 inch and the Lowell Observatory's 42 inch telescope, all showing a flat bottom transit with a depth of ∼1.5 %.
Finally we observed Cyg1-03024 with high resolution spectroscopy, first with the Keck telescope (Fig. 2.15). These observations showed intriguing radial velocity variations in phase with a putative orbit. Later, I observed Cyg1-3024 with the SOPHIE spectrograph. The upper plot of Fig. 2.16, shows all radial velocity measurements, i. e. Keck/HiRES and OHP/SOPHIE. I see no variation in the SOPHIE data set, but the HiRES set shows variations. I note that during my run at the OHP I had partially bad weather and the measurements might have been affected by thin clouds. The 2nd graph in Fig. 2.16 shows slight systematics in the radial velocities with the mask used for cross-correlation, the 3rd graph shows no correlation of the bisectors with phase, but there might be a correlation of the bisector with the radial velocities. Despite not withstanding the stellar density test and likely the presence of out-of-transit modulations, this is currently still a good planet candidate due to the intriguing RV variations of the HiRES observations and will be re-observed with SOPHIE in the near future.

TABLE 2.5— Results of the trapezoidal fit for Cyg1-03024.

Parameter	Value
Final chisq	0.09
Total duration [hours]	2.75
Depth [mags]	0.011
Ingress time [hours]	0.66
Flat time [hours]	1.43
Central star density [Solar units]	0.260
$\log \frac{\rho}{\rho_\odot}$	-0.58
Impact parameter b	0.81

TABLE 2.6— Parameter estimates from the J-K color for Cyg1-03024.

Parameter	Value
J-K	0.290
$\log \frac{\rho}{\rho_\odot}$	-0.10
Spectral type of the star	F5
Radius assuming main sequence star	1.14
Planetary radius	1.12

TABLE 2.7— Results of the fit of I_k to the phased light curve part outside the transit of Cyg1-03024.

a_0	a_{c1}	a_{s1}	a_{c2}	a_{s2}
-4.75 $\times 10^{-5}$	3.37 $\times 10^{-4}$	-2.34 $\times 10^{-4}$	-2.55 $\times 10^{-4}$	4.19 $\times 10^{-4}$
σ_0	σ_{c1}	σ_{s1}	σ_{c2}	σ_{s2}
9.39 $\times 10^{-5}$	1.27 $\times 10^{-4}$	1.38 $\times 10^{-4}$	1.40 $\times 10^{-4}$	1.26 $\times 10^{-4}$
D_0	D_{c1}	D_{s1}	D_{c2}	D_{s2}
-5.06	2.66	-1.69	-1.82	3.33

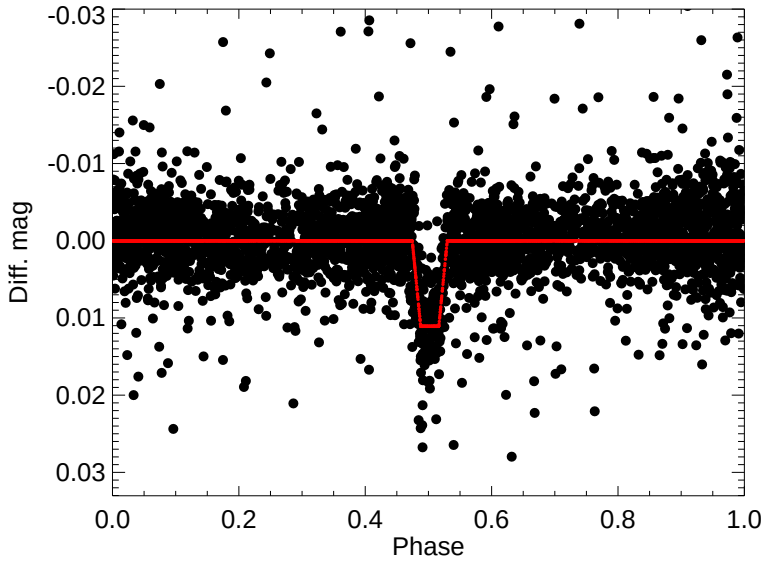

FIGURE 2.11— Phased light curve of Cyg1-03024 observed with TrES telescopes and with a best fit trapezoid over-plotted (red line).

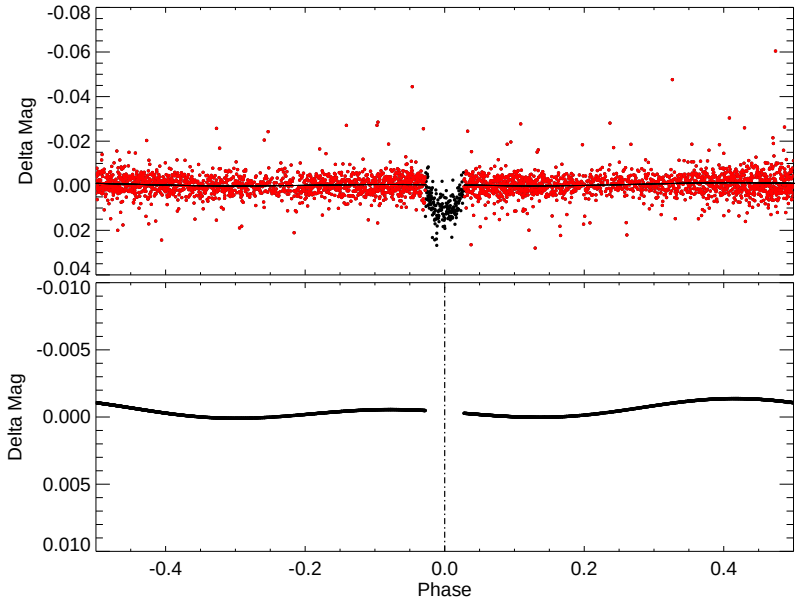

FIGURE 2.12— Upper plot: red dots for out-of-transit part and black dots for transit part of Cyg1-03024. Lower plot: best fit I_k (Eq. 2.10).

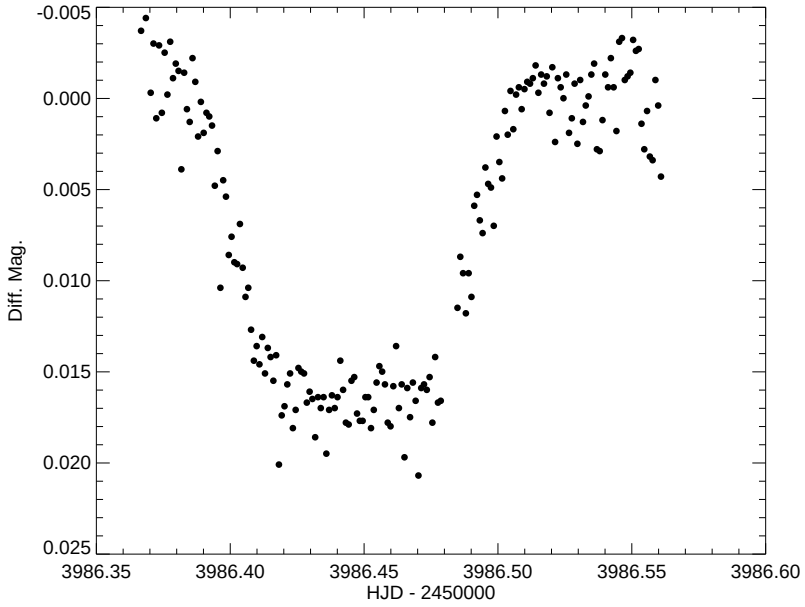

FIGURE 2.13— Photometric follow-up observations of Cyg1-03024 with the IAC80 in I-Filter, on Sept. 07, 2006.

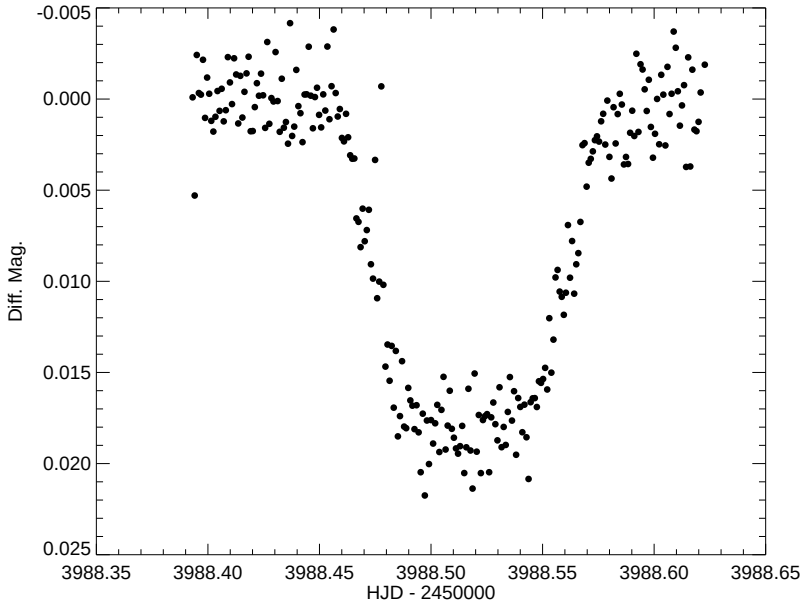

FIGURE 2.14— Photometric follow-up observations of Cyg1-03024 with the IAC80 in I-Filter, on Sept. 09, 2006.

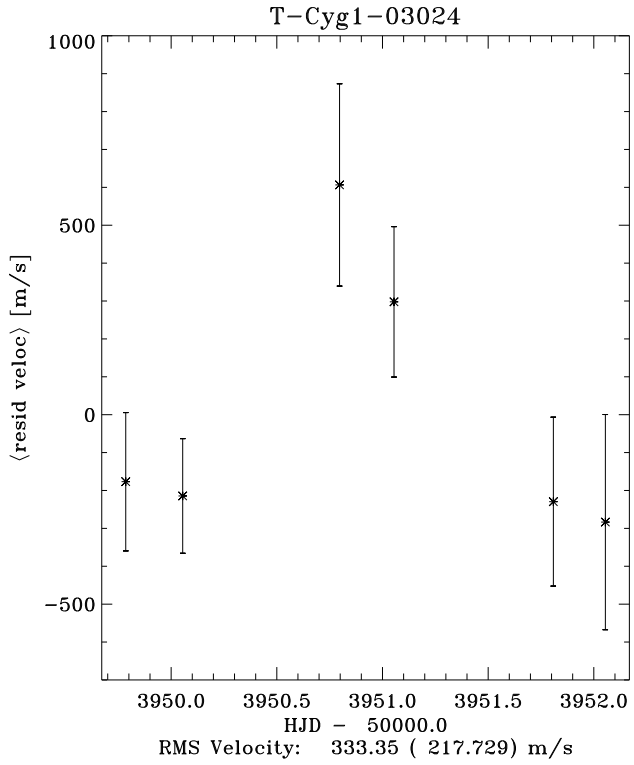

FIGURE 2.15— High precision radial velocity measurements of Cyg1-03024 using Keck/HiRES.

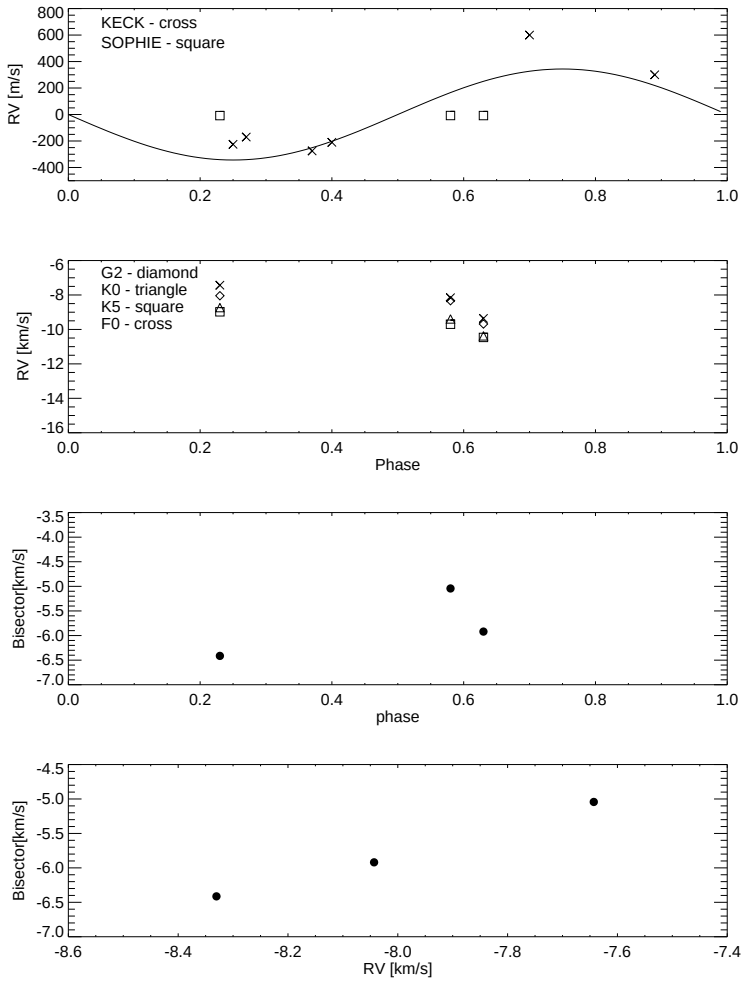

FIGURE 2.16— From top to bottom for Cyg1-03024: High precision radial velocity measurements (taken in Sept. 2008) from SOPHIE and Keck/HiRES in phase with photometric period and best-fit sine function over-plotted (solid line), radial velocity measurements of SOPHIE cross-correlated with different masks, bisector velocity span over phase and bisector velocity span vs. radial velocity, respectively.

TABLE 2.8— Results of the trapezoidal fit for Lac0-14888.

Parameter	Value
Final chisq	0.193
Total duration [hours]	1.81
Depth [mags]	0.012
Ingress time [hours]	0.51
Flat time [hours]	0.79
Central star density [Solar units]	1.995
$\log \frac{\rho}{\rho_\odot}$	0.2999
Impact parameter b	0.84

2.7.3 Lac0-14888

Another interesting candidate is Lac0-14888. The TrES light curve showed an eclipse depth of 0.012 with a duration of 1.81 hours and a period of 5.39 days (see Table 2.8 and Fig. 2.17 and for the J-K parameter estimate see Table 2.9). I then searched this candidate for ellipsoidal variations (Table 2.10 and Fig. 2.18) and found that the most significant term is $a_{c1} \cos p_k$ with 2.6 sigmas, which we consider as statistically low significant.

The two intermediate resolution spectroscopic observations taken by D. Latham (Fig. 2.20), spanning 3 days, showed a rotational velocity of 9.0 km/s and a variation in radial velocity of 0.81 km/s. This candidate was then observed photometrically with larger aperture telescopes (IAC80, TELAST and FLWO 1.2m). Fig. 2.19 shows all photometric transit observations phased and over-plotted, where I did two of these observations. We see a good correspondence between transit times and transit depths in all observations.

Finally, Lac0-14888 was observed with the HiRES spectrograph at the Keck telescope. However no radial velocity variation of significance was found and the lack of variation in radial velocities is not very promising. This candidate has therefore been discarded as possible being a faint background eclipsing binary diluted by a bright star.

TABLE 2.9— Parameter estimates from the J-K color for Lac0-14888.

Parameter	Value
J-K	0.51
$\log \frac{\rho}{\rho_\odot}$	0.0626
Spectral type of the star	K0
Radius assuming main sequence star	0.90
Planetary radius	0.91

TABLE 2.10— Results of the search for ellipsoidal variation.

a_0	a_{c1}	a_{s1}	a_{c2}	a_{s2}
-3.15 $\times 10^{-4}$	-4.92 $\times 10^{-4}$	3.52 $\times 10^{-5}$	-4.44 $\times 10^{-4}$	-2.99 $\times 10^{-4}$
σ_0	σ_{c1}	σ_{s1}	σ_{c2}	σ_{s2}
1.37 $\times 10^{-4}$	1.87 $\times 10^{-4}$	1.99 $\times 10^{-4}$	1.99 $\times 10^{-4}$	1.89 $\times 10^{-4}$
D_0	D_{c1}	D_{s1}	D_{c2}	D_{s2}
-2.29	-2.61	0.18	-2.23	-1.58

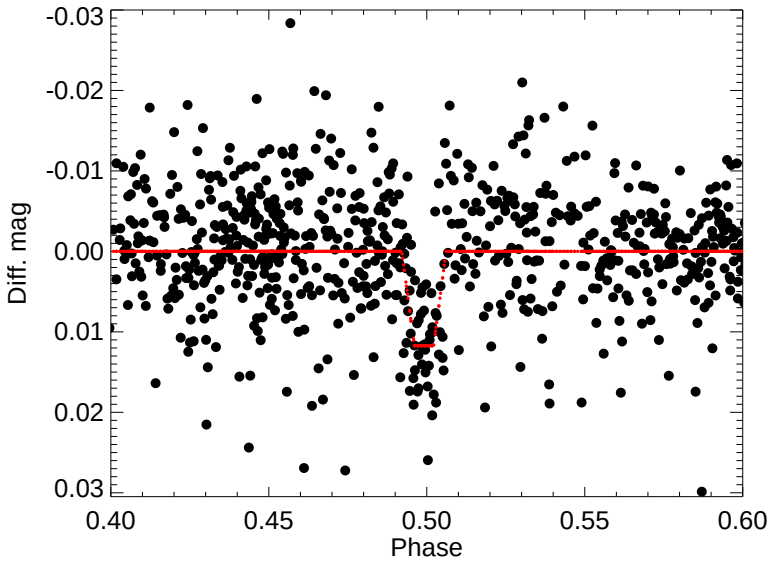

FIGURE 2.17— Phased light curve of Lac0-14888 observed with the small wide-field network cameras and with best fit trapezoid over-plotted (red line).

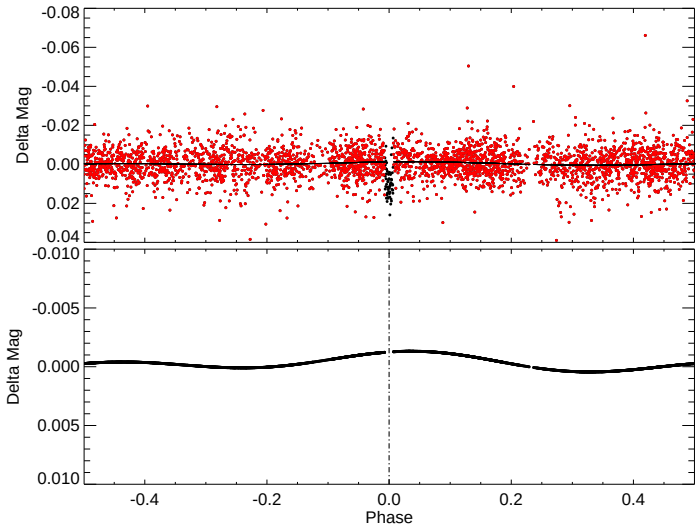

FIGURE 2.18— Upper plot: red dots for out-of-transit part and black dots for transit part of Lac0-14888. Lower plot: best fit I_k (Eq. 2.10).

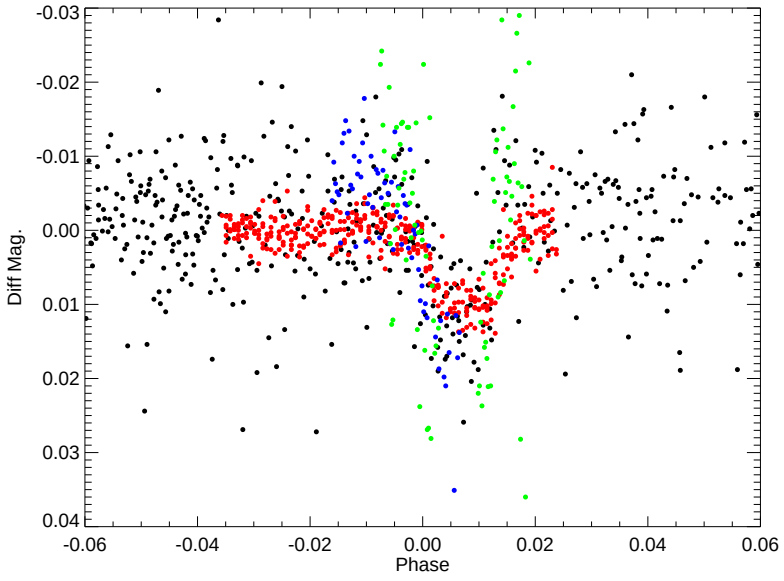

FIGURE 2.19— Black: transit observations of all TrES telescopes, blue: transit observation with the IAC80 on Sept. 15, 2007, green: transit observations with TELAST on Oct. 21, 2007, red: observations on the FLWO 1.2m with Kepler Cam on Oct. 19, 2008.

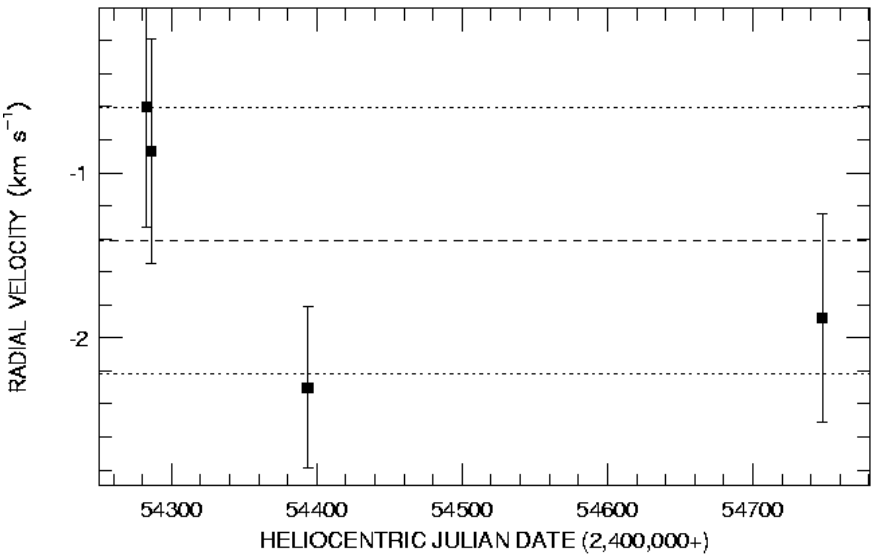

FIGURE 2.20— Intermediate radial velocity observations of Lac0-14888 from D. Latham. Dotted horizontal lines show RV variation of 0.81 km/s. Dashed line shows zero point.

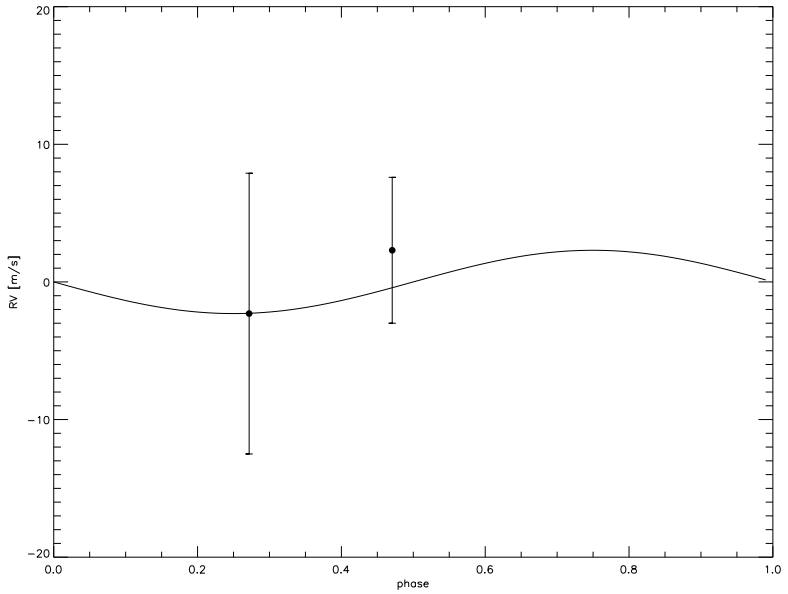

FIGURE 2.21— High precision radial velocity observations of Lac0-14888 with Keck/HiRES. Solid line indicates non-eccentric Keplerian orbit.

2.7.4 Cyg0-03908

In the light curve of Cyg0-03908 we found a transit with a duration of 4.47 hours and a period of 7.5 days. This candidate was only observed with high resolution spectroscopy at the 1.93m OHP (Fig. 2.22). I found a variation in radial velocity of 20 m/s, but not in phase with the photometric transit period. The second graph in Fig. 2.22 shows that there is a big offset between the K0 mask and the rest, indicating a K-type primary in a blended binary system. Based on my observations with the SOPHIE spectrograph, the system can be discarded as a blended system.

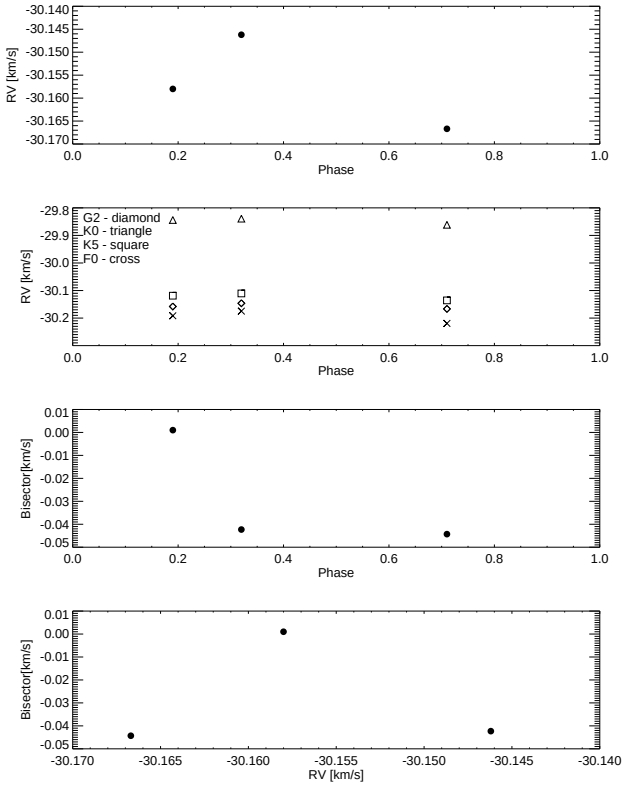

FIGURE 2.22— Radial velocity observations of Cyg0-03908 from the SOPHIE spectrograph. From top to bottom: Stellar spectra cross-correlated with mask of highest contrast, cross-correlated with different masks, bisector velocity span over phase and bisector velocity span vs. radial velocities, respectively.

2.7.5 LMi0-01447

This candidate showed an eclipse depth of 0.008 mag, a duration of 1.5 hours and a period of 1.0 day. I observed this candidate with the IAC80 on Apr. 22, 2008. In Fig. 2.23 we plot the result of the aperture photometry for different diameters used for the photometry. We see that I reach a precision of 0.003 mag. and therefore, the transit should be visible. However, I did not detect an ingress. This may be due to an error in the ephemeris and due to the short observations span with the IAC80. This candidate still remains a potential planet.

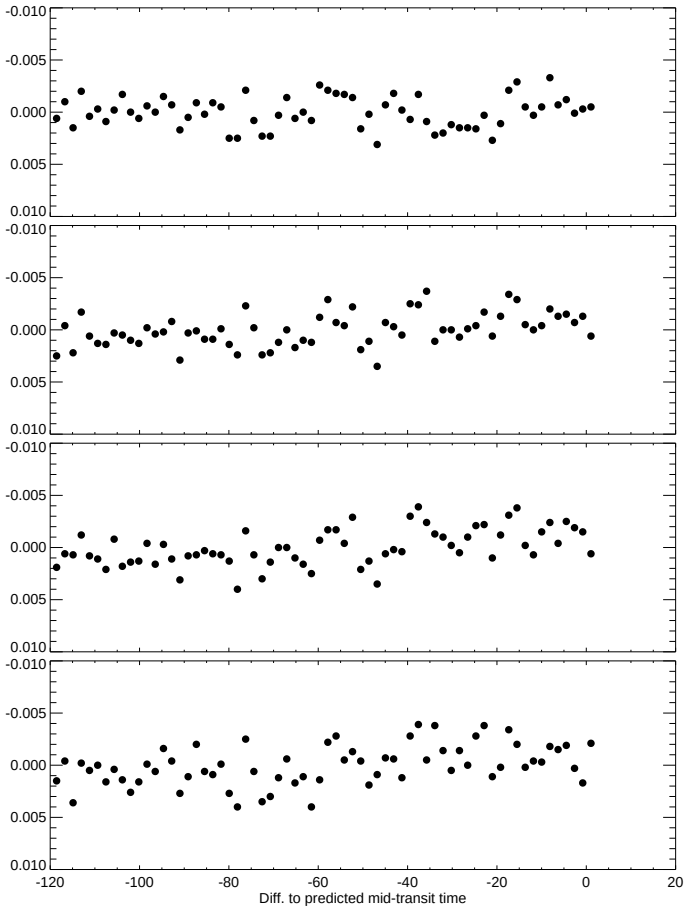

FIGURE 2.23— Photometric observation of LMi0-01447 with different apertures used for photometry, from top to bottom: 10, 15, 20 and 30 pixels.

2.7.6 UMa0-00216

UMa0-00216 showed a transit with a duration of 2.0 hours, a depth of 0.019 mag and a period of 3.0 days. I also observed this candidate with the TELAST telescope on two different days and with different filters, namely R- and B-filter on Apr. 2 and May 11, 2008 (Fig. 2.24). In the lower plot in Fig. 2.24 we see, that the transit depth changes with filter. Therefore, I could classify this candidate based on multi-color photometry as an eclipsing binary system.

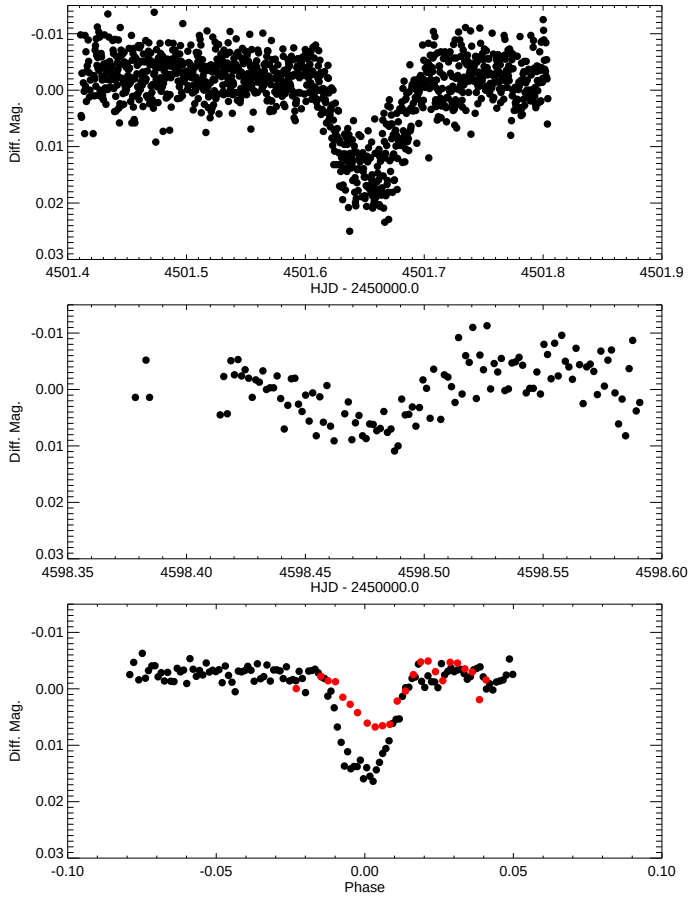

FIGURE 2.24— Photometric observation of UMa1-00216 in different filters with TELAST. Upper plot: R-filter on Apr. 2, 2008. Middle plot: B-filter on May 11, 2008. Lower plot: Both observations in phase for comparison.

2.7.7 Cyg0-04140

This is a candidate showing a transit with a duration of 2.45 hours and a period of 5.6 days and it was observed with intermediate resolution spectroscopy five times (Fig. 2.25), spanning 207 days. By means of the intermediate resolution spectroscopy we obtained a rotational velocity of 5.8 km/s. Additionally, this object was observed with Keck/HiRES and with the OHP/SOPHIE. The upper graph in Fig. 2.26 shows the radial velocity measurements obtained by the SOPHIE spectrograph, but the radial velocity variations are not in phase with the photometric transit ephemeris, a similar result was obtained with the Keck/HiRES observations. However, Cyg0-04140 remains still a reliable candidate. We assume the error in the ephemeris is large and we may have missed the transit. Therefore, we are concentrating our follow-up observations of this candidate to try to recover the transit, and we have it scheduled for re-observation at the SOPHIE spectrograph in the near future, with the aim to better constrain the period with RV measurements.

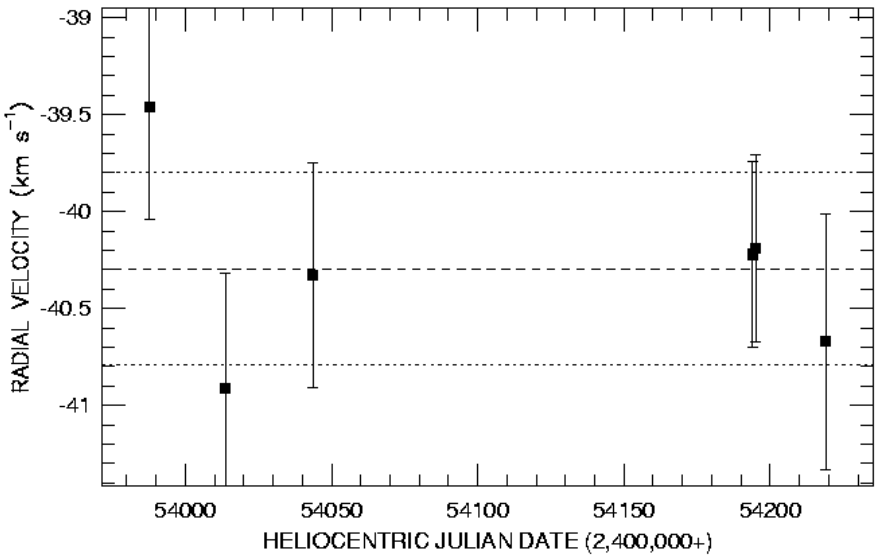

FIGURE 2.25— Intermediate resolution radial velocity observations of Cyg0-04140 from D. Latham. Dotted horizontal lines show RV variation of 0.5 km/s. Dashed line shows zero point.

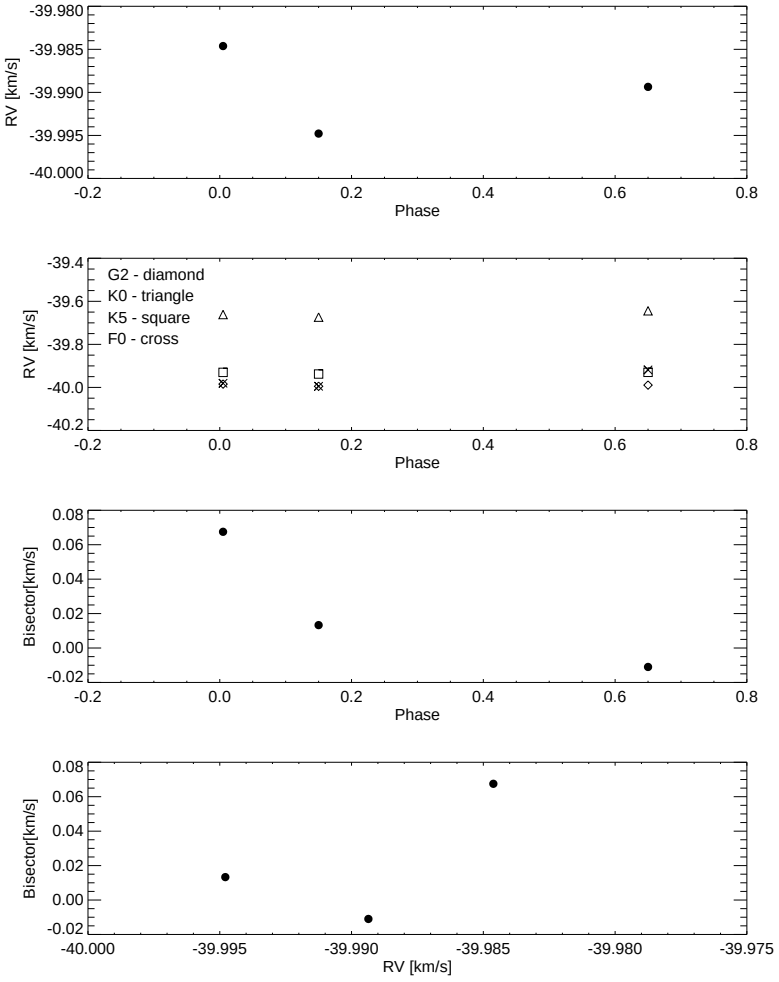

FIGURE 2.26— Radial velocity observations (taken in Sept. 2008) of Cyg0-04140 from the SOPHIE spectrograph. From top to bottom: Stellar spectra cross-correlated with mask of highest contrast, cross-correlated with different masks, bisector velocity span over phase and bisector velocity span vs. radial velocity, respectively.

2.8 Discovery of TrES-2

This last section deals with the discovery of TrES-2 (O'Donovan et al., 2006) and shows how its parameters were obtained from light curve analysis and high-precision radial velocities.

It were the TrES telescopes Sleuth and PSST who first observed the transit of TrES-2, see top of Figure 2.27. For technical reasons, STARE was not operating at that time. The transit was found in data from the Lira-field, which was observed in the period from Jun. 16, to Sept. 3, 2005. After subjecting the candidate to the protocol of eliminating false alarms, as explained before, Lyr1-01383 (aka TrES-2) was a primary candidate to be subjected to follow-up observations. In a first step, T-Lyr1-01383 was observed with the CFA Digital Speedometer in order to obtain intermediate precision parameter estimates. The precision of the CFA Digital Speedometer is enough to detect stellar companions. This Echelle spectrograph obtains spectra centered at 5 187 Å with a spectral range of 45 Å and a resolution of $\lambda/\Delta\lambda = 35000$. The radial velocities indicated a companion with a mass of less than 8 M_{Jup}. The spectrum gave an effective temperature $T_{eff} = 5960 \pm 100$ K, a surface gravity of $\log g = 4.4 \pm 0.2$ dex and a rotational velocity of $v \sin i = 2.0 \pm 1.5$ km s^{-1} for the host star. These values indicated that the host star is of spectral type G0V.

The last step was the final confirmation of the planetary character through high resolution radial velocity measurements, precise enough to detect the planetary mass around the star, using the Keck/HiRES instrument. The spectra were calibrated using a iodine cell. We measured an amplitude of the radial velocity of K = 181.3 ± 2.6 ms^{-1} (see Fig. 2.28), and assuming a stellar mass of 1.08 $M_\odot$, based on the spectral type of a G0V-star, we obtained a planetary mass of $M_P \sin i = 1.28$ M_{Jup}.

I carried out photometric observations with the IAC80 and TELAST telescopes (Figure 2.27), both with a greater aperture than Sleuth and PSST. Using the IAC80, I obtained data during a transit on Aug. 10, 2006 in the B- and I-filters. These observations were crucial for the confirmation of the planetary character of TrES-2 since they showed that the transit depth is the same in the B- and I-filter. Additionally, these observations helped us to get an precise radius and inclination estimate. For TrES-2, I observed a 1.4 % eclipse depth permitting to estimate a radius of 1.24 R_J and an inclination of 83.9°.

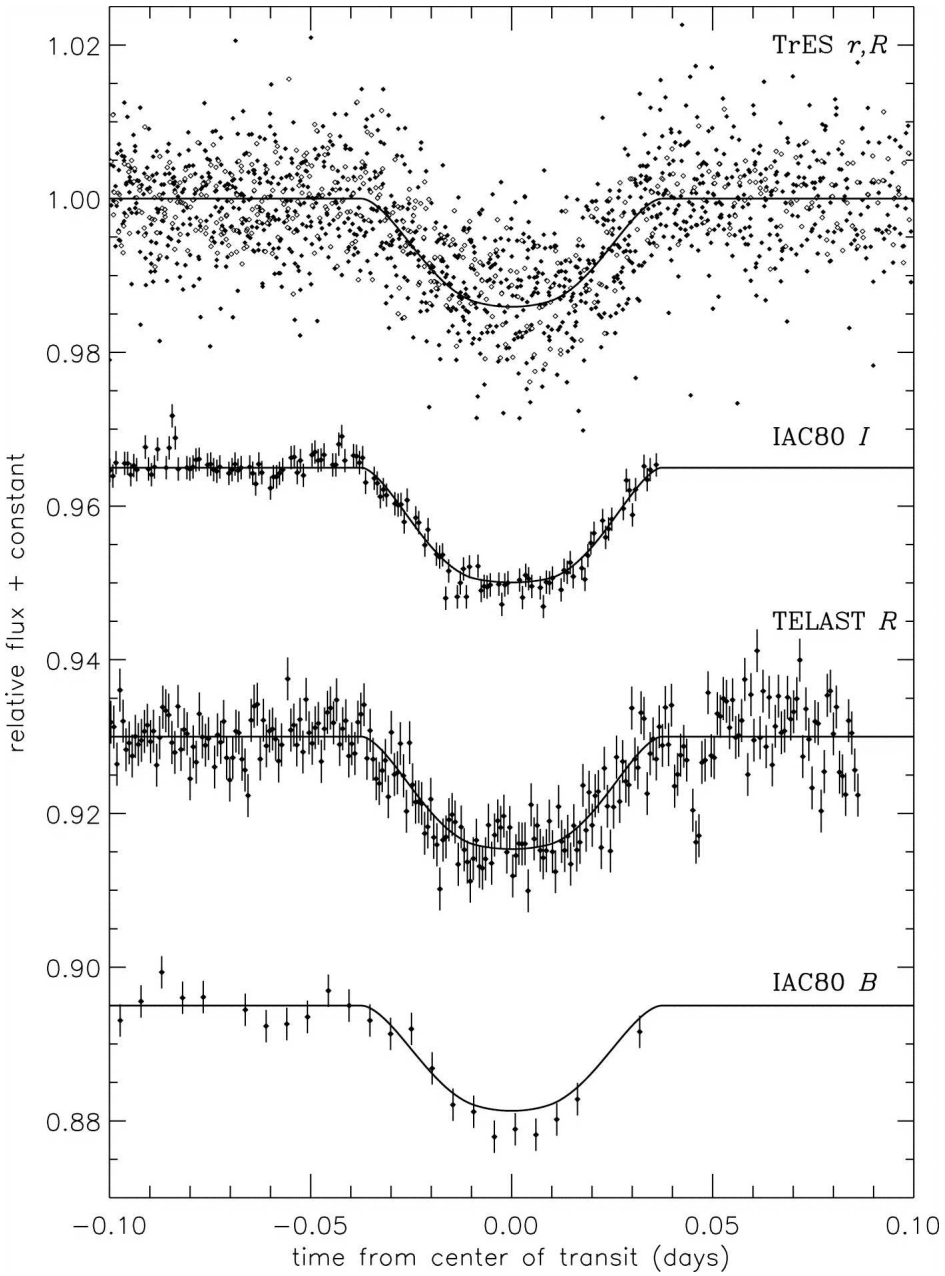

FIGURE 2.27— Light curve observations of TrES-2 with small aperture (10 cm) and intermediate aperture (30 cm to 80 cm) telescopes (O'Donovan et al., 2006).

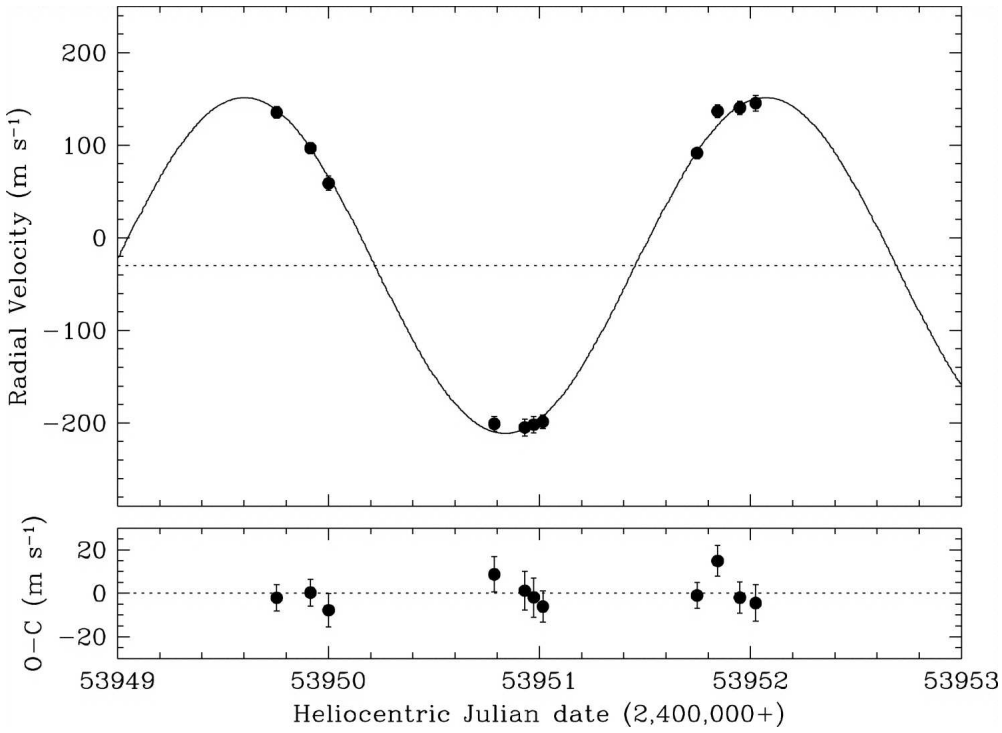

FIGURE 2.28— Radial velocities of TrES-2 as obtained with the Keck/HiRES spectrograph. These observations finally confirmed the planetary character of TrES-2. The solid line is a best-fit sine function representing a circular Keplerian orbit (O'Donovan et al., 2006).

2.9 Conclusions

A complete protocol for the search of transiting planets of a wide-field survey has been introduced and all necessary steps have been shown: realization of regular observations, analysis and reduction of data, elimination of false alarms, follow-up observations, final confirmation of transiting exoplanets and subsequent characterization of these.
My work showed that the protocol works well. After I reduced the images of STARE, we obtained promising candidates. I was able to reject candidates as false positives by continuous light curve observations in one or different filters and by intermediate and high-resolution radial velocity observations.
In the bisector analysis of the candidate And1-04334, I found a correlation between the phase of observation and radial velocity variation; this candidate was hence rejected as a possible eclipsing binary. For Cyg1-03024, I was able to reproduce the transit with higher precision and I also found intriguing radial velocity variations. We will re-observe Cyg1-03024 in the near future with SOPHIE. Keck/HiRES observations showed no radial velocity variation for the candidate Lac0-14888 so its most likely interpretation is one of a faint background eclipsing binary. Cyg0-03908 was observed with the SOPHIE spectrograph and cross-correlated with different masks, and I found a large offset between the K0 mask and the other masks. This indicates possibly a diluted binary system. For LMi-01447, the transit could not be reproduced, possibly due to an error in the ephemeris, but it still remains a potential candidate. UMa-00216 was discarded as a false positive due to different transit depths in different filters. Cyg0-04140 showed radial velocity variations with Keck/HiRES and the SOPHIE spectrograph, but not in phase with the photometric period. This candidate will be re-observed in order to recover the transit ephemeris. We still have three interesting candidates which may be transiting planets. In summary, over the period of my thesis I have followed-up 30 candidates of which I showed the most interesting cases. I discarded 8 candidates, whereas 22 are still in process and 3 interesting cases of them will be re-observed with high resolution spectroscopy at the OHP.
For TrES-2 I observed a 1.4 % deep eclipse in B- and I-filters. This allowed a confirmation of the planetary character of TrES-2 and an improvement of the precision of some of the planet's parameters.

3

High-precision near-infrared photometry of transiting systems

In this chapter I discuss high-precision photometric observations and light curve analysis in the infrared (IR) wavelength range. The relative brightness of a planet increases in the infrared wavelength relative to the star. Therefore, IR observations are an excellent technique to probe exoplanets in two ways: One can try to detect the emission of the planet by observing the secondary eclipse, i. e. when the planet disappears behind the star, whereas in primary transits, transit parameters can be determined more accurately due to the low stellar limb darkening in the IR.

3.1 Introduction

The infrared (IR) wavelength range comprises length between 0.78 μm (the visibility limit of the human eye) and 1 000 μm, though in astronomy the short limit is commonly taken around 0.9 μm due to different detector technologies between the optical and IR sensors and the atmospheric transparency cut-off towards longer wavelength. In astronomy the infrared spectral region is divided into three groups, namely the near-IR (0.9 to 5 μm), the mid-IR (5 to 40 μm) and the far-IR (40 to 350 μm). The atmosphere is generally opaque in the IR wavelength range, except for some wavelength regions, so-called windows, where the transmission increases (Fig. 3.1). Ground-based IR observations are centered in these windows. Table 3.1 shows the most important filters in this wavelength range and their observation windows. Whereas ground-based near-IR observations are pretty standard, mid-IR observations are still challenging,

using the windows between 8-13 μm and 16-25 μm. The most important space-based IR telescopes are the Spitzer Space telescope, covering 3.6 - 24 μm and the recently launched Herschel mission (55 - 672 μm). In the following, I will show some examples of near-IR photometry taken with ground-based facilities. For the work in this thesis, I define a primary transit, or simply transit, as the partial occultation of a star due to the planet crossing its stellar disk and I refer to a secondary eclipse, or simply eclipse, as the planet disappearing behind the star.

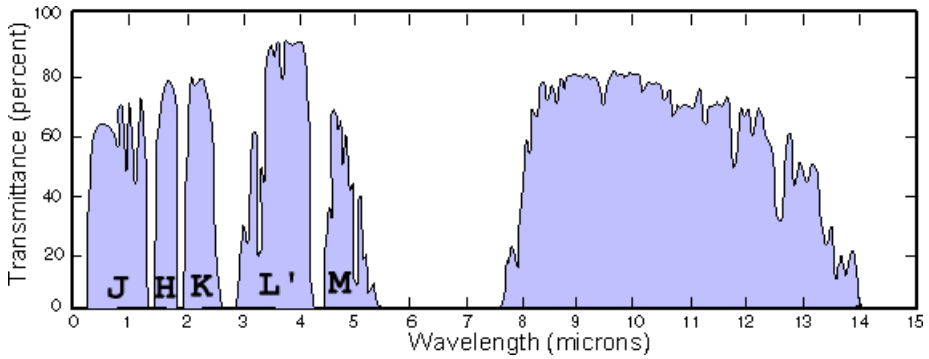

FIGURE 3.1— Earth's atmosphere transmittance as a function of wavelength. Blue shaded areas indicate the observing window and for the near-IR the commonly used filters are indicated.

TABLE 3.1— Most important near-IR photometric filters and their observing windows.

Filter	window [nm]
J	1000 - 1350
H	1450 - 1800
K/K$_s$	2000 - 2400
L'	2900 - 4100
M	4500 - 5200

Since 2005, secondary eclipses have been detected for several Hot Jupiters, like TrES-1 (Charbonneau et al., 2005), HD 209 458b (Deming et al., 2005b; Knutson et al., 2008), HD 189 733b (Deming et al., 2006; Charbonneau et al., 2008; Agol et al., 2009), GJ 436b (Deming et al., 2007; Demory et al., 2007), HD 80 606b (Laughlin et al., 2009) and for several other planets, all of them with the Spitzer Space Telescope at wavelengths between 3.6 and 24 μm. Recently,

the application of this technique has also been proven with the first ground-based detection of a secondary eclipses of TrES-3 in the IR (de Mooij & Snellen, 2009). In the following sections of this chapter, I will show secondary eclipse observations of CoRoT-2b with the 4.2m William Herschel Telescope (WHT) at the Roque de los Muchachos Observatory and further ones for HD 189 733b with the 1.5m Carlos Sánchez Telescope (CST) at the Teide Observatory.
Important observations of primary transits in the IR wavelength range have been made by e. g. Richardson et al. (2006); Gillon et al. (2007a); Alonso et al. (2008a); Nutzman et al. (2009) and Agol et al. (2009), including evidence for water absorption during transit by Tinetti et al. (2007) and Beaulieu et al. (2008). Two of the teams (Alonso et al., 2008a; Agol et al., 2009) observed primary transits mainly in order to put constraints on the parameters of additional planets in the respective system, by measuring the transit duration or transit timing variation. A better parameter estimation of the planet, especially precise measurement of the mid-transit time and/or transit duration, can be achieved by IR photometry because of the weak limb darkening in this wavelength range (Fig. 3.2). Observations in the IR wavelength range can also be used to reject false alarms, which in the case of a transiting planet, as opposed to an eclipsing binary, should show a similar eclipse depth as in the optical. Primary transit observations of HD 189 733b and of GJ 436b (Alonso et al., 2008a), both observed with the CST, will be discussed in the following sections of this chapter.

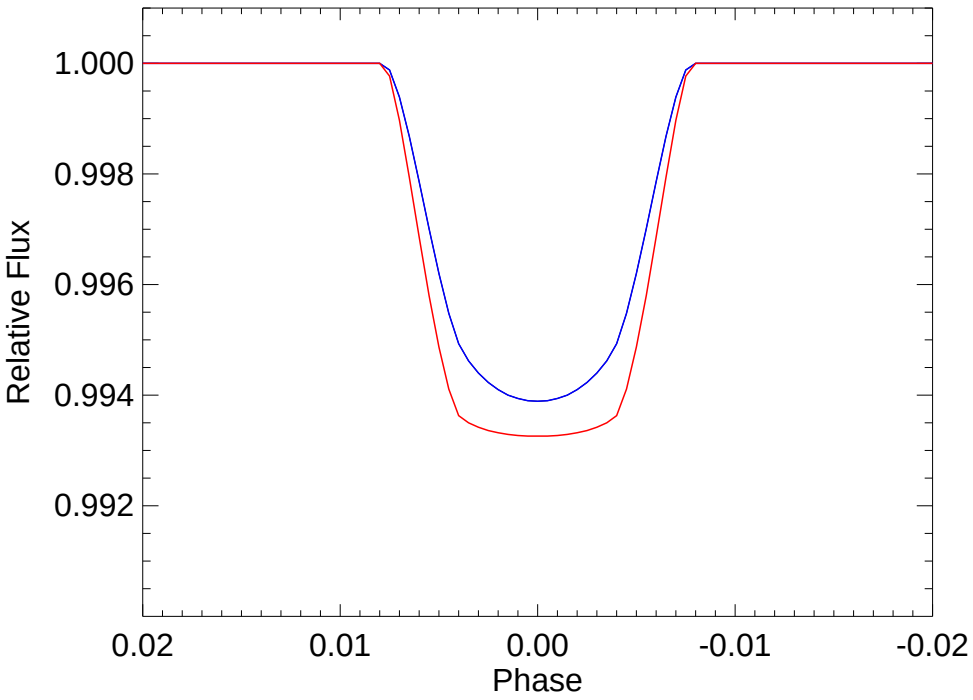

FIGURE 3.2— Simulated primary transit light curve of GJ436b, using a quadratic limb darkening law and two different sets of limb darkening coefficients, for the V-band (blue curve) and for the K-band (red curve).

3.2 Near-IR emission from Hot-Jupiter planets

Hot Jupiters are objects orbiting their host stars in orbits $\leq$ 0.05 AU. This proximity to the star causes Hot Jupiters to have temperatures around 1 000 K and, hence, the observation of Hot Jupiters in the IR wavelength range is more favorable than in the visible wavelength range, because on one hand, the ratio $\frac{F_S}{F_P}$ improves, where F_S and F_P are the observed fluxes from star and planet, respectively, and, on the other hand, the light received from the planet is dominated by the thermal radiation over the reflected light as was shown in Fig.1.18 in the Introduction. In the near-IR, the planet emission is a mixture of reflected light from the central star - indicative of the planet albedo - and of the planet's thermal emission - indicative of its temperature. In the upper plot in Fig. 1.18 (Chapter 1) and above a wavelength of $\sim$1 μm (start of the IR wavelength range), one can see that the thermal emission starts to dominate the radiation of the planet. Similarly, in the lower plot, above $\sim$1 μm the planet-star flux ratio starts to increase.
In secondary eclipse observations, the eclipse depth is given by $\Delta F_{\rm sec} = \frac{F_{\rm off} - F_{\rm on}}{F_{\rm off}}$, where the on-eclipse flux $F_{\rm on}$ is the flux of the star (F_S) only and $F_{\rm off}$, the off-eclipse flux, is the flux of the star and planet ($F_S + F_P$), obtaining for the eclipse depth $\Delta F_{\rm sec} = \frac{F_P}{F_S + F_P}$. For $F_P << F_S$ we can rewrite the eclipse depth as $\Delta F_{\rm sec} \approx \frac{F_P}{F_S}$.
Secondary eclipse observations also permit to estimate an observed brightness temperature T_b in a certain wavelength range or filter, which can be compared to the theoretical equilibrium temperature T_{eq} of the planet due to the stellar flux. A discrepancy between observed brightness temperature and theoretical equilibrium temperature might indicate an additional energy source in the planetary system. The brightness temperature is the temperature of a blackbody that would produce the same flux as was measured in a given filter. The equation for the brightness temperature can be derived by starting with the Planck's law integrated over all solid angles and as a function of wavelength λ:

$$I_B(\lambda, T) = \pi \frac{2hc^2}{\lambda^5} \frac{1}{\exp^{\frac{hc}{kT\lambda}} - 1}, \tag{3.1}$$

where I_B is the intensity emitted per surface unit of a blackbody, k is the Boltzmann's constant, h is the Planck's constant, T the temperature of the blackbody and c is the speed of light. We further have the total flux or luminosity of the star $L_S = 4\pi R_S^2 \int I_S(\lambda) d\lambda$ and planet $L_P = 4\pi R_P^2 \int I_P(\lambda) d\lambda$, respectively, where I_S and I_P are their respective intensities. At a given value for λ, e. g. at the central wavelength of the filter used for observation, and substituting for the intensities the Planck's law, the ratio of the luminosities of

planet and star is then:

$$\frac{L_P}{L_S} = \frac{R_P^2}{R_S^2} \frac{\exp^{\frac{hc}{kT_S\lambda}} - 1}{\exp^{\frac{hc}{kT_P\lambda}} - 1}, \tag{3.2}$$

where T_S is the black body temperature of the star and T_P the one of the planet, i. e. $T_P = T_b$. The term $\frac{R_P^2}{R_S^2}$ can also be substituted with the primary transit depth $\Delta F_{\rm prim}$, see Eq. 1.3. One then obtains the relation between secondary eclipse and primary transit depths:

$$\Delta F_{\rm sec} = \Delta F_{\rm prim} \frac{\exp^{\frac{hc}{kT_S\lambda}} - 1}{\exp^{\frac{hc}{kT_P\lambda}} - 1}. \tag{3.3}$$

In the following sections I will show some estimation of the brightness temperature T_b, where I used for λ simply the central wavelength of the corresponding filter of observation.
The equilibrium temperature T_{eq} is the temperature of the planet after it reached complete thermal equilibrium with the incoming stellar radiation. The equation to calculate the equilibrium temperature can be derived from the energy balance equation between the re-radiated energy and the absorbed energy:

$$4\pi R_P^2 F_{S,P} = (1 - A_B)\, F_{S,S} \left(\frac{R_S}{a}\right)^2 \pi R_P^2, \tag{3.4}$$

where $F_{S,P}$ and $F_{S,S}$ are the surface flux of the planet and star, respectively and A_B is the bond albedo. In this equation the right hand side describes the energy absorbed and the left hand side the one emitted by the planet. The bond albedo A_B is the total radiation reflected from an object compared to the total incident radiation and it is related to the geometric albedo p by $A_B = pq$, where q is the phase integral. The geometric albedo is the amount of radiation relative to that from a flat Lambertian surface which is an ideal reflector at all wavelengths. The phase integral is a function of the phase angle ϕ, defined between 0 and π and is given by $q = 2\int_0^\pi \frac{F(\phi)}{F(\phi=0)} \sin\phi d\phi$, where $F(\phi)$ is the flux reflected from the body at the corresponding phase angle ϕ. Typically, geometric albedos for Close-in Extrasolar Giant planets are low, e. g. Snellen et al. (2009b) gave an upper limit for the geometric albedo in the visible light of CoRoT-1b of <0.20. In order to describe a possible re-distribution of heat/energy from the planet's star-lit side to the entire sphere of the planetary surface, a re-radiation factor f, which gives the fraction of emission from the star-lit cross-section (which is a disk of area πR_P^2) relative to the entire planet surface of area $4\pi R_p^2$, is

introduced in Eq. 3.4 by multiplying the left hand side with $f/4$. Table 3.2 shows different re-radiation factors and their physical interpretation. Assuming blackbody radiation over all wavelengths, one can substitute the surface fluxes of the star and planet, respectively, in Eq. 3.4 with the Stefan Boltzmann law: $F_{S,P} = \sigma_R T_{eq}^4$ and $F_{S,S} = \sigma_R T_{\mathrm{eff},S}^4$, where σ_R is the Stefan-Boltzmann constant, T_{eq} the planetary equilibrium temperature and $T_{\mathrm{eff},S}$ is the effective temperature of the star. By reordering, one obtains the following equation for the planetary equilibrium temperature:

$$T_{eq} = T_{\mathrm{eff},S} \left[f(1 - A_B)\right]^{1/4} \left(\frac{R_S}{a}\right)^{1/2}. \tag{3.5}$$

TABLE 3.2— Re-radiation factor and their physical interpretation.

Re-radiation factor f	Physical interpretation
1/4	Uniform temperature and emission around planet, corresponding to a radiation of the energy into $4\pi R_P^2$ (pL-class planets)
1/2	Uniform emission from the day side hemisphere, corresponding to a radiation of the energy into $2\pi R_P^2$ (not physical)
2/3	Instantaneous re-emission of absorbed radiation from planet's day side hemisphere without advection due to inefficient transport of incident flux from the day to the night side, corresponding to a radiation of the energy into $1.5\pi R_P^2$ (pM-class planets)

Comparing the planet's T_{eq} (which does not depend on eclipse observations) with T_b derived from secondary eclipse and primary transit observations, and using Eq. 3.3, one is able to indicate if there are any serious discrepancies between the two temperatures that cannot be resolved by adjusting the value f in Eq. 3.5, and might be indicative of internal heat sources in the planet. Note that in the IR, A_B can usually be set to zero.

A further application of secondary eclipse observations, using the time of the eclipse, may restrict the eccentricity of the planetary orbit more precisely than parameters obtained from radial velocity measurements, by using Eq. 1.16 from Chapter 1.

As also mentioned in Chapter 1, there are different types of planets. Planets that are warm enough to prevent Ti and V-bearing compounds from condensation are termed pM-class. In the IR, these planets will appear "anomalously"

bright in secondary eclipse and will have a large day/night side effective temperature contrast with $f \approx 2/3$. Planets are termed pL class if the temperature is small enough to allow for condensation of Ti and V-bearing compounds leading to a better temperature redistribution. These planets will have significantly smaller secondary eclipse depths in the IR and a smaller effective temperature contrast between day and night side, indicating $f \approx 1/4$.
Assuming a blackbody radiation for the planet is a first order approximation. However, a real planet does show different molecular absorption features. These features can be accounted for by introducing atmospheric models. Fig. 3.3 shows simulated primary transit depths as a function of wavelength for HD 189 733b (red line) and some observations (blue crosses) and Fig. 3.4 shows simulated secondary eclipse depths for different heat re-distribution parameters (red, blue, green line) as a function of wavelength, also with some observations included (black and red dots). For both simulations, atmospheric models were used. Comparing Fig. 3.4 and Fig. 1.18, at certain wavelengths absorption features in the planetary atmosphere can be identified. These absorption features in the planetary atmosphere change the secondary eclipse depth if present and hence the secondary eclipse depth at different wavelengths can be used to probe their presence. The molecule H_2O is expected to suppress flux between 4 and 10 μm. In Fig. 3.4 one can identify a peak between 3.6 and 4.5 μm and a rise between 5 and 10 μm, both revealing the presence of water (Burrows et al., 2005). CO abundances will lower the planet/star flux ratio at 4.5 μ (Burrows et al., 2005). The peak at $\sim$6-6.5 μm in Fig. 3.4 might have been caused by the vibrational bending mode of water (Grillmair et al., 2008).

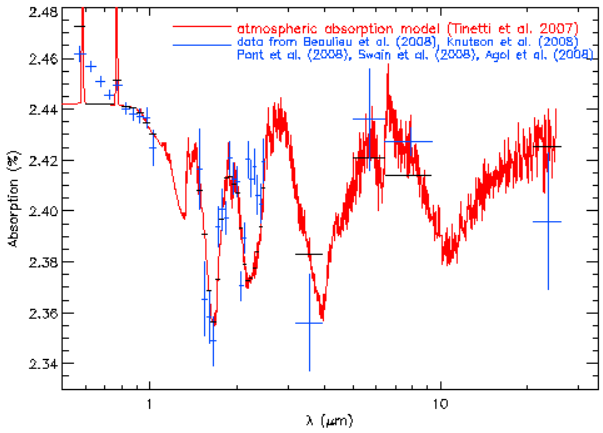

FIGURE 3.3— Taken from Agol et al. (2009): Compilation of data on primary transit depths (given as 'absorption' in %) of HD 189 733b. The solid (red) curve is a binned version of a model from Tinetti et al. (2007); horizontal lines (black) are the mean of this model over the bandwidths of each of the crosses that corresponds to observations (blue), which indicate 1-σ error bars.

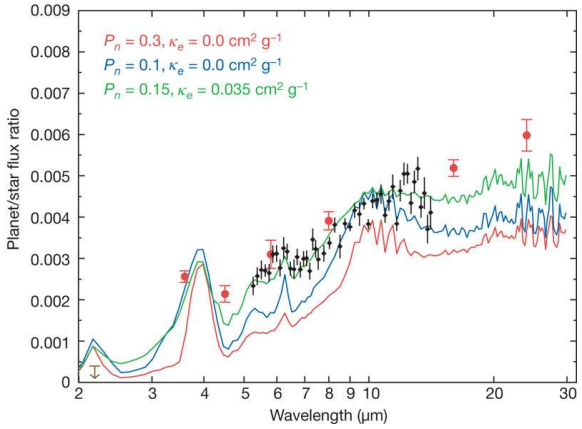

FIGURE 3.4— Secondary eclipse observations and model spectra of HD 189 733b from Grillmair et al. (2008): The black points show the mean planet/star flux ratios for six second-order spectra (5-8μm) and four first-order spectra (7.5-14 μm) taken with the Spitzer Space Telescope. The filled red circles show broadband measurements from Charbonneau et al. (2008) with the Spitzer Space Telescope at 3.6, 4.5, 5.8, 8.0, 16 and 24 μm (error bars on this data, s.e.). The upper limit at 2.2 μm is derived from Keck spectroscopy (Barnes et al., 2007). The red, blue and green traces are atmospheric model predictions for three values of a day-side night-side heat redistribution parameter, P_n, and two values of the extra upper-atmosphere opacity, κ_e. P_n is the fraction of the stellar energy intercepted by the planet that is redistributed to the night side; P_n =0 means no redistribution. The model predictions have not been scaled in any way.

3.3 Observation and Data analysis

I observed secondary eclipses using mainly two telescopes, the William Herschel Telescope and the Carlos Sánchez Telescope. The Carlos Sánchez Telescope (CTS) is a 1.52m telescope at the Teide Observatory, operated by the IAC. For all IR observations on the CST the detector CAIN with a Fowler readout mode, performing 8 readouts per image and rejecting 2 of them, was used. CAIN is a powerful and versatile instrument designed and built by the IAC. The detector consists of a mosaic of 256 × 256 HgCdTe photoelectric elements (NICMOS technology 3), sensitive in the range between 1 and 2.5 μm, with four electronic bias channels and independent reading, each controlling one quadrant. The physical size of each pixel is 40 microns. The focal plane of the optical field has two settings: one is to get a narrow field "*N*" with a pixel scale of $0''.39$ per pixel and a field-of-view of $100''\times 100''$, the other setting is to observe with a wide field-of-view "*W*" of $256''\times 256''$ and a pixel scale of $1''.00$ per pixel.
For observations on the 4.2m William Herschel Telescope (WHT) at the Roque de los Muchachos observatory, the Long-slit Intermediate Resolution Infrared Spectrograph (LIRIS) was used. This is a near-IR imager/spectrograph, built and developed by the IAC. LIRIS uses a 1k × 1k HAWAII detector for the range between 0.8 and 2.5 μm. The field-of-view is $4'.27 \times 4'.27$ with a pixel scale of $0''.25$ per pixel.
For all observations, the same technique was used in order to avoid saturation of the detector by bright stars and to minimize the effect of detector cosmetics. Following standard technique in IR photometry, a series of 50 images of the dome with the dome light 'on' and 'off' were taken. In order not to include environmental effects in the flat image, a master flat field image was built by subtracting a combination of images taken with the lights 'on' from a combination of images with the lights 'off'. Unfortunately, noisier results were obtained when attempting to correct the images by a division of this flat field, and thus no flat-fielding corrections were performed. The success of the observations arises from the repartition of the bright stellar flux among different pixels, using high defocusing and obtaining a ring-shaped PSF with an outer radius between 20 and 26 pixels (Fig. 3.5), which helps to minimize effects of bad pixels, tracking, and atmospheric seeing changes. The stars were placed in an area in each detector with few hot or dead pixels. Furthermore, in order to achieve a good stability of the system, no usual dithering patterns were employed. To account for hot pixels inside the target's PSF, the telescope was moved every 1-2 hours to a close zone of the sky with no stars visible in the detector (*offset images*). Pixels with a low or zero sensitivity (dead pixels) were located in flat images of the dome under slight artificial illumination.

The reductions of the raw frames to the light curves were in all cases the

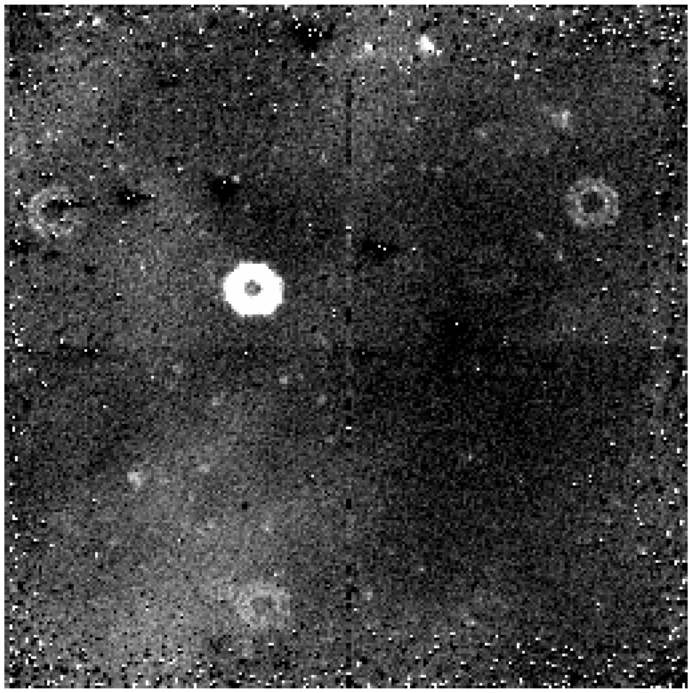

FIGURE 3.5— Example CCD frame of HD 189 733 taken with the CST on Aug. 16, 2008 in the K_s filter. The defocussing and ring-shape of the observed star are clearly visible.

same and will be outlined briefly. The *offset images* of each night were median combined. A mean sky background level, measured in a region without stars, was then subtracted from this combined *offset image*. The best results were obtained, by subtracting the previous image from the following images, without performing any other standard calibration. From each science image a sky background level, that had been measured in a region without apparent star, was subtracted. The centroid of the target star was calculated by fitting a Gaussian with a non-zero revolution axis to the ring shape PSF. The flux was then summed inside a circular aperture with different sizes and centered on each star. Residual background levels were measured in a ring around each star. Finally, the light curve time series were obtained.

3.4 Infrared observations of HD 189 733b

The transiting planet HD 189 733b (Bouchy et al., 2005), orbiting a very close and bright early-K star, is an excellent target for IR observations, as it is expected to have a stronger emission in the IR than both HD 209 458b and TrES-1 (Burrows et al., 2006). Therefore, we observed HD 189 733 around primary and secondary eclipse phases in the IR wavelength range with the CST and the CAIN detector.

The first secondary eclipse for HD 189 733b was obtained by Deming et al. (2006) with the Spitzer Space Telescope at 16 μm, measuring the day side planet-star brightness contrast. Grillmair et al. (2007) obtained the first mid-IR spectra between 7.5 and 14.7 μm of HD 189 733b during its secondary eclipse. Primary transit observations of HD 189 733b, together with their estimated planet-to-star area ratio, have been reported by Beaulieu et al. (2008) at 1.6 and 5.8 μm and Knutson et al. (2007) at 8 μm, where Knutson et al. (2007) also observed a secondary eclipse to map the day-night contrast. Later, Ehrenreich et al. (2007) reobserved primary transits of HD 189 733b with the Spitzer Space telescope at 3.6 and 5.8 μm to search for signatures of water, with the result of having too high error bars to detect water. However, Grillmair et al. (2008) found a strong water absorption by observing ten secondary eclipses between 5 μm and 10 μm. Swain et al. (2008b) observed primary transits between 1.4 and 2.5 μm to confirm the presence of methane. The spectroscopic observations from Swain et al. (2008b) were also co-added to match the H and K bands in order to be able to create transit light curve models based on available published nonlinear limb-darkening coefficients.

By observing around the secondary eclipse phase, Barnes et al. (2007) tried to detect absorption signatures of H_2O and CO in HD 189 733b at $\sim$2.2 μm, but they were only able to put limits on the planet/star flux ratio of $\log_{10}(F_P/F_S) \sim -3.16$. Charbonneau et al. (2008) published secondary eclipse depths at 3.6 μm, 4.5 μm, 5.8 μm, 8.0 μm, 24 μm and reanalyzed data at 16 μm from Deming et al. (2006). In order to search for molecular signature, like CO, CO_2 or H_2O, in the secondary eclipses of HD 189 733b, Swain et al. (2009) observed secondary eclipses with the Hubble Space telescope and NICMOS between 1.4 and 2.5 μm. Similar to Knutson et al. (2007), Knutson et al. (2009) reobserved HD 189 733b, but at 24 μm. Desert et al. (2009) observed primary transits of HD 189 733b at 4.5 and 8.0 μm to probe the planetary atmosphere for carbon monoxide. Four consecutive transit and four consecutive secondary eclipses of HD 189 733b were observed by Agol et al. (2009) with the Spitzer Space Telescope. This uninterrupted observation in the IR band put further constraints on the transit timing variation and transit duration variation. Additionally,

Agol et al. (2009) analyzed the depth of the secondary eclipses for variations. Agol et al. (2009) reported that no significant transit timing variations nor significant eclipse depth variations were present. Table 3.3 shows a compilation of primary transit and secondary eclipse observations from the literature.

In total, we observed around eleven primary transit and four secondary eclipse phases with the CST and the CAIN instrument in the K_s filter, except in the night of Sept. 6, 2007, when we alternated between the K_s and H filter. For these observations the wide "*W*" field-of-view was used. After the image analysis, as outlined in Sect. 3.3 and done by Roi Alonso, eleven primary transit (Fig. 3.6) and four secondary eclipse (Fig. 3.8) light curves were obtained. In Fig. 3.6, the gaps in the the lowest light curve are due to switching the filters.

In order to obtain the best-fit primary transit light curve parameters, I first phased and binned all eleven primary transit observations into one light curve (Fig. 3.7), and then I fitted the resulting light curve for $k = \frac{R_P}{R_S}$, $rr = \frac{R_P+R_S}{a}$ and the inclination i, fixing the limb darkening coefficient and assuming a quadratic limb darkening law. Table 3.4 shows the initial and fitted parameters. As initial parameters, the values from Southworth (2008) were used and the limb darkening coefficients were fixed to the values given in Table 3.4, based on coefficients given by Claret (2000). For a transit model, I used the FORTRAN routines from Giménez (2006a) and the simplex-downhill fitting algorithm (Press et al., 1992). The best-fit transit model is also over-plotted in Fig. 3.7. I note that the depths of our primary transit observations in the K_s band of 2.39 % are consistent with other observations from the literature in the same band, see Table 3.3.

I also phased and binned all four secondary eclipse observations into one light curve (Fig. 3.9), but I found no visible secondary eclipse. Therefore, in order to establish limits on the depth and central time of the secondary eclipse, I used the light curve, built from all four observations, to explore the χ^2 distribution of residuals from a fit to a trapezoidal model in a grid of eclipse centers, between -60 and +60 minutes from the expected center-time, and depths from 0.01 % to 0.1 % of the secondary eclipse. The minimum χ^2 and the 1, 2, 3 and 4-σ confidence levels are presented in Fig. 3.10. These levels might indicate a detection of an eclipse of 0.049 $\pm$ 0.005 % depth some 10 minutes later (at phase 0.5031) than expected for a circular orbit (at phase 0.5), which would imply an eccentricity of $e \cos \omega = 0.02$. However, since none of the eclipse observations in the literature in Table 3.3 of HD 189 733b indicate any eccentricity, I prefer to quote the result of these observations being a 2-σ upper limit of 0.057 %; consistent with previous results at 2.2 μm by Barnes et al. (2007) taken with the Keck 10m telescope.

Next, I calculate the theoretical equilibrium temperature T_{eq} of HD 189 733b,

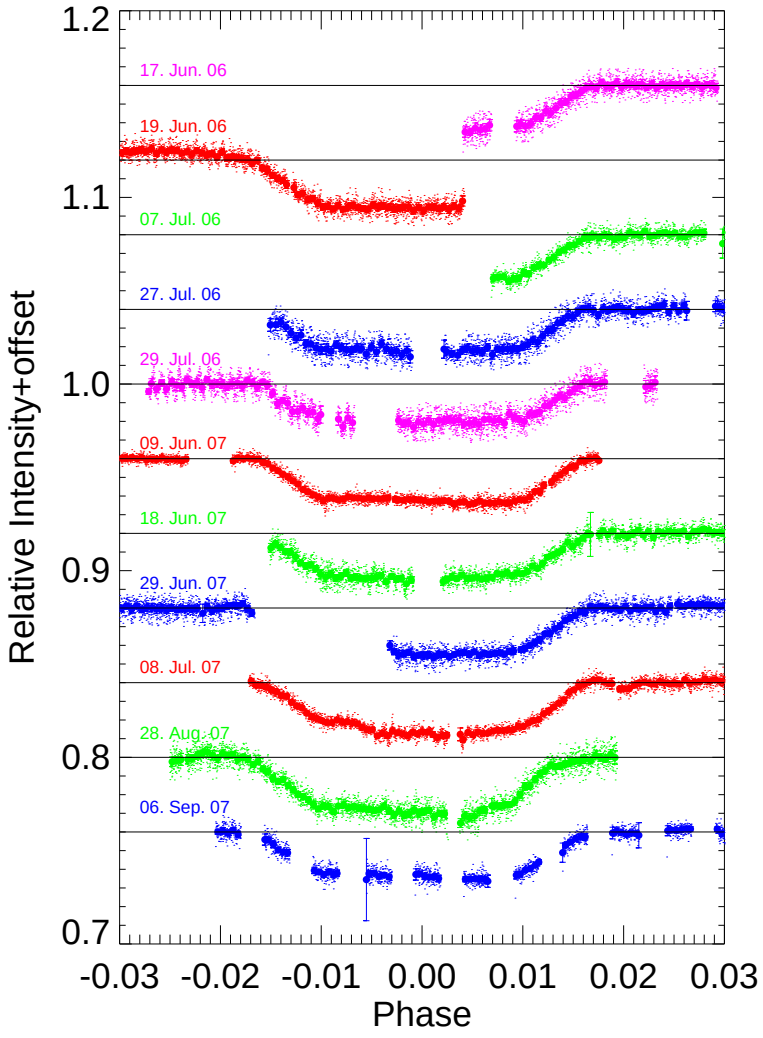

FIGURE 3.6— Primary transit observations with the CST in the K_s filter. Big dots are bins of 0.0005 in phase and 3-σ errors for each bin.

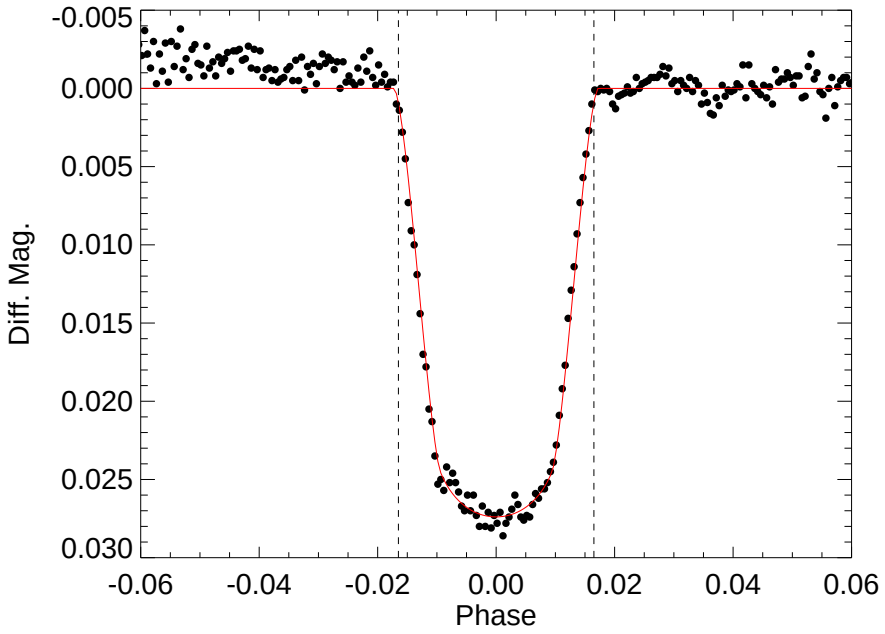

FIGURE 3.7— Binned (0.0005 in phased) primary transits from Fig. 3.6 and best fit transit model with parameters from Table 3.4 over-plotted.

using Eq. 3.5. Therefore, I assumed a bond albedo of zero, because in the IR wavelength range A_B is close to zero, and obtained a zero-albedo (A_B=0) equilibrium temperature of T_{eq}=1 200 K; using the parameters from Torres et al. (2008): $T_{\mathrm{eff},S}$= 5040 K, a/R_S=8.81 and a re-radiation factor f= 1/4. I used the calculated theoretical equilibrium temperature together with Eq. 3.2 to estimate the expected transit depth; assuming $T_b = T_{eq}$, i. e. no internal energy sources, and using R_P=1.156 R_J, $T_{\mathrm{eff},S}$=5040 K, R_S=0.753 $R_\odot$ and for the K_s-band ($\lambda_c = 2.2\mu$m). I obtained a transit depth of 0.03 %, which is consistent with the results from the literature and the upper limit of the observations.

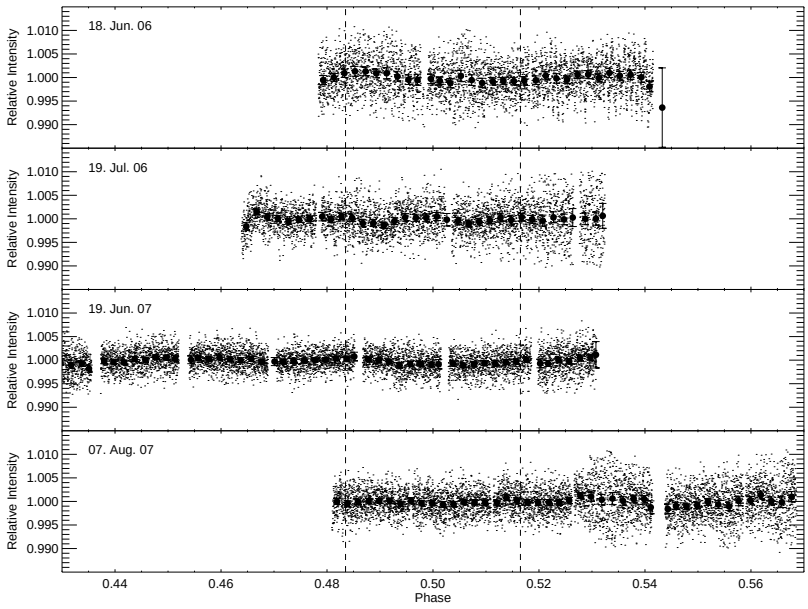

FIGURE 3.8— Observed secondary eclipses of HD 189 733b with the CST in the K_s filter. Big dots are data binned 0.002 in phase with 3-σ error bars (nearly invisible). Vertical dashed lines indicate the expected secondary eclipse phase, assuming zero eccentricity.

TABLE 3.3— Overview of observed primary transit and eclipse depth estimations for HD 189 733b in the IR wavelength range.

Eclipse/Transit	Depth [%]	Source
2.2 μm Primary transit	2.39	1
1.6-1.8 μm Primary transit	$\sim$2.4	7
2.0-2.4 μm Primary transit	$\sim$2.4	7
3.6 μm Primary transit	2.43	6
3.6 μm Primary transit	2.39	12
3.6 μm Primary transit	2.36	4
4.5 μm Primary transit	2.42	12
5.8 μm Primary transit	2.44	4
5.8 μm Primary transit	2.37	6
5.8 μm Primary transit	2.39	12
8 μm Primary transit	2.39	5
8 μm Primary transit	2.43	14
8 μm Primary transit	2.38	12
24 μm Primary transit	2.40	11
2.2 μm Secondary eclipse	< 0.05	1
1.98-2.38 μm Secondary eclipse	0.04	10
2.2 μm Secondary eclipse	< 0.04	8
3.6 μm Secondary eclipse	0.26	9
4.5 μm Secondary eclipse	0.21	9
5.8 μm Secondary eclipse	0.31	9
8 μm Secondary eclipse	0.34	5
8 μm Secondary eclipse	0.39	9
8 μm Secondary eclipse	0.35	14
7.5-14.7 μm Secondary eclipse	0.49	3
16 μm Secondary eclipse	0.52	9
16 μm Secondary eclipse	0.55	2
24 μm Secondary eclipse	0.60	9
24 μm Secondary eclipse	0.54	11
5-14 μm Secondary eclipse	see Fig. 3.4	13

Sources: 1) this work, 2) Deming et al. (2006), 3) Grillmair et al. (2007), 4) Beaulieu et al. (2008), 5) Knutson et al. (2007), 6) Ehrenreich et al. (2007), 7) Swain et al. (2008b), 8) Barnes et al. (2007), 9) Charbonneau et al. (2008), 10) Swain et al. (2009), 11) Knutson et al. (2009), 12) Desert et al. (2009), 13) Grillmair et al. (2008) 14) Agol et al. (2009)

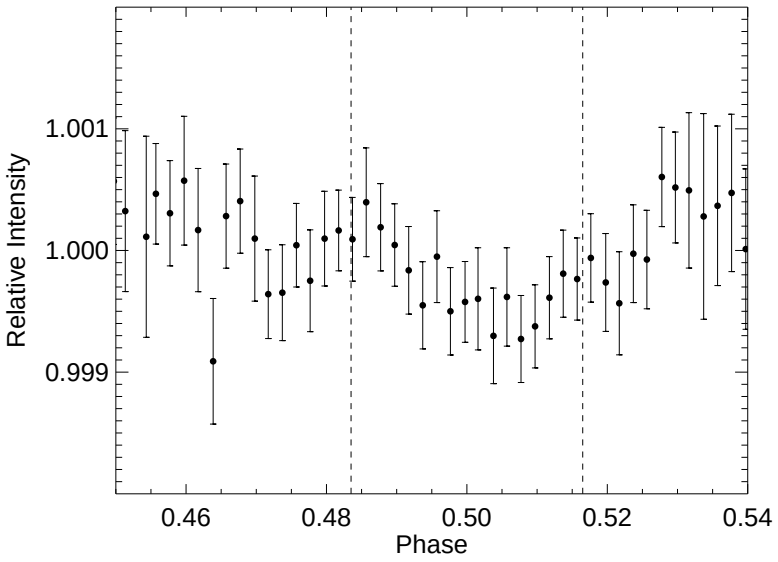

FIGURE 3.9— Binned (0.002 in phase) secondary eclipse from Fig. 3.8. Vertical dashed lines indicate the expected phase of the secondary eclipse, assuming zero eccentricity.

TABLE 3.4— Parameters of HD 189 733b.

Parameter	initial values	best fit value
k	0.1568 ± 0.0024	0.1545
rr	0.1287 ± 0.0036	0.1315
i	85.78 ± 0.25	85.65
u_a	0.471	-
u_b	-0.037	-

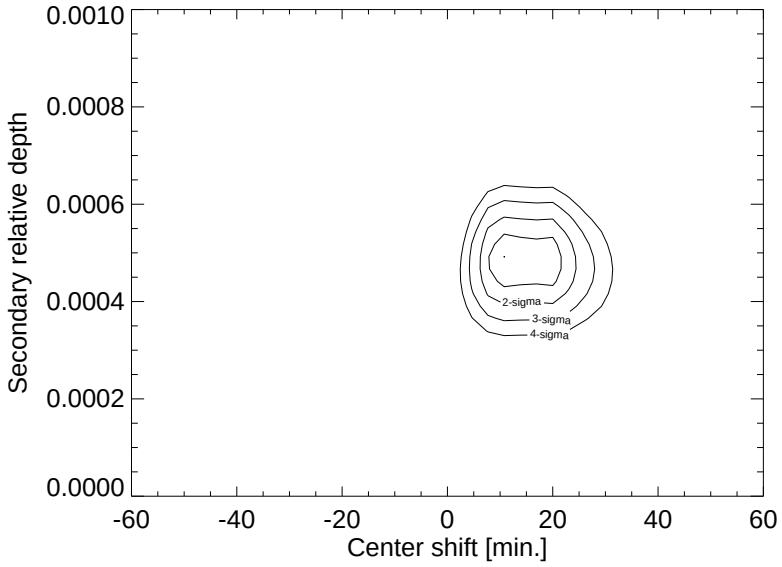

FIGURE 3.10— The χ^2 space for different eclipse center times and depths of HD 189 733b in the K_s-filter, indicating the 1, 2, 3 and 4-σ confidence limits.

3.5 Secondary eclipse observation of CoRoT-2b

Orbiting an active G star with a 1.74 days period, the massive planet (3.3 M_J) CoRoT-2b (Alonso et al., 2008b) shows an intriguing large radius of 1.47 R_J. While several of the Hot Jupiters show this anomalous and currently poorly understood bloating, the large mass of CoRoT-2b poses additional theoretical challenges. CoRoT-2b falls in the pM-class of planets according to the classification of Fortney et al. (2008), which exhibit hot stratospheres (temperature inversions).

CoRoT-2b was observed during the two nights of Jun. 12 and Jun. 19, 2008, where I participated in the latter one. The observations were conducted on the 4.2m WHT using the LIRIS instrument. The observations were scheduled around new moon, and the weather conditions were very good, with a seeing varying smoothly between 0″.45 and 0″.95 on the night of Jun. 12, 2008 and between 0″.6 and 1″.6 on Jun. 19, 2008. The image mode of the LIRIS instrument was used, with a K_s filter on the first night, and a H filter on the second one. The exposure time was 15 s on the first night and 17 s on the second one, with a typical overhead to read the detector and store the data of about 3 s. The flux on individual pixels of the target's PSF was never above 15k ADUs, a dynamical regime where the detector is known to have a good linearity. Therefore, it was not necessary to perform non-linearity corrections of the data as done by de Mooij & Snellen (2009). In total, 1380 useful frames on the night of Jun. 12 and 1096 on Jun. 19 were obtained, observing in both nights for about 7.5 h around the expected times of secondary eclipses. Finally, the procedure explained in Sect. 3.3 was applied to obtain the light curves in the H filter (Fig. 3.11) and K_s filter (Fig. 3.12).

No significant detection of the secondary eclipse in the H filter was found (Fig. 3.13) whereas in the K_s filter, the observations showed a tentative secondary eclipse (Fig. 3.14). In order to safely provide a 3-σ upper limit for the secondary eclipse in H-band, the χ^2 distribution was mapped, similar to Sect. 3.4 (Fig. 3.15). In the case of CoRoT-2b, a grid of eclipse centers from -20 to +20 minutes and depths from 0.01 % to 0.2 % was established, with the best fitted depth of 0.07±0.05%. A lowest 3-σ depth of 0.17 % was obtained, which was used as 3-σ upper limit. The χ^2 mapping for the K_s-filter (Fig. 3.16) resulted in an eclipse depth of 0.16 ± 0.05 %. The mapping was also performed on two check stars, re-assuring the detection of the secondary eclipse in K_s-band was not present in the two other stars.

Using Eq. 3.5 and the parameters from Alonso et al. (2008b): $T_{\mathrm{eff},S}$= 5625 K, a/R_S=6.70 and a re-radiation factor f= 2/3, the zero-albedo (A=0) equilibrium temperature for CoRoT-2b was estimated to be T_{eq}=1964 K. Again, T_{eq}

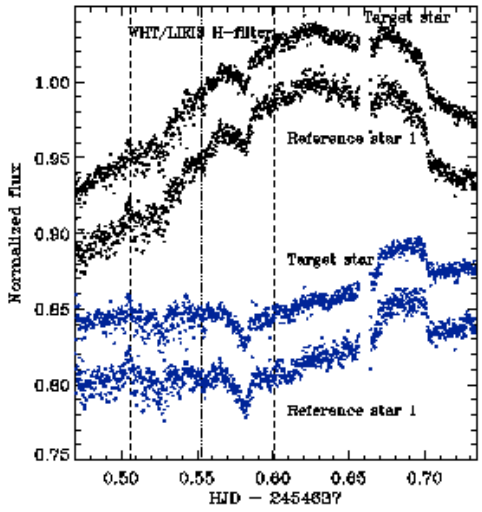

FIGURE 3.11— Similar to Fig. 3.12, giving the light curves for the target and reference star in the H filter, before (top, black dots) and after correcting for changing airmass (bottom, blue dots).

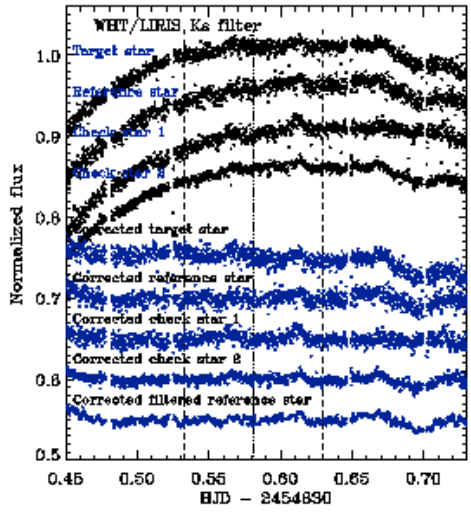

FIGURE 3.12— Secondary eclipse light curves of CoRoT-2b and the reference stars observed with the WHT in the K_s filter, before correcting for the changing airmass (top black points) and after correcting (bottom, blue points). Vertical lines show the expected moments of eclipse ingress, center and egress.

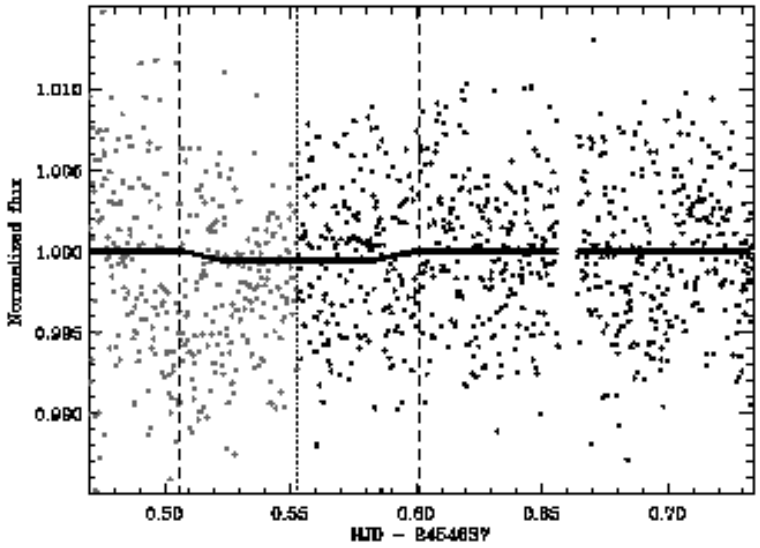

FIGURE 3.13— Fully corrected secondary eclipse light curve of CoRoT-2b with the WHT in the H filter. Vertical lines show the expected moments of eclipse ingress, center and egress. The solid line shows the best-fit trapezoid of the second-half of the secondary eclipse (points in black). The data points before the center of the eclipse (points in grey) are suspicious of uncorrected instrumental effects and have not been considered for the eclipse depth determination.

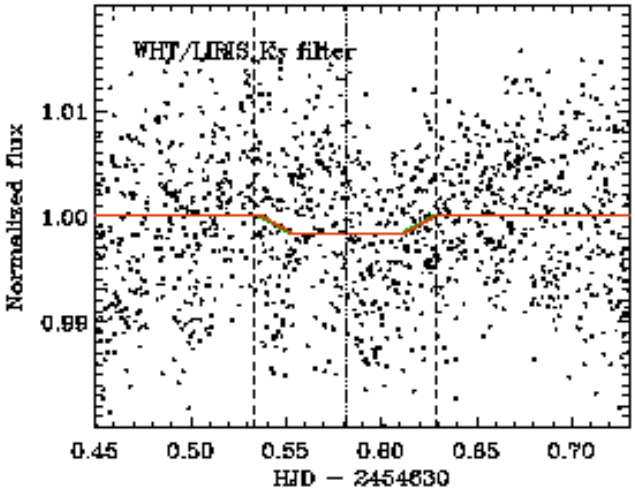

FIGURE 3.14— Observed light curve of CoRoT-2b with the WHT in the K_s filter around the phase of secondary eclipse. The vertical lines show the expected times of first contact, eclipse center and fourth contact, according to the ephemeris in Alonso et al. (2008b). In green, the best-fit trapezoid with the eclipse center time fixed to the ephemeris.

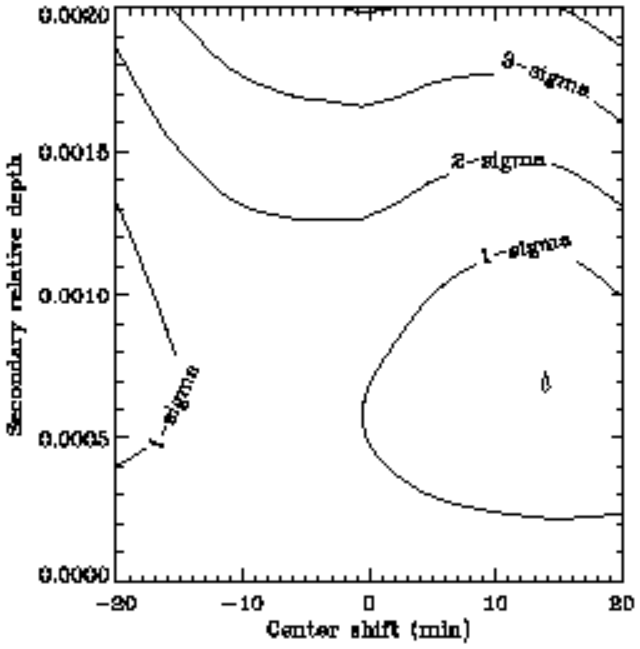

FIGURE 3.15— The χ^2 space for different eclipse center times and depths of CoRoT-2b in the H-filter, indicating the 1, 2, 3 and 4-σ confidence limits.

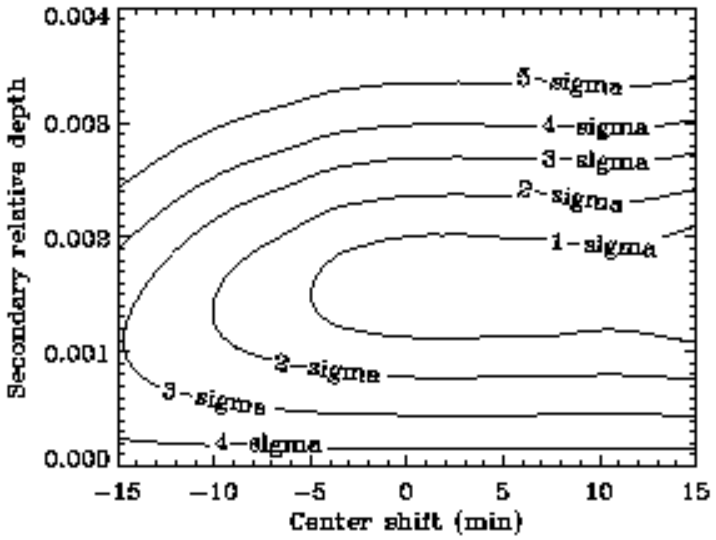

FIGURE 3.16— The χ^2 space for different eclipse center times and depths of CoRoT-2b in the K_s-filter, indicating the 1, 2, 3, 4 and 5-σ confidence limits.

was used to calculate the expected eclipse depth, using Eq. 3.2 and the parameters: R_P=1.465 R_J and R_P = 0.902 $R_\odot$, then for the H-band ($\lambda_c = 1.6\mu$m), an estimated secondary eclipse depth of 0.11 % was obtained, whereas for the K_s-band ($\lambda_c = 2.2\mu$m) the estimated depth is 0.23 %. Comparing these depths with the results of the observations presented here, then for the H-band the the 3-σ upper limit is consistent with the estimated one and, similarly in the K_s-band, the best fitted depth of 0.16 $\pm$ 0.05 % is consistent with 0.23 %.

3.6 Primary transit observations of GJ 436b

GJ 436b (Butler et al., 2004) was the first Neptune mass exoplanet discovered by means of radial velocity measurements. The planet orbits its M2.5 host star (V=10.68 mag.) with a period of 2.6 days. During the year 2004, no transits could be found on this system, but a transit was first detected in 2007 by Gillon et al. (2007b) indicating that the orbital parameters of this planet are changing. A further high-precision primary transit light curve with Spitzer at the 8 μm band was obtained by Gillon et al. (2007a), which allowed precise parameter estimates of the system.
Ribas et al. (2008) proposed a possible second 4.8 $M_\oplus$ planet GJ436c with a

5.2 d orbit, for two reasons: A) No transit was reported in the discovery paper (Butler et al., 2004). B) Radial velocity residuals permitted to solve the Keplerian orbit of GJ 436 for more than one planet. In order to confirm, discard or at least put limits on this proposed planet a primary transit of GJ 436b in the IR wavelength range was observed with my participation, using the CST during the night of March 8, 2008. The H filter and the detector CAIN-II was used. The resulting light curve, after applying the image analysis procedure outlined in Sect. 3.3, is shown in Fig. 3.17, which has been published by Alonso et al. (2008a).

One of the predicted effects of a further planet with similar characteristics

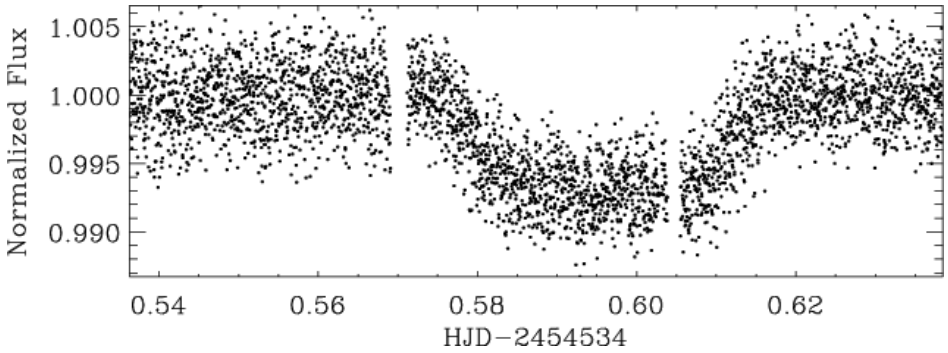

FIGURE 3.17— Normalized primary transit light curve of GJ 436 on the night of Mar. 8, 2008, observed with the CTS using the H-filter. The dispersion of the data out of transit phases is 0.0023, with a median sampling of 2.35 s.

as that proposed by Ribas et al. (2008) is a variation of the orbital inclination of GJ 436b, which could generate an observable variation in the duration and depth of the transit. Therefore, the observed transit was compared with one obtained by Spitzer at 8 μm on Jun. 29, 2007 (Gillon et al., 2007a). However, measuring the absolute orbital inclination using transits is a challenging task, due to the effects of uncertainties on the limb darkening coefficients and the possible effects of active regions on the star. A simpler approach consists of measuring the relative inclination changes of the same object by a more precise determination of the total transit duration, under the assumption that the radii ratio of the planet and star stays constant.

The CST data were first grouped into bins with a width of $\sim$0.00012 in phase, corresponding to $\sim$27 s (Fig. 3.18). The errors of this light curve were estimated as the standard dispersion of the points inside each bin, divided by the square root of the number of points inside that bin. For the transit modelling, the formalism of Giménez (2006a) was used. This formalism is also valid for eccentric

orbits, as is the case of GJ 436b. The best fit was found by a minimization of the χ^2 by applying the AMOEBA algorithm (Press et al., 1992). The free fitting parameters were k, the ratio of the radii of the planet and the star, θ_1 the phase of transit ingress in the reference system as defined by Gimenez & Garcia-Pelayo (1983), the inclination i and the limb darkening coefficients u_+ and u_-, assuming a linear limb darkening law.

To estimate the errors of each of the fitted parameters, 100 fits in different sets of light curves were performed. Each set was constructed by subtracting the best-fit model, shifting circularly the vectors of the residuals and their errors by a random number, and again adding the best-fit model. This bootstrapping procedure allowed for the identification of possible low-frequency structures of the residuals due to uncorrected systematic effects.

The solution that provided the best fit is presented in Table 3.5. The fitted limb darkening coefficients are in good agreement with the values reported by Claret (2000) for a star with $T_{\rm eff} = 3\,500$ K and $\log g = 4.5$. Finally, a difference in orbital inclination of Δi_{obs} of $0.02 \pm 0.04^\circ$ between this observation (i=86.78°) and the published Spitzer observation (i=86.54°) was obtained, or $0.03 \pm 0.05^\circ$ yr^{-1}, if one assumes that Δi_{obs} behaves linearly in these timescales. Also, no significant transit time variation (TTV) was found. Both, the low Δi_{obs} and the absence of significant TTV argue strongly against the proposed low-mass planet by Ribas et al. (2008). Further attempts to observe primary transits with the CTS during Spring 2009 failed due to bad weather at the Teide Observatory.

TABLE 3.5— Best fit parameters and associated 1-σ errors.

Parameter	Value	Error
θ	0.00801	0.00008
k	0.0841	0.0011
i [deg.]	86.78	0.21
u_+	0.43	0.17
u_-	-0.69	0.13

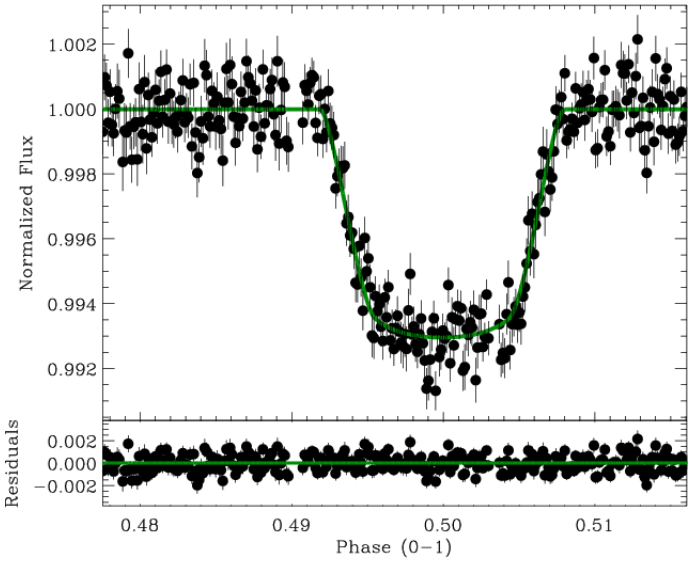

FIGURE 3.18— TCS H-band phased light curve of GJ 436 and best-fit model (green line), and the residuals from the best-fit model (bottom). The bin size corresponds to ∼27 s, and the 1-sigma error bars have been estimated from the dispersion of the points inside each bin. The standard deviation of the residuals is 0.00077.

3.7 Discussion

Primary transit and secondary eclipse observations in the IR are a powerful tool to analyze the characteristics of transiting planetary systems. The main advantage of primary transit observations in the IR is that they are less affected by limb-darkening. This can be seen in Figs. 3.6 and 3.7 for HD 189 733b primary transits and in Figs. 3.2, 3.17 and 3.18 for GJ 436b primary transits, noting the flat transit bottom and edged ingress/egress phases. This permits more precise transit timing and transit duration estimates than in the visual wavelength range, since the timing errors in high-precision transit observations are dominated by the uncertainties in limb darkening.
The low depth of the secondary eclipses (below 1 %) makes it necessary to obtain high-precision time series observations in order to detect them and to estimate their parameters, like eclipse depth, duration and timing. From these parameters, one can estimate physical properties of the system which are only accessible by secondary eclipse observations. For example, the eclipse depth is a direct measurement of the planet's emission and one can compare the expected depth, based on theoretical atmosphere models, with the observed one and confirm or point out problems in the modelling or derive constraints on the heat distribution across the planet. Differences between primary mid-transit times and secondary mid-eclipse times may constrain the eccentricity of planetary orbits better than radial velocity measurements.
In the case of HD 189 733b I showed that the primary transit and secondary eclipse observations are consistent with others from the literature, namely the primary transit depth in K_s is 2.39 % and the 2-σ upper limit for a secondary eclipse is 0.057 %. I estimated the zero-albedo equilibrium temperature to be T_{eq}=1 534 K and based on this temperature; I obtained an expected secondary eclipse depth of 0.03 %.
For CoRoT-2b, a 3-σ upper limit of 0.17 % on the secondary eclipse depth in H-band was established and a tentative secondary eclipse of 0.16 $\pm$ 0.05 % was detected in K_s filter. The zero-albedo effective temperature of the planet was estimated to be T_{eq}=1964 K. This temperature implies an expected secondary eclipse depth in H-band of 0.11 % and in K_s-band of 0.23 %. Both are consistent with the observation.
Against the proposed 4.8 $M_\oplus$ planet in a 5.2 d orbit (Ribas et al., 2008) in the system GJ 436 argue the small difference in inclination of $\Delta i_{obs} = 0.02 \pm 0.04°$ between two observations and the absence of significant TTV. IR primary transit observations from ground and from space allowed to put higher constraints on a prediction of GJ 436c. This work was published by Alonso et al. (2008a).
In conclusion, I have shown in this chapter the procedure and application of

primary transit and secondary eclipse observations in the IR wavelength range. An observing protocol of defocussed imaging that avoids the 'dithering' common in IR observations was established that led to some of the best-quality ground-based near-IR time-series obtained to date. I showed the advantages of transit observations in the IR over the visible wavelength range on examples like HD 189 733b and GJ 436b. I also showed the possibility to observe secondary eclipses from ground in the IR wavelength range on HD 189 733b and CoRoT-2b, which helped to constrain the eccentricity and to compare the observed secondary eclipse depth with the predicted one.

4

A cool starspot or a second transiting planet in the TrES-1 system?

Here, I investigate the origin of flux increases found during a transit of TrES-1, observed with the HST (Hubble Space Telescope) and the IAC80 telescope. These features cannot be attributed to noise and are supposedly dark areas on the stellar surface of the host star eclipsed by TrES-1 during its transits. I investigate the likelihood of two possible hypotheses for its origin: Starspots or a second transiting planet. The research described in this chapter has been published as Rabus et al. 2009 in Astronomy and Astrophysics, Volume 494, Issue 1, pp.391-397.

4.1 Introduction

TrES-1 was the first planet transiting a bright star that was discovered by a wide-field survey (Alonso et al., 2004b), and it has become a frequently observed and well characterized exoplanet. It orbits a bright K0V star with a period of 3.03 days and with an apparent magnitude of V=11.79, approximately 157 pc away from us. A detailed light curve analysis allowed Winn et al. (2007) to lower the errors of the star/planet parameters. Charbonneau et al. (2005) obtained the first direct detection of light emitted from an exoplanet using the Spitzer Space Telescope by an observation of the TrES-1 secondary eclipse. Sozzetti et al. (2004, 2006) analyzed the chemical composition of the host star and compared it with other known planet-hosting stars. They found no chemical peculiarity compared to the other stars.
With the aim of acquiring a very precise transit light curve of TrES-1, our group observed several transit events with the Hubble Space Telescope (GO-

10441) in the year 2005. The most relevant finding has been a flux increase during one transit, which is clearly a feature coming from the TrES-1 system itself, for a preliminary description see Charbonneau et al. (2007). Coverage of many other transits events was obtained between 2004 and 2007 with the IAC 80-cm telescope (IAC80). The motivation for these observations was for one a long-term study of transit-timing variations, but also as a follow-up of the HST observations.

Both on TrES-1 (Charbonneau et al., 2007) and on other systems (HD 209 458, by Silva 2003 based on data from Deeg et al. 2001; HD 189 733 by Pont et al. 2007), there have been reports of potential stellar spots detected from flux-rises during planetary transits. In starspots, intense magnetic fields can suppress the convection of heat to the surface, and hence, that area will radiate less light, causing a dark area on the stellar surface. Starspots could cover up to 55 % of the stellar surface (O'Neal et al., 1998) and are generally 500 to 2 000 K cooler than the surrounding area. The possibility to detect these during transits was first discussed by Silva (2003). Their simulations showed that a starspot fully or partly occulted by the transiting planet leaves a short brightness increase in the light curve of a transit. The flux variation feature from a starspot depends on two parameters: Its duration depends on the transit path-length across the spot and across the stellar surface, on the rotational velocity of the parent star, and on the projected orbital speed of the transiting planet. The ratio of transit path-lengths may be interpreted in first order, assuming a central impact, as an area ratio between spot and the transiting planet (Silva, 2003). The feature's amplitude for another, depends on the temperature difference between the normal stellar surface and the spot as well as on the fraction of the planet's shadow that grazes over the spot, unless the projected planet comes to lie fully within the starspot, in which case only the temperatures are relevant.

For example, Pont et al. (2007) found clear evidence of starspots on the star HD 189 733 by observing a transit of its planet with the HST at a high signal-to-noise ratio. They found an increase in flux of 0.001 mags and attributed this to the planet occulting a starspot. On TrES-1, there has been a previous ground-based search for spots during transits by Winn et al. (2007) with negative results. They gave an upper 2 σ limit for spots of $f < 4 \times 10^{-4}$, where f is the product of area ratio and the intensity contrast.

In this chapter, I will present a second hypothesis for the origin of the short flux-rise observed with the HST, occurring if two planets transit simultaneously, and one of the planets occults the other: In a system of two transiting planets with different orbits, the known one has a short period (planet A) and the hypothetical other one has a much longer period (planet B). Assuming that the transit of the short-period planet, i. e. planet A, is being observed and that

the centers of both transits coincide more or less in time, then planet B can be considered as moving slowly across the stellar disc. When planet A is eclipsing planet B; it is causing in this moment a flux increase in the combined transit light curve. Due to the short observation span, the ingress and egress of the much longer transit events of planet B might neither have been observed nor detected, see Fig. 4.6 for an arbitrary example light curve. For a light curve of two transiting planets, the flux variation depends on the area ratio and on the impact parameter between both planets, whereas the duration depends on the area ratio and on the respective orbital velocities of both planets.
In Sect. 4.2 the HST and IAC80 observations and data reductions will be described. An increase in flux in one HST transit observation was identified. Diagnostics to differentiate between the two origins of the flux rise are presented in Sect. 4.3, where its color dependency from red to blue will be evaluated and then the flux variability of the other IAC80 light curves will be investigated. A discussion of the results will take place in Sect. 4.4.

4.2 Observations and data reduction

Table 4.1 gives an overview of the observations, where I did the IAC80 observations. The epochs refer to the planetary orbit; for the calculated mid-transit times I used the ephemeris from Alonso et al. (2004b), $T_c = 2\,453\,186.8060 + 3.030065 \times \mathrm{Epoch}$. Partial transits were observed in three 'visits' by the HST on Nov. 19 2004, Jan. 19 2005 and March 29 2005. These observations followed the protocol established by Brown et al. (2001), where a complete transit light curve is obtained from phased overlay of data from several short 'visits' of the transiting system during slightly different phases. This phasing is necessary to overcome the interruptions due to Earth's occultation of the HST. For these HST observations the ACS/HRC instrument with the grism G800L was used. Spectra in the wavelength range between 5 794 Å and 10 251 Å were collected. The exposure time was 95 s.
Analysis of the HST images started with the pipeline-calibrated data, which subtracts zero point offset (based on over-scan mean), a two-dimensional bias and a dark (scaled by the exposure time) image. A wavelength dependent flat field, appropriate to position along the dispersion direction, has been derived by fitting a quadratic polynomial in wavelength to the eight broad-band flats over a range from 435 to 850 nm. A global sky level is computed by taking the median within a large region offset from the first order spectrum; this sky level was then subtracted from the images. A total of 20 bad pixels (out of an extraction box totaling 10 700 pixels) were flagged as bad and linearly inter-

polated over, before proceeding. Cosmic rays are eliminated by sigma-clipping over stacks of 108 images on a per pixel basis, taking into account fluctuations of the flux, which are correlated with minor x-y image motions and changes of the focus. The pointing offsets in x and y are evaluated by taking first moments of the (nearly point source) zeroth order image, and focus changes are tracked by fitting Gaussians in cross-dispersion along the spectrum and averaging them. For photometry summing over the whole first order spectrum sums are taken out to an isophote, at which the per image counts (in a mean image) have fallen to 220 electrons (compared to a peak of 108 000). Sums in 500 Å bins use the same cross-dispersion limits, and contiguous blocks of columns most closely matching the desired ranges are formed. In addition a smaller bin of about 62 Å wide is formed at H-α.
Summation over the full spectrum results in total counts of about 4.5×10^7 electrons per exposure. Normalisation is done by taking the mean over all points in orbits 2 and 5 and dividing by this. This sum spans wavelengths from 5 392 to 10 650 Å. Similar normalisations are applied separately to the wavelength restricted bin time series. De-correlations are performed by evaluating a linear least-squares fit to points outside the transit as a function of x-y offsets, the cross-dispersion spectrum width and the time to remove any linear trends in each visit. The resulting function is evaluated at all points including inside the transit and then divided out. Our final scatter in the time series of individual 500 Å bands is increased by about 9 % over the sum of Poisson and readout noise. Any residual band-to-band correlated noise must be relatively small given the close approach to being Poisson noise limited.
I gathered at eleven nights between 2004 and 2007, rapid cadence photometry of TrES-1 transits with the IAC80 telescope at the Observatorio del Teide, Spain. I did all observations in the Johnson R filter. In the first two years, a camera with a 1k × 1k CCD was used, whereas in 2006, it was replaced by a camera with a 2k × 2k chip. The pixel scale of this new CCD is 0.305 ″, resulting in a field-of-view of 10.25 × 10.25 ′. Out of the eleven IAC80 transit observations, I only used the seven that cover full transit events for further investigations.

TABLE 4.1— Observing log.

Day of observation	Epoch	Calculated mid-transit time HJD-2 450 000	Telescope and instrument	Filter	Cadence [s]	Standard deviation off-transit part [mmags]
19. Nov. 04	47	3 329.2191	HST-ACS/HRC	G800L	130	0.18
19. Jan. 05	67	3 389.8204	HST-ACS/HRC	G800L	130	0.18
29. Mar. 05	90	3 459.5119	HST-ACS/HRC	G800L	130	0.18
10. Jul. 05	124	3 562.5341	IAC80 old CCD	R	57	1.9
16. Jul. 05	126	3 568.5942	IAC80 old CCD	R	97	1.8
08. Aug. 06	254	3 956.4425	IAC80 new CCD	R	79	1.0
11. Aug. 06	255	3 959.4726	IAC80 new CCD	R	80	1.4
16. Jun. 07	357	4 268.5392	IAC80 new CCD	R	70	1.5
19. Jun. 07	358	4 271.5693	IAC80 new CCD	R	60	1.7
22. Jun. 07	359	4 274.5993	IAC80 new CCD	R	70	1.7

I calibrated the images of each night using standard IRAF procedures and carried out aperture photometry with `VAPHOT` (Deeg & Doyle, 2001) on the target and on five to eight comparison stars of similar brightness within the same CCD frame. In `VAPHOT`, differential photometry is obtained by dividing the target flux by the reference flux, which was constructed from a weighted ensemble of comparison stars. The flux was then converted into magnitudes. Finally, I corrected for differential extinction by subtracting a parabolic fit to the off-transit parts of each individual light curve and estimated the photometric error using the standard deviation outside the transit, see Table 4.1. Figure 4.1 shows the transit light curves of TrES-1 observed with the IAC80.

By visually inspecting the phased HST light curve (see Fig. 4.2), one can identify an increase in flux during the transit on the night of November 19, 2004. The feature has a height of 2.7 mmags, whereas the standard deviation out of transit is 0.18 mmags. Hence, this feature cannot be attributed to noise. The feature also is highly unlikely to be caused by instrumental effects. No correlated variations in x-y pointing or focus are present at the time of the flux rise, i. e. nothing suggestive of an instrumental effect. During the several HST orbits, outside of the transit no features similar to this have been seen. The short flux increase during the TrES-1 transit is $\sim$ 10 min. long. This correspond to 1/15 of the whole transit of TrES-1. This kind of flux increase can occur when TrES-1, during the transit, passes over a darker area on the stellar surface.

4.3 Analysis of the observed flux rise

The two hypotheses I presented previously (e. g. that the darker patch is caused by a) a cooler starspot or b) a second transiting planet), would differ in the following:

- A starspot should show a flux-rise with a wavelength dependency, with a higher flux rise in the blue than in the red wavelength range. A flux rise from a mutual planet-planet occultation should not have any significant wavelength dependency.

- A starspot is a temporary phenomena on time-scales of weeks to months; spots appear and disappear with different sizes at different positions. The planet-planet occultation would be a very rare event, except if the two planets are in a resonant orbit.

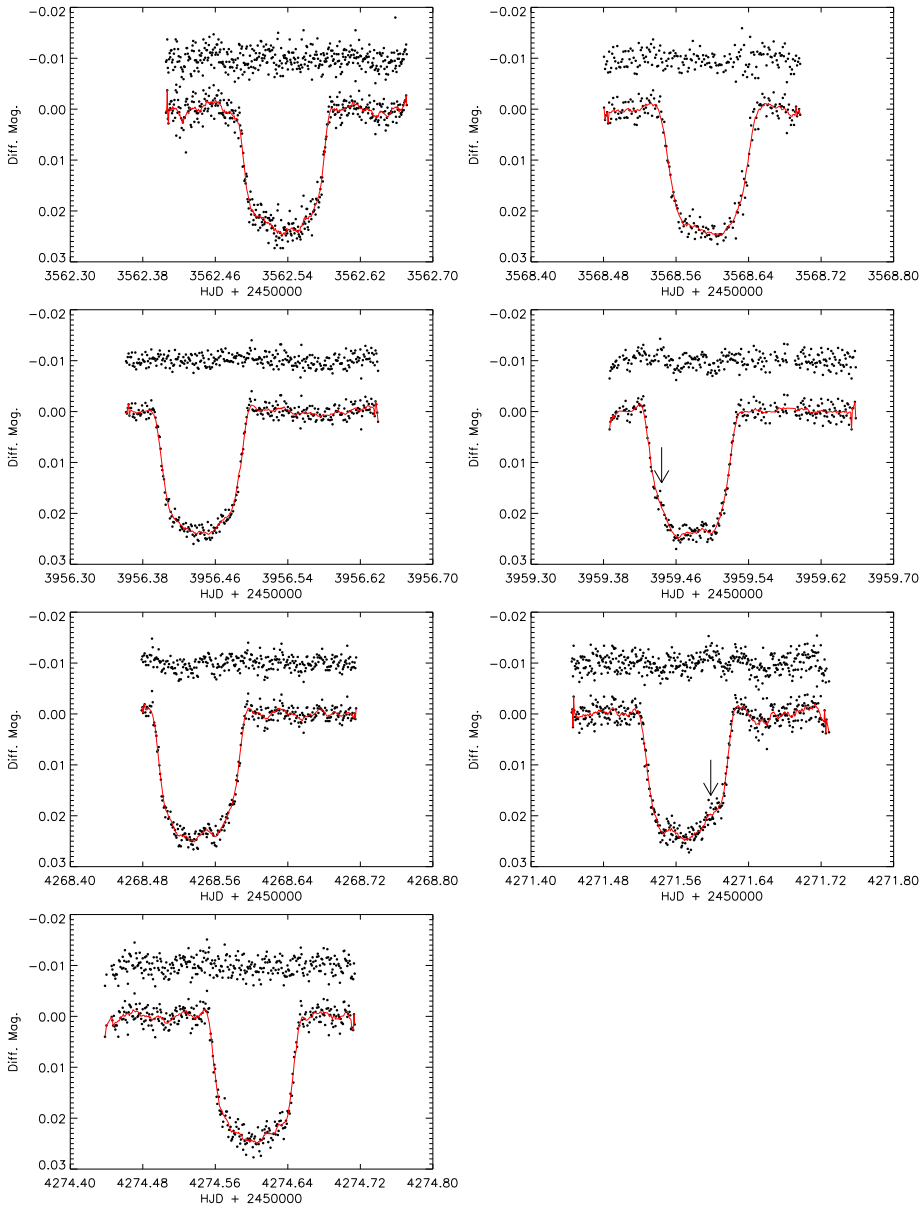

FIGURE 4.1— Corresponding to Table 4.1, IAC80 observations of TrES-1 transits. The upper light curve is after subtracting a common transit model of TrES-1. The lower curve shows the observed light curve with the solid (red) line being a boxcar smoothing and the arrows indicating possible low significance detection of similar flux rises as seen in the HST data.

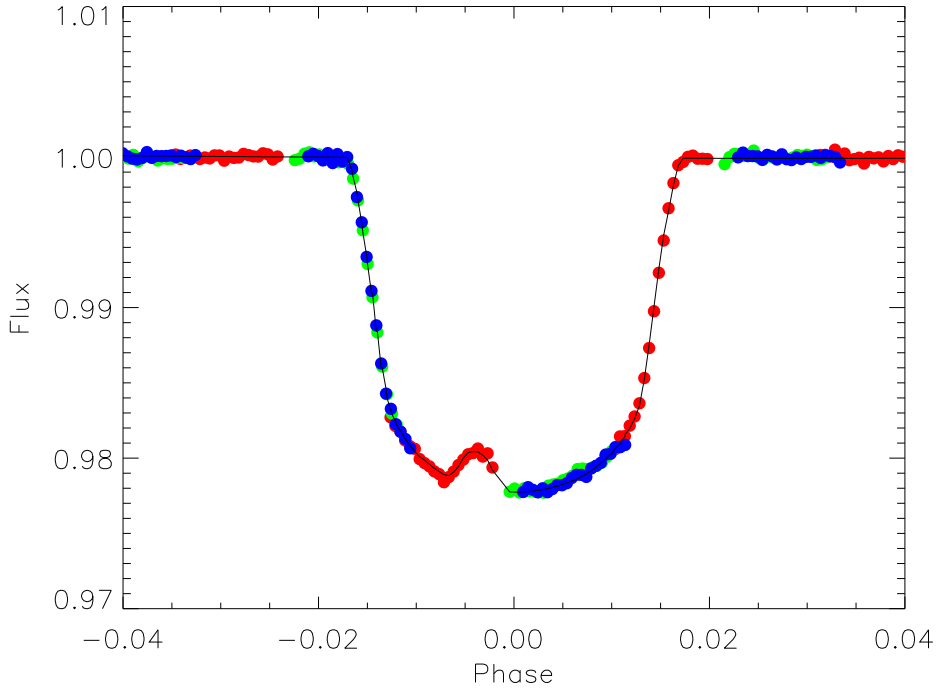

FIGURE 4.2— Phased light curve of all three HST visits using the first order spectrum, each color represents a different day, i. e. red corresponds to November 19, 2004 , green to January 19, 2005 and blue to March 29, 2005. A flux increase is seen in the transit light curve on November 19, 2004. The black solid line is an example of a model for a simultaneous transit of TrES-1 and an arbitrary second transiting planet using UTM (see text Sect. 4.4). In this example, the second planet has an arbitrary period of 300 days and radius of 4.25 $R_{\oplus}$. A nearly grazing impact between TrES-1 and the second planet was simulated.

In the following, I checked, whether there is any wavelength dependency of the flux rise feature during the transit of TrES-1. To this end, I created a HST transit light curve model by using the phased light curve of all three first order spectra HST observations and assigning a zero statistical weight to the data points of the feature, i. e. I did not consider the flux rise for the following modelling. For transit modelling I used the FORTRAN routines from Giménez (2006a) and the simplex-downhill fitting algorithm (Press et al., 1992), minimizing χ^2. The free parameters were the ratio between the stellar and planetary radii, $k = R_p/R_*$, the sum of the projected radii, $rr = (R_*/a) + (R_p/a)$, and the limb darkening coefficient u_1 and u_2. Next, I used the color bins of the HST grism spectra to fit the limb darkening coefficient in each wavelength bin, keeping rr and k constant, as obtained by the best fit of the first order spectra. The residuals are plotted in Fig. 4.3.

I used the model-subtracted light curves to estimate the slope of the flux increase in each wavelength bin, following the procedure by Pont et al. (2007), see Fig. 4.3 and then normalized the estimated slopes with the slope estimated from the summed light curve. Figure 4.4 shows the estimated normalized slopes for each wavelength bin and their corresponding error bars. The slope in the H-α bin is a little higher; if real, this would indicate that TrES-1 occults a H-α rich region during transit. However, the light curve in H-α is also noisier and its error bars are higher, indicating that its higher slope might not be real. The slope of the bin with the central wavelength of 7 750 Å is lower, but this can be attributed to a single outlier. Also, the bin centered at 10 251 Å has high error bars due to a noisier light curve.

I used the above estimated slope values to fit twice a linear polynomial of the form $y = A + B\lambda$ to them, where λ is the central wavelength of the bin and y the normalized slope. In the first fit, I fitted for both parameters, A and B, and in the second one, I kept B at zero and fitted for A only. The first case indicates a wavelength dependency, the second case indicates a wavelength independence of the flux rise. For the first case I obtained a reduced χ^2 of 2.8 and for the latter case a reduced χ^2 of 2.3. After applying the F-test, I found that there is no significant difference between both hypotheses, wavelength dependency and independence, within a 5 % confidence interval.

Furthermore, I used the IAC80 data to check whether these observations contain the same or similar features of flux-rises during transit. However, the IAC80 observations are noisier and hence, similar features cannot be seen as easily as in the case of the HST light curve. Therefore, I created a best-fit model for the transits from the IAC80 observations, using the same approach as before, and then I subtracted the respective model from the observations. Then I used the flux rise event of the HST light curve as a template and applied a matched

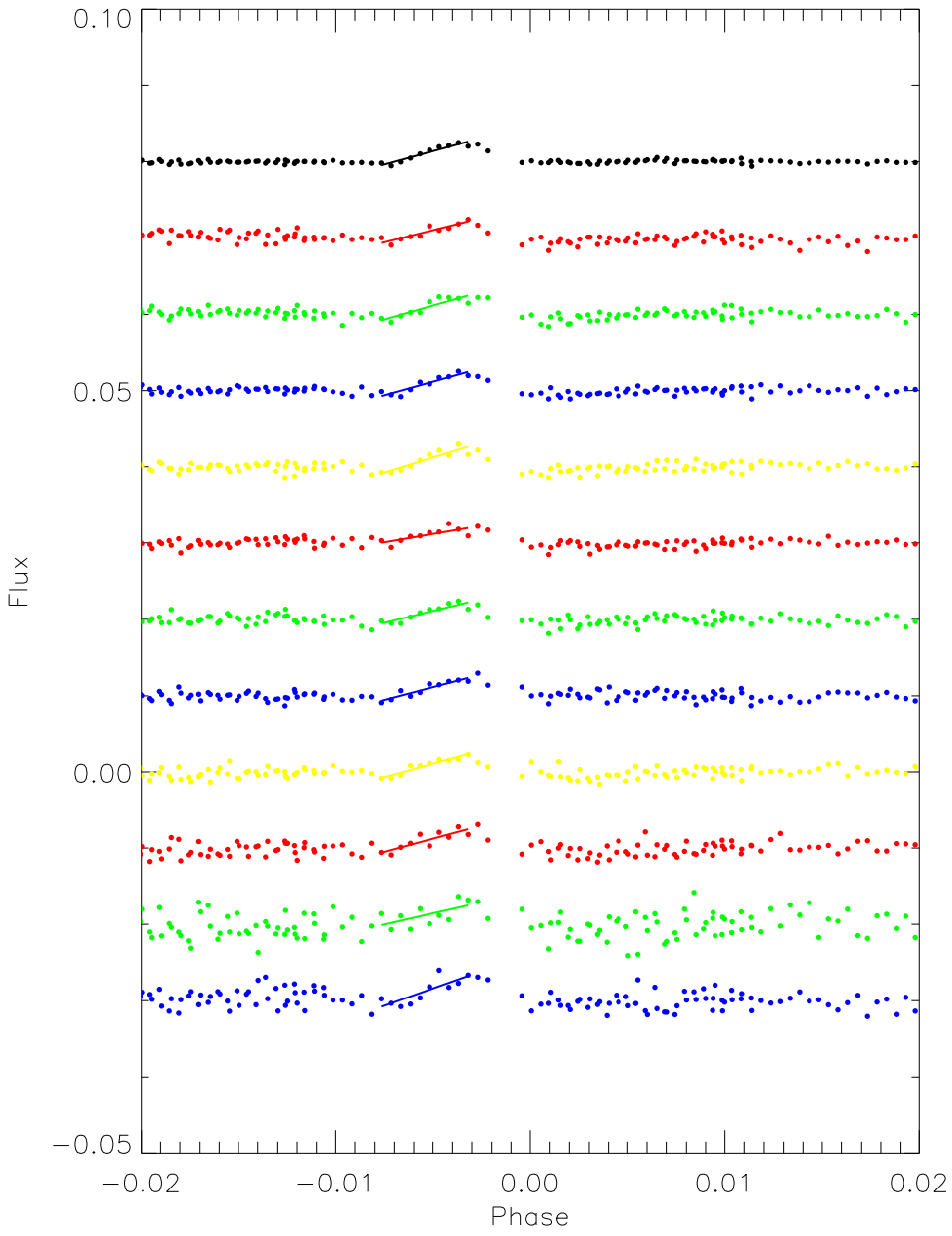

FIGURE 4.3— Phased light curve of all HST observations with the best-fit transit model subtracted. At the top is the sum over all wavelengths. The short inclined solid lines indicate the slope that was fitted to the flux rise. From the bottom to the top are the light curves in the bins with central wavelength of H-α, 10 251, 9 753, 9 247, 8 745, 8 245, 7 750, 7 260, 6 762, 6 250, 5 790 Å.

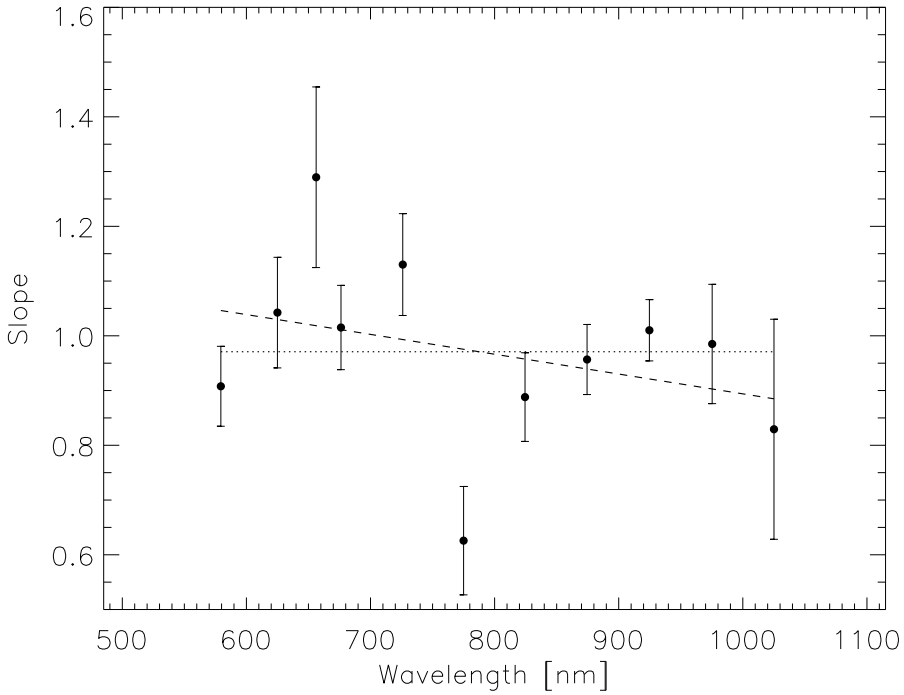

FIGURE 4.4— Values of normalized fitted slopes for the flux rise in each wavelength bin and corresponding error bars. The dashed line is a two parameter linear fit and the dotted line a one parameter linear fit. The two parameter linear fit indicates a wavelength dependency and the one parameter fit a independence.

filter detection against this event to the model-subtracted IAC80 observations as follows: I shifted the template in time along the model-subtracted IAC80 light curves, fitting in each shift for $M_{\rm fit} = M_{\rm HST} * f$, where $M_{\rm HST}$ is the magnitude of the template and f is a multiplication factor, which is also the fitting parameter. The cadence of the HST observations is lower than of the IAC80 and, hence, the template is interpolated, using a spline interpolation. The best fit for f over time can be seen on the left side in Fig. 4.5 and a histogram of f is shown on the right side. In the histograms, the value of f should concentrate around 0 if there are no features, while a value close to 1 may mean a detection of a similar feature than observed with HST. Taking the off-transit standard deviation of f with ~ 0.27 into account, I considered values of $f \geq 0.8$ as candidates for the detection of such a feature. Inspecting the histograms in Fig. 4.5, I identified two low significant events on HJD-245 000 = 3 959.41 and 4 271.60. These events are also indicated with arrows in Figs. 4.1 and 4.5. However, the IAC80 data is too noise to provide a firm detection.

4.4 Discussion and Conclusions

Transits of TrES-1 in 2004 and 2005 were observed with the HST and an intriguing flux rise during one transit was identified. In addition, I followed-up transits of TrES-1 during the years 2004 to 2007 from the ground, finding two more possible flux rises, and I used the color information in the HST data to assess the origin of this feature. I can identify two possible causes, one is the possibility of a circular starspot occulted by TrES-1 during transit and the other is the detection of a second smaller transiting planet in an orbit larger than TrES-1.

I obtained a good fit for the feature's shape by using a circular dark patch on the stellar surface and neglecting deformation of a circular disc due to projection on a sphere. Assuming in addition that the dark patch and TrES-1 have a central impact on each other and using the orbital velocity for TrES-1 of $v = 140$ km/s, then, in a time interval of 10 min., TrES-1 crosses 84 000 km, which gives a lower limit for the diameter of the occulted patch. The real diameter depends on the stellar rotation (for the starspot hypothesis) or on the orbital velocities of the transiting planets (for the planet-planet hypothesis).

The host star of TrES-1 is an active star (Sozzetti et al., 2004) which is favouring the spot scenario. In that case, first the spot radius was calculated. Since the parent star of TrES-1 is slowly rotating with a rotational velocity of $I_{\rm S} = 1.08$ km/s (Laughlin et al., 2005), corresponding to a rotation period of 38.4 days, the stellar rotation can be neglected and under the assumption of a

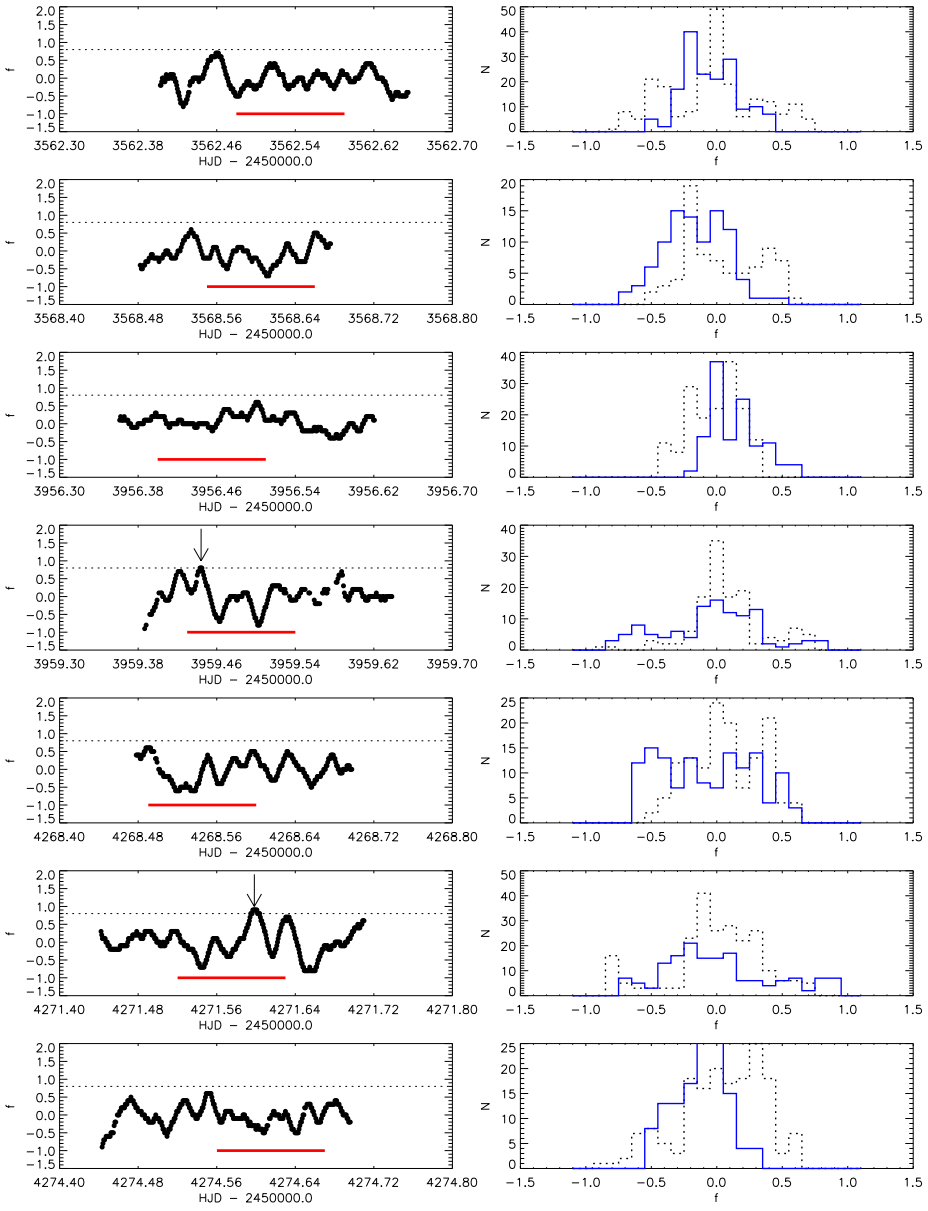

FIGURE 4.5— Left side: Best-fit f for each transit, where f is a multiplication factor of a model template, see text in Sect. 4.3. The solid (red) lines below indicate the duration of the transit of TrES-1, the vertical dotted black lines indicate the threshold value of 0.8 and the arrows indicate a possible low-significance detection of a similar feature in the IAC80 data. Right side: Histograms of f. The dotted lines give histograms for the out-of-transit part, the solid (blue) lines represent histograms of the transit part.

central impact between TrES-1 and spot, the spot radius is simply half the diameter as obtained previously, i. e. 42 000 km. An effective temperature of the stellar surface of 5 250 K was obtained by Sozzetti et al. (2004) and combined with the equation 1 given by Silva (2003), the spot temperature was estimated to be approximately 4 690 K for a starspot with the radius of 42 000 km. These values are perfectly reasonable for a large sunspot.

To generate a realistic model that shows that the observed HST transit light curve might as well arise from two occulting planets, I used "Universal Transit Modeller" (UTM, Deeg 2008). UTM is an IDL-routine permitting one simulations of transit light curves of multiple bodies, including rings and moons, and the fitting of observed light curves. First I fitted the summed HST light curve without considering the flux rise part. As fit parameters I used the radii of the host star and of the planet TrES-1, respectively; the limb darkening coefficient, assuming a quadratic limb darkening law, the inclination and the distance. Then I used the best-fit parameters and introduced a second transiting planet, but in an expanded orbit. However, one lacks the determination of a unique period for the putative second transiting planet due to the singularity of the observed event and there is no significant evidence in the IAC80 data to derive a period.

Hence, I can only give as an example a model of two transiting planets, see Figs. 4.2 and 4.6. Figure 4.6 shows a complete example model, including ingress and egress of an arbitrary putative second planet. The introduced second planet has an arbitrary period of 300 days and radius of 4.25 $R_{\oplus}$. Its transit duration is 10 hours and the depth is 2.7 mmags. It is very unlikely that a complete transit of this second planet would have been observed, because the transit duration is too long for nightly observations and it is even more difficult to keep a sufficient high photometric precision from ground over such a long time span due to changing atmosphere, extinction and airmass. All IAC80 observations were done in time spans shorter than 10 hours and even under ideal conditions, i. e. at low airmass, the differential photometry applied to the transit observations did not correct completely for extinction. Therefore, as noted in Sect. 4.2, I corrected the extinction by subtracting a second order polynomial fit from the observed light curves which removed all possible hints to a second planet's transit from the light curve's off-transit part.

Whereas a mutual occultation would be an extremely rare event, limits for the presence of transits from a second planet can be derived from size-estimates of this planet. Its minimum size can be obtained from the amplitude of the mutual transit event and assuming that TrES-1 and the other planet have a central impact on each other. In this case, the flux increase is directly related to the area of overlap of the projection of the two planets into the star, and is

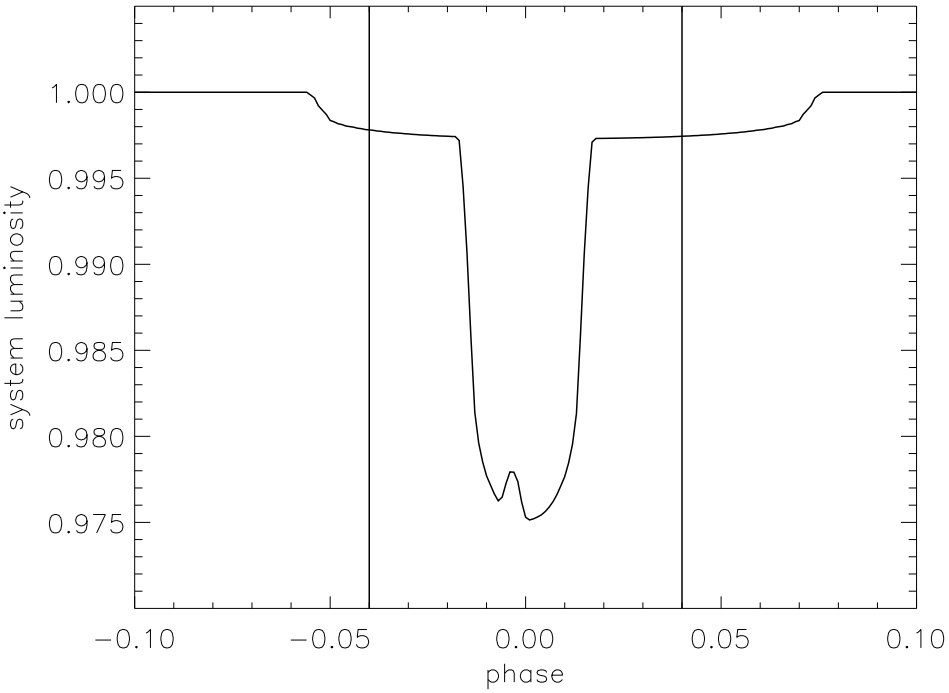

FIGURE 4.6— Example of the same planet-planet transit model as shown in Fig. 4.2, for TrES-1 and an arbitrary additional transiting planet, but showing the model over longer time span, so that the ingress and egress of a possible second planet are visible. The vertical solid lines indicate the usual observation span of 6 hours centered at the mid-transit of TrES-1. Noting that during this 6 hours time span the apparent transit depth of TrES-1 is identical with or without a second planet.

independent of the period. For TrES-1, I obtained a transit depth of 23 mmags and the flux rise height is 2.7 mmags, and hence I get an area of overlap of 1/8.5 of the cross section of TrES-1. Knowing the radius of TrES-1, 1.081 R_J (Winn et al., 2007), I obtained a minimum size of a second planet of 0.37 R_J. However, the shape of the flux rise indicates a more grazing impact between TrES-1 and the hypothetical second planet, favouring a bigger radius.

The original STARE and PSST data of the field where TrES-1 has been discovered cover a time span of 96 days (Alonso et al., 2004b). This is a time span long enough to possibly detect a putative second planet on a longer orbit, but no transit has been detected in this data. Therefore, based on an assumption of a standard deviation of 10 mmags in the TrES-1 discovery data, I can set an upper limit for the size of a possible second planet. In the limiting case, a transit with a depth of 10 mmags would not have been detected. This 10 mmags corresponds to a transit depth of a planet with a radius of 0.72 R_J, which constitutes an upper detection limit for the radius of a possible second planet.

For a putative long-period outer planet and due to the limited and gaped observations of the TrES-1 field the detection depends mostly on the probability of having observed a transit. Therefore, I constraint the period range in which this upper radius limit is valid and applied a statistical analysis to a time vector which contains the time of observation. For this analysis, I established 2 000 trial periods between a period of 4 days and 100 days on the STARE/PSST discovery data. Within each trial period 300 epochs were set randomly and tested how often one could recover a transit signal. I set a detection limit for a possible planet at periods where the recovery rate drops below 95 %. For the original STARE and PSST data this occurs at a period of 10.5 days. Hence, for periods of less than 10.5 days, I can set an upper limit for the radius of 0.72 R_J for a possible second planet. However, larger planets in longer periods are possible.

Based on the conventional interpretation of flux-rise features during transits, one may conclude that a starspot has been detected in the HST data, whereas the ground-based IAC80 data is inconclusive to provide a firm detection and I can only give two star spot event candidates. I presented an alternative hypothesis of a mutual planet-planet occultation, which would be a rare but not impossible event. The verification or exclusion of this hypothesis is difficult unless a wavelength-dependency of the flux-rise features can be demonstrated, or until the presence of the second planet can either be verified or excluded, be it from observations of its own transits or from radial velocity measurements.

5

Transit timing analysis of the exoplanets TrES-1 and TrES-2

The aim of this chapter is a detailed analysis of the transit light curves of TrES-1 and TrES-2 over a period of three to four years, in order to search for variabilities in observed mid-transit times and to set limits for the presence of additional third bodies. The research described in this chapter has been submitted by Rabus et al. to Astronomy and Astrophysics.

5.1 Introduction

In 1992, the first exoplanets around the pulsar PSR B1257+12 were discovered by detecting anomalies in the pulsation period (Wolszczan & Frail, 1992). Similarly, by studying variations in the time of transit occurrence, transiting exoplanets give another possibility to find additional companions, even down to Earth masses. There are different mechanisms causing these variations. For one the gravitational influence of a perturbing body can alter the orbital period of the transiting planet (Holman & Murray, 2005; Agol et al., 2005). This effect is particularly sensitive to detect additional bodies in mean-motion resonances with the transiting planet or to detect moons around that planet. For another, a perturbing mass in an orbit larger than the transiting planet can cause the "star - transiting planet" system to wobble around the barycenter and alter the observed periodicity, something that is known as the light-time effect (Irwin, 1959; Schneider & Doyle, 1995; Doyle & Deeg, 2004; Schneider, 2005). These anomalies are reflected in the times of the transit occurrence. Hence, using a linear ephemeris and several observations of transits, it is possible to get the difference 'O-C' between the observed transit times and the calculated ones

from the ephemeris. From this difference one can learn about perturbations on strict orbital periodicity due to a possible companion object which has not been detected yet.
Motivated by the possible detection of low-mass companions around transiting planets, we started a long-term campaign to observe transits of the exoplanets TrES-1 (Alonso et al., 2004b) and TrES-2 (O'Donovan et al., 2006) over several years. Here I present the results of our observations and a study of the transit timing variations that were found.
Searches for planet-mass objects from the light time effect were first proposed for low-mass eclipsing binaries by Doyle et al. (1998) and have been performed in-depth on the system CM-Draconis, with ambiguous results to date (Deeg et al., 2000, 2008; Morales et al., 2009). They were soon followed by several studies of timing effects in transiting planet systems: TrES-1 (Steffen & Agol, 2005), HD 189 733 (Miller-Ricci et al., 2008a), HD 209 458 (Agol & Steffen, 2007; Miller-Ricci et al., 2008b), GJ 436 (Alonso et al., 2008a; Bean & Seifahrt, 2008) and for CoRoT-1b (Bean, 2009). In all cases the authors could only constrain the parameters of a potential second planet.
The first search for variability in the transit times of TrES-1 was conducted by Steffen & Agol (2005). They fitted perturbing planets in different orbits, using transit timing observations from Charbonneau et al. (2005). Steffen & Agol (2005) did not find any strong evidence of a third object. Winn et al. (2007) observed three additional transits of TrES-1; they found that the transit times of these three observations occurred progressively later. However, as mentioned by the authors, these three measurements were not enough to make any firm conclusions. Recently, Raetz et al. (2009b) reported a transit timing analysis of TrES-1 with the only result of being an improved ephemeris. Previous studies of transit timings for TrES-2 have been performed by Holman et al. (2007) and Raetz et al. (2009a), neither finding evidence for an unseen perturbing planet. Very recently Mislis & Schmitt (2009) analysed transit time durations between 2006 and 2008, indicating a possible change of inclination.
In Section 5.2 I describe the procedure to fit our observations to a transit model and to obtain the observed mid-transit times and their error estimates. These values are then used in Section 5.3 to interpret the O-C diagram by means of different models. Finally I discuss the results in Section 5.4.

5.2 Light curve fitting

I performed most of the observations reported here with the IAC 80cm telescope (IAC80) at the Teide Observatory, Tenerife. I used the same observing

and analysis procedure for both TrES-1 and TrES-2. For further investigation described here, I only used observations where a complete transit light curve was acquired. A detailed description of the analysis leading from the telescope images to the light curves can be found in Rabus et al. (2009), where a study of flux variations during transits due to starspots or additional transiting planets for TrES-1 was presented. I decorrelated the light curves against the airmass by subtracting a quadratic polynomial fit. Due to a slight defocusing of the telescope during observations, the centroids are not well defined and decorrelation against the target's detector position is not applicable. However, the de-focusing and spread of the flux over several pixels will lower the noise correlated with the target's detector position.

For TrES-1 I obtained eight useful transit observations (Table 5.2) over a period of three years and for TrES-2 five observations (Table 5.3) over a period of two years. In order to measure the observed mid-transit times, I first created a template of the transit event from a folding in phase and by binning (6-point bins, with a mean size of 66 s for TrES-1 and 90 s for TrES-2) of all observations of the respective transiting planet (Figure 5.1). The standard deviations inside the individual bins were ~ 1.63 mmag for TrES-1 and ~ 1.79 mmag for TrES-2, whereas the standard deviation outside the transit part of the binned light curve is 0.7 mmag for TrES-1 and 0.8 mmag for TrES-2.

I used these phased and binned light curves to create a model of the transit light curve, using the formalism from Giménez (2006a) and the simplex-downhill fitting algorithm (Press et al., 1992). I fitted for the planetary and stellar radii ratio, k, the sum of the projected radii, rr, and orbital inclination, i, while I kept the eccentricity fixed at zero and the limb darkening coefficient fixed, as obtained by the tables of Claret et al. (1995), assuming quadratic coefficients. The best-fit models are plotted over phased data in Fig. 5.1 and the best-fit parameters are shown in Table 5.1. One can see that our light curve model parameters are consistent with the parameters from Southworth (2008) for both TrES-1 and TrES-2.

I then shifted in time my model with the fixed best-fit parameters against each individual observed light curve and calculated the χ^2 residuals for each shift. The fit with the minimum χ^2 value gave me the observed mid-transit time. I estimated the timing error within a 68 % (1-σ) confidence interval of the χ^2 values, given by the range where the χ^2 residuals increases by 1 over the minimum value. I also calculated the timing precision of each individual light curve, δ_t, by propagating their respective photometric precision, δ_L, using the equation

(Doyle & Deeg, 2004):

$$\delta_t = \delta_L \left[\sum_i^N \left(\frac{L(t_{i-1}) - L(t_{i+1})}{2\Delta t} \right)^2 \right]^{-\frac{1}{2}}, \tag{5.1}$$

where $L(t_i)$ is the stellar brightness at t_i, Δt is the cadence and the sum goes over all brightness values within the eclipse event. Comparing the estimated error, based on the 1-σ interval, with the error calculated using Equation 5.1, I found a good agreement; both error values are indicated in Tables 5.2 and 5.3. Generally the estimated 1-σ errors are higher than the propagated errors, but in four cases the error based on the 68 % confidence interval were lower. My timing errors are possibly underestimated due to correlated noise. However, I do not modify them in order to stay consistent with the timing measurements and associated errors that I took from the literature.

Finally I subtracted the observed mid-transit times from the calculated ones,

TABLE 5.1— Comparison between best-fit values of this work and parameters from Southworth (2008) for transit light curve models of TrES-1 (upper values) and TrES-2 (lower values).

Parameter	This work	Southworth (2008)
TrES-1		
k	0.1350	0.1381 ± 0.0014
rr	0.1104	0.1097 ± 0.0022
i [°]	88.67	88.67 ± 0.71
TrES-2		
k	0.1260	0.1268 ± 0.0032
rr	0.1462	0.1460 ± 0.0042
i [°]	83.70	83.71 ± 0.42

obtaining the O-C values. The calculated mid-transit times for TrES-1 were obtained from the ephemeris $T_c = 2\,453\,186.8060 + 3.0300737\times$ Epoch (Winn et al., 2007) and for TrES-2 I used $T_c = 2\,453\,957.6348 + 2.470621\times$ Epoch (Holman et al., 2007).

In the following transit timing analysis I included several published mid-transit observations, by Charbonneau et al. (2005), Winn et al. (2007) and Hrudková et al. (2009) for TrES-1 (Table 5.2), and for TrES-2 by Holman et al. (2007) (Table 5.3). I considered only O-C times with errors below 60 sec, which led to the rejection of some O-C values from Charbonneau et al. (2005). In the O-C residuals of TrES-1 I also removed two outliers at Epoch 255 and 358 which have been identified by Rabus et al. (2009) as transits with possible starspots.

TABLE 5.2— Overview of TrES-1 transits used in this work.

Epoch	observed transit time HJD-2 450 000	O-C [s]	1-σ error [s]	Calculated timing precision [s]	Source
-4	3174.6864	60	35	-	1
-1	3183.7752	-63	43	-	1
0	3186.8061	9	26	-	1
20	3247.4075	2	35	-	1
124	3562.5352	14	20	13	2
126	3568.5952	-6	22	25	2
234	3895.8430	-24	16	-	3
235	3898.8734	8	12	-	3
236	3901.9037	28	16	-	3
254	3956.4445	-15	14	20	2
255	3959.4760	107	17	23	2
357	4268.5418	-44	14	17	2
358	4271.5716	-66	17	16	2
359	4274.6028	32	18	17	2
386	4356.4142	-24	9	-	4
387	4359.4443	-18	13	-	4
388	4362.4742	-31	17	-	4
490	4671.5412	-56	26	29	2

Sources: 1) Charbonneau et al. (2005), 2) This work, 3) Winn et al. (2007), 4) Hrudková et al. (2009)

TABLE 5.3— Same as Table 5.2, for TrES-2.

Epoch	observed transit time HJD-2 450 000	O-C [s]	1-σ error [s]	Calculated timing precision [s]	Source
4	3967.5180	92	37	22	1
13	3989.7529	0	25	-	2
15	3994.6939	-15	27	-	2
34	4041.6358	-10	26	-	2
140	4303.5209	-72	26	20	1
142	4308.4613	-169	39	22	1
274	4634.5828	-184	26	24	1
276	4639.5232	-257	27	21	1

Sources: 1) this work, 2) Holman et al. (2007)

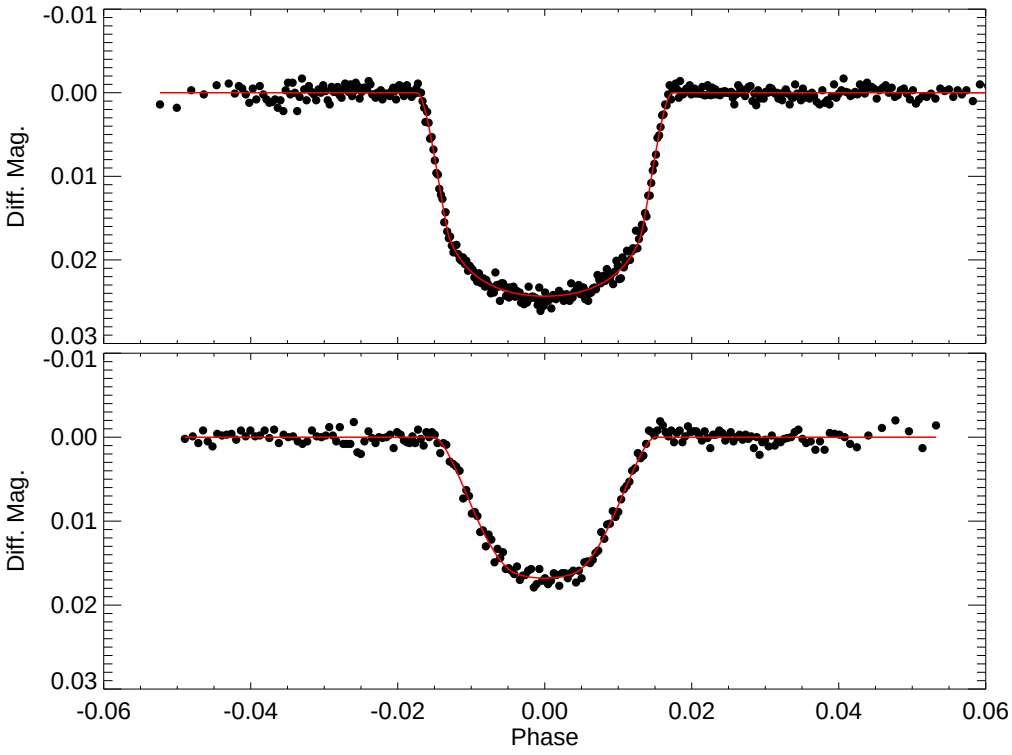

FIGURE 5.1— Phased and binned light curve of all IAC80 observations of TrES-1 (top) and TrES-2 (bottom) transits with the solid (red) line being the best-fit model light curve.

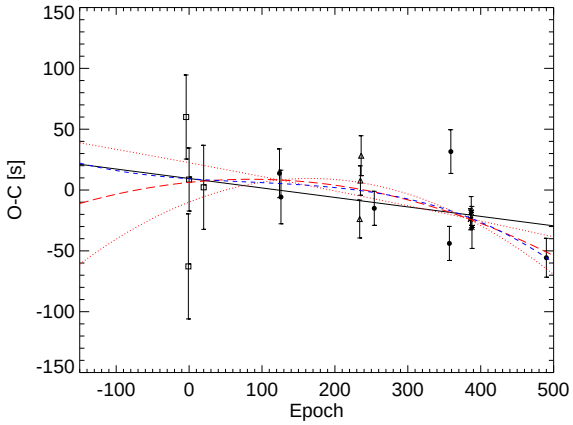

FIGURE 5.2— Difference between calculated (based on ephemeris from Winn et al. (2007)) and observed mid-transit times for TrES-1. Filled dots are O-C values obtained with the IAC80, squares are taken from Charbonneau et al. (2005), triangles from Winn et al. (2007) and asterisk are from Hrudková et al. (2009). The lines show different polynomial fits, where the solid black line indicates a linear fit, the long-dashed (red) line a quadratic and the short-dashed (blue) line a cubic polynomial. The dotted (red) lines show the fits corresponding to the variation of the quadratic term within 1-σ confidence limits.

Several further transit times of TrES-1 and TrES-2 were recently reported by Raetz et al. (2009a,b), respectively, and for TrES-2 by Mislis & Schmitt (2009), but I did not include these in my study, since they had individual errors and an internal scatter several times larger than the rest of data included in this study. The transit mid-time corresponding to Epoch 0 of TrES-2, reported by O'Donovan et al. (2006) has also been removed due to its high error of >60 s. I obtained for TrES-1 an O-C diagram spanning four years, with 16 points (Figure 5.2) and for TrES-2 a diagram spanning two years, with 8 points (Figure 5.3).

5.3 Transit timing analysis

Two mechanisms have been brought forward that may cause deviations of transit times from strict periodicity. For one the light time effect and for another the influence of a third body on the transiting planet's intrinsic periodicity.

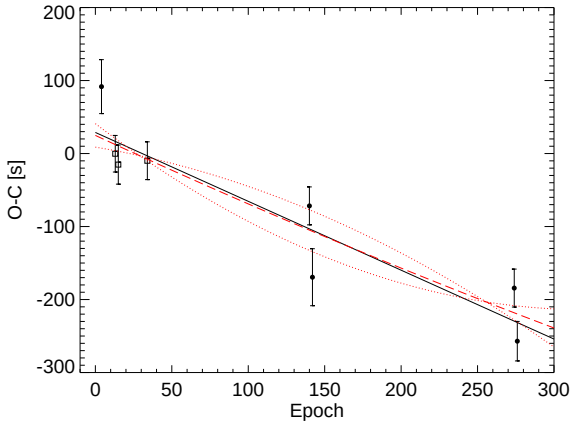

FIGURE 5.3— Similar as Figure 5.2 (based on ephemeris from Holman et al. (2007)) including only polynomials fits and corresponding 1-σ confidence limits, but for TrES-2. Filled dots are O-C values obtained with the IAC80 and squares are taken from Holman et al. (2007).

5.3.1 Search for the light time effect

I first consider the light time effect, where the barycenter of the binary system, in my case the system "star - transiting planet", is offset against the barycenter formed by an additional third body. This will cause the light to travel a longer or shorter distance to the observer and hence the observer will see a different period, where the intrinsic period is unknown.
For the analysis of the O-C times, I fitted three polynomials of different orders to the O-C values, namely a linear, $OC_{fit} = \kappa_0 + E\kappa_1$, a parabolic, $OC_{fit} = \kappa_0 + E\kappa_1 + E^2\kappa_2$, and a cubic polynomial, $OC_{fit} = \kappa_0 + E\kappa_1 + E^2\kappa_2 + E^3\kappa_3$, where E is the Epoch number and κ the fitted polynomial coefficients. I also analyzed the case of fixed original ephemeris ($OC_{fit} = 0$) and the case of maintaining the original period and fitting only for a constant offset in O-C ($OC_{fit} = \kappa_0$). Table 5.4 shows the obtained best fit coefficient for TrES-1 and TrES-2 respectively, and Figs. 5.2 and 5.3 show a plot of the respective polynomials. In order to quantify the improvement of the different fits, I calculated the False Alarm Probability (FAP), which is the significance level of the fit quality improvement and indicates the probability of making a type I error. Therefore, I first calculated the F-values according to equation:

$$F = \frac{(\chi_1^2 - \chi_2^2)/(\nu_1 - \nu_2)}{(\chi_2^2/\nu_2)}, \tag{5.2}$$

where χ_1^2 are residuals from the lower order fit, χ_2^2 are residuals from the higher order fit, and $\nu_{1,2}$ are the corresponding degrees of freedom (Table 5.4). I then used the F-value to calculate the significance using the IDL-routine `MPFTEST` from the Markwardt IDL library, which gives the probability for a value drawn from the F-distribution to equal or exceed the given F-value. For TrES-1, FAPs were calculated against the original ephemeris, against the offset-only case and against the linear polynomial. One can see that the original ephemeris is unlikely to be the best solution with the linear and quadratic fits being the most likely descriptions, having low χ^2 residuals and a low FAP. For TrES-2 a linear trend in the O-C residuals (Fig. 5.3) is apparent. The statistical analysis shows no clear preference between a linear or a quadratic polynomial (Table 5.4). The distribution of the observations of TrES-2 into three groups, acting as pivot points, does not support fits of orders higher than the quadratic one. Therefore, I fitted no cubic polynomial to the TrES-2 data.
As for the linear coefficients κ_0 and κ_1 these are without relevant physical meaning, but indicate a slightly different ephemeris than used, where κ_0 is an offset of the mid-transit time at epoch 0 and κ_1 a correction to the period of the ephemeris. However, one can give a physical meaning to the quadratic coefficient. The quadratic term (κ_2), gives the system's acceleration along the line of sight by using the equation (Deeg et al., 2008):

$$a_{\parallel} = 2\frac{c\kappa_2}{P^2}, \tag{5.3}$$

where c is the speed of light and P is the observed period.
In order to estimate the error of the quadratic term, I stepped through different values of κ_2, fitting for κ_0 and κ_1. The κ_2 values which increased the best-fit χ^2 residuals by 2.3 gave the 1-σ confidence limits (see Table 5.4); dotted lines in Figs. 5.2 and 5.3 show the corresponding fits at these limits. My best fit parabola model for TrES-1 gave a quadratic term of $\kappa_2 = -3.6 \pm 3.4 \times 10^{-4}$ s. Solving Eq. 5.3 I obtained an acceleration of $a_{\parallel} = -3.2 \pm 3.0 \times 10^{-6}$ m s^{-2} and $\frac{a_{\parallel}}{c} = -1.1 \pm 1.0 \times 10^{-14}$ s^{-1}. The cubic term κ_3 would indicate a constant change in acceleration; however the cubic fit is also less likely than the quadratic one and will not be further discussed.
For the quadratic solution of TrES-2 I obtained a best-fit value of κ_2 smaller than its error. This high error is consistent with a low significance of the quadratic solution, therefore I support the linear case, with a 1-σ upper limit for accelerations of $a_{\parallel} \leq 3.2 \times 10^{-5}$ m s^{-2}.
Considering the clear linear trend of O-C times in Figs. 5.2 and 5.3, and using the coefficients from the linear fit, I indicate here an improved ephemeris for

TrES-1, given by:

$$T_c = 2\,453\,186.80611(16) + 3.0300728(6) \times \text{Epoch}, \tag{5.4}$$

where the values in parenthesis give the uncertainty in the last two digits and for TrES-2:

$$T_c = 2\,453\,957.63512(28) + 2.4706101(18) \times \text{Epoch}. \tag{5.5}$$

5.3.2 Search for a perturbation of the intrinsic period

The other cause for transit timing variations could be a perturbation of the intrinsic planet period P' due to the gravitational influence of a third body on the transiting planet. Regarding such perturbations, there exist no analytical equations that describe the gravitational influence on a transiting planet due to an undetected third body. Generally, N-body simulations are used, iterating over a large orbital parameter space for a maximum possible mass range, see e. g. Holman & Murray (2005); Steffen & Agol (2005); Agol et al. (2005); Agol & Steffen (2007); Miller-Ricci et al. (2008b,a); Nesvorný & Morbidelli (2008).
In order to find the parameter space of third bodies compatible with the observed transit times, I created a numerical 2-dimensional simulation of a three body system by integrating over the equations of motion. I considered the problem in two dimensions, assuming that the orbits of the exoplanetary system and its respective perturber are co-aligned. I further considered the problem in an helio-centric frame, with the star in the center of the coordinate system, meaning that I neglect the light-time effect in this context. To integrate the equation of motion I used the Burlisch-Stoer algorithm (Press et al., 1992) with a 1 second time step and an accuracy of 10^{-10}.
I considered the problem for an inner and an outer perturber separately and neglected the 1:1 mean motion resonance (MMR). Each simulation started with a perturber 0.005 AU away from the transiting planet, with an initial zero eccentricity and with a phase shift towards the transiting planets between 0° and 315° in steps of 45°. I advanced the simulations in orbital steps of 0.001 AU and used 100 mass steps from 1 $M_\oplus$ to 100 $M_\oplus$ for the perturbing object. I simulated 1000 transits, corresponding to approximately eight years coverage for TrES-1 and seven years coverage for TrES-2. I used a mass of 0.61 M_J for TrES-1 and a mass of 0.88 $M_\odot$ for its host star (Torres et al., 2008), and a mass of 1.2 M_J for TrES-2 and 0.98 $M_\odot$ for its host star (Sozzetti et al., 2007). After obtaining the simulated O-C diagrams, I applied a Fourier transformation to the synthetic O-C diagrams (Miller-Ricci et al., 2008b,a) and derived the maximum obtained O-C amplitudes as a function of the perturber's semi-major

axis; showing them for masses of 10, 20 and 40 $M_\oplus$ in Fig. 5.4, where also the MMRs are indicated by vertical lines. Figs. 5.5 and 5.6 show some examples of synthetic O-C diagrams for TrES-1.

To establish potential third body orbital parameters, I fitted for each perturber distance the observed O-C diagram to all synthetic ones that had been generated for masses of 1 - 100 $M_\oplus$. I left three parameters open in the fits: one parameter to shift the O-C diagrams in Epoch, corresponding to the best moment for the first real observation (E=0) within the simulated data, and two parameters describing linear deviations between simulated and modelled O-C diagrams, which have no relevant physical meaning.

In order to calculate an upper mass limit above which I can reject perturber masses due to a high increase in χ^2, I first set a χ^2 threshold corresponding to a 90 % FAP against the linear fit. I then increased the masses for each semi-major axis until the χ^2 residuals reached the previously established thresholds, the masses at the threshold gave me the upper mass limit. Masses above the threshold can be rejected with a FAP higher than 90 %(Fig. 5.7). One can see a general trend to higher masses for perturbers closer to the host star and at larger semi-major axis, and one can also identify the mean-motion resonances, where the best fit for a consistent perturber indicates lower masses (vertical lines in Fig. 5.7). At larger orbits for the perturber, the best-fit perturber's mass increases and it increases more steeply for TrES-2 than for TrES-1. This is due to TrES-2 having a higher mass than TrES-1 and being closer to the central star. The high χ^2 peaks at the 2:3 and 2:1 MMRs for TrES-1 reveal that a >1 $M_\oplus$ planet in that configuration might have been detected in our data set.

Again, in order to quantify the improvement of the simulated O-C fits in the lower MMRs and the best-fit simulated O-C against the linear polynomial, I calculate the FAPs. In these cases it is better not to use Eq. 5.2 to calculate the F-value, since this equation is better suited for cases where one expects small changes for additional parameters, whereas for the simulated O-C values, I expect big changes. Therefore, I used $F = \frac{(\chi_1^2/\nu_1)}{(\chi_2^2/\nu_2)}$ to calculate the F-value for the `MPFTEST`-routine. In Table 5.4, I show the χ^2 and FAPs for some special cases of our simulated O-C values.

For TrES-1 I found that most of the χ^2 values for the simulated O-C models were below the one of the linear fit, but based on the available data, I can exclude the cases of 2:3 and 2:1 MMRs for planets more massive than 1 $M_\oplus$ with high FAPs. I found a best-fit for a perturber with a mass of 2 $M_\oplus$ and a semi-major axis of 0.05 AU, but this peak is not outstandingly low. Similarly, for TrES-2, all χ^2 values for the O-C models are below the one from the linear

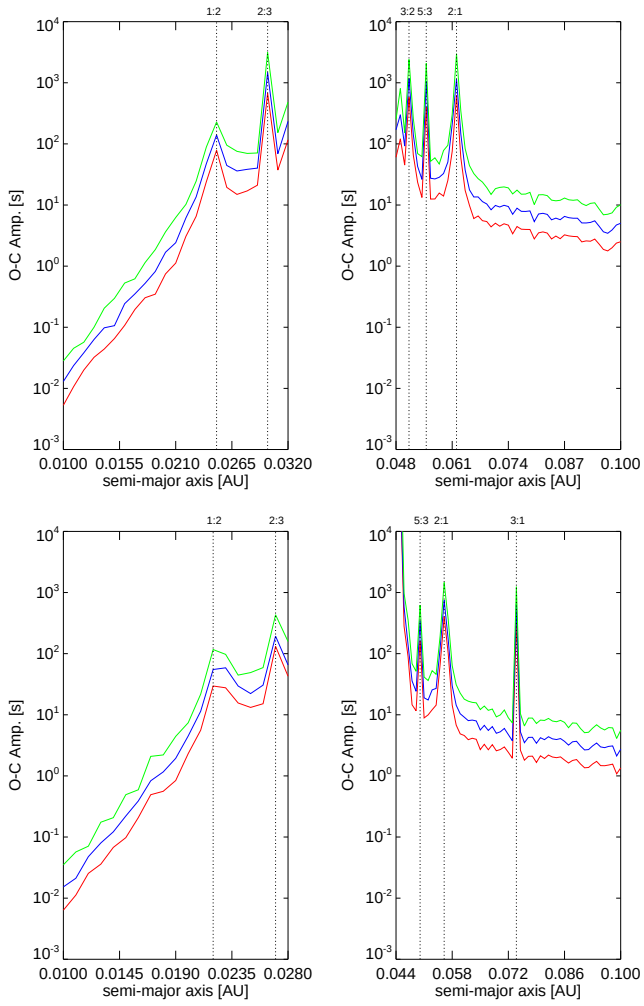

FIGURE 5.4— Maximum O-C amplitudes of a 2 dimensional N-body simulation for the system TrES-1 (upper two panels) and TrES-2 (lower two panels) due to a perturber during 1000 transits plotted against the semi-major axes of the perturber. The colored solid lines correspond to different perturbing masses, namely 10 $M_\oplus$ (red), 20 $M_\oplus$ (blue) and 40 $M_\oplus$ (green). Left side: inner perturber, right side: outer perturber. Vertical lines indicate the MMR.

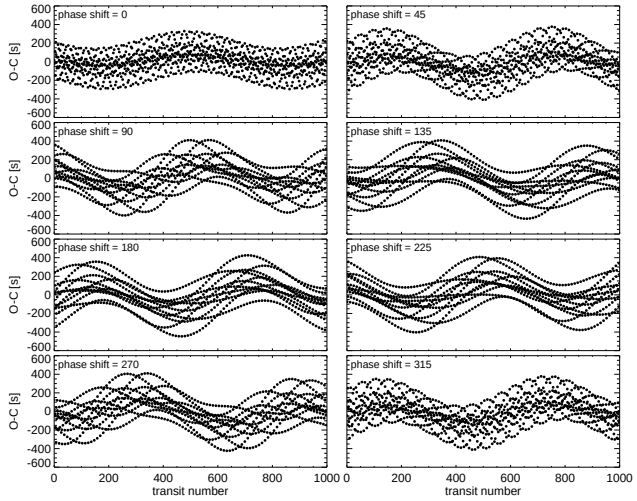

FIGURE 5.5— Example synthetic O-C diagrams for TrES-1 and a perturber of 30 $M_{\oplus}$ at 0.053 AU and with different phase shifts between them. Note that the appearance of several lines is due to an aliasing effect between consecutive transits. For a given transit number there is only one O-C time.

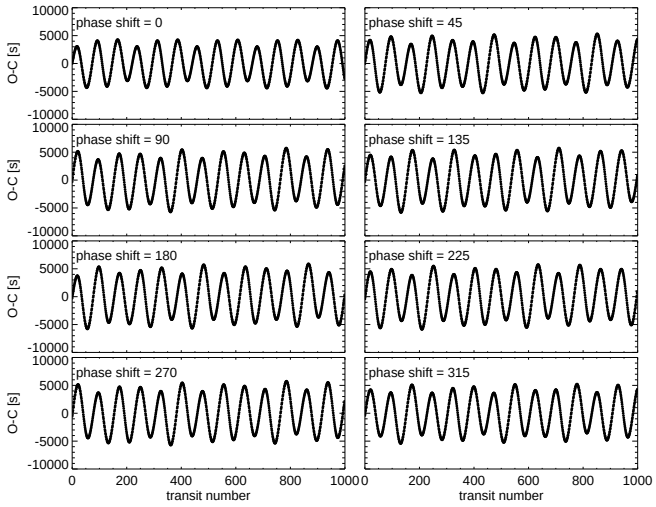

FIGURE 5.6— Same as Fig. 5.5, but for a perturber distance of 0.062 AU (2:1 MMR)

fit. One can identify some low χ^2 peaks, with the lowest at 0.051 AU ($\chi^2 = 0.3$) for a perturbing mass of 18 $M_\oplus$. Fig. 5.8 shows for TrES-2 the O-C simulation for the lowest χ^2 with the observed O-C residuals over-plotted. Given that none of the simulated perturbers indicate a uniquely low χ^2, I do not find support for any of them.

5.3.3 Search for a sinusoidal transit timing variability

In order to search for any sinusoidal periodicity in the data with periods on the order of the campaign duration and shorter, I fitted amplitude and phase of a sinusoidal function to the O-C residuals after subtracting the linear fit with the parameters of Table 5.4. A sinusoidal transit timing variation might be caused by an exomoon around the transiting planet (Sartoretti & Schneider, 1999; Doyle & Deeg, 2004; Simon et al., 2007; Kipping, 2009). For this fit I stepped through different trial periods between 1500 days (6.6×10^{-4} cycl/d) and 0.1 days (10 cycl/d) for TrES-1 and for TrES-2 between 600 days (1.6×10^{-3} cycl/d) and 0.1 days (10 cycl/d) in steps of 0.00001, 0.0001, 0.001, 0.01 and 0.1 cycl/d. For each trial period I then logged the χ^2 residuals at the best fitting amplitude and phase.
From Fig. 5.9, showing the result of the χ^2 sine fit, one can see that we lack outstanding peaks of low χ^2 values for TrES-1 and TrES-2, being it very unlikely that a real sinusoidal signal has more than one period. However, I also calculated the FAPs of the best sinusoidal fit against the linear polynomial, as described in Sect. 5.3.2 and show the results in Table 5.4 for comparison. I note that the best sinusoidal fit for TrES-1 with a period of 16.7 days and an amplitude of 25 s (Fig. 5.10, upper graph) does not give a significant improvement against the linear polynomial, having a lower χ^2 residual but a high FAP, but for TrES-2 I found a good sinusoidal fit with a FAP of 1 % for a period of 0.2 days and an amplitude of 57 s (Fig. 5.10, lower graph).

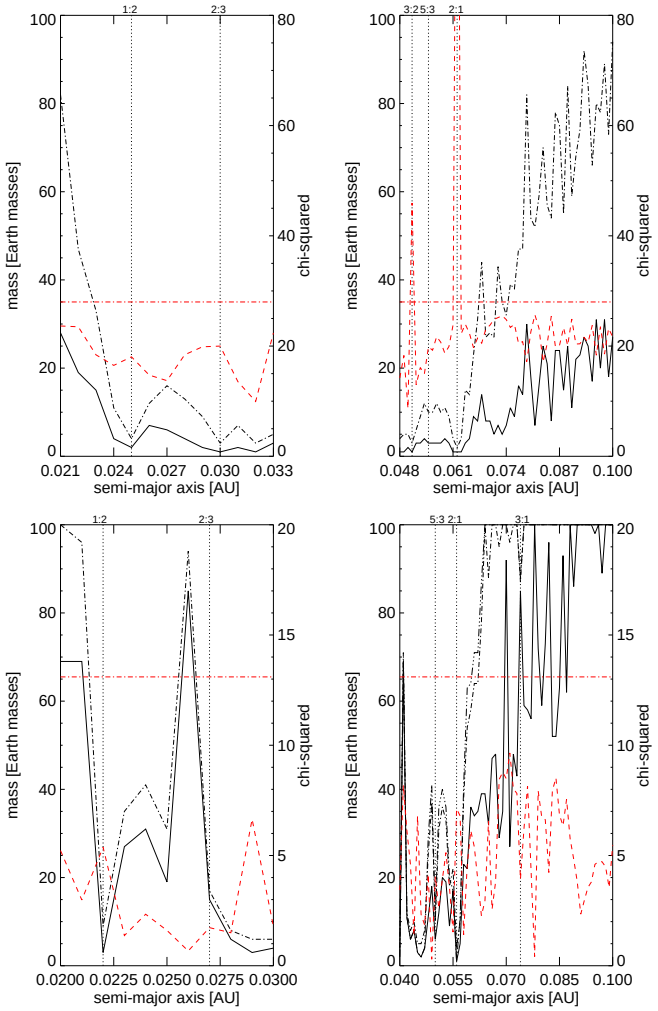

FIGURE 5.7— Masses of third bodies with the lowest χ^2 (solid black line), based on the best fit of the observed O-C values to the synthetic O-C values for each semi-major axis, and upper mass limits resulting in a FAP of 90% (dashed-dotted black line) with respect to the linear fit for each semi-major axis. Red lines show the lowest χ^2 values (dashed red line) corresponding to the best-fit masses and the χ^2 value of the linear fit is indicated by a horizontal dashed-dotted red line. The upper plot is for TrES-1 and the lower plot for TrES-2. Mean motion resonances are indicated by vertical dotted lines.

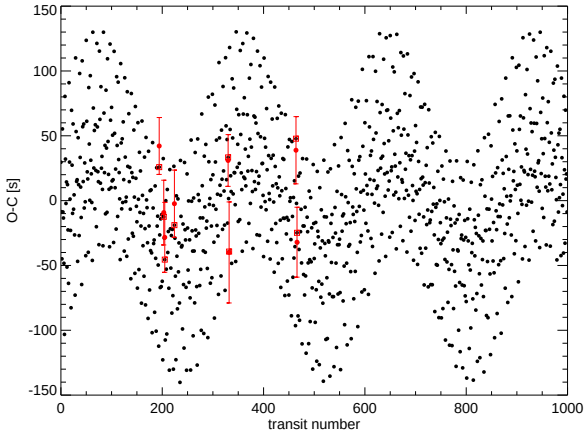

FIGURE 5.8— Simulated O-C diagram of TrES-2 and the best fit perturber with a mass of 18 $M_{\oplus}$ and an orbit of 0.051 AU. The red dots correspond to the observations and the squares to the corresponding simulated O-C values.

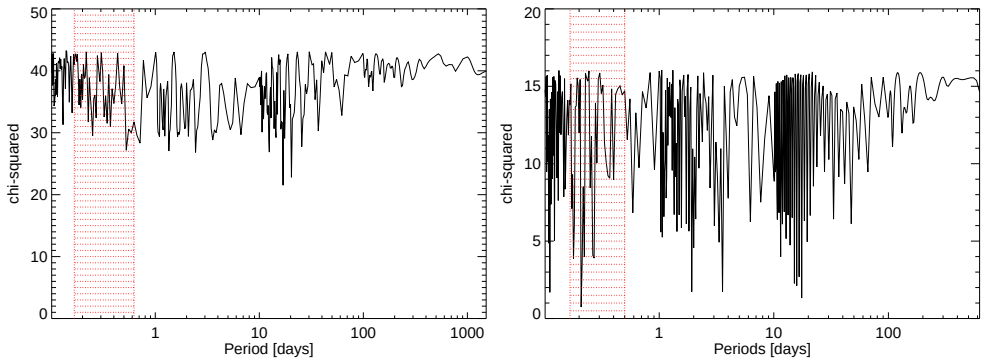

FIGURE 5.9— Results of the χ^2 sine fitting as function of trial frequencies. The red shaded areas show possible frequencies which might have been introduced by a moon. Top: TrES-1, bottom: TrES-2.

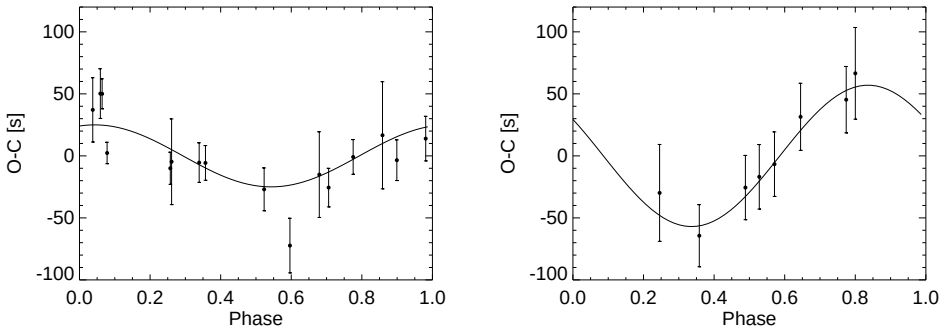

FIGURE 5.10— Best fit sine function (solid line) and observed O-C values with error bars for TrES-1 and TrES-2, phased with period of that fit. This period is 0.06 cycles/day or 16.7 days for TrES-1 and 4.8 cycles/day or 0.21 days for TrES-2.

5.4 Discussion

For TrES-1 I obtained eight new O-C values and made use of 10 previously published values of which I removed two observations with a high probability of containing star spots. The standard deviation of the O-C values is ∼33 s and the maximum O-C deviation from the established ephemeris (Winn et al., 2007) is ∼60 s. Similarly, for TrES-2 I observed five transits and made use of three additional published mid-transit times (Holman et al., 2007). The transit timing estimation at epoch 0 for TrES-2 had an error greater than 60 s and was hence removed. After correcting the ephemeris, the standard deviation of this O-C diagram is ∼43.9 s and the maximum O-C deviation, is 66.5 s.
In order to search for a light time effect, I fitted different polynomials. Assuming the validity of the quadratic function for TrES-1, I can use the quadratic term to estimate a possible acceleration and its corresponding 1-σ error of $\frac{a_\parallel}{c} = -1.1 \pm 1.0 \times 10^{-14}$ s^{-1}, the negative value indicating a decelerating system. Comparing this deceleration to the acceleration for the solar system of a few 10^{-19} s^{-1} (Zakamska & Tremaine, 2005) and CM Draconis of $\sim 10^{-17}$ s^{-1} (Deeg et al., 2008), the acceleration of TrES-1 could be several order of magnitudes larger, but is not well constrained given the current data. Following Deeg et al. (2008), the minimum mass of a third body causing a given acceleration in dependence of its lateral distance $r_\perp$ is given by

$$\frac{m_3}{M_\odot} \geq 438.26 \left(\frac{a_\parallel}{\text{m s}^{-2}}\right) \left(\frac{r_\perp}{\text{AU}}\right)^2 . \tag{5.6}$$

I note that this is independent of the mass of the accelerating system. Using the distance to TrES-1 of 157 pc (Sozzetti et al., 2004) and above value for $a_\parallel$, I obtain the minimum mass of a possible third body as a function of angular separation from TrES-1 of

$$\frac{m_3}{M_\odot} \geq 34 \left(\frac{\theta}{\text{arcsec}}\right)^2 . \tag{5.7}$$

This relation allows the identification of nearby objects found in any future high-resolution imaging; that is, any possibly found object has to fulfill Eq. 5.7 in order to be a potential source of the observed acceleration. For example, for a third object at a distance of 0.05″ the object's mass has to be at least 0.09 M$_\odot$ in order to cause the previously mentioned acceleration ($\frac{a_\parallel}{c} = -1.1 \pm 1.0 \times 10^{-14}$). The angular separation of 0.05″ translates into an orbit for a third object of 7.8 AU, corresponding to a period of 21.8 years. This stellar object would have caused a semi-amplitude in the radial velocity measurements of 1.0 km s^{-1}. However, the observation span of the available radial velocity measurements is

only 49 days (Alonso et al., 2004b; Laughlin et al., 2005), which is 0.6 % of the exemplary third object's period. Therefore, this object would not have been detected in existing radial velocity measurements. This example also shows that the value obtained for the acceleration is reasonable.
A second approach has been to assume the presence of perturbing objects in nearby orbits. For TrES-1, a perturber with a mass >1 $M_\oplus$ at the 2:3 and 2:1 MMRs are very unlikely due to the high χ^2 residual with high FAPs against the linear fit. However, none of the simulated perturbers indicated a uniquely low χ^2 peak. Therefore, I do not find support for any perturber outside the MMRs, but I established upper mass limits above which I would obtain a FAP of 90 %. For TrES-2, I obtained some low χ^2 peaks; none of them in a low-order MMR. For the best-fit simulated O-C I obtained a perturber of 18 $M_\oplus$ and 0.051 AU. Due to the χ^2 residuals below the one from the linear fit, none of the MMRs could be excluded and again I established upper mass limits for perturbers in the TrES-2 system.
Steffen & Agol (2005) did an analysis of transit times of TrES-1, but they found no convincing evidence for a second planet. I also found generally a higher χ^2 near to the low-order MMRs. Steffen & Agol (2005) gave upper limits for additional planets in the system TrES-1, whereas I give additionally the best-fitting mass for any orbital distance. In general, their upper mass limit for additional planets decreases closer to the transiting planet, similar to our findings in Fig. 5.7. I also found that additional planets with masses above 5 $M_\oplus$ at the MMRs are very unlikely, which is consistent with the results from Steffen & Agol (2005), indicating that at the low-order MMRs and near zero eccentricity, the mass of the additional planet has to be below 10 $M_\oplus$.
Assuming sinusoidal transit timing variations, I note that I find a good O-C fit for TrES-2 with a FAP of 1.1 %. However, since I find several good periods beyond the best one of 0.2 days, I conclude that I need more observations and maybe with higher precision in order to confirm any one of them as a possible exomoon. Whereas for TrES-1, I found no evidence that a sinusoidal function improved the fit significantly with respect to the linear one.
Sartoretti & Schneider (1999), Doyle & Deeg (2004), Simon et al. (2007) and recently Kipping (2009) discussed the possibility to detect moons around extrasolar planets using a timing offset induced by the wobble of the planet around the planet-moon barycenter. For a given timing offset δt the mass of the possible moon M_m can be estimated using (Sartoretti & Schneider, 1999):

$$M_m \approx \frac{\pi a_P M_P}{a_M P_P} \delta t, \tag{5.8}$$

where a_P is the semi-major axis of the planet, M_P the mass of the transiting planet, a_M semi-major axis of the moon and P_P the period of the planet. A moon around the transiting planet should have a semi-major axis which is between the Roche limit r_{Roche} and the Hill radius r_{Hill} (Kipping, 2009). The Roche limit is given by:

$$r_{Roche} = R_P \left(2\frac{\rho_P}{\rho_m}\right)^{1/3}, \tag{5.9}$$

where ρ_p is the density of the planet and ρ_m the density of the moon. As can be seen from Eq. 5.9, if $\rho_m > 2\rho_p$, the Roche limit is inside the planet. This is most likely the case for a rocky moon around a gas giant planet. Therefore, I do not further consider the Roche limit as lower orbit limit, but the planetary radius. On the other hand, the Hill radius is given by:

$$r_{Hill} = a_P \left(\frac{M_P}{3M_*}\right)^{1/3}, \tag{5.10}$$

where M_* is the mass of the star. Using the radius of the transiting planets, i. e. $R_{P,TrES-1} = 1.081$ R_J or $R_{P,TrES-2} = 1.272$ R_J and Eq. 5.10, I obtain possible orbital periods for a moon around the transiting planets of 4.2 h $< P_m <$ 15 h for TrES-1 and 3.9 h $< P_m <$ 12 h for TrES-2. If I consider only the corresponding period ranges in Fig. 5.9 (red shaded areas), I also find no clear peak there for TrES-1, but for TrES-2 the best peak of 0.2 days is in the range for an exomoon. Using Eq. 5.8 I obtain a possible moon mass of 52 $M_\oplus$ for the best-fit amplitude of this peak.

I note that Barnes & O'Brien (2002) gave an analytical expression for an upper mass limit of possible moons. Generally, the more massive the moon the shorter its lifetime. Lubow et al. (1997) estimated that close-in orbiting planets spin down into synchronous rotation very quickly. Therefore I use the procedure from Barnes & O'Brien (2002) to estimate the upper mass limit of a moon around TrES-1 and TrES-2. I obtain an upper mass limit around TrES-1 on the order of $\sim 10^{-6}$ $M_\oplus$ and around TrES-2 on the order of $\sim 10^{-7}$ $M_\oplus$, similar to one obtained for HD 209 458b by Barnes & O'Brien (2002). This means that moons with masses greater than 10^{-6} $M_\oplus$ will not have survived until now. This upper mass limit is clearly way below my detection limit for masses causing transit timing variations in the system TrES-1 and TrES-2. The closest moon at this upper mass limit would cause a timing amplitude of the order of 10^{-6} s, which is not detectable even from space by several orders of magnitude. Transit duration investigations on TrES-2 performed by Mislis & Schmitt (2009) indicated a decrease of 3 min. between 2006 and 2008 in the duration. However,

in my transit timing analysis, I do not find non-linear deviations of O-C times with a similar magnitude. While I can not provide any firm detection, I can put upper mass limits which are consistent with my observations for TrES-1 and TrES-2, respectively. However, due to the gaped data, it might have been possible that I missed important points in the observed O-C diagram, like e. g. a transit timing measurement at the highest amplitude at the mean-motion resonances. I need at least about 3 years of continuous transit observations and with several transit observations per year in order to avoid the missing of windows of high-amplitude O-C deviations from perturbing bodies, with the maximum amplitudes being observable only during a few transit events, see Fig. 5.6. But even for low-mass perturbers such amplitudes should be easily measurable from ground at mean-motion resonances. On the other hand, outside the mean-motion resonances, I need higher precisions than obtainable from ground to detect the small amplitudes caused by a perturbing body of planetary mass, something that may be expected from the current satellite missions in operation.

Since TrES-2 lies within the field-of-view of the Kepler Space Telescope, a 0.95m space telescope launched in March 2009, any transit timing variation in TrES-2 may be expected to be confirmed in the near future by observations done with this telescope. It will acquire continuous transit observations of TrES-2, observing each transit over a period of 3.5 years, and hence provide better constraints on the transit timing variations.

TABLE 5.4— Comparison of different χ^2 residuals for TrES-1 (upper values) and TrES-2 (lower values).

Fit	χ^2	κ_0 s	κ_1 s	κ_2 10^{-4} s	κ_3 10^{-6} s	ν	False Alarm Probability vs. original ephemeris	offset	linear polynomial
TrES-1									
original ephemeris	50.6	0.0	0.0	-	-	15	-	-	-
offset	39.3	-13.4	0.0	-	-	14	0.065	-	-
linear	28.0	9.5	-0.1	-	-	13	0.021	0.039	-
quadratic	23.7	6.3	0.1	-3.6 ± 3.4	-	12	0.024	0.048	0.17
cubic	23.5	9.3	0.0	1.7	-0.7	11	0.058	0.12	0.38
simulated best-fit O-C	8.7	-	-	-	-	11	-	-	0.05
simulated 1:2 MMR	18.0	-	-	-	-	11	-	-	0.32
simulated 2:3 MMR	20.0	-	-	-	-	11	-	-	0.39
simulated 3:2 MMR	46.0	-	-	-	-	11	-	-	0.85
simulated 5:3 MMR	19.9	-	-	-	-	11	-	-	0.39
simulated 2:1 MMR	158.4	-	-	-	-	11	-	-	0.999
best-fit sinusoidal fit	21.5	-	-	-	-	12	-	-	0.38
TrES-2									
linear	13.1	28.9	-0.9	-	-	5	-	-	-
quadratic	12.6	24.8	-1.0	2.9 ± 21.7	-	4	-	-	0.72
simulated best-fit O-C	0.3	-	-	-	-	3	-	-	0.011
simulated 1:2 MMR	5.3	-	-	-	-	3	-	-	0.39
simulated 2:3 MMR	1.7	-	-	-	-	3	-	-	0.11
simulated 5:3 MMR	4.0	-	-	-	-	3	-	-	0.30
simulated 2:1 MMR	7.1	-	-	-	-	3	-	-	0.49
simulated 3:1 MMR	3.9	-	-	-	-	3	-	-	0.30
best-fit sinusoidal fit	0.7	-	-	-	-	4	-	-	0.011

6

Conclusion and future work

Since the first discoveries of exoplanets, their research is evolving at an astonishing pace. Comparing the different observation techniques, transit observations provide the best method to date to measure physical parameters of these intriguing objects. It is only for transiting exoplanets, where one can obtain a radius estimate, the orbital inclination and can probe the atmosphere. Combining the radius estimation, from transit observations, with the mass estimation, from radial velocity measurements, can yield the planetary density, which can provide clues about its formation history. The discovery of new transiting planets from ground and space facilities will continue to increase our knowledge of these objects.

6.1 Conclusions

Through this work I have reached the following conclusions:

- For the analysis of observations made with the TrES-network and particularly the STARE telescope, a procedure for the detection of transiting planets in photometric surveys has been developed. I begun the analysis by reducing the original images of the telescope to the light curves which have been decorrelated against systematic noise. As a result of transit search in them, numerous candidates have been obtained by TrES. For these candidates, I showed that it is possible to discard some of them through a detailed analysis of their light curves. Detailed photometric and spectroscopic follow-up observations are performed on the surviving candidates. Through these observations I could further eliminate many

false positives, where three of the most promising candidates have to be confirmed with still to be performed high precision radial velocity measurements. However, confirmation of another candidate, TrES-2, in which I contributed with multi-color photometric observations, shows the benefits of this procedure.

- I showed the applications and advantages of IR observations on several examples like HD 189 733b, GJ 436b and CoRoT-2b:
  - HD 189 733b was observed during different primary transit and secondary eclipse phases in the IR wavelength range (K_s filter). I found that both the primary transit depth (2.39 %) and the 2-σ limit of the secondary eclipse depth (< 0.057 %) is consistent with observations from the literature. I estimated the zero-albedo equilibrium temperature to be T_{eq} =1 200 K. Assuming that the planet is in thermal equilibrium ($T_{eq} = T_b$), I estimated an expected secondary eclipse depth in K_s-band of 0.03 %, which is consistent with our observations.
  - Near infrared photometry using the LIRIS instrument on the 4.2m WHT, in the H and K_s filters was performed. CoRoT-2b system was monitored around two expected secondary eclipses in two nights under very good observing conditions. For the depth of the secondary eclipse in H-band a 3-σ upper limit of 0.17 % was found, whereas a tentative eclipse with a depth of 0.16 ± 0.09 % in the K_s-band was detected. The equilibrium temperature of CoRoT-2b was estimated to be 1 964 K. Based on this equilibrium temperature, the expected transit depth was estimated to be 0.11 % in the H-band and to be 0.23 % in the K_s-band. Both depths are consistent with the results from the observations.
  - I presented H-band observations of a transit of the hot Neptune GJ 436b. Once combined to achieve the same sampling equivalent to achieved observations with the Spitzer Space Telescope, our measurements reach comparable precision levels. Both sets of observations were analyzed in a consistent way and the rate of orbital inclination change was measured to be $0.02 \pm 0.04^\circ$ in the time span between the two observations (253.8 d, corresponding to $0.03 \pm 0.05^\circ$ yr^{-1} if extrapolated linearly). The measured times of the transit centers of

the system do not show any departure from linear ephemeris. Put together, these results argue against a further planet candidate, GJ 436c, that had been proposed in the literature.

- I made use of several transit observations of TrES-1 from space with the HST and from ground with the IAC 80-cm telescope (IAC80). On the basis of these observations I performed a statistical study of flux variations in each of the observed events, to investigate whether similar flux increases are present in other parts of the data set. The HST observation present a single clear flux rise during a transit, whereas the ground observations led to the detection of 2 further such events but with low significance. In the case of having observed a starspot being the source of the event in the HST data, assuming a central impact between the spot and the transiting planet, one would obtain a lower limit for the spot radius of 42 000 km. For this radius, the spot temperature would be 4 690 K, 560 K lower than the stellar surface of 5 250 K. For the alternative of a second transiting planet, I can set a lower limit for its radius at 0.37 R_J and for periods of less than 10.5 days, I can also set an upper limit at 0.72 R_J. Assuming a conventional interpretation, the HST observation then constitutes the detection of a starspot. Alternatively, this flux rise might also be caused by an additional transiting planet, which would be the first detection of a system with 2 transiting planets.

- Using the IAC80 telescope, I observed transits of TrES-1 and TrES-2 over several years. Based on these observations and previously published work, I studied the observed light curves and searched for variations in the difference between observed and calculated (based on a fixed ephemeris) transit times. To model possible transit timing variations, I used polynomials of different orders, simulated O-C diagrams corresponding to a perturbing third mass and sinusoidal fits. For each model I calculated the χ^2 residuals and the False Alarm Probability (FAP). I found for TrES-1 that the linear and quadratic polynomial fits describe the general trends in data best. I found no significantly low peak in the χ^2 residuals fitting N-body simulations to my observations, but I found two high χ^2 values at the 3:2 and 2:1 MMRs and additionally I put upper limits on the masses of perturbers consistent with my observations. I also found no significantly low χ^2 values for a sine fit to the O-C residuals of TrES-1. As for TrES-2, the linear fit indicated a different ephemeris. I obtained several low χ^2

values for simulated perturbers, but none of them in the MMRs and I put upper limits on possible perturber's masses. A good fit for TrES-2 with a low FAP was found for a sine function with a period of 0.2 days, compatible with a moon around TrES-2, and an amplitude of 57 s, but it was not a uniquely low χ^2 value that would indicate a clear signal. In conclusion, for TrES-1 I can exclude planetary companions (> 1 $M_\oplus$) in the 3:2 and 2:1 MMRs with high FAPs based on my transit observations from ground. Additionally, the presence of a light time effect in the system TrES-1, caused by a potential body fulfilling $\frac{m_3}{M_\odot} \geq 34 \left(\frac{\theta}{\mathrm{arcsec}}\right)^2$, is possible. This equation will help to constrain the mass of stars appearing in high-resolution images. As for TrES-2, I found a better ephemeris of $T_c = 2\,453\,957.63512(28) + 2.4706101(18) \times \mathrm{Epoch}$. In both cases, TrES-1 and TrES-2, I was able to put upper limits on the presence of additional perturber masses. I also conclude that any sinusoidal variations that might be indicative of exomoons need to be confirmed with higher statistical significance by further observations, noting that TrES-2 is in the field-of-view of the Kepler Space Telescope.

6.2 Future work

Future work will mainly concentrate on the detection of smaller transiting planets, i. e. those of less than Neptune mass. In particular, it will focus on the investigation of the properties of this class of planet – e. g. their abundance around stars in the Solar neighborhood, their eccentricity, their mass function and the metallicity of their host-stars – and compare them to those of known transiting gas giants. These goals will be accomplished through space-based mission like the CNES-led CoRoT mission or the NASA's Kepler mission. In fact, space-based missions like the CNES-led CoRoT mission, the ESA's PLATO mission or the NASA's Kepler, SIM, TESS and JWST mission will become of highest importance in exoplanetary science.
However, ground-based surveys have also improved their detection capabilities down to Neptune mass exoplanets, like recently shown by the HAT network with the discovery of HAT-P-11b. HAT-P-11b is the only Neptune mass planet discovered by a ground-based photometric exoplanet survey. So far the HAT network has only observed in the northern hemisphere, but it will expand towards the southern one in 2009. Multiple sites in Chile, Australia and Namibia will allow near round-the-clock observations. HAT South is supposed to detect 25 planets transiting bright stars every year.
The network TrES pioneering in the field of wide-field surveys for transiting

exoplanets around bright stars found 4 transiting planets. However, TrES is out-dated; its small, compared to WASP and HAT, sky coverage is no more competitive and it will be decommissioned soon. WASP, which has been operating for several years in La Palma, has also generated increasing number of planet detections, leading to the discovery of 10 planets only in 2008.
So far the high-precision spectrograph HARPS is the only instrument in the world reaching a Doppler precision below 1 m/s. Therefore, new ground-based instruments are underway to confirm smaller mass exoplanet, like HARPS North for the WHT; ESPRESSO which is proposed as a VLT instrument of second generation and the spectrograph CODEX for the future E-ELT.
In addition, we start to explore the atmospheres of hot Jupiters and to determine their composition even from ground. Until recently it was only possible for space-based missions like Spitzer and HST to probe the atmosphere; the possibility from ground will allow to observe more systems in shorter time and hence allow first statistical studies.
The quest to discover additional multi-planet systems will continue, in particular ones that exhibit transits. To this point, no extrasolar planetary system with multiple transiting planets has been detected. Establishing the co-planarity of multi-planet systems is an important investigation, either using the existence of multiple transiting components or of narrow-angle astrometry in upcoming space mission like SIM.
The start of the Gran Telescopio Canarias (GTC) in 2009 offers us excellent opportunities to characterize discovered exoplanets. GTC is a telescope with a 10.4 meters primary mirror composed of 36 segments. One idea would be to observe transits in different filters with the OSIRIS instrument. We expect to observe minor differences in the transit depths with wavelengths, as lighter elements extend further into the space than heavier ones. Using spectroscopic observations with OSIRIS and its tunable filters, we could examine the different layers of the atmosphere and measure the absorption lines during the transit. This may help us understand the atmospheric models of extrasolar planets. During observations we would choose the narrowest bandwidth possible and simultaneously maintain a photometric precision and a high cadence, without unnecessarily increasing the exposure time. GTC/OSIRIS may also allow the follow-up of exoplanets showing a swallower transit like e. g. CoRoT-7b with high-precision photometry. One way to obtain this aim would be to observe CoRoT-7b using the fast photometry mode of OSIRIS and another possibility would be to use the 36 GTC mirror segments to obtain 36 images of the target by displacing the actuators of the segments in a regular pattern; both configurations are the subject of proposals on which I participate.
This wealth of potential observations shows that the topic of exoplanet research

has gone from a phase of discovery into one aiming at a best-possible characterization of the systems found.

Bibliography

Agol, E., Cowan, N. B., Bushong, J., Knutson, H., Charbonneau, D., Deming, D., & Steffen, J. H. 2009, in IAU Symposium, Vol. 253, IAU Symposium, 209–215

Agol, E., Steffen, J., Sari, R., & Clarkson, W. 2005, MNRAS, 359, 567

Agol, E., & Steffen, J. H. 2007, MNRAS, 374, 941

Alard, C. 2000, A&AS, 144, 363

Alard, C., & Lupton, R. H. 1998, ApJ, 503, 325

Allen, C. W. 1976, Astrophysical Quantities (Astrophysical Quantities, London: Athlone (3rd edition), 1976)

Alonso, R. 2005, PhD thesis, Universidad de La Laguna, La Laguna, Spain

Alonso, R., Barbieri, M., Rabus, M., Deeg, H. J., Belmonte, J. A., & Almenara, J. M. 2008a, A&A, 487, L5

Alonso, R., Deeg, H. J., Brown, T. M., & Belmonte, J. A. 2004a, Astronomische Nachrichten, 325, 594

Alonso, R., et al. 2004b, ApJ, 613, L153

—. 2008b, A&A, 482, L21

Bakos, G. Á., et al. 2009, ArXiv e-prints

Barbieri, M., et al. 2007, A&A, 476, L13

Barnes, J. R., Barman, T. S., Prato, L., Segransan, D., Jones, H. R. A., Leigh, C. J., Collier Cameron, A., & Pinfield, D. J. 2007, MNRAS, 382, 473

Barnes, J. W., & O'Brien, D. P. 2002, ApJ, 575, 1087

Bean, J. L. 2009, ArXiv e-prints

Bean, J. L., & Seifahrt, A. 2008, A&A, 487, L25

Beaulieu, J. P., Carey, S., Ribas, I., & Tinetti, G. 2008, ApJ, 677, 1343

Bouchy, F., & Halbwachs, J.-L. 2006, Formation planétaire et exoplanètes, Ecole thématique du CNRS, Goutelas (Loire), 23 - 27 mai 2005 Edited by J.-L. Halbwachs, D. Egret, and J.-M. Hameury. Strasbourg: Observatoire astronomique de Strasbourg et Société Française d'Astronomie et d'Astrophysique (SF2A), 2006, p. 27-53 http://astro.u-strasbg.fr/goutelas/g2005/, 28, 27

Bouchy, F., et al. 2005, A&A, 444, L15

Brown, T. M. 2003, ApJ, 593, L125

Brown, T. M., Charbonneau, D., Gilliland, R. L., Noyes, R. W., & Burrows, A. 2001, ApJ, 552, 699

Burrows, A., Budaj, J., & Hubeny, I. 2008, ApJ, 678, 1436

Burrows, A., Hubeny, I., & Sudarsky, D. 2005, ApJ, 625, L135

Burrows, A., Sudarsky, D., & Hubeny, I. 2006, ApJ, 650, 1140

Butler, R. P., Vogt, S. S., Marcy, G. W., Fischer, D. A., Wright, J. T., Henry, G. W., Laughlin, G., & Lissauer, J. J. 2004, ApJ, 617, 580

Charbonneau, D., Brown, T. M., Burrows, A., & Laughlin, G. 2007, in Protostars and Planets V, ed. B. Reipurth, D. Jewitt, & K. Keil, 701–716

Charbonneau, D., Brown, T. M., Latham, D. W., & Mayor, M. 2000, ApJ, 529, L45

Charbonneau, D., Brown, T. M., Noyes, R. W., & Gilliland, R. L. 2002, ApJ, 568, 377

Charbonneau, D., Knutson, H. A., Barman, T., Allen, L. E., Mayor, M., Megeath, S. T., Queloz, D., & Udry, S. 2008, ApJ, 686, 1341

Charbonneau, D., et al. 2005, ApJ, 626, 523

Claret, A. 2000, A&A, 363, 1081

Claret, A., Diaz-Cordoves, J., & Gimenez, A. 1995, A&AS, 114, 247

de Mooij, E. J. W., & Snellen, I. A. G. 2009, A&A, 493, L35

Deeg, H. J. 1998, Earth Moon and Planets, 81, 73

—. 2008, ArXiv e-prints, 807

Deeg, H. J., & Doyle, L. R. 2001, in Third Workshop on Photometry, p. 85, ed. W. J. Borucki & L. E. Lasher, 85–+

Deeg, H. J., Doyle, L. R., Kozhevnikov, V. P., Blue, J. E., Martín, E. L., & Schneider, J. 2000, A&A, 358, L5

Deeg, H. J., Garrido, R., & Claret, A. 2001, New Astronomy, 6, 51

Deeg, H. J., Ocaña, B., Kozhevnikov, V. P., Charbonneau, D., O'Donovan, F. T., & Doyle, L. R. 2008, A&A, 480, 563

Deleuil, M., et al. 2008, A&A, 491, 889

Deming, D. 2009, in IAU Symposium, Vol. 253, IAU Symposium, 197–207

Deming, D., Brown, T. M., Charbonneau, D., Harrington, J., & Richardson, L. J. 2005a, ApJ, 622, 1149

Deming, D., Harrington, J., Laughlin, G., Seager, S., Navarro, S. B., Bowman, W. C., & Horning, K. 2007, ApJ, 667, L199

Deming, D., Harrington, J., Seager, S., & Richardson, L. J. 2006, ApJ, 644, 560

Deming, D., Seager, S., Richardson, L. J., & Harrington, J. 2005b, Nature, 434, 740

Demory, B.-O., et al. 2007, A&A, 475, 1125

Desert, J.-M., Lecavelier des Etangs, A., Hebrard, G., Sing, D. K., Ehrenreich, D., Ferlet, R., & Vidal-Madjar, A. 2009, ArXiv e-prints

Doyle, L. R., & Deeg, H.-J. 2004, in IAU Symposium, Vol. 213, Bioastronomy 2002: Life Among the Stars, ed. R. Norris & F. Stootman, 80–+

Doyle, L. R., et al. 1998, in Astronomical Society of the Pacific Conference Series, Vol. 134, Brown Dwarfs and Extrasolar Planets, ed. R. Rebolo, E. L. Martin, & M. R. Zapatero Osorio, 224–+

Dunham, E. W., Mandushev, G. I., Taylor, B. W., & Oetiker, B. 2004, PASP, 116, 1072

Ehrenreich, D., Hébrard, G., Lecavelier des Etangs, A., Sing, D. K., Désert, J.-M., Bouchy, F., Ferlet, R., & Vidal-Madjar, A. 2007, ApJ, 668, L179

Fabrycky, D. C., & Winn, J. N. 2009, ApJ, 696, 1230

Fortney, J. J. 2009, in IAU Symposium, Vol. 253, IAU Symposium, 247–253

Fortney, J. J., Lodders, K., Marley, M. S., & Freedman, R. S. 2008, ApJ, 678, 1419

Fossey, S. J., Waldmann, I. P., & Kipping, D. M. 2009, MNRAS, L224+

Gaudi, B. S., & Winn, J. N. 2007, ApJ, 655, 550

Gillon, M., et al. 2007a, A&A, 471, L51

—. 2007b, A&A, 472, L13

Giménez, A. 2006a, A&A, 450, 1231

—. 2006b, ApJ, 650, 408

Gimenez, A., & Garcia-Pelayo, J. M. 1983, Ap&SS, 92, 203

Grillmair, C. J., Charbonneau, D., Burrows, A., Armus, L., Stauffer, J., Meadows, V., Van Cleve, J., & Levine, D. 2007, ApJ, 658, L115

Grillmair, C. J., et al. 2008, Nature, 456, 767

Hébrard, G., et al. 2008, A&A, 488, 763

Henry, G. W., Marcy, G. W., Butler, R. P., & Vogt, S. S. 2000, ApJ, 529, L41

Hog, E., & et al. 2000, The Tycho-2 catalogue : positions, proper motions and two-colour photometry of the 2.5 million brightest stars (The Tycho-2 catalogue : positions, proper motions and two-colour photometry of the 2.5 million brightest stars [machine-readable files] /E. Hog ... [et al] Copenhagen : Copenhagen University, 2000. (ISO 9660 CD- ROM.) CD-25.)

Holman, M. J., & Murray, N. W. 2005, Science, 307, 1288

Holman, M. J., et al. 2007, ApJ, 664, 1185

Hrudková, M., Skillen, I., Benn, C., Pollacco, D., Gibson, N., Joshi, Y., Harmanec, P., & Tulloch, S. 2009, in IAU Symposium, Vol. 253, IAU Symposium, 446–449

Irwin, J. B. 1959, AJ, 64, 149

Jha, S., Charbonneau, D., Garnavich, P. M., Sullivan, D. J., Sullivan, T., Brown, T. M., & Tonry, J. L. 2000, ApJ, 540, L45

Kalas, P., et al. 2008, Science, 322, 1345

Kane, S. R. 2007, MNRAS, 380, 1488

Kipping, D. M. 2009, MNRAS, 392, 181

Knutson, H. A., Charbonneau, D., Allen, L. E., Burrows, A., & Megeath, S. T. 2008, ApJ, 673, 526

Knutson, H. A., et al. 2007, Nature, 447, 183

—. 2009, ApJ, 690, 822

Konacki, M., Torres, G., Jha, S., & Sasselov, D. D. 2003, Nature, 421, 507

Kovács, G., Bakos, G., & Noyes, R. W. 2005, MNRAS, 356, 557

Kovacs, G., & Bakos, G. A. 2006, ArXiv Astrophysics e-prints

Kovács, G., Zucker, S., & Mazeh, T. 2002, A&A, 391, 369

Laughlin, G., Deming, D., Langton, J., Kasen, D., Vogt, S., Butler, P., Rivera, E., & Meschiari, S. 2009, Nature, 457, 562

Laughlin, G., Wolf, A., Vanmunster, T., Bodenheimer, P., Fischer, D., Marcy, G., Butler, P., & Vogt, S. 2005, ApJ, 621, 1072

Lovis, C., et al. 2006, Nature, 441, 305

Lubow, S. H., Tout, C. A., & Livio, M. 1997, ApJ, 484, 866

Mandel, K., & Agol, E. 2002, ApJ, 580, L171

Marois, C., Macintosh, B., Barman, T., Zuckerman, B., Song, I., Patience, J., Lafrenière, D., & Doyon, R. 2008, Science, 322, 1348

Mayor, M., & Queloz, D. 1995, Nature, 378, 355

Mazeh, T., Tamuz, O., & Zucker, S. 2006a, ArXiv Astrophysics e-prints

Mazeh, T., Tamuz, O., Zucker, S., Udalski, A., & The Wasp Consortium. 2006b, in Tenth Anniversary of 51 Peg-b: Status of and prospects for hot Jupiter studies, ed. L. Arnold, F. Bouchy, & C. Moutou, 165–172

McLaughlin, D. B. 1924, ApJ, 60, 22

Miller-Ricci, E., et al. 2008a, ApJ, 682, 593

—. 2008b, ApJ, 682, 586

Mislis, D., & Schmitt, J. H. M. M. 2009, A&A, 500, L45

Morales, J. C., et al. 2009, ApJ, 691, 1400

Moutou, C., et al. 2009, A&A, 498, L5

Nesvorný, D., & Morbidelli, A. 2008, ApJ, 688, 636

Nutzman, P., Charbonneau, D., Winn, J. N., Knutson, H. A., Fortney, J. J., Holman, M. J., & Agol, E. 2009, ApJ, 692, 229

O'Donovan, F. T., Charbonneau, D., & Kotredes, L. 2003, in Bulletin of the American Astronomical Society, 583–+

O'Donovan, F. T., et al. 2006, ApJ, 651, L61

O'Neal, D., Saar, S. M., & Neff, J. E. 1998, ApJ, 501, L73+

Papaloizou, J. C. B., & Terquem, C. 2006, Reports on Progress in Physics, 69, 119

Perryman, M. A. C. 2000, Reports of Progress in Physics, 63, 1209

Pont, F. 2006, in Tenth Anniversary of 51 Peg-b: Status of and prospects for hot Jupiter studies, ed. L. Arnold, F. Bouchy, & C. Moutou, 153–164

Pont, F., Knutson, H., Gilliland, R. L., Moutou, C., & Charbonneau, D. 2008, MNRAS, 385, 109

Pont, F., Zucker, S., & Queloz, D. 2006, MNRAS, 1146

Pont, F., et al. 2007, A&A, 476, 1347

Press, W. H., Teukolsky, S. A., Vetterling, W. T., & Flannery, B. P. 1992, Numerical recipes in FORTRAN. The art of scientific computing (Cambridge: University Press, —c1992, 2nd ed.)

Rabus, M. 2007, Master's thesis, Universidad de La Laguna, La Laguna, Spain

Rabus, M., et al. 2009, A&A, 494, 391

Raetz, S., et al. 2009a, ArXiv e-prints

—. 2009b, ArXiv e-prints

Redfield, S., Endl, M., Cochran, W. D., & Koesterke, L. 2008, ApJ, 673, L87

Ribas, I., Font-Ribera, A., & Beaulieu, J.-P. 2008, ApJ, 677, L59

Richardson, L. J., Deming, D., Horning, K., Seager, S., & Harrington, J. 2007, Nature, 445, 892

Richardson, L. J., Harrington, J., Seager, S., & Deming, D. 2006, ApJ, 649, 1043

Rossiter, R. A. 1924, ApJ, 60, 15

Sartoretti, P., & Schneider, J. 1999, A&AS, 134, 553

Schneider, J. 2005, in Astronomical Society of the Pacific Conference Series, Vol. 335, The Light-Time Effect in Astrophysics: Causes and cures of the O-C diagram, ed. C. Sterken, 191–+

Schneider, J., & Doyle, L. R. 1995, Earth Moon and Planets, 71, 153

Seager, S., & Mallén-Ornelas, G. 2003, ApJ, 585, 1038

Seager, S., & Sasselov, D. D. 2000, ApJ, 537, 916

Silva, A. V. R. 2003, ApJ, 585, L147

Simon, A., Szatmáry, K., & Szabó, G. M. 2007, A&A, 470, 727

Sing, D. K., & López-Morales, M. 2009, A&A, 493, L31

Sirko, E., & Paczyński, B. 2003, ApJ, 592, 1217

Snellen, I. A. G., de Mooij, E. J. W., & Albrecht, S. 2009a, ArXiv e-prints

—. 2009b, Nature, 459, 543

Southworth, J. 2008, MNRAS, 386, 1644

Sozzetti, A., Torres, G., Charbonneau, D., Latham, D. W., Holman, M. J., Winn, J. N., Laird, J. B., & O'Donovan, F. T. 2007, ApJ, 664, 1190

Sozzetti, A., Yong, D., Carney, B. W., Laird, J. B., Latham, D. W., & Torres, G. 2006, AJ, 131, 2274

Sozzetti, A., et al. 2004, ApJ, 616, L167

Steffen, J. H., & Agol, E. 2005, MNRAS, 364, L96

Stetson, P. B. 1987, PASP, 99, 191

Stetson, P. B. 1992, in ASP Conf. Ser. 25: Astronomical Data Analysis Software and Systems I, ed. D. M. Worrall, C. Biemesderfer, & J. Barnes, 297–+

Swain, M. R., Bouwman, J., Akeson, R. L., Lawler, S., & Beichman, C. A. 2008a, ApJ, 674, 482

Swain, M. R., Vasisht, G., & Tinetti, G. 2008b, Nature, 452, 329

Swain, M. R., Vasisht, G., Tinetti, G., Bouwman, J., Chen, P., Yung, Y., Deming, D., & Deroo, P. 2009, ApJ, 690, L114

Tamuz, O., Mazeh, T., & Zucker, S. 2005, MNRAS, 356, 1466

Terquem, C., & Halbwachs, J.-L. 2006a, Formation planétaire et exoplanètes, Ecole thématique du CNRS, Goutelas (Loire), 23 - 27 mai 2005 Edited by J.-L. Halbwachs, D. Egret, and J.-M. Hameury. Strasbourg: Observatoire astronomique de Strasbourg et Société Française d'Astronomie et d'Astrophysique (SF2A), 2006, p. 99-129 http://astro.u-strasbg.fr/goutelas/g2005/, 28, 99

—. 2006b, Formation planétaire et exoplanètes, Ecole thématique du CNRS, Goutelas (Loire), 23 - 27 mai 2005 Edited by J.-L. Halbwachs, D. Egret, and J.-M. Hameury. Strasbourg: Observatoire astronomique de Strasbourg et Société Française d'Astronomie et d'Astrophysique (SF2A), 2006, p. 131-154 http://astro.u-strasbg.fr/goutelas/g2005/, 28, 131

Tinetti, G., & Beaulieu, J.-P. 2009, in IAU Symposium, Vol. 253, IAU Symposium, 231–237

Tinetti, G., et al. 2007, Nature, 448, 169

Torres, G., Konacki, M., Sasselov, D. D., & Jha, S. 2004, ApJ, 614, 979

Torres, G., Winn, J. N., & Holman, M. J. 2008, ApJ, 677, 1324

Udalski, A., et al. 2002, Acta Astronomica, 52, 1

Vidal-Madjar, A., Lecavelier des Etangs, A., Désert, J.-M., Ballester, G. E., Ferlet, R., Hébrard, G., & Mayor, M. 2003, Nature, 422, 143

Vidal-Madjar, A., et al. 2004, ApJ, 604, L69

Vogt, S. S., et al. 1994, in Presented at the Society of Photo-Optical Instrumentation Engineers (SPIE) Conference, Vol. 2198, Proc. SPIE Instrumentation in Astronomy VIII, David L. Crawford; Eric R. Craine; Eds., Volume 2198, p. 362, ed. D. L. Crawford & E. R. Craine, 362–+

Winn, J. N., Holman, M. J., & Roussanova, A. 2007, ApJ, 657, 1098

Wolszczan, A., & Frail, D. A. 1992, Nature, 355, 145

Wuchterl, E. 2007, Extrasolar Planets (Eds. H. Deeg, J. A. Belmonte & A. Aparicio, Cambridge University Press, p. 89), in preparation

Zakamska, N. L., & Tremaine, S. 2005, AJ, 130, 1939